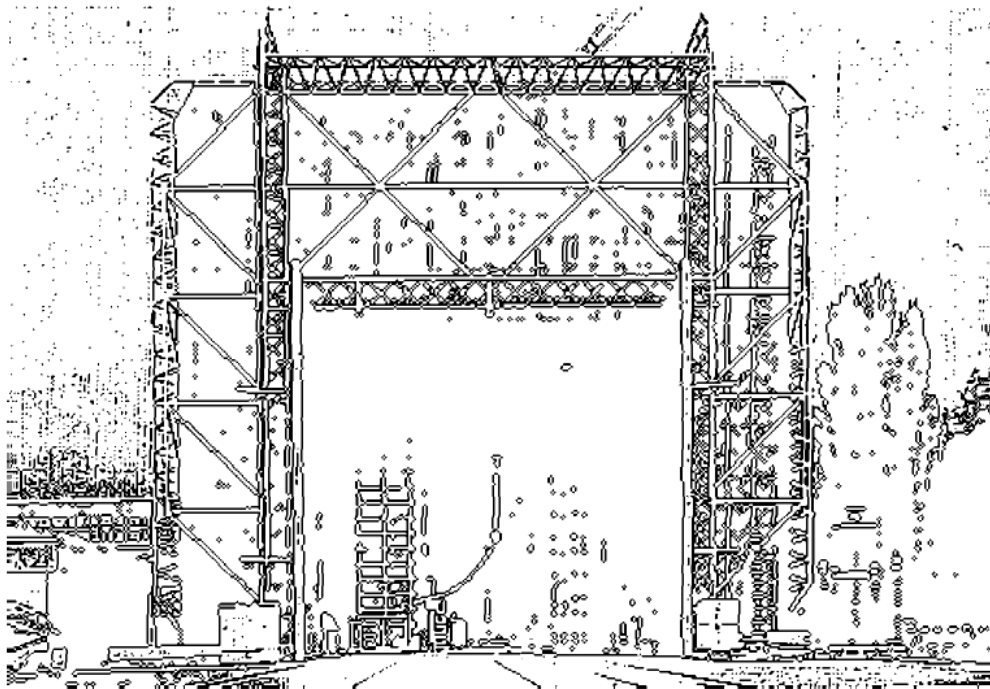




TECHNISCHE UNIVERSITÄT GRAZ

DISSERTATION



INSTITUT FÜR HOCHSPANNUNGSTECHNIK
UND SYSTEMMANAGEMENT

LHC Beam Dump System: Analysis of beam commissioning, performance and the consequences of abnormal operation

Analyse des Systems für Strahlextraktion im Large Hadron Collider hinsichtlich anormaler Betriebsparameter und deren Auswirkungen auf Inbetriebnahme und Betrieb.

DISSERTATION

zur Erlangung des Grades eines Doktors der technischen Wissenschaften

von

Dipl.-Ing. Thomas Kramer

1. Begutachter: o.Univ.-Prof. Dipl.-Ing. Dr. techn. Dr. h.c. Hans Michael Muhr
2. Begutachter: Privatdoz. Dipl.-Ing. Dr.techn. Michael Benedikt
CERN Betreuer: Dr. Brennan Goddard

Institut für Hochspannungstechnik und Systemmanagement
Technische Universität Graz

Genf, im Mai 2011

EIDESSTATTLICHE ERKLÄRUNG

Ich erkläre an Eides statt, dass ich die vorliegende Arbeit selbstständig verfasst, andere als die angegebenen Quellen/Hilfsmittel nicht benutzt und die den benutzten Quellen wörtlich und inhaltlich entnommenen Stellen als solche kenntlich gemacht habe.

Graz, am

.....
(Unterschrift)

Englische Fassung:

STATUTORY DECLARATION

I declare that I have authored this thesis independently, that I have not used other than the declared sources / resources and that I have explicitly marked all material which has been quoted either literally or by content from the used sources.

.....
date

.....
(signature)

Kurzfassung

Im LHC werden bei nomineller Intensität Protonen auf bis zu 7 TeV beschleunigt und erreichen insgesamt eine Energie von 360 MJ je Strahl, ausreichend um eine Menge von annähernd 500 kg Kupfer zu schmelzen. Die im LHC eingesetzten Magnetsysteme speichern durch ihre Induktivitäten darüber hinaus bei maximalem Strom eine Energie von bis zu 10 GJ. Es ist offensichtlich, dass bei Beschleunigeranlagen dieser Größenordnung schwerwiegende maschinengefährdende Situationen auftreten können. Um dem entgegenzuwirken, wurde ein ausgeklügeltes Maschinenschutzsystem entwickelt. Ein wesentlicher Aktuator dieses Systems ist das LHC Beam Dump System (LBDS) zur schnellen Strahlextraktion. Das LBDS dient sowohl zur geplanten Extraktion von Teilchen z.B. nach der Beendigung eines Kollisionsexperimentes, als auch zur sicheren und schnellen Entsorgung von voraussichtlich nicht mehr beherrschbarem Strahl. Die Installation in Punkt 6 des LHC umfasst hierbei je Strahlrichtung 15 schnelle „Kicker“-magneten (MKD) mit horizontaler Ablenkung, gefolgt von 15 DC „Septum“-Magneten mit vertikaler Ablenkung und 10 „Diluter“-Magneten zur horizontalen und vertikalen Intensitätssteuerung am Target.

Diese Dissertation beschäftigt sich mit der Analyse des LBDS hinsichtlich der schnellen Extraktion von Teilchen im Normalbetrieb, wie auch im Falle auftretender Fehler und den Umständen besonderer kritischer Systemparameter. Dazu wurde unter Zuhilfenahme des Beschleunigersimulationscodes MAD-X eine variantenreiche und parallel arbeitende Simulationsumgebung zur Bestimmung der Teilchenflugbahnen unter den besonderen Betriebsparametern des LBDS geschaffen. Hierbei werden realistische Teilchenverteilungen erzeugt und eine den realen Betriebsumständen möglichst nahe Simulationsmaschine aufgesetzt, welche Magnetfeldfehler, Ausrichtungs- und Vermessungstoleranzen, mechanische Aperturen und Messfehler der Strahlinstrumentierung genauso berücksichtigt wie die Einstellungen der installierten Schutzelemente und Kollimatoren. Ein wesentlicher Punkt der Simulationsarchitektur ist hierbei die Berücksichtigung des in $2.8 \mu\text{s}$ ansteigenden Magnetfeldes der „MKD-Kicker“-Magnetgruppe auf einer 5 ns Zeitbasis um umlaufaktualisierte Magnetfeldeinflüsse abbilden zu können sowie die Position des variablen Hauptkollimators TCDQ. Der hierfür entwickelte Simulationscode nutzt die am CERN zur Verfügung stehende IT-Infrastruktur unter Ausnutzung von parallelen Algorithmen und variabler Verteilung der Simulation auf die zur Verfügung stehende CPU Anzahl.

Mit der entwickelten Methodologie wurde in einem ersten Schritt die Grundlage geschaffen, bereits vor der Erstinbetriebnahme wesentliche sicherheitsrelevante Parameter des LBDS durch Simulationen zu ermitteln bzw. zu überprüfen.

Die Resultate dieser Arbeit zeigen auch, dass die Auslegung des LBDS wesentliche strahlphysikalische Risiken einer Extraktion bei hoher Intensität und/oder Energie unter Normalbedingungen sehr gut berücksichtigt. Eventuelle Möglichkeiten von partiellem Strahlverlust unter anormalen Betriebsumständen werden diskutiert.

Die zukünftig genauere Validierung der Simulationsergebnisse durch Messung und Beobachtung wird es erlauben, die sichere Betriebsparametereinstellung von Schutzsystemen für höhere Energiebereiche von Anfang an besser zu ermöglichen. Dies ist von besonderem Interesse, da für solche Energiebereiche direkte Messungen bzw. Tests aus Gründen der Maschinensicherheit und auch auf Grund sehr langer Strahlproduktionszyklen nur erschwert durchführbar sind und so mit Hilfe von Simulationserkenntnissen wertvolle Maschinenentwicklungszeit gezielt genützt werden kann.

Abstract

The LHC accelerates proton beams to a momentum of up to 7 TeV/c. At this energy level and with nominal beam intensity the stored energy of 360 MJ per beam is sufficient to melt 500 kg of copper. In addition up to 10 GJ are stored within the LHC magnet system at top energy. It is obvious that such a machine needs well designed safety and protection systems. The LHC Beam Dump System (LBDS) is such a system and one of the most critical once concerning machine protection and safe operation. It is used to dispose of high intensity beams between 450 GeV and 7 TeV and is thus designed to fast extract beam in a loss free way and to transfer it to an external absorber. For each ring systems of 15 horizontal fast kicker magnets (MKD), 15 vertically deflecting magnetic septa (MSD) and 10 diluter kicker magnets (MKB) are installed.

This thesis is concerned with the analysis of the LBDS performance under normal operating parameters as well as under abnormal conditions like in the event of asynchronous beam abort or missing MKD elements. Therefore a sophisticated simulation environment was developed based on the use of the MAD-X tracking code. A system of tracking jobs was set up to study failure cases and losses for various dump events. Those jobs can be distributed to available CPU power and be calculated in parallel.

Studies into the consequences of abnormal beam dump actions have been performed. Different error scenarios have been evaluated including an asynchronous dump action, prefire cases, and the impact of different orbit and collimator settings. Losses at locations in the ring and the beam dump transfer lines have been quantified as a function of different settings of the dump system protection elements. The implications for the setup and operation of these protection elements are discussed.

Particle distributions can be created according to the used orbit. Simulations with different orbit parameters (including magnet field errors, beam position read out errors, misalignments, mechanical apertures and tolerances) as well as different collimator settings for the TCDQ protection system in IR6 can be done in parallel, considering time dependent kicks as applied for the fast MKD and MKB magnets with a 5ns resolution.

The developed architecture allows simulating on the basis of realistic machine settings and allowed to verify in a first step some safety relevant LBDS design parameters already before the actual beam commissioning started.

The results obtained show that the LBDS is very well designed, with sufficient margin to accept the failure cases which are expected to happen during its operation. Eventual partial beam losses during abnormal operation parameters are discussed.

The future precise validation of simulation results will allow to use such techniques to evaluate safety and operation parameter settings for higher energy levels. This is particularly interesting as machine development and measurement at top energy is time consuming due to long beam generation cycles as well as it is a concern of machine safety. Hence simulations can give useful starting points to minimize the measurement effort.

Acknowledgement

The author would like to thank everybody who directly or indirectly supported this work.
This is more appreciated than many words could tell.

This thesis was performed within the Austrian Doctoral Student Program at CERN and financed by the
Austrian Federal Ministry of Science and Research.

Contents

Introduction	4
1 The LHC Accelerator and its Machine Protection System.....	7
1.1 The CERN injector chain	8
1.2 The LHC operating cycle	9
1.3 Classification of beam losses in the LHC.....	9
1.3.1 Normal beam losses.....	9
1.3.2 Abnormal beam losses.....	9
1.4 The LHC Machine Protection System (MPS)	10
1.4.1 The Beam Loss Monitor system (BLM)	10
1.4.2 The LHC BPMs.....	10
1.4.3 The Quench Protection System (QPS)	10
1.4.4 The Powering Interlock System	10
1.4.5 The Fast Magnet Current change Monitors (FMCM)	11
1.4.6 Safe Machine Parameter System (SMP) and Software Interlock System (SIS).....	11
1.4.7 The Beam Interlock System (BIS)	11
1.4.8 The Beam Dump System.....	12
1.5 The LHC beam cleaning and collimation system.....	12
2 Introduction to Accelerator Physics.....	14
2.1 Basic relativistic relations:	14
2.2 Reference coordinate system.....	15
2.2.1 The MAD-X coordinate system	15
2.3 Charged particle focussing and guiding	15
2.3.1 Magnet multipoles	16
2.3.2 Lorentz force	16
2.3.3 Equation of motion.....	18
2.3.4 Transfer matrices	20
2.3.5 Dispersion.....	21
2.3.6 Emittance and acceptance	21
2.3.7 Tune.....	22
2.3.8 Chromaticity.....	23
2.3.9 Longitudinal dynamics	23
3 Methodology of Particle Tracking Simulations	25
3.1 The crucial performance limitation: CPU time	25
3.2 The MAD-X code.....	25
3.2.1 Frequently used MAD-X modules	26
3.3 The LHC MAD-X Model.....	27
3.4 Random numbers.....	28
4 Beam Dump and Extraction Systems	30
4.1 Main machine elements used for beam dump and extraction systems.....	30
4.1.1 Kicker magnets.....	30
4.1.2 Magnetic septa.....	32
4.1.3 Electrostatic septa.....	33
4.1.4 Dump elements.....	34
4.2 Overview of beam dump and extraction systems.....	34
4.2.1 Fast beam extraction systems	34
4.2.2 Slow beam extraction systems	36
4.3 Commissioning of the SPS LSS6 beam extraction for LHC.....	37
4.4 Investigation of abnormal operation of the SPS beam dump system.....	39
4.4.1 The SPS and its beam dump system.....	39
4.4.2 Failure cases	40

4.4.3	Tracking studies - Methodology.....	41
4.4.4	Beams and Aperture Model.....	41
4.4.5	Post Processing.....	41
4.4.6	Simulation results for the asynchronous dump (sweep) cases	41
4.4.7	Simulation results for the kicker failure (spark) cases	42
4.4.8	Measurements.....	43
4.4.9	Conclusions	44
4.5	Design considerations for the PS2 beam dump system.....	44
4.5.1	Functions and Beam Loads	44
4.5.2	Dump concepts.....	46
4.5.3	Residual dose rate issues	47
4.5.4	Conclusions	48
5	The LHC Beam Dump System (LBDS)	49
5.1	The extraction region layout.....	49
5.2	The LBDS architecture.....	50
5.3	The beam dump trigger and retrigger system.....	51
5.3.1	The MKD generators.....	53
5.3.2	Retrigger, prefire and asynchronous dumps.....	55
5.4	Beam energy tracking system (BETS)	55
5.5	Main hardware components of the extraction system	57
5.5.1	The beam extraction kicker (MKD)	57
5.5.2	Q4 Quadrupole	57
5.5.3	Extraction septa MSD	58
5.5.4	Septum protection elements – TCDS	59
5.5.5	Alignment of the TCDS and MSD	60
5.5.6	Fast-pulsed dilution magnets MKB.....	61
5.5.7	The TCDQ/TCSG/TCDQM protection devices	61
5.5.8	Beam dump absorber block TDE	63
5.5.9	Beam instrumentation.....	63
5.5.10	Abort gap cleaning and abort gap monitor	64
5.6	Reliability of the LBDS.....	64
6	LBDS – Results of Tracking Studies.....	66
6.1	Simulation principle, methods and used tools	66
6.1.1	Tracking Methodology	66
6.1.2	Core tracking routine used within the various jobs	67
6.1.3	Particle numbers	68
6.2	Simulation set up and input parameters.....	68
6.2.1	Magnet field strengths and errors	68
6.2.2	Alignment errors and mechanical tolerances	68
6.2.3	Beam position monitor reading errors	69
6.2.4	Closed orbit correction	69
6.2.5	Optics perturbation and correction	71
6.2.6	Initial particle distribution	72
6.2.7	Apertures in the beam dump region LSS6	73
6.2.8	Collimator settings	74
6.2.9	Mechanical tolerances	74
6.3	Failure cases considered.....	75
6.4	Simulation results	75
6.4.1	Normal beam dump	75
6.4.2	Asynchronous beam dump and MKD kicker pre-trigger	76
6.4.3	Missing MKD kickers	80
6.4.4	Retriggering failure (one MKD-kicker only)	84
6.4.5	Q4 or MSD strength error	85
6.4.6	IR6 orbit error.....	87

6.4.7	TCDQ positioning error	88
6.4.8	TCDQ positioning error with IR7 collimators retracted	94
6.4.9	Analysis of particle transmission through the TCDQ system onto the TCT's	95
6.4.10	Analysis of simulation deviations	100
6.5	Summary tables of tracking results	102
6.6	Discussion	104
6.6.1	Consequences for Machine Elements and Experiments.....	104
6.6.2	Directions for further simulation.....	105
7	LHC Beam Dump - Abort Gap Cleaning	106
7.1	Introduction	106
7.1.1	Abort gap filling	106
7.1.2	Abort gap cleaning hardware.....	106
7.1.3	The principle of abort gap cleaning using the transverse damper	107
7.2	Results of 2007 SPS Machine development sessions dedicated to AGC.....	109
7.3	LHC simulations.....	111
7.3.1	Results from tracking studies with filled abort gap.....	111
7.3.2	Results from dedicated LHC- AGC simulations done at FNAL	112
7.4	Conclusions	113
8	Beam Commissioning of LHC	114
8.1	SPS extraction beam tests.....	114
8.2	SPS to LHC transfer line beam tests	115
8.3	LHC sector tests and ring commissioning.....	116
8.3.1	Beam dump commissioning during the 3 rd sector test.....	117
8.3.2	LHC ring commissioning	118
8.4	Aperture scans	118
8.4.1	Measurement technique.....	118
8.4.2	Measurement results in the injection regions	119
8.4.3	Measurement results for beam dump systems.....	120
8.5	Beam dilution	121
8.6	Beam loss monitors	122
8.7	Measurements during 2010 commissioning.....	124
8.8	Conclusions	124
9	Summary, Conclusions and Outlook	126
9.1	Outlook.....	128
	Appendix	129
	Bibliography	131

Introduction

The European organisation for Nuclear Research (CERN) is the world's largest laboratory for particle physics. The name itself - CERN (Conseil Européen pour la Recherche Nucléaire) is originally the name of the convention set in place in the early fifties to found and build the laboratory.

The Large Hadron Collider (LHC) is a proton or lead-ion collider, built in a 26.7 km diameter underground tunnel on the Swiss-French border near Geneva. The accelerator relies on superconducting magnet technology and is one of the biggest and most complex machines ever built. It is, at the time of writing, the world's newest, most powerful and highest energy particle accelerator, designed with a proton energy of 7 Tera-electron-Volts (TeV) for each of its two counter rotating beams. In four interaction regions the main high-energy physics experiments ATLAS, ALICE, CMS and LHCb will take data from the 14 TeV centre-of-mass proton-proton collisions. The beam commissioning of LHC began in late summer 2008, with circulating beam achieved in early September.



Figure 1.1: Aerial view of the LHC ring and the CERN injector complex.

LHC is a discovery machine, and its physics motivation is wide-ranging. One of the main objectives is the discovery of the Higgs boson, which is needed to complete the Standard Model and which is postulated to explain the mass differences between elementary particles. In addition, the LHC detectors will also be searching for physics beyond the Standard Model, including supersymmetry, dark matter particles, evidence of extra dimensions and for signs of string theory. The heavy ion program will investigate ultra-high energy density phenomena such as quark-gluon plasma. To maximise the discovery potential, the LHC energy and the LHC particle collision rate are required to be as high as possible.

The principal motivation to collide higher and higher energy beams comes from quantum mechanics, which basically describes particles as waves. The wavelength is related to the momentum of the particle as $\lambda = h/p$ and was firstly described by De Broglie in 1924 [1]. Higher momentum brings shorter wavelength which is able to reveal finer details in the structure of matter. In addition, higher energy allows the production of heavier elementary particles, according to Einstein's famous relationship $E = mc^2$.

To achieve the 7 TeV energy per beam the LHC tunnel (26659 m circumference) is filled with 9300 magnets, comprising 1232 superconducting main dipoles operating at 1.9 Kelvin (K) and a peak field

of 8.3 Tesla (T), 858 quadrupoles and several thousand corrector magnets. There are also 8 accelerating radiofrequency cavities per beam.

A high event rate is required, measured by the luminosity at the experiments. The luminosity is a function of the beam intensity and the beam size at the collision points. For the LHC the design luminosity value is $10^{34} \text{ cm}^{-2}\text{s}^{-1}$, which requires a very large beam intensity of 3×10^{14} protons. At 7 TeV this corresponds to a stored energy per beam of 360 MJ.

The protection of the LHC machine against accidental beam loss is a major design challenge, since the uncontrolled loss of even 0.01% of the beam would cause damage to the accelerator, requiring many months to repair. Uncontrolled loss of the whole beam could destroy a substantial fraction of the whole machine. Several machine systems are therefore dedicated to protection. One of the most important is the beam dump system which is designed to safely remove the LHC beam from the accelerator in a very short time if required due to the failure of another machine system.

In order to be able to correctly set up the beam dump system, and also to evaluate the risk to the machine in the event of a functional failure of one of its component parts, numerical simulations were carried out using a detailed model of the accelerator and of the beam dump system and its failure modes. The study also comprised an application of the techniques developed to the SPS accelerator, where benchmark experiments were carried out with the SPS beam dump system. This thesis presents the work done on these topics and quantifies the effects of a failure of the LHC beam dump system functionality in terms of beam losses on the aperture limits around the accelerator.

In *Chapter 1* the LHC accelerator and its machine protection systems are presented. The context of the beam dump system is explained together with the reliability requirements and the particular failure modes of interest. The LHC injector chain is briefly reviewed.

Chapter 2 presents the basic concepts of accelerator physics required to understand the simulation results and terminology used in the remaining chapters. The author summarized the transverse dynamics of charged particle beams in a synchrotron, linear transverse beam optics, Twiss parameterization and basic longitudinal dynamics.

Chapter 3 gives an overview of the numerical simulation tools and methodology used for the beam abort simulations whilst *Chapter 4* briefly describes different beam dump systems in the LHC injector chain and a beam abort simulation for the less complex SPS beam dump system.

Chapter 5 presents the LHC beam dump system in detail and describes its main components and relations important to this thesis.

Chapter 6 describes the results of the tracking studies for different failure cases of the LHC beam dump system.

Chapter 7 gives a brief overview of the issues of abort gap population and the simulations made for abort gap cleaning as well as a summary of participation in abort gap cleaning tests with SPS beam.

In *Chapter 8* first results from the LHC beam commissioning are presented and, where possible, compared to the simulation results. Finally *Chapter 9* presents the conclusions and a brief summary.

Work done by the Candidate and scientific aspects:

The candidate declares that this thesis was authored independently, as the work carried out. However every activity in a challenging accelerator field like the LHC represents, mostly requires the help of hundreds of engineers and scientists e.g. to run the machine its subsystems and pre-accelerators. This help is indispensable for every measurement and gratefully acknowledged.

The candidate studied literature, available knowledge and systems used at CERN to summarize in his own words the background of the thesis in Chapter 1, the interrelation to accelerator physics in Chapter 2 and the environment of the used simulation program in Chapter 3. Considerations of the

candidate on computing time and simulation structures as well as on the simulation methodology when using random numbers generators are also presented in Chapter 3.

Chapter 4 already contains an overview of specific topic related systems. The candidate summarized available information in his own words and describes subjects investigated during operation of CERN equipment. The candidate had the gratefully acknowledged opportunity to participate in the SPS to LHC extraction region and transfer line commissioning. This work is presented in section 4.3. The candidate was co-author of a paper published on the results of that work at the Particle Accelerator Conference 2007 (PAC07) [31].

First results of development work done by the candidate for the SPS beam extraction systems are presented in section 4.4. The intention of this work was the deployment of novel “tracking” ideas to a well known system so that newly introduced features could be verified in a reasonable way on a running accelerator system. Those results were published at (PAC07) [32]. The chapter is rounded off by considerations concerning a developed extraction and dump concept for a possibly new accelerator at CERN. Those results were published at the European Particle Accelerator Conference 2008 (EPAC08) [39].

In Chapter 5 the candidate studied available information on the LHC extraction system and its protection elements and summarized in his own words. Sections 5.5.2 to 5.5.5 represent LBDS specifications reworked by the candidate. MAD-X aperture models for the dump lines TD62 & 68 were created by the candidate as well as models for the IR6 extraction region were reviewed and upgraded.

Chapter 6 represents the work done by the candidate concerning the development of tracking jobs and the simulation results for specific extraction events. The developed “MAD-X thin lens optics” tracking job comprises a modularised parallel architecture capable of applying turn dependent kick strength parameters and using a wide range of changeable parameters like the inclusion of error tables for magnets as well as corrector and collimator settings all set up in a Monte Carlo like approach. This development yielded in a novel way of asynchronous dump simulations for the LHC. Especially for the interaction region 6 (IR6) and both dump lines (TD62 & TD68) this was the first time that such a methodology had been applied. Hence the developed methodology and its conversion into a working tracking job gave proof that numerical methods can nowadays also perfectly assist in evaluating and preparing safety relevant aspects for accelerator commissioning in such complex problem sets as the LBDS requires. The methodology developed for the LBDS particle tracking and the results achieved form the scientific claim of this thesis. The candidate was main author of papers presented on that core topic at EPAC08 [82], PAC09 [84] and IPAC10 [125] as well as co-author for a contribution to the journal “Physical Review Special Topics - Accelerators and Beams“ [2].

The candidate took part in machine development sessions for “abort gap cleaning” which are summarized together with basics and simulation results (courtesy A. Koschik) in Chapter 7. This work was presented at EPAC08 [113] (Co-author).

The first phase of LHC beam commissioning is described in Chapter 8. The candidate took part in the commissioning test of the new SPS to LHC extraction, the SPS to LHC transfer lines and finally in the initial LBDS commissioning phase. The Candidate contributed as co-author to publications at EPAC08 [119], PAC09 [121] as well as [3] and as main author at IPAC10 [125].

The candidate summarizes the key items of the work and its outcome in Chapter 9.

1 The LHC Accelerator and its Machine Protection System

The LHC is divided into eight sectors. Each sector consists of arc (bending) cells, the insertion regions (IRs) in the straight sections and dispersion suppressor (DS) cells between the arcs and straight sections (Figure 1.1). The layout of the each arc cell comprises six superconducting dipoles and two superconducting quadrupoles as well as smaller corrector and higher order multipole magnets. One arc consists of 23 such cells. The LHC circumference (26659 m) is thus filled with more than 9300 magnets (main machine elements: 1232 superconducting dipoles, 858 quadrupoles and 8 cavities per beam).

The eight insertion regions contain the four LHC experiments as well as special systems including beam transfer and machine protection: Beam injection in point 2 and 8, the RF-cavities are in point 4, the experiments are in point 1, 2, 5 and 8, the collimation areas in point 3 and 7 and finally the beam extraction systems are in point 6. The detailed layout of IR6 is shown and further explained in Chapter 5.

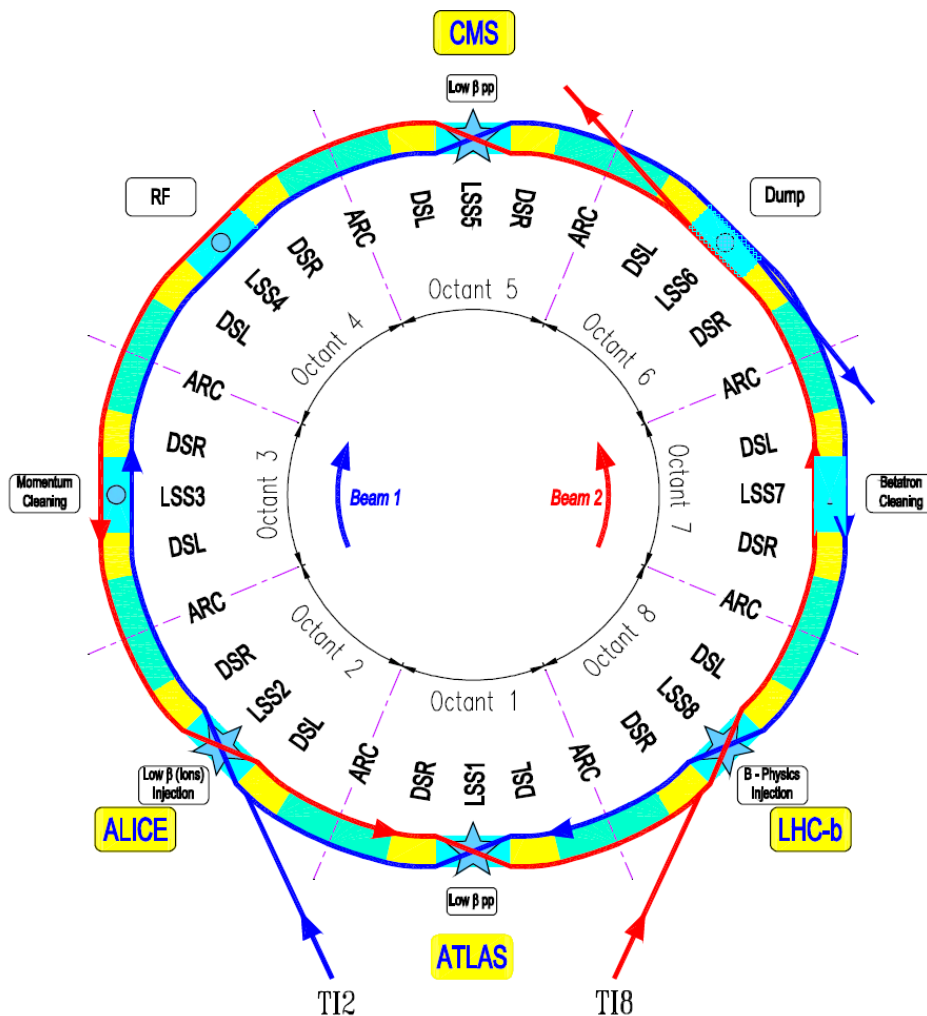


Figure 1.1: Schematic layout of the LHC octants.

1.1 The CERN injector chain

All particles which are accelerated in the LHC have to first travel through a chain of accelerators in the CERN complex (Figure 1.2), since each accelerator has a limited energy range, typically a factor 10-20. The LHC Protons start from a source from which they are extracted with a current of 180 mA. After being accelerated to 50 MeV by a linear accelerator (Linac 2) the particles are injected into the circular Proton Synchrotron Booster (PSB) and accelerated to 1.4 GeV. The beams are then extracted into the CERN-Proton Synchrotron (PS) which accelerates them up to 26 GeV. The PS beam is then transferred to the 6.9 km circumference Super Proton Synchrotron (SPS) which accelerates it to 450 GeV. Finally the particles are extracted and send to the LHC ring “Beam 1” (clockwise) via the transfer line TI 2 or to the LHC ring “Beam2” (counter clockwise) via TI 8. This entire process is repeated 12 times per ring to fill the LHC; the LHC then accelerates the full beam to 7 TeV.

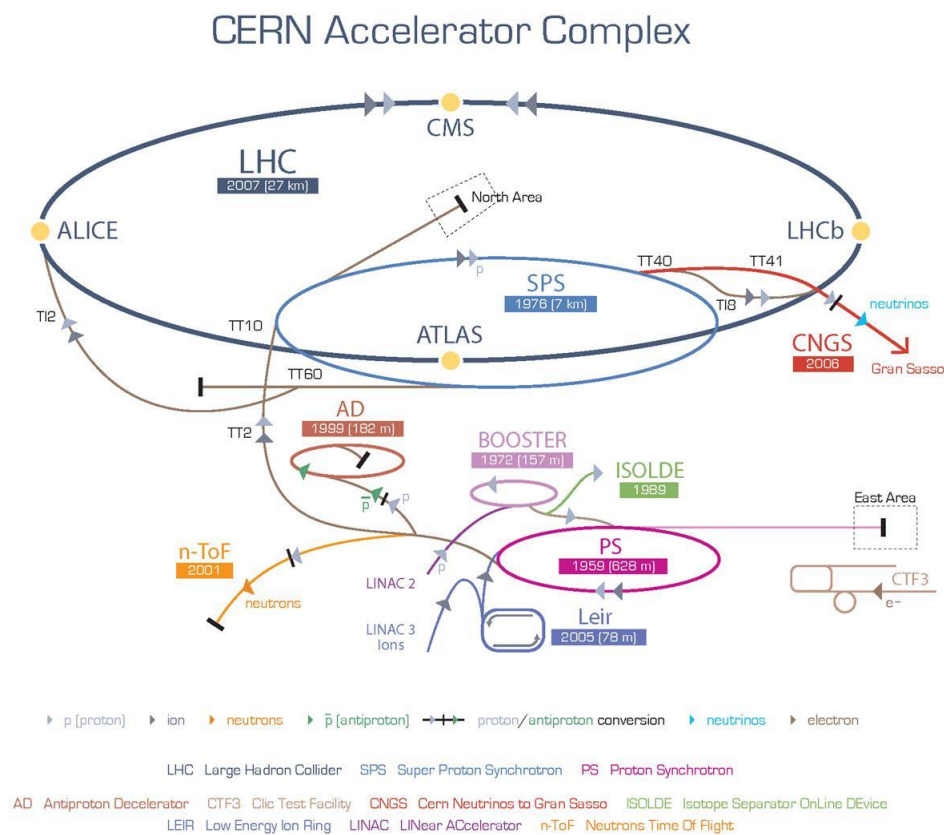


Figure 1.2: Schematic overview of the CERN accelerator complex.

Particles are accumulated in bunches with typical lengths of around 1 ns, with the nominal intensity for LHC being 1.15×10^{11} protons per bunch. The bunch spacing of 25 ns is determined by the frequency of the accelerating radiofrequency system, together with beam dynamics and experiments’ data-taking considerations. A number of consecutive bunches form a “batch” and several batches form a “train”.

Due to the growth in circumference, the next synchrotron in the injector chain always needs several batches or trains to be filled. A full LHC beam comprises 2808 bunches and requires 12 injections from the SPS, giving a LHC filling time of about 4 minutes per beam.

In the LHC, after being accelerated for 28 minutes to the top energy of 7 TeV, the two beams will be collided together, producing around 600 million proton-proton collisions per second. The beams are left colliding for about 12 hours, until the intensity has decreased to a level where recycling and refilling is necessary.

1.2 The LHC operating cycle

A LHC “physics run” follows a well defined machine cycle (Figure 1.3), which basically consists of the preinjection, the 15 min long injection phase and the 30 min long acceleration phase (“ramp”). When the beam reaches its desired energy a dedicated phase (“squeeze”) is used to prepare the machine for optimized collision optics by reducing the beam sizes at the interaction points, and the beams are brought to collision at the interaction points one, two, five and eight. The data taking phase can last for 12-24 hours depending on the actual beam lifetime and the consequent luminosity values. After the dump at collision energy the accelerator has to go back to the preinjection level by a ramp down phase.

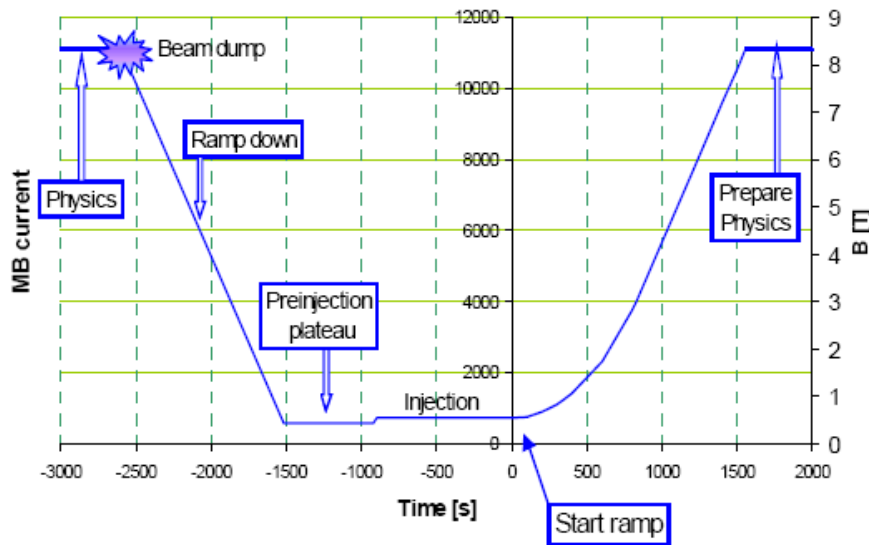


Figure 1.3: The LHC baseline cycle parameters. [4]

1.3 Classification of beam losses in the LHC

Beam losses are an extremely important phenomenon for machine performance. Low levels of beam loss are normal and can be tolerated, and are captured by the collimation system. Higher levels of beam loss may deposit sufficient energy in the superconducting magnet coils to cause the conductor to become resistive, leading to a ‘quench’. Even higher levels of loss can cause direct material damage. The losses can occur over different time scales.

1.3.1 Normal beam losses

During operation with nominal beam 1.15×10^{11} particles per bunch and a total of 3.1×10^{14} particles per beam will circulate in the LHC machine. Depending on vacuum and beam optics conditions complex beam dynamics processes will continuously drive some particles to large amplitudes and fill a so called “primary beam halo” due to space charge effects, scattering of particles with residual gas, intra beam scattering, and beam-beam effects. This halo will spread out and thus be continuously lost at aperture bottlenecks. Consequently the total beam intensity will slowly decrease over time due to these steady losses. A significant parameter to valuate this process is the beam lifetime (τ). It is the amount of time after which the beam intensity is reduced by $1/e$.

The LHC beam lifetime has been estimated to 18.4 hours at 7 TeV [5]. However the beam lifetime will vary over the LHC cycles and also within each cycle (e.g. higher losses at the start of acceleration due to uncaptured beam being lost). Worst case beam life times of 0.1 h for injection and 0.2 h for high energy have been considered for the collimation system design which corresponds to 8.6 and 4.3×10^{11} lost particles per second. [6]

1.3.2 Abnormal beam losses

Abnormal losses are unplanned losses which can be divided into four types [7]:

- Slow losses: Losses due to e.g., optics errors, movement of elements into the beam (e.g. slowly moving collimator), moderate vacuum leaks etc., which develop over seconds.
- Fast losses: Losses in less than 1 second but not faster than 10 ms (e.g. beam instabilities, RF-failures...).
- Very fast losses: Losses develop in less than 60 turns (some ms) (e.g. fast powering failures for some special magnets, wrong magnet strength settings at injection energy...)
- Ultra fast or single-turn losses: Losses within ns up to several μ s. (e.g. injection failure, extraction kicker failure...).

1.4 The LHC Machine Protection System (MPS)

One nominal LHC beam at 7 TeV has a stored energy of around 360 MJ which is enough to heat and melt more than 500 kg of (1.9 K temperature) copper. Another 10 GJ of energy are stored in the huge inductance of the LHC magnet system. Such huge energies require proper protection system which avoids unwanted dangerous operations and can handle a wide scope of potential malfunction possibilities. The machine protection strategy for beam is always to detect redundantly any problem as early as possible and to extract the beam with a reliable and safe beam extraction system onto a special 7.8 meter long graphite block before significant beam losses could seriously damage the accelerator elements. As the LHC is based on superconducting magnet technology it is also mandatory to avoid frequent magnet quenches (superconducting to resistive transitions) as this would significantly affect the machine availability.

1.4.1 The Beam Loss Monitor system (BLM)

Around 3500 nitrogen filled ionisation chambers and 400 secondary emission monitors are installed around the ring at each quadrupole and collimator as well as in regions of special interest (aperture bottlenecks, dump region...). The signal acquisition is based on a current to frequency conversion, where the measurement current is sampled every 40 μ s and integrated for periods variable between 80 μ s and 100 s. Calculated values are compared with predefined threshold values, and can generate a beam dump request. [8]

1.4.2 The LHC BPMs

Around 520 Beam Position Monitors (BPM) are installed in the LHC per ring which allow measuring the beam orbit in both the horizontal and vertical planes. Such a system is very important to detect orbit deviations from the ideal orbit before any losses occur. Dedicated interlocks have been implemented in IP6 where specifications for the beam position require any orbit deviation to be not greater than 4 mm to ensure a proper extraction process. These local BPMs generate a dump request if the orbit offset exceeds 3.5 mm.

1.4.3 The Quench Protection System (QPS)

A “Quench” is a fast process where a superconducting magnet locally loses its superconducting state, for example due to energy deposited from beam losses. The magnet current produces more heat over this resistance which is a positive feedback and causes a very fast rise of heat deposition, which can quickly lead to melting of the conductor material. To avoid this, a quench detection system has been installed in the LHC superconducting magnets which detects any resistive voltage. Special resistors - so called quench heaters - are installed to then uniformly warm up the coil in order to get the whole conductor into a resistive state rapidly and thus distribute the dissipated energy to avoid damage at the quench origin. The magnets are grouped in series to powering circuits, and in case of a quench the QPS deviates the circuit current into special discharge resistors.

1.4.4 The Powering Interlock System

Guiding the beam very accurately through the accelerator vacuum chamber requires several thousand magnets, hundreds of instruments and beam related detectors, a complex controls system and many more electrical energy dependent systems. It is obvious that any malfunction in the powering of these complex accelerator systems could immediately lead to beam losses. For this reason all crucial

systems are connected to powering interlock controllers (PIC) which detect powering failures and request a beam dump.

1.4.5 The Fast Magnet Current change Monitors (FMCM)

For some magnet circuits the response time of the PIC is too slow as it processes signals coming from the power converters on a ms timescale. If the current changes rapidly significant losses could develop before the dump signal is finally produced by the PIC.

For these circuits special Fast Magnet Current Change Monitors have been developed which are capable to detect small but fast changes in the magnet current directly and hence can send a interlock signal within 60 μ s. [9]

1.4.6 Safe Machine Parameter System (SMP) and Software Interlock System (SIS)

The Safe Machine Parameters system distributes via software important machine parameters like beam energy and machine mode. The Software Interlock System is used to identify and prevent wrong or dangerous settings in the higher software layers of the control room applications. However it cannot prevent dedicated equipment specialists from intentionally changing settings to wrong or potentially dangerous levels. The SIS can be used to easily create complex interlock conditions, but its response time is more than one second. [10]

1.4.7 The Beam Interlock System (BIS)

The BIS consists of 21 Beam Interlock controller units with over 10,000 connected devices. This hardware system collects all interlocks and finally generates the beam permit signal which allows injection of and operation with beam in the LHC. The beam permit flag (one for each ring) ensures that at injection all systems are ready for beam. Any absence inhibits injection into the LHC (and beam transfer to that LHC ring) and sends a trigger signal to the LHC Beam Dump System (LBDS). Figure 1.4 shows an overview of the BIS and its connected systems.

Two optical fibre signal loops per ring carry the \sim 10 MHz beam permit signal. If one of the BICs receives a dump request it opens the loop and the missing signal is consequently detected by the LBDS in IR6 where the dump request is then immediately performed. The delay for generation of the dump trigger varies between 20 and 120 μ s depending on which equipment generates the request [11].

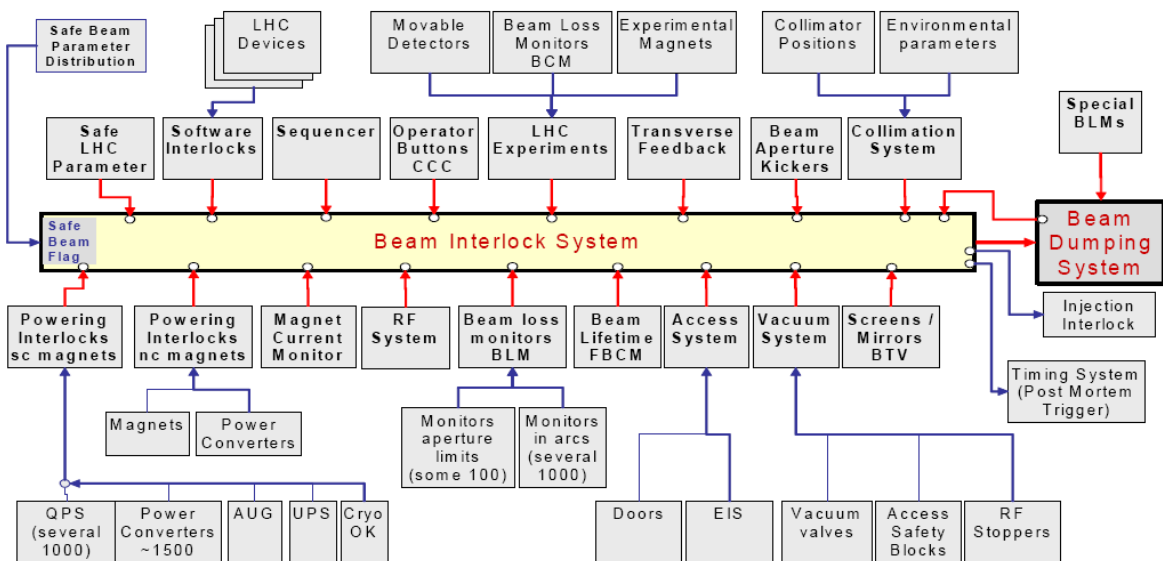


Figure 1.4: The beam Interlock System (BIS) and its interfaces. [12]

1.4.8 The Beam Dump System

Every dump request is finally processed and executed by the LHC Beam Dump System. This uses fast pulsed and DC magnets to extract the beam from the LHC and transport it to a large shielded block where it can be safely absorbed. A full description of this important system is given in Chapter 5.

1.5 The LHC beam cleaning and collimation system

The LHC collimation system was mainly designed for an efficient cleaning of the beam halo during operation to avoid quenches and to reduce the halo induced noise in the experiment detectors. However this system also protects machine elements in case of abnormal beam losses, discussed in detail in Chapter 6.

Figure 1.5 shows the setting hierarchy of primary (TCP), secondary (TCS) and tertiary (TCT) collimators. The primary collimators are closest to the beam and made out of carbon blocks with a relatively low density. They do not absorb the full beam energy but dilute the beam and create secondary showers. Most of the particle shower is then absorbed in the secondary collimators which are further away from the beam centre. Particles also escaping the secondary stage (tertiary shower) are then intercepted by tertiary absorbers made out of a relatively dense material like tungsten or copper. Any quaternary shower should then be small enough to be lost on the cold aperture without causing a quench. The longitudinal position and the rotation of the collimator jaws is optimized considering the phase advance and optical functions to achieve a full coverage of the halo phase space.

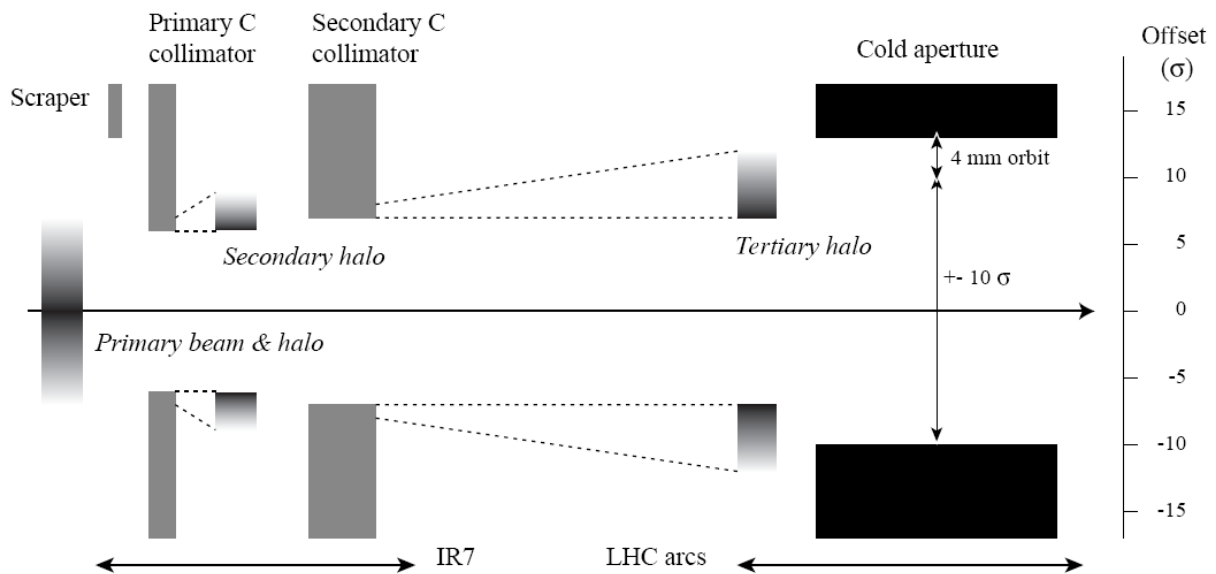


Figure 1.5: Principle of the staged betatron cleaning at injection energy (from [13]).

The overall collimation layout follows a phased installation. In phase 1 (Figure 1.6) a two stage cleaning in IR3 & 7 is installed whilst tertiary collimators are placed at the insertions only. All in all 88 collimators are in place along the LHC ring. The main devices are primary (TCP), secondary (TCSG) and absorbing (TCLA) collimators. Phase 2 will bring 30 low impedance hybrid secondary collimators which are used at top energy and stable conditions only to reduce the impedance by retracting the more robust standard TCS and finally phase 3 and 4 are foreseen for additional upgrades to exceed the nominal beam intensity. Protection elements against single turn losses for injection (TDI, TCLI) extraction (TCDS, TCDQ plus one TCSG) and experiments will be in place for all phases. The collimator settings used for calculations in this thesis are discussed in Chapter 6.

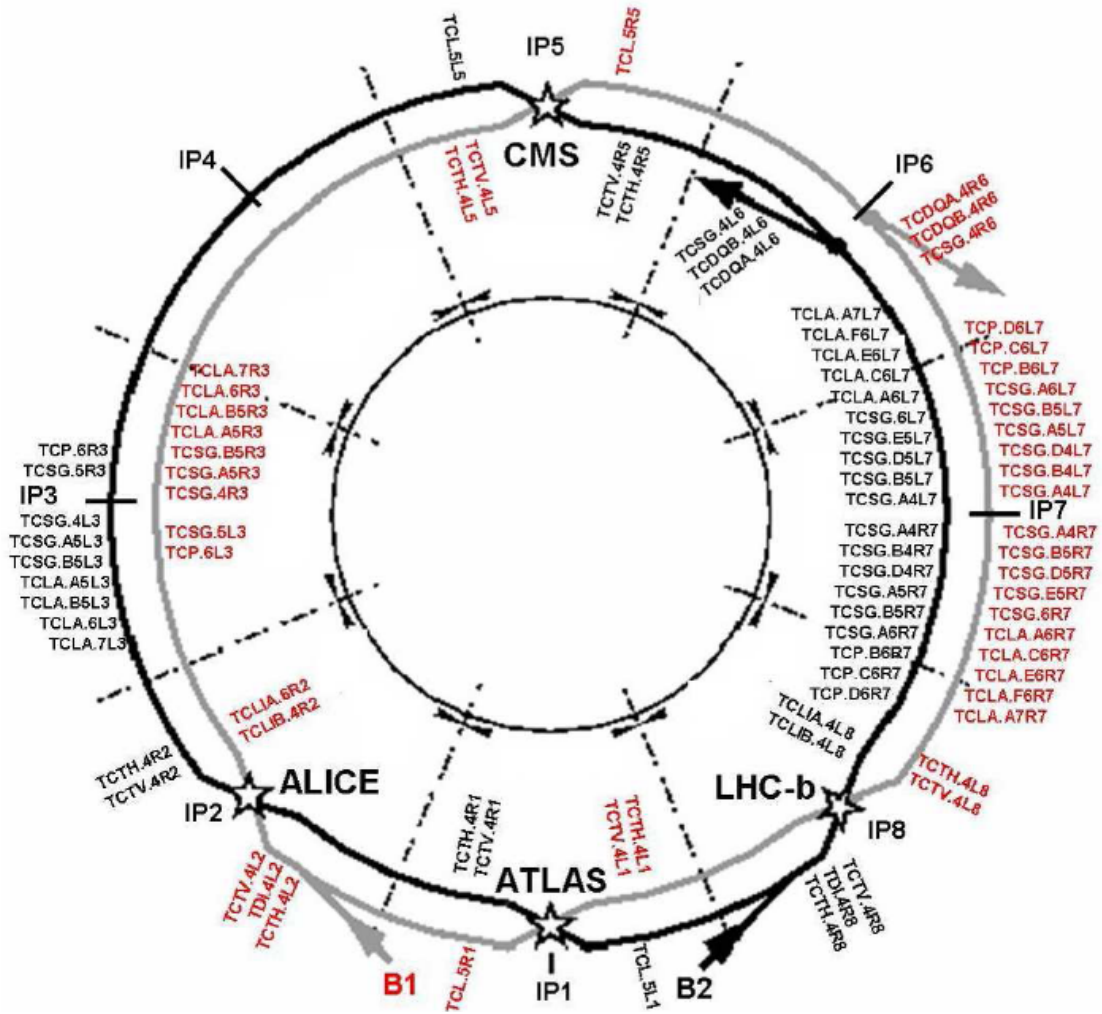


Figure 1.6: Schematic overview of the collimators position in the LHC, phase 1 for beam 1 (red) and beam 2 (black) [14].

2 Introduction to Accelerator Physics

This chapter introduces the basic concepts of accelerator physics and beam dynamics. These topics are very extensive and only the most important and frequently used relations and formulae pertaining to synchrotrons are covered. Complementary and more detailed information can be found in [15-18].

For practical considerations the units commonly used in particle and accelerator physics are often non-SI. Energy is most frequently expressed in units of electron-Volts (eV), where one electron-Volt is the discrete energy increase amount of energy E of an electron traversing an accelerating potential difference of one Volt (2.1) where q is the charge of the particle in Coulomb (C) and U is the voltage in Volt (V):

$$E = q \cdot U \quad (2.1)$$

Hence 1 eV is 1.602×10^{-19} Joule. This energy also corresponds to a certain relativistic velocity. At LHC injection (450 GeV) protons travel with a velocity of about $0.999997828 \times c$ and at top energy (7 TeV) with $0.999999991 \times c$. It is obvious why energy and not velocity is used.

2.1 Basic relativistic relations:

The relativistic gamma (2.2) is defined as the ratio between the total energy and the rest energy of the particle whilst the relativistic beta (2.3) represents the ratio of the particles velocity to the speed of light:

$$\gamma = \frac{E}{E_0} \quad (2.2)$$

$$\beta = \frac{v}{c} \quad (2.3)$$

The total energy E is the sum of the kinetic energy T and the particle rest energy E_0 , and one can modify the relation between gamma and beta as shown in (2.5).

$$E = T + E_0 \quad (2.4)$$

$$\beta = \sqrt{1 - \gamma^{-2}} = \sqrt{1 - \left(\frac{E_0}{T + E_0} \right)^2} \quad (2.5)$$

For calculations with accelerated particles it is important to consider the relativistic mass of a particle which can be expressed as in (2.6).

$$m_v = \frac{m_0}{\sqrt{1 - \beta^2}} = \gamma \cdot m_0 \quad (2.6)$$

Thus also the classical momentum of such a particle becomes the relativistic momentum p :

$$p = m_v \cdot v = \gamma \cdot m_0 \cdot v \quad (2.7)$$

2.2 Reference coordinate system

The path of a particle circulating in an accelerator theoretically only made of ideal bending magnets defines the (ideal) reference orbit. It is defined under the assumption that all elements are perfectly aligned so that no magnet fringe fields or imperfections and no beam interaction disturbs the ideal motion. Such an ideally moving particle is accompanied by a tripod which spans a local right handed coordinate system (x, y, s) . The local s -axis is the tangent to the reference orbit, the x -axis points to the outer side of the ring (in the bending plane) for anti-clockwise motion and the positive y -axis is pointing upwards. The closed orbit is the path of a particle which is perfectly closed after one turn; this deviates from the reference orbit because of unavoidable errors in alignment and magnetic field. The many particles which circulate in the accelerator perform betatron oscillations about this unique closed orbit.

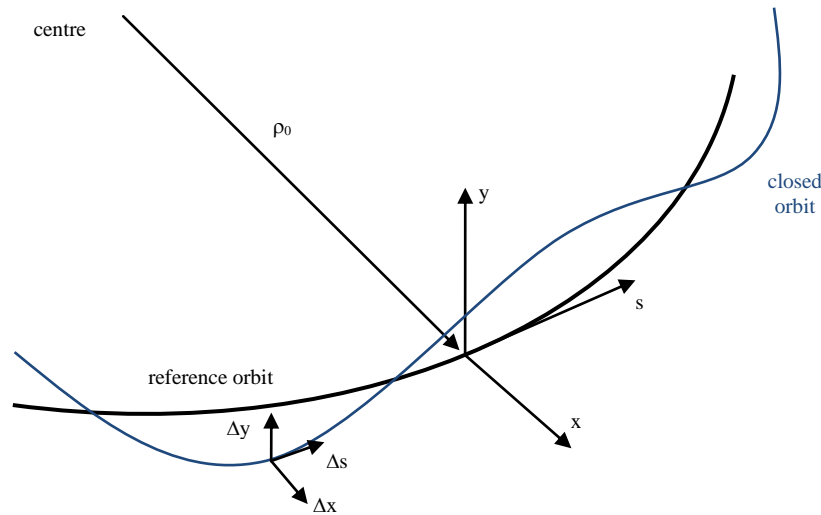


Figure 2.1: Reference coordinate system

2.2.1 The MAD-X coordinate system

MAD-X is a computer code used to calculate accelerator optics and perform particle tracking. It uses the ideal reference orbit as its reference, which consists of a series of straight drift segments and circular arcs.

Due to various errors like misalignments, field errors, fringe fields, momentum error etc., the closed orbit does not coincide with the reference orbit but it is described with respect to the reference orbit, using the local reference system x, y, s . A particle on the reference orbit has zero x and y deviation.

The definition of the bend angles is for a positively charged particle as follows: a positive horizontal bend angle in the MAD-X coordinate system represents a bend to the right (for clockwise translation), i.e. towards negative x . This is different for kicker elements where a positive kick increases px (or py) which means that a positive horizontal kick bends to the left.

2.3 Charged particle focussing and guiding

A synchrotron is a quasi-circular accelerator where particles are stored for many hours, making millions or billions of turns. To keep particles on a well defined circular track or “orbit”, a horizontal bending force has to be applied. This is achieved with uniform vertical magnetic fields produced by dipole magnets.

Small errors will disturb the ideal motion and lead to deviations from the ideal orbit. In addition any real initial distribution of particles has a spread in angle and position. Special elements are therefore required to focus the particles to avoid the beam being rapidly lost. This is achieved with a periodic structure of alternating vertical and horizontal quadrupolar magnetic fields, which results in a net

focussing effect in both vertical and horizontal planes. These fields are produced by quadrupole magnets.

The space between the bending dipole magnets and the quadrupole focusing magnets contains various other magnet systems, beam diagnostics, high energy physics experiments or even simple vacuum drift spaces. All of these elements together form a basic structure called a “lattice” which generally has several levels of periodicity.

2.3.1 Magnet multipoles

The magnetic field in a certain point in the region between the gap of magnet poles can be described by a Taylor expansion as shown for the horizontal plane in (2.8). The dipole and quadrupole components, Table 2.1, produce linear forces, while the sextupole and higher order multipoles are non-linear.

$$B_{y(0)} = B_{y0} + \frac{1}{1!} \left(\frac{dB_y}{dx} \right)_0 x + \frac{1}{2!} \left(\frac{d^2 B_y}{dx^2} \right)_0 x^2 + \frac{1}{3!} \left(\frac{d^3 B_y}{dx^3} \right)_0 x^3 + \dots \quad (2.8)$$

Table 2.1: Overview of basic multipoles.

Taylor expression	Beam optics	Multipole
$\left(\frac{dB_y}{dx} \right) x$	$\frac{1}{\rho}$	Dipole
$\frac{1}{2!} \left(\frac{d^2 B_y}{dx^2} \right) x^2$	K	Quadrupole
$\frac{1}{3!} \left(\frac{d^3 B_y}{dx^3} \right) x^3$	M	Sextupole

2.3.2 Lorentz force

The Lorentz force F (2.9) acts on a particle with charge q moving through an electrostatic field E or magnetic field B with velocity v :

$$\vec{F} = q \cdot \vec{E} + q \cdot (\vec{v} \times \vec{B}) \quad (2.9)$$

We can derive the equation of motion by equalising all relevant forces for a constant momentum particle on a circular path using only a uniform magnetic component to maintain the trajectory.

$$\vec{F} = \frac{d\vec{p}}{dt} = q \cdot \vec{v} \times \vec{B} \quad (2.10)$$

Since this force always acts perpendicular to the particle velocity vector, only the direction of movement changes without affecting the magnitude of velocity. This also implies that a longitudinal acceleration can only come from an electrostatic field.

$$\frac{d\vec{p}}{dt} = \gamma \cdot m \cdot \frac{d\vec{v}}{dt} \quad (2.11)$$

$$\frac{d\vec{v}}{dt} = a_n = \frac{v^2}{\rho} \quad (2.12)$$

$$\gamma \cdot m \frac{v^2}{\rho} = q \cdot v \cdot B \quad (2.13)$$

$$B \cdot \rho = \frac{p}{q} \quad (2.14)$$

The beam rigidity $B \cdot \rho$ (2.14) describes the relation between the particle momentum p and the magnetic field B needed to keep the particle (with the charge q) on a circular trajectory of radius ρ . The higher the particle momentum, the higher the field needed to keep the particle on the synchrotron design orbit. During acceleration the magnetic field therefore has to be ramped according to the particle momentum.

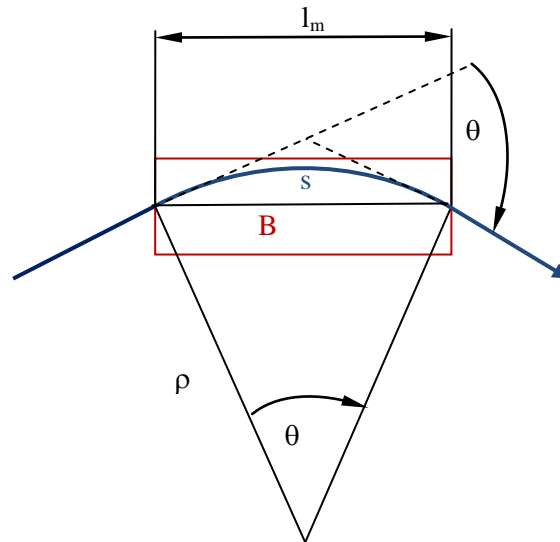


Figure 2.2: Schematic trajectory through a bending magnet (seen from above)

Eq. (2.15) is the arc length s of the trajectory through the bending magnet whilst (2.16) represents the secant (which is in fact the magnet length l_m) for this arc. For very small angles the sinus is close to the angle itself and the arc length is similar to the secant so that (2.17) is valid for such cases.

$$s = \theta \cdot \rho \quad (2.15)$$

$$l_m = 2 \cdot \rho \cdot \sin\left(\frac{\theta}{2}\right) \quad (2.16)$$

For many systems it is useful to know the deflection θ caused by an applied field. This so-called “kick angle” is:

$$\theta = \int \frac{ds}{\rho} \Leftrightarrow \theta = \frac{l_m}{\rho} \quad (2.17)$$

Using equation (2.14):

$$\theta = \frac{B \cdot l_m}{p} \cdot e \quad (2.18)$$

$$\theta[\text{rad}] = B[\text{T}] \cdot l_m[\text{m}] \cdot 0.2998 \cdot \frac{1}{p[\frac{\text{GeV}}{c}]} \quad (2.19)$$

Equation (2.19) shows the total deflection for a particle with unit charge traversing a uniform magnetic field. It has to be noted that the relation $\nabla \cdot \vec{B} = 0$ is true for B-fields outside of magnetic conductors in the absence of current density J . Thus the bending force only occurs in one plane perpendicular to the direction of movement, which also indicates that no accelerating forces are seen by the particle in the longitudinal plane.

This is especially interesting for the total deflection of a quadrupole magnet. For the quadrupole field the B field is described by:

$$\frac{\partial B_y}{\partial x} = \frac{\partial B_x}{\partial y} \quad (2.20)$$

$$\vec{B} = B_x \hat{x} + B_y \hat{y} \quad (2.21)$$

$$\vec{B} = \left(B_{x0} + \frac{\partial B_x}{\partial y} y + \frac{\partial B_y}{\partial x} x \right) \hat{x} + \left(B_{y0} + \frac{\partial B_y}{\partial x} x + \frac{\partial B_x}{\partial y} y \right) \hat{y} \quad (2.22)$$

Equation (2.22) shows that for small displacements (x,y) from the design orbit, linear force components are produced which are equivalent due to the curl condition (2.20). Thus this magnet is focusing in one plane and defocusing in the other plane.

The beam rigidity for other particles than protons (2.23) where A is the atomic number and Z is the charge number of the particle can also be expressed as a function of the particle's energy (2.24).

$$B \cdot \rho = \frac{1}{0.2998} \cdot p \cdot \frac{A}{Z} \quad (2.23)$$

$$B \cdot \rho = \frac{\sqrt{E^2 - E_0^2}}{e \cdot c} \quad (2.24)$$

2.3.3 Equation of motion

The equation of motion is intensively discussed in various publications; thus this section only briefly covers basic relations needed for a better understanding of the particle motion. More detailed information can be found in [16], [17].

$$x_s'' - k_s \cdot x_s = \frac{1}{\rho_s} \cdot \frac{\Delta p}{p} \quad (2.25)$$

The right side of this equation represents dispersive effects which will not be further considered as the momentum deviation $\frac{\Delta p}{p}$ is assumed to be zero for these explanations. The remaining equation can be solved with an ansatz like (2.26).

$$x_s = A \cdot u_s \cdot \cos(\psi_s + \phi) \quad (2.26)$$

The amplitude factor A and the phase ϕ are integration constants. We replace A by the square root of the emittance ($\sqrt{\varepsilon}$) and u_s by the square root of the betatron function ($\sqrt{\beta}$).

$$x_s = \sqrt{\varepsilon \cdot \beta_s} \cdot \cos(\psi_s + \phi) \quad (2.27)$$

The first derivative is then as follows:

$$x'_s = -\frac{\sqrt{\varepsilon}}{\sqrt{\beta_s}} \cdot [\alpha_s \cdot \cos(\psi_s + \phi) + \sin(\psi_s + \phi)] \quad (2.28)$$

x and x' describes the particles trajectory in the horizontal plane.

$$\sin^2 \theta + \cos^2 \theta = 1 \quad (2.29)$$

Using relation (2.29) and transforming equation (2.27) and (2.28) into (2.31) and (2.30) the phase advance can be eliminated (2.32).

$$\cos(\psi_s + \phi) = \frac{x_s}{\sqrt{\varepsilon \cdot \beta_s}} \quad (2.30)$$

$$\sin(\psi_s + \phi) \cdot x_s = \frac{\sqrt{\varepsilon \cdot \beta_s} \cdot x'_s}{\sqrt{\varepsilon}} + \frac{\alpha_s \cdot x_s}{\sqrt{\varepsilon \cdot \beta_s}} \quad (2.31)$$

$$\frac{x_s^2}{\beta_s} + \left(\frac{\alpha_s}{\sqrt{\beta_s}} x_s + \sqrt{\beta_s} \cdot x'_s \right)^2 = \varepsilon \quad (2.32)$$

$$\gamma_s = \frac{1 + \alpha_s^2}{\beta_s} \quad (2.33)$$

With (2.33) the elimination of the phase advance finally yields an invariant of the motion which is known as the ‘‘Courant & Snyder Invariant’’ [18]:

$$\gamma_s \cdot x_s^2 + 2\alpha_s \cdot x_s \cdot x'_s + \beta_s \cdot x_s'^2 = \varepsilon \quad (2.34)$$

2.3.4 Transfer matrices

A useful way to calculate parameters of particles moving from position s_0 (with $\alpha_{(0)}$, $\beta_{(0)}$, $\gamma_{(0)}$) to position s_1 (with α , β , γ) in an accelerator is to use the transfer matrix formalism. A general transfer matrix can be derived by expanding eq. (2.27) into two terms

$$x_s = a_1 \sqrt{\beta_s} \cos(\psi_s) + a_2 \sqrt{\beta_s} \sin(\psi_s) \quad (2.35)$$

The general solution of Hill's equation (2.36) can be expressed in a matrix (2.37) where C and S represent cosine and sinus like solutions of the differential equation and $K_{(s)}$ represents the periodic s -dependent focusing properties of the lattice.

$$x_s'' - K_s \cdot x_s = 0 \quad (2.36)$$

$$\begin{pmatrix} x_{s_1} \\ x'_{s_1} \end{pmatrix} = \begin{pmatrix} C_{(s)} & S_{(s)} \\ C'_{(s)} & S'_{(s)} \end{pmatrix} \begin{pmatrix} x_{s_0} \\ x'_{s_0} \end{pmatrix} \quad (2.37)$$

a_1 and a_2 can then be replaced by the solutions for C (2.38) and S (2.39) considering the starting boundary conditions $C_{(0)}=1$ and $S_{(0)}=0$.

$$a_1 = \frac{1}{\sqrt{\beta_0}}; \quad a_2 = \frac{\alpha_0}{\sqrt{\beta_0}} \quad (2.38)$$

$$a_1 = 0; \quad a_2 = \sqrt{\beta_0} \quad (2.39)$$

This finally yields in the matrix M:

$$M = \begin{pmatrix} \sqrt{\frac{\beta}{\beta_0}} (\cos \psi + \alpha_0 \sin \Delta \psi) & \sqrt{\beta_0 \cdot \beta} \sin \Delta \psi \\ \frac{\alpha_0 - \alpha}{\sqrt{\beta \cdot \beta_0}} \cos \Delta \psi - \frac{1 + \alpha \cdot \alpha_0}{\sqrt{\beta \cdot \beta_0}} \sin \Delta \psi & \sqrt{\frac{\beta_0}{\beta}} (\cos \Delta \psi - \alpha \sin \Delta \psi) \end{pmatrix} \quad (2.40)$$

This notation is called the Twiss parameterisation of the motion, and the Twiss parameters α , β and ψ are functions of the S coordinate and are defined by the accelerator lattice. For one full revolution one can set (the so-called periodic condition): $\alpha=\alpha_{(0)}$, $\beta=\beta_{(0)}$, and $\Delta\psi=\mu$.

$$M = \begin{pmatrix} \cos \mu + \alpha \sin \mu & \beta \sin \mu \\ -\gamma \sin \mu & \cos \mu - \alpha \sin \mu \end{pmatrix} \quad (2.41)$$

The particle parameters for the new position can now be easily obtained using Eq. (2.42).

$$\begin{pmatrix} x_{s_1} \\ x'_{s_1} \end{pmatrix} = M \begin{pmatrix} x_{s_0} \\ x'_{s_0} \end{pmatrix} \quad (2.42)$$

M can also be written as:

$$M = \cos \mu \begin{pmatrix} 1 & 0 \\ 0 & 1 \end{pmatrix} + \sin \mu \begin{pmatrix} \alpha & \beta \\ -\gamma & -\alpha \end{pmatrix} \quad (2.43)$$

where the cosines part is multiplied with the unity matrix and the sinus part fulfils:

$$\det \left[\sin \mu \begin{pmatrix} \alpha & \beta \\ -\gamma & -\alpha \end{pmatrix} \right] = \beta\gamma - \alpha^2 = 1 \quad (2.44)$$

Considering Hills equation the Twiss parameters can be expressed as:

$$\gamma_{(s)} = \frac{1 + \alpha_{(s)}^2}{\beta_{(s)}} \quad (2.45)$$

$$\alpha_{(s)} = -\frac{\beta'_{(s)}}{2} \quad (2.46)$$

2.3.5 Dispersion

As shown in (2.23) the actual bending radius not only depends on the magnetic field but it is also dependent on the particle momentum. Thus a bunch consisting of many particles with small deviations in momentum will show a spread in trajectories through a bending magnet. This effect is called dispersion.

The solution for the inhomogeneous differential equation (2.25) is only a simple extension term to the homogeneous solution (2.27) where D is known as the dispersion function (2.48):

$$x_s = \sqrt{\varepsilon \cdot \beta_s} \cdot \cos(\psi_s + \phi) + D_{(s)} \frac{\Delta p}{p_0} \quad (2.47)$$

$$D_{(s)} = \frac{\sqrt{\beta_{(s)}}}{2 \sin(\mu/2)} \int_s^{s+c} \frac{1}{\rho_0} \sqrt{\beta_{(\bar{s})}} \cos \left[\psi_{(\bar{s})} - \psi_{(s)} - \frac{\mu}{2} \right] \cdot d\bar{s} \quad (2.48)$$

2.3.6 Emittance and acceptance

The emittance is the area of the Courant Snyder ellipse which contains a certain percentage of all particles. For example the “95 % emittance” is then defined as the area of an ellipse containing 95 % of the particles. Another way to describe this area is to use the sigma parameter of a Gaussian distribution. One sigma is then defined as the distance given by one standard deviation from the distribution mean. A so-called one sigma beam size based on an initial Gaussian distribution would therefore contain 68.2 % of the whole beam. In this thesis, unless stated otherwise, all emittances are defined as one sigma emittances.

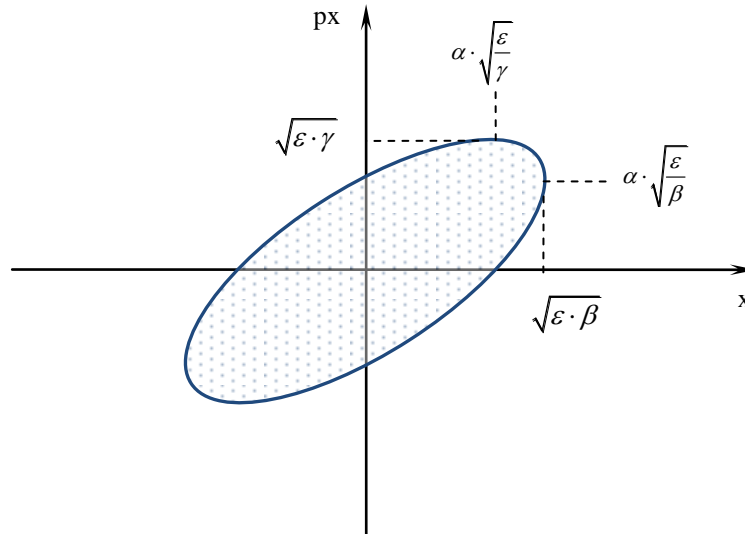


Figure 2.3: The transverse beam emittance in phase space

The acceptance is the size of the physical aperture limits transferred into phase space and thus associated with the largest possible phase space area covered by the beam. A vacuum chamber with the semi axis aperture r would then have an acceptance of:

$$A = \frac{r^2}{\beta} \quad (2.49)$$

2.3.7 Tune

The tune (Q) is the number of betatron oscillations in the vertical or horizontal plane that one particle sees in one complete revolution (2.50).

$$Q = \frac{1}{2\pi} \oint \frac{ds}{\beta_{(s)}} \quad (2.50)$$

Since the change in phase advance is inverse proportional to the beta function (2.51) the tune can also be expressed as shown in (2.52).

$$\frac{1}{\beta_{(s)}} = \frac{d\psi_{(s)}}{2s} \quad (2.51)$$

$$Q = \frac{\Delta\Psi_{(s)}}{2\pi} \quad (2.52)$$

The fractional part of the tune is essential for the stability of the beam. Integer tunes or resonant fractional tunes such as $\frac{1}{2}$, $\frac{1}{3}$ etc. cause beam instabilities, as the effect of any magnetic imperfections will add up over several turns. For example, if the fractional tune is set at 0.5, a quadrupole error at a certain location will deflect the beam at exactly the same phase in its motion every second turn, such that the particle amplitude will grow very rapidly and the beam become quickly unstable. For proton colliders such as the LHC, it is common to need to avoid resonances of order 10 or above.

2.3.8 Chromaticity

Chromaticity effects are caused by the fact that focussing lattice elements have a momentum dependence of the focal properties. In a quadrupole lens particles with different momentum are focused at different focal length, which produces a dependence of the particle tune on a particle's momentum. Chromaticity consequently manifests itself as a tune spread which depends on the momentum spread.

$$Q' = \frac{\Delta Q}{\Delta p / p} \quad (2.53)$$

Chromaticity effects can be corrected globally using sextupole magnets. The sextupole field produces an amplitude dependant quadrupole focussing, and if the sextupole is placed in a dispersive region, the particle amplitude depends on the momentum offset and so the chromaticity can be compensated. This is rather complicated to achieve in reality, and careful arrangement of the sextupole elements is required.

2.3.9 Longitudinal dynamics

A particle circulates around the machine (radius r) with a certain frequency f :

$$f = \frac{\beta \cdot c}{2\pi r} \quad (2.54)$$

Such particles can be accelerated by an oscillating electrostatic field as present in Radio Frequency (RF)-cavities. The field within a cavity is described in (2.55) where V is the maximum RF voltage, d the cavity gap and φ the (electrical) phase of the RF-wave.

$$E_0 = \frac{\hat{V}}{d} \cdot \sin(\omega t + \varphi) \quad (2.55)$$

Any circulating particle arriving with the desired phase lag ϕ_s in respect to the rising zero crossing of the RF-wave is called a synchronous particle. In a collider like the LHC it is mandatory to fill the ring longitudinally at many places. Thus a RF-frequency much higher than the revolution frequency (f_{rev}) is needed. In fact the LHC has a RF-frequency 35640 times higher than f_{rev} which is called the harmonic number. In principal there would be 35640 locations in the accelerator where a bunch of particles could be placed; however only 2808 such buckets are filled in the LHC, with a spacing of 25 ns, in order to optimize the machine concerning collective effects and obtain manageable data rates for the detectors.

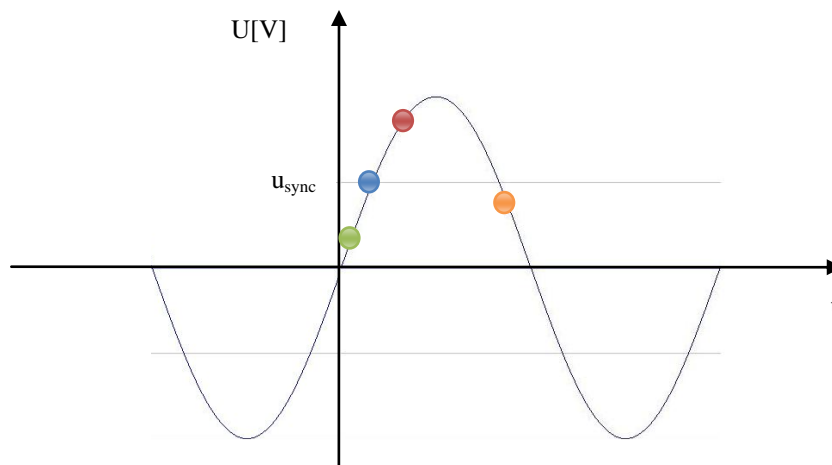


Figure 2.4: Simplified situation of particles arriving synchronous (blue), with a small lag (red), a big lag (orange) and earlier (green) at the RF-cavity.

The particles in a bunch have a spread in momentum and arrival time at the location of the RF cavity. Figure 2.4 shows a RF-signal applied to a cavity together with a simplified set of arriving particles. Particles which arrive in time (blue) with the ideal synchronous particle will see the accelerating voltage U_{sync} . Particles which arrive later than the synchronous one will see a higher voltage and thus a higher accelerating field than particles which arrived earlier. This means they are able to catch up with the synchronous particle as they gain more in momentum each time they pass by the cavity. Particles with a higher velocity than the synchronous particle arrive before and do not get so much acceleration so that the synchronous particle catches up.

This simplified explanation is only true if the particles oscillation in phase does not get bigger than $\phi = \pi - \phi_s$ and the particle stays non-relativistic. Any particle exceeding this phase limits (orange) would get unstable as it receives an acceleration which moves it even further away from the synchronous particle. The orange particle in Figure 2.4 for instance is much slower than the synchronous phase but arrives so late that it already exceeded the phase constraint and thus sees a lower voltage than it would need in order to receive a higher acceleration than the synchronous particle. Hence for this particle the momentum gap increases further and it's longitudinal motion gets unstable and it is finally lost in the accelerators aperture. The boundary between the stable and unstable particles is called separatrix, the area within the separatrix is the RF-bucket.

A second constraint of the simplified view is that the explanations given are only true if the particles are non-relativistic. In principal the same explanation approach is valid for relativistic particles but one has to consider an effect inherent to the relativistic relation between velocity and momentum: From a certain point on the particles velocity is increasing slower than its momentum. Hence the particles path gets longer (for the same dipole field strength) but the gain in velocity does not compensate for the additional path length.

This means that any off momentum particle arriving too late at the cavity - compared to the synchronous particle - would see a higher E-field in the cavity and would again increase its momentum more than its velocity which results in an even longer orbit and thus again in a later time of arrival. It is obvious that such a particle would become longitudinally unstable. In the extreme case very close to the speed of light any acceleration would increase the momentum but velocity (and revolution frequency) would nearly stay at the same level. The slip factor η defines this relation between frequency and momentum change (2.56). Equation (2.57) shows the relation between momentum change and orbit length change which is called the momentum compaction factor.

$$\eta = \frac{\frac{\Delta f}{f}}{\frac{\Delta p}{p}} = \frac{1}{\gamma^2} - \frac{D}{R} \quad (2.56)$$

$$\alpha_p = \frac{\Delta R / R}{\Delta p / p} \quad (2.57)$$

Particles accelerated from zero to the speed of light would see both effects described above. The point where the longitudinal particles behaviour would change from stable to unstable due to the relativistic functions (for a normal lattice the slip factor changes sign) is called "transition" and can be compensated by a jump in RF-phase when crossing this point.

3 Methodology of Particle Tracking Simulations

This chapter gives a brief overview of the basic principal and tools used for the tracking simulations performed for this thesis. A short example explains the computational challenge and a brief introduction to the MAD-X program is discussed.

3.1 The crucial performance limitation: CPU time

Given the huge dimension of the LHC accelerator and its numerous different lattice elements, it is a major computational challenge to describe every piece of it in detail. It is computationally impossible to model the motion of each particle in the nominal LHC beam (up to 3.1×10^{14} particles) even with the most powerful computers available today at CERN.

To get a feeling of the order of magnitude we can assume the following simplified example (in reality times will be longer as any additional calculation task will significantly change this numbers to higher levels):

If we take one full LHC beam and track it around the ring for one turn, then with the full aperture model one particle needs around 25,000 CPU cycles.

Extending this to the full beam we get the following numbers:

3×10^{14} particles \cdot 1 turn \cdot 25000 cycles = 7.5×10^{18} CPU cycles,

7.5×10^{18} cycles divided by 2×10^9 (cycles per s on a 2 GHz CPU) = 3.75×10^9 sec \approx 1200 years.

Thus simplifications must be made in order to fit the actual situation into a model that can be computed by the available equipment.

One way is to use a reduced number of particles, but still a valid distribution which is representative. Such particles are then often called macro-particles, since each particle in the simulation represents many thousands of real particles. Another way is to simplify the accelerator model (e.g. by using fewer slices in the thin lens version). In practise both ways are needed to arrive at reasonable computation times.

A practical value of a standard beam abort simulation as performed for chapter 6 is 15,000 seconds for 8×10^4 particles tracked through the most sophisticated LHC model including apertures, tolerances, alignment and magnet field errors.

3.2 The MAD-X code

MAD-X (Methodical Accelerator Design) [19] is a widely used accelerator design tool for calculating charged particle optics in alternating gradient accelerators or beam lines. MAD-X has developed over many years with many different modules, and is programmed in two different languages: Fortran 77 and C.

The main program is written in C whilst the tracking code “Thintrack” used extensively for this thesis is written in Fortran 77. Thintrack only allows a thin lens sequence which can be obtained from a thick lens one by using the MAKETHIN command. The code uses the thin lens approximation to convert “lenses” with a certain length into lenses with zero length (“bending plane” in the middle of the thick lens). Therefore the approximation is made that each particle sees its deflection according to its transverse position only at a transverse plane in the middle of the lens. The longitudinal space in front and after this plane is treated like drift space. It is obvious that particles going through this drift space will hit the middle plane slightly different then particles getting their deflection over the total lens length. This mismatch can be reduced by converting one element not only into one thin lens plane in the middle but by splitting the magnet into several equally long pieces which are then individually converted into thin lenses. By doing that one thick lens is replace by several thin lenses and the angle mismatch at the middle plane is reduced. Any small errors still obtained by such a

conversion to thin lens optics have to be corrected by rematching of the thin lens quadrupole strength which can be done with the MATCH module.

Another essential feature of THINTRACK and the thin lens version is that it supports the allocation of errors. Misalignment errors can be assigned by using EALIGN whilst field errors can be assigned by the EFCOMP command.

3.2.1 Frequently used MAD-X modules

This section briefly summaries the most often used modules and gives an overview of the actual module order used in the individual simulation jobs (Figure 3.1). More detailed information can be found in [20], [21].

The TWISS module:

The TWISS module is one of the main MAD-X modules. This command causes computation of the Twiss linear lattice functions, and optionally of the chromatic functions. It is possible to set initial optics values for computation of the Twiss matrix, which is necessary for handover between different sequences. An option is to choose the position for the Twiss calculation within an element. (Start, Centre, End). It has to be noted that the CENTRE option includes any misalignment in the output orbit coordinates.

The THINTRACK module:

Particle trajectories can be tracked either for single passage (option onepass), or for many turns (default option). In all cases the tracking is performed element per element. Only thin elements are allowed, which guarantees the simplicity of the coordinate transformation.

The MAKETHIN module:

This module converts a sequence with thick elements into one composed entirely of drifts and thin multipole elements as required by THINTRACK. The optics generally needs to be rematched back to the nominal one after this command.

The MATCH command:

Before a match operation at least one sequence must be selected by means of a USE command. Matching is then initiated by the MATCH command, to achieve the desired Twiss parameters, e.g. at the experimental interaction points. The matching module can act on more than one sequence simultaneously by specifying more than one sequence when initiating the matching mode. From this command to the corresponding ENDMATCH command MAD accepts various matching commands.

The ERROR module:

It is possible to assign alignment errors (EALIGN) and field errors (EFCOMP) to single beam elements or to ranges of beam elements with the SELECT command. Errors can be specified both with constant or random values. It is mandatory to activate a sequence with the USE command before assigning any errors. With EOPTION it can be chosen if errors should add up or if each existing error should be overwritten by a new value. It has to be noted that any further USE command will reset all assigned errors which limits the degrees of freedom when programming the MAD-X applications. The command ESAVE can be used to save and reload all error settings for selected elements. However it is so far not implemented to reload corrector settings.

The *CORRECT* module:

The *CORRECT* statement makes a complete closed orbit or trajectory correction using the computed values at the monitors from the Twiss table. Thus the orbit correction must always be preceded by *TWISS* commands which generate Twiss tables. The most recent Twiss table is assumed to contain the optical parameters and the distorted orbits, whilst Twiss tables generated before (under different names) can be used as target orbits. An option allows activating or disabling ring monitors separately and all monitor and corrector values can be written into tfs-files. However an easy read back of such corrector values is not implemented yet.

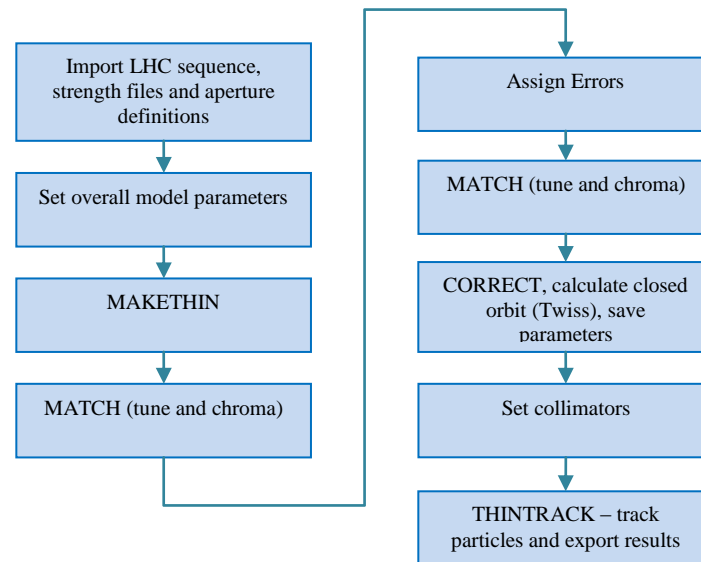


Figure 3.1: Schematic overview of a simple MAD-X tracking job.

3.3 The LHC MAD-X Model

Different LHC optics have been developed over the past decade. An overview is given in [22]. For this thesis version V6.503 has been used. Each LHC optics version consist of the LHC sequence, the strength files, the aperture and tolerances files and several special optics files e.g. the local settings for different beta functions in the collision points.

Only the sequence and strength file is needed to calculate the Twiss parameters and beam trajectories. However these trajectories have to be compared to the mechanical boundaries within the accelerator (usually an installed vacuum chamber or a magnet, beam screen, collimator yoke...). Therefore an aperture model is available and can be easily included. *THINTRACK* then compares the trajectory with the actual elements aperture and detects any trajectory which reaches the aperture.

A proper model of the machine imperfections is mandatory for the type of tracking studies done in this work. MAD-X supports misalignments and field errors. Misalignments are important as they change the available aperture and for magnets also the resulting field. A horizontally misaligned quadrupole gives an additional deflection like a bending magnet which significantly changes the beam trajectory. Misalignments are specified for every type of element and are discussed in detail in Chapter 6. Multipolar field errors have complex non linear effects on the beam trajectory. A repository of measured field errors is available for the main LHC magnets and was used for this study. Further details are explained in Chapter 6.

The imperfections cause a distorted orbit which would have amplitude deviations too large to fit into the design aperture. Thus corrector magnets are installed to apply small corrections so that the orbit offset can be kept within a specification of 1 mm RMS and a maximum of 8 mm peak to peak (ptp). For the tracking job this orbit correction has to be done using the *CORRECT* module which applies a *MICADO* [23] algorithm. This algorithm finds the corrector magnets which could affect the RMS orbit value most and also finds suitable strength values to decrease the RMS orbit. This process is iterative and redone until the RMS orbit is below the initially specified one.

The assigned errors and the applied correction also perturb the optics function and thus tune and chromaticity have to be matched to their nominal values. The tune usually changes dramatically due to the applied errors. Hence during the matching procedure the crossing of tune resonances cannot be avoided and this together with the presence of higher field errors (non linear machine) are a very demanding cases for the MAD-X matching routines.

The resulting orbit even after matching of the optical functions is still different from the ideal one. This is important for the collimators which need to be set at a certain distance in beam sigma from the actual orbit; hence in the simulation the collimator positions are adjusted after the orbit and optics is corrected. This is necessary because the orbit changes position, but also because the optics is perturbed which changes the beam sigma at the collimator locations.

After this setup the tracking routine can be started. However THINTRACK cannot change magnet strength values over time, which is essential for modelling the effects of the beam dump kickers. Every step in strength (or time) has to be calculated separately which required the development of a loop-based THINTRACK job and post processing for data visualization. This process is further explained in Chapter 6. Figure 3.1 shows a simplified overview of a MAD-X THINTRACK program flow.

3.4 Random numbers

Random numbers are at the crucial input of every Monte Carlo simulation. In this thesis they were needed to generate different independent initial beam distributions.

In theory there are two types of random numbers: true- and pseudo-random numbers. Whilst true random numbers are often obtained by measurement of a physical phenomenon expected to be random (e.g. thermal noise), pseudo-random numbers are calculated with special algorithms that produce long sequences of apparently random results, which are in fact determined by a initial value, known as a seed. MAD-X uses only such a simple pseudo-random numbers generator (PRNG). It proved impossible to create suitable independent distributions for the tracking tasks done in this work with the implemented PRNG due to the fact that it always gives the same sequence of numbers for one seed. A pragmatic solution was found by calling a shell scripts which reads a time & CPU clock dependent random number from the system and saves this number into a short MAD-X script. This script is then read by the MAD-X main program and the independent number is used as a seed of the MAD-X-PRNG. This step is repeated several thousand times and each random number is used to calculate a x , p_x or y , p_y coordinate of the initial distribution. For the tracking job itself again this random number principal is used to pick a line out of the distribution table which is then used as the initial tracking coordinates for that run. Unfortunately this concept requires many system shell calls and read sequences which is quite CPU intensive and limits the program performance. Figure 3.2 shows the cross-correlation between the x and y coordinates of on initial set of 7400 particle coordinates at the top and the auto-correlation for the x coordinate at the bottom. One can only see the spike around 7400 steps when the MATLAB algorithm fully circulates through the set for the first time. The same is true for p_x and p_y relations. All tested correlations are at low level without any unwanted peaks. Thus the created particle coordinates can be considered as unique. The exact calculation of the initial Gaussian beam distribution is discussed in more detail in Chapter 6 as well as a more detailed analysis of the distribution shape.

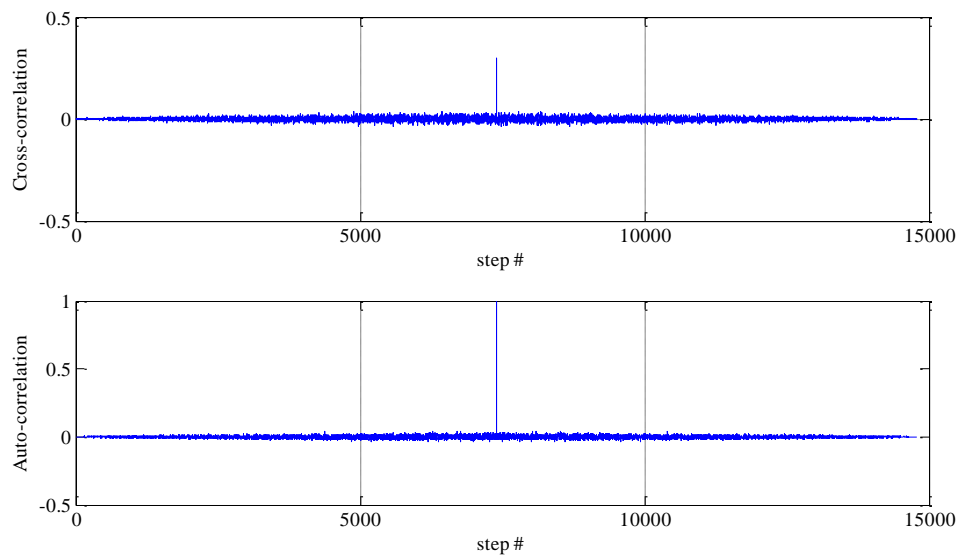


Figure 3.2: Cross-correlation between x and y values (top) and auto-correlation of one random number series (bottom).

4 Beam Dump and Extraction Systems

This chapter gives an overview of general extraction systems and beam dumps. Firstly the main elements of beam extraction systems are explained and their interaction in different designs is briefly discussed, followed by three practical examples. The first example explains the commissioning of the single turn fast extraction system used in the SPS to transfer beam to the LHC. The second section is a detailed study of the internal SPS dump system, including results of tracking studies used to test the methods deployed for the LHC studies, and the third section presents the preliminary design considerations for the dump systems for the PS2 accelerator, proposed as an upgrade of the LHC injector chain. The work of all three examples has been published at particle accelerator conferences (PAC07 and EPAC08) [31,32,39].

4.1 Main machine elements used for beam dump and extraction systems

An extraction system comprises all the equipment needed to move the beam trajectory precisely onto a new orbit into a transfer line. A dump system comprises all the equipment needed to safely dispose the beam onto a special (shielded) device (dump block). This section describes the main hardware elements of such systems.

4.1.1 Kicker magnets

Kickers are dipole magnets which are built in such a way that they can switch on and off their field in a required (short) time window. Figure 4.1 shows a simplified sketch of a kicker with a window frame design. Kickers usually need complex power supplies to deliver the requested waveform and have challenging requirements for the power supply switches. The magnet is often within the vacuum, built into a special tank which requires machining, cleaning and selection of the material in order to fulfil the demanding vacuum and pulsed high voltage requirements.

The kicker rise and fall times are important performance parameters, with 10 ns to a few μ s as typical values. For special applications, for example CLIC [24], the specified rise time is a few ns. The kicker pulse shape or waveform quality is also important, since any deviation from an ideal trapezoidal pulse shape will cause different parts of the beam to be deflected with different angles. A maximum flat-top variation of 1% is a typical specification.

For high energy (or intensity) it becomes important to build extraction and transfer systems which are capable to make loss free beam transfer. This requires a precise timing of the kicker magnets within special gaps in the beam pattern. For dump kickers usually the rise time only is crucial, whereas for extraction or injection kickers the fall time can also be important, as it is often the case that only a certain part of the beam is demanded by different beam lines.

For the LHC a set of beam dilution kickers is used in addition to the beam extraction kickers. The dilution kickers are installed in the transfer line between the extraction point and the dump. They use orthogonal sinusoidal and cosinusoidal kick waveforms to paint the beam onto the dump during the extraction process in order to dilute the beam intensity over a bigger area so that the dump material is not damaged.

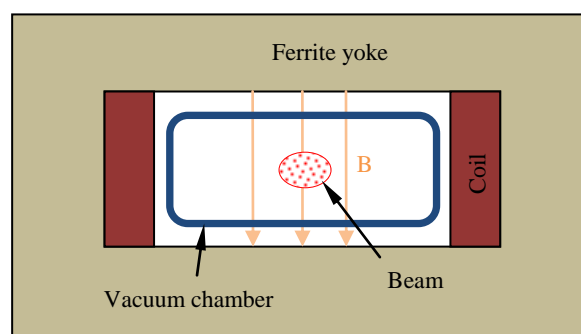


Figure 4.1: Schematic sketch of a kicker dipole with its main components.

Due to their fast rise/fall time kicker magnets are always designed and developed together with their power supplies. Figure 4.2 shows the simplified design of a typical kicker magnet power supply circuit. A Resonant Charging Power Supply (RCPS) [25] charges a Pulse Forming Network PFN (or a Pulse Forming Line PNL) which is then discharged over the switch and the transmission line into the kicker magnet. In order to avoid unwanted reflections all system parts have to be matched to the same impedance Z . For this reason a terminating resistor also has to be installed after the magnet – otherwise unwanted reflections would superimpose with the created waveform.

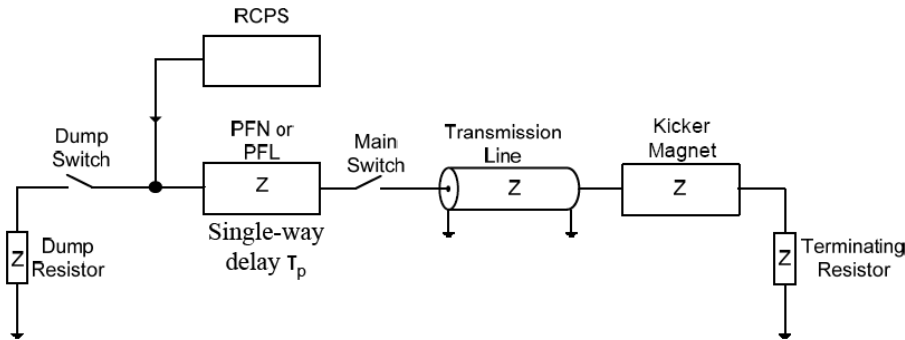


Figure 4.2: Typical schematic design of a kicker magnet power supply [26].

Figure 4.3 describes the general function of a pulse forming line charged to the Voltage V . The parameters α and β (4.1) (where Z_L is the load impedance and Z_0 the characteristic PFL impedance) give the ratio of the voltage divider and the reflection coefficient. For the matched case $\alpha=0.5$ and thus the PFN charging voltage has to be set to the double of the voltage required at the magnet. The reflection factor for the load end is zero (matched case) and set to $+1$ at the charging end of the line.

$$\alpha = \left(\frac{Z_L}{Z_0 + Z_L} \right) \quad \Gamma = \beta = \left(\frac{Z_L - Z_0}{Z_L + Z_0} \right) \quad (4.1)$$

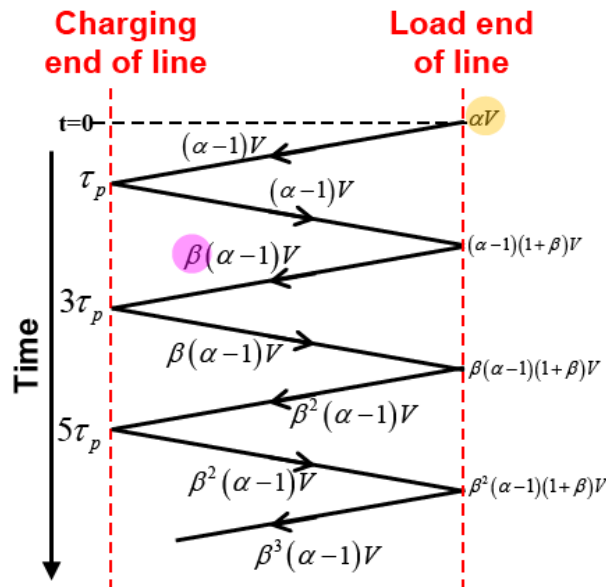


Figure 4.3: General schematic description of a pulse forming circuit [26].

The magnet impedance is very important as it influences all systems when being matched. Also the induced voltage in the coils is the inductance times dI/dt . As the rise time is fixed by the functional specifications the maximum voltage can be limited by having a low product of inductance and

current. Therefore a small pole gap (lower current) and a low number of windings (lower circuit impedance) is of advantage. The maximum allowed voltage is mostly determined by the isolation design and the power switch capability.

In modern accelerators two main types of switches are used: Thyratrons and power semiconductor switches. Deuterium Thyratrons are still widely used, which achieve their function by rapidly ionising a neutral gas. This is initiated by free charges crossing the switch gap under an electrical field. Gas molecules are then ionised (producing new free charges) and positive charged ions are accelerated towards the lower potential electrode where they cause the release of secondary electrons. If this process occurs with sufficient energy under right circumstances it becomes self-sustaining, the voltage breakdown over the switch happens and the Thyatron commutates. Such switches can be built for voltages up to 250 kV and peak currents of up to 100 kA whilst providing very fast rise times (150 kA/ μ s). [27] A disadvantage of Thyatron switches is their tendency for erratic turn-on. Therefore Thyratrons were not considered for the LHC dump system, where accidental turn-on of one kicker switch could have serious consequences for the machine. Instead semiconductor switches are used which have significantly reduced erratic rates as well as less maintenance requirements. However the maximum rate of rise current is limited to around 20 kA/ μ s.

4.1.2 Magnetic septa

In general, high deflection strength and fast rise time are mutually exclusive, and all possible measures are taken to reduce required kicker strength. Septum magnets are dipole magnets with a special asymmetric design in order to minimise the kicker strength needed in an injection or extraction region. Septum magnets are designed to allow moving the deflecting element very close to the circulating beam. They are comprised of a thin element (the Septum) which separates the zero field region from the full dipole field. This minimises the distance for which the kicker magnets have to provide the deflection to change the beam trajectory into the septum dipole field. The septum itself (as shown in Figure 4.4) is commonly made out of copper and is used as the return conductor of the magnet coil, to produce a dipole field in the magnet gap.

A major design criterion for septa magnets is to reduce the stray field seen by the circulating beam in the nominally field-free region. Thin magnetic screens can be used to separate the septum area from the circulating beam region. In order to keep the thickness of the septum low (and also the number and length of magnets) it is mandatory to use liquid-cooled coils. In addition many septa magnets are built within vacuum to avoid having two additional beam pipes (and their wall thickness) for the circulating and extracted or injected beam. Magnetic septa can be powered in DC mode or with pulses of some 10-100s of ms length.

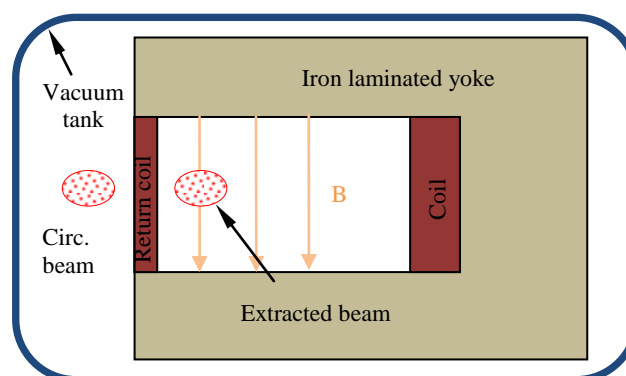


Figure 4.4: Schematic overview of the main elements of a magnetic Septum.

For the LHC a special septum design was used in order to accommodate the two circulating beams without increased separation, within a reliable back-to-back septum design. The principal design of these so-called “Lambertson Septa” is shown in Figure 4.5. In the LHC the 15 septa for beam one are installed in IP 6 back-to-back with the 15 septa for beam two (Chapter 5 gives a detailed description).

An advantage of the Lambertson design is that the coil is out of the beam area and therefore better protected against accidental beam losses. This construction allows thinner septum blades whilst still using water cooled coils carrying high currents. On the other hand a more massive yoke construction might be necessary (depending on the intended working point) to prevent from saturation in the septum area. [28]

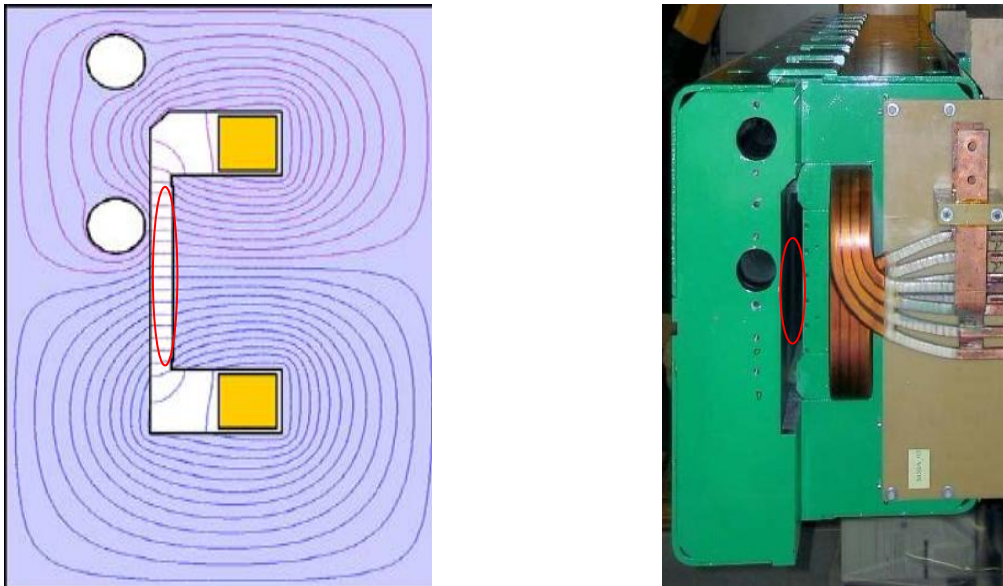


Figure 4.5: Left: Principal design of a Lambertson septum with yoke (gray), coils (yellow), circulating beam channels (white circular area) and field lines within the yoke. Right: Lambertson septa as build for the LHC. The region of the deflecting field is marked in red; beam is deflected in the vertical plane.

4.1.3 Electrostatic septa

The electrostatic septum is a device which basically has the same function as the magnetic one, but is used in applications where very thin septum elements are required to minimise beam losses, such as slow extraction where beam is removed from the accelerator over many thousands of turns. A totally different approach for the design has to be followed as it is impossible to carry high currents in very thin (0.1 mm) septum blades. Electrostatic fields are therefore used, even though the performance in terms of total deflection angle is far below that possible with magnetic fields. High voltages (several 100 kV) have to be applied to a flat anode/cathode construction where one electrode is made out of a thin foil (or wires). The required vacuum level is in the range of 10^{-9} to 10^{-12} mbar and the field levels reached are around 10 MV/m. [29]

With such a construction it is possible to build septa magnets with a septum of less than 0.1 mm thickness. This means that the distance which the beam has to “jump” over is very small compared to a magnetic septa (minimum 4-5 mm thick).

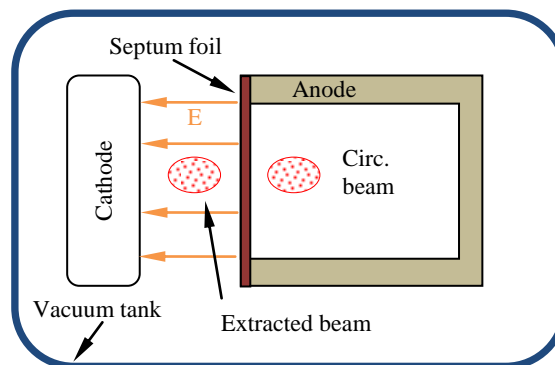


Figure 4.6: Schematic sketch of an electrostatic Septum.

4.1.4 Dump elements

Dump elements vary considerably in their construction, depending on the beam energy, beam size and total intensity. Hence their material varies in a wide range from steel, copper, tungsten for lower energies to carbon for higher energies like in the SPS and LHC. Figure 4.7 shows an image of the internal SPS high energy dump installed in the SPS tunnel, which comprises a carbon core surrounded by a 27 t steel shielding block. For the external LHC dump a carbon composite is used, where the density varies over the length to keep the energy deposited within acceptable limits while minimising the overall length. The central carbon core is surrounded by heavy shielding to reduce the ambient radiation dose.



Figure 4.7: Internal SPS TIDV dump element (green) with beam instrumentation tank in front.

4.2 Overview of beam dump and extraction systems

This Section gives a brief overview of beam extraction systems used for LHC pre-accelerators in the GeV range. It is split into two subsections dedicated to fast and slow beam extraction systems.

4.2.1 Fast beam extraction systems

4.2.1.1 Internal beam dump systems

The internal dump is a widely used concept. It comprises a set of dump kickers and a beam dump device which is inside the main accelerator. The principal is to deflect the beam with fast rising kickers onto a dump block which is within the vacuum near the circulating beam. Figure 4.16 shows a schematic overview of the SPS internal beam dump design. In this case the dump is designed as a single turn beam dump, where all the beam is deflected onto the dump block within a single turn of the machine (23 μ s for the SPS). However if the machine aperture is big enough and the dump block is close enough to the circulating orbit it is possible to sweep the beam onto the dump block over several turns, which relaxes requirements for the dump magnet design and is therefore cheaper to build. For single turn solutions the dump kickers are usually the most challenging part of the system, since for machines providing higher energies or intensities the kicker fields have to rise extremely quickly within a particle-free abort gap to avoid dangerous losses during the ‘sweep’ where the field is still increasing.

The SPS dump is split into two blocks which are a few meters (and one quadrupole) from each other in order to cover a bigger energy area. A detailed explanation of the SPS system is given with some practical simulations later in this chapter.

Another advantage of internal dump blocks is that they can be arranged to limit the overall machine aperture and as they are designed to cope with a full intensity beam they often represent some kind of an ultimate protection device, as an element where beam losses can be concentrated. However there are also some negative aspects like additional impedance of the dump and the kicker system seen by the beam.

4.2.1.2 Fast extraction

Figure 4.8 shows the simplified principal of a fast single turn extraction system as it is also used in the CERN SPS accelerator to transfer beam to LHC. During a gap in the beam pattern (abort gap), the orbiting beam is kicked by a set of fast rising kicker magnets, receives an additional deflection by the subsequent quadrupole and is finally extracted by a set of septum magnets. Shortly before the extraction kicker magnets are switched on a closed orbit bump is created which brings the orbiting beam closer to the septum to reduce the required kicker strength. For dump processes such a bump is not reasonable, since for emergency reasons the dump function must be operable whenever beam is in the machine, and as a result such bumpers would have to be as fast as the kickers.

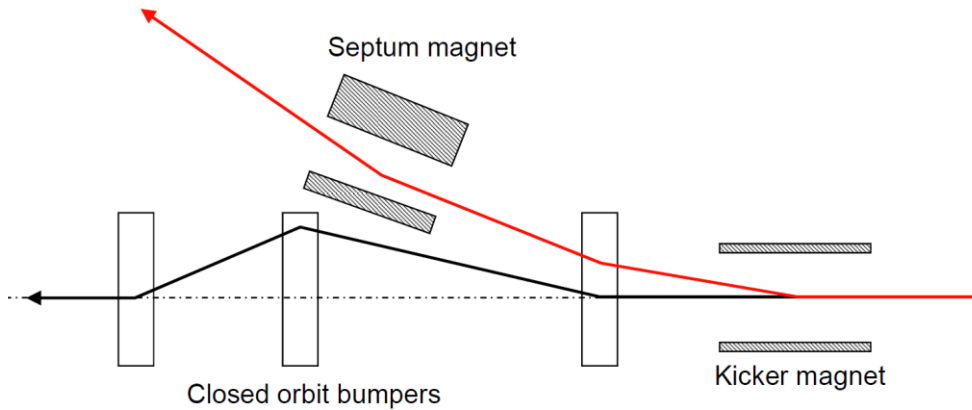


Figure 4.8: Principal of fast extraction with one set of kicker magnets and one set of septa. [30]

A beam extracted in such a way travels down a transfer line where it can either end up on a fixed target experiment, be injected in to a subsequent accelerator or is simply dumped onto an external beam dump.

4.2.1.3 Multiturn extraction (non resonant)

Multiturn extraction is an extraction method used to divide the stored intensity of an accelerator into integer parts. The principal is to partially kick the beam into a thin electrostatic septum blade which cuts the beam into two differently sized parts. It deflects then only a certain amount of it which is further deflected and finally extracted by the magnetic septa. With the machine tune set at the quarter integer, the remaining part of the beam takes another turn and due to the accelerators phase advance another part of it is cut away when it arrives again at the septum. This process repeats over a total of four turns, and then the remaining phase space core is left. This is then fully moved into the septum by an additional deflection coming from the kickers.

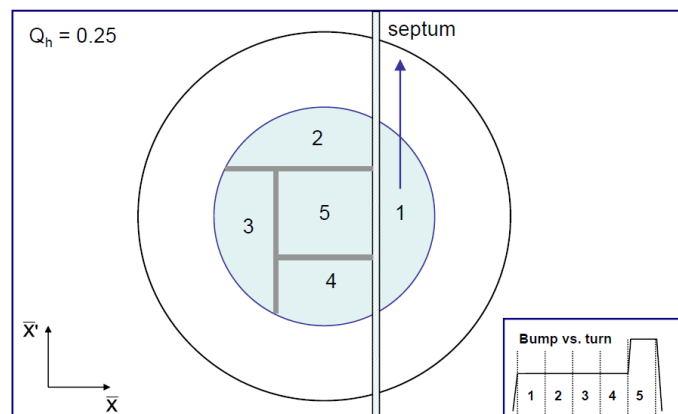


Figure 4.9: Principal of a multiturn extraction as used for beam transfer from the PS to the SPS. [30]

4.2.2 Slow beam extraction systems

4.2.2.1 Closed orbit bump dump system

Another way for beam disposal is to bump the beam into an aperture restriction. This can take from several to many turns and requires an accelerator with a suitable aperture so that for all energies beam is only lost at the dump device. The beam is essentially scraped away. This principal is mainly used in smaller machines, where the deposited intensity will not cause damage and also where the revolution time is so small that a reasonable abort gap would fill a huge part of the actual machine circumference and therefore would limit the intensity too much.

4.2.2.2 Resonant extraction

Resonant extraction is a sophisticated slow extraction concept, usually using the third-order resonance. A sextupole field drives the beam into resonance so that parts of the beam move to a well defined but unstable outer orbit, which then passes into the extraction channel of the electrostatic septum. The intensity of the actually extracted particle flow depends on the exact setting of the resonance and can be precisely controlled over many thousands of turns.

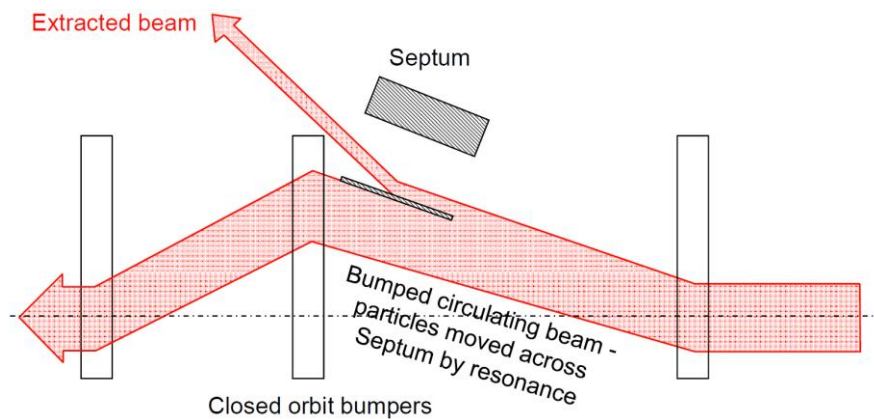


Figure 4.10: Simplified overview of a resonant slow extraction area (extraction elements only) [30].

A simplified overview of the beam extraction elements in a resonant extraction area is shown in Figure 4.10 with the circulating and extracted beam indicated in red. Figure 4.11 shows the transversal phase space of a beam driven into third order resonance with a septum blade indicated in orange and the electrostatic field deflecting particles in the extraction channel.

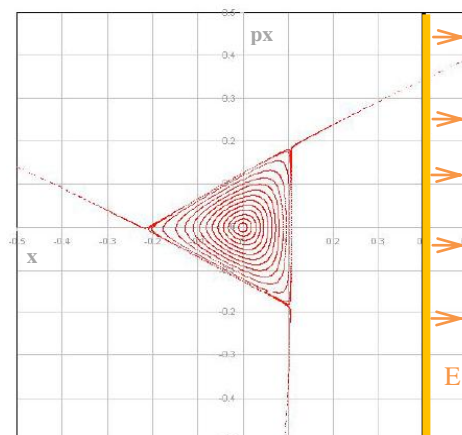


Figure 4.11: Third integer resonant extraction, with beam already following the separatrix arms (red) and the septum blade (orange). (modified from [30])

4.3 Commissioning of the SPS LSS6 beam extraction for LHC

In 2006 the extraction channel in LSS6 of the SPS was modified, to switch the beam from the SPS into the TI 2 transfer line for injection into LHC beam 1. The new extraction system is a conventional fast single turn system working in the horizontal plane. It comprises horizontal closed orbit bumpers, extraction kickers and magnetic septa as well as protection devices, beam instrumentation, interlocks and controls. [31]

The beam extracted in LSS6 for LHC operation travels down the TT60 line which is the first part of the TI 2 transfer line between the SPS and the LHC. In late 2006 the extraction systems and all elements up to the temporary beam dump (TED) in TT60 were commissioned with beam.

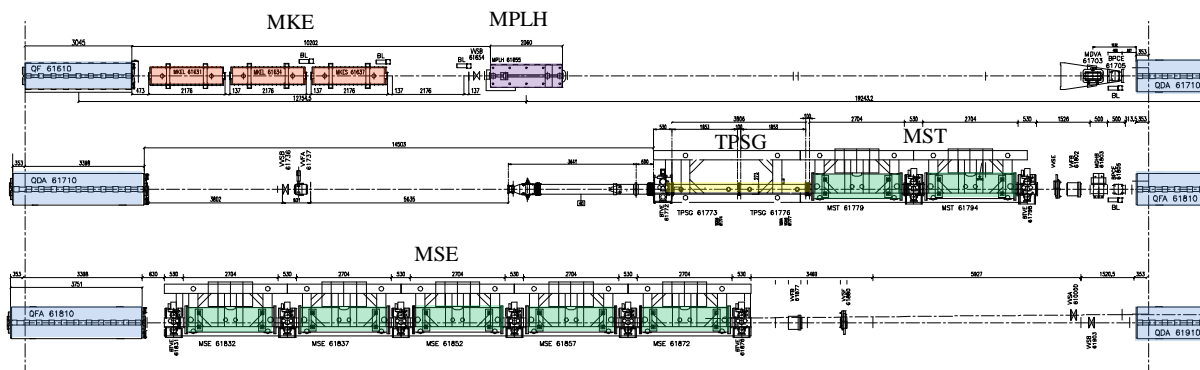


Figure 4.12: Detailed overview of the extraction area in LSS6 with quadrupoles QF & QD (indicated in blue), kickers MKE (red), bumpers MPLH (purple), protection device TPSG (yellow) and septa MST & MSE (green). The beam direction is from left to right.

Figure 4.12 shows a detailed overview of the three half-cells used for the LSS6 extraction system. Four horizontal and four vertical bumper magnets are used to control the circulating beam orbit at extraction. The bumped beam is horizontally deflected across the septum by a total of 0.4 mrad using three fast pulsed kicker magnets (MKE). The beam is then deflected out of the SPS machine by a total of ~ 12 mrad using DC septa magnets: two thin (4 mm septum) units (MST) and five thick (16 mm) units (MSE). An interlock system surveys the beam positions, losses, bumper and septum magnet currents, kicker charging voltages, etc. A graphite diluter and aluminium absorber (TPSG) protects the first septum from beam impact arising from kicker failures. The magnets in the TT60 line are conventional warm DC types. The movable beam dump (TED) in TT60 is capable of safely absorbing the full extracted beam, and has a graphite core surrounded by cast iron. The TED is retracted if beam is supposed to travel further down to the LHC. The beam instrumentation includes beam loss monitors BLMs, beam position monitors BPMs and profile monitors BTVs in the extraction channel and TT60, and a beam current transformer BFCT in front of the TED.

A series of measurements with beam were made during commissioning: The performance of beam instrumentation was checked, kicker waveforms were measured and the kickers were run at a higher voltage (in order to use only 3 out of 4 and keep on as hot spare); therefore the ferrite saturation was checked; MSE and MST apertures were measured and the correct alignment validated with beam as well as the MST good field region.

Figure 4.13 shows an aperture scan done with beam during the 2006 commissioning, made by bumping low intensity beam shots over the septa aperture and monitoring the beam losses. This allowed the alignment of the installed devices and their final mechanical apertures to be determined in respect to the beam.

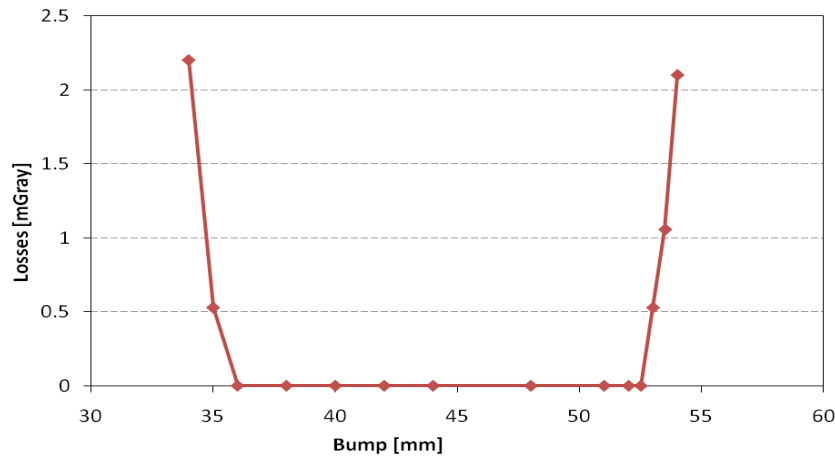


Figure 4.13: Scan of the LSS6 Septa aperture with beam.

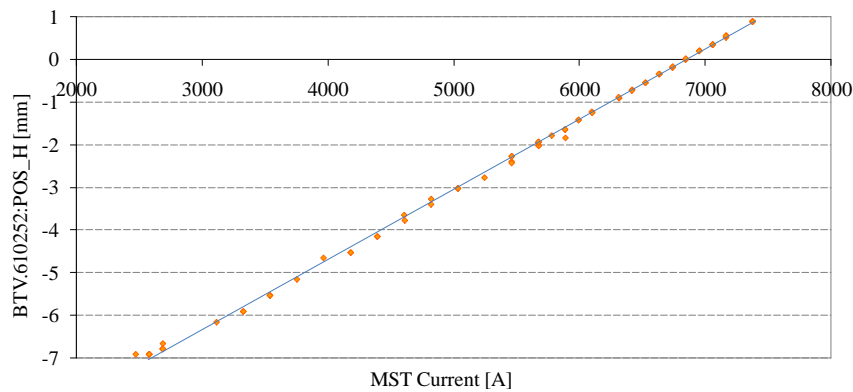


Figure 4.14: MST linearity measurement.

Figure 4.14 shows the result of the linearity measurements done for the MST septa. The septa current is displayed against the extracted beam position and shows no sign of non linearity. Figure 4.15 shows the measurement of the MKE kicker waveform done for the kickers in LSS4, where the beam position was recorded on a luminescent BTV screen located at a suitable phase advance downstream. The $10\ \mu\text{s}$ flat top for the extraction of one LHC batch is indicated (note that the min. flat top requirement is $8\ \mu\text{s}$). The overall ripples at flat top were $\pm 0.6\%$ which is slightly outside the specification needed in order to preserve the beam emittance for LHC. The kicker PFN was modified as a result, in the following shutdown.

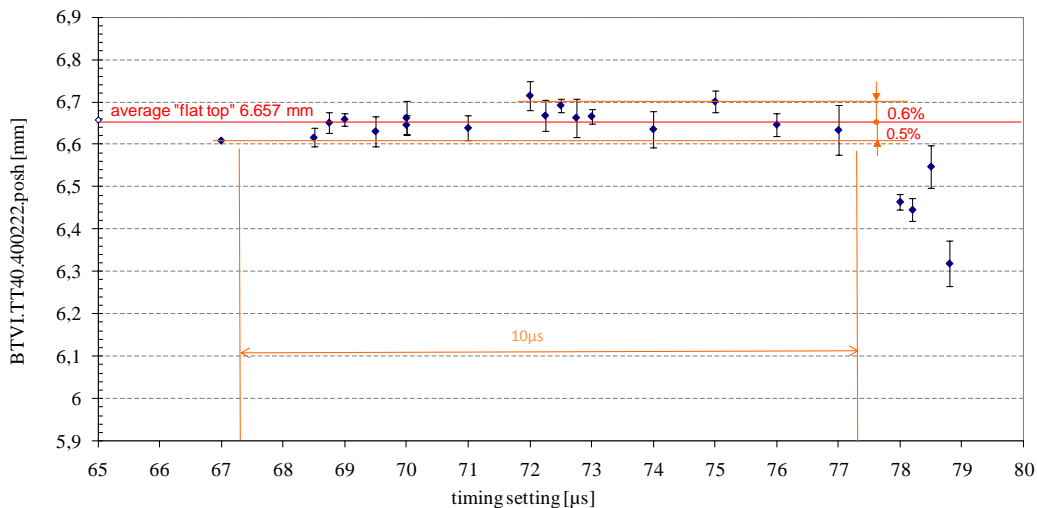


Figure 4.15: Measured MKE kicker pulse form in SPS LSS4.

4.4 Investigation of abnormal operation of the SPS beam dump system

This section briefly describes the SPS beam dump process, and presents the tracking studies carried out for failure cases. The SPS beam dump was studied in detail to develop the tools needed for the LHC. The study was used to investigate the possibility of operation with reduced kicker voltage and to better understand the trajectories and loss patterns of miss-kicked beam. The simulation results are compared to the results of measurements made with low intensity beam. [32]

4.4.1 The SPS and its beam dump system

The CERN Super Proton Synchrotron, accommodated in a 6.9 km long tunnel, was switched on in 1976 when it was the largest accelerator at CERN. It was originally designed to accelerate particles up to an extraction energy of 300 GeV for protons – however nowadays it can accelerate protons up to 450 GeV. Amongst the 1317 normal conducting magnets are 744 6.4 m long dipoles and 216 3.2 m long quadrupoles arranged in a separated function FODO lattice with 6 long straight sections (LSS). The dipole bending field is 1.8 T with a tolerable field error of 5×10^{-4} . [33]

The SPS beam dump system consists of the fast kicker magnets MKDV and MKDH and the internal dump blocks TIDH and TIDV. The system is installed in SPS long straight section 1 (LSS1). A schematic layout of the system is shown in Figure 4.16. In the vertical plane two MKDV magnets provide a deflection with a rise time of about 1 μ s, Figure 4.18. The three MKDH magnets provide a horizontal sweep with a rise time of about one full SPS turn (23 μ s), Figure 4.19. The combination of horizontal and vertical deflection sweeps the beam across the front face of the TIDV core, distributing the high beam energy over a large volume of the absorber block (example in Figure 4.21) to reduce the peak temperature rise. The kinetic energy of a beam of 3×10^{13} 450 GeV protons is about 2 MJ, sufficient to melt 0.7 kg of steel [34].

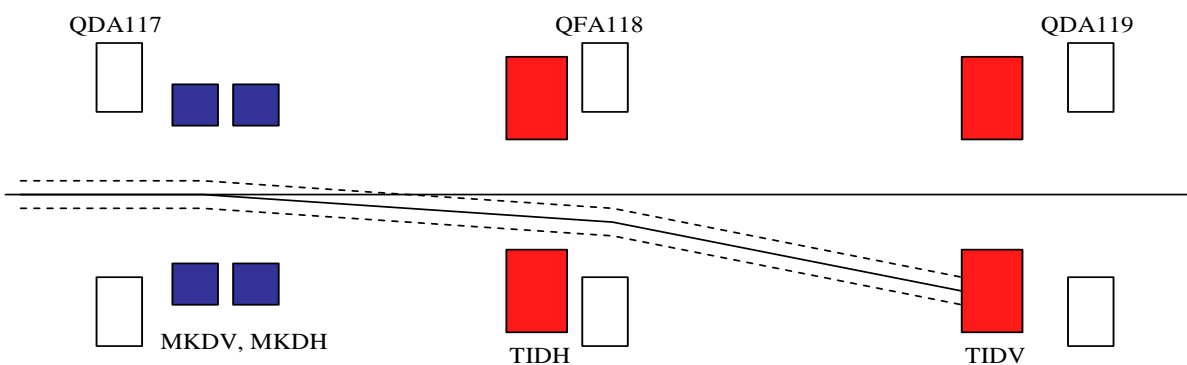


Figure 4.16: Schematic layout (side view) of the SPS beam dump system, showing the vertical and horizontal kicker systems (MKDV, MKDH) and the two beam dump blocks TIDH and TIDV.

For beam energies of up to 37 GeV the beam is dumped on the TIDH block; for energies above 105 GeV the beam is deposited on the TIDV. The 4 m long TIDV consist of a graphite absorber core inside a copper yoke, surrounded by a cast iron shielding block. The quadrupoles QDA117, QFA118 and QDA119 are transversely displaced to realise a closed orbit bump of about 7 mm in both planes which allowed the TIDV block to be installed closer to the design orbit. Dumped beams receive an additional kick from QFA118.

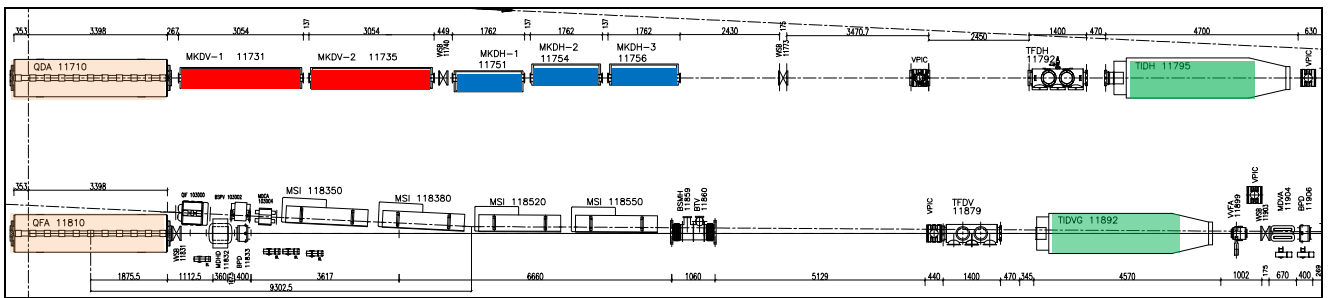


Figure 4.17: Detailed layout of the SPS beam dump region with vertical kickers MKDV (red), horizontal kickers MKDH (blue), the quadrupoles QD & QF (orange) and the dump elements TIDH & TIDV (green).

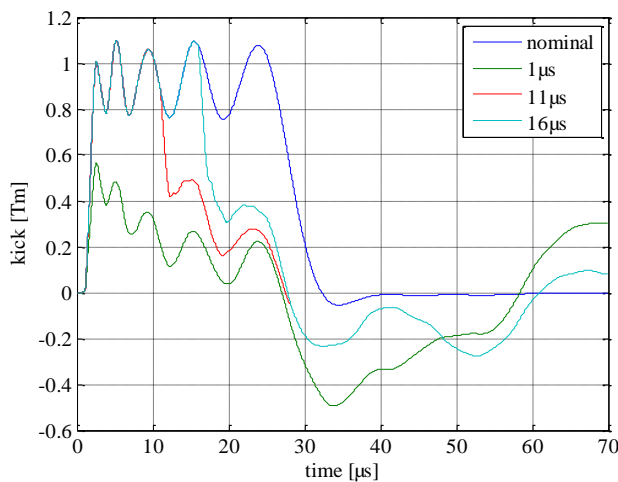


Figure 4.18: Simulated MKDV kicker pulses, 47 kV, nominal case (blue) and with sparks after 1 (green), 11 (red) and 16 µs (turquoise).

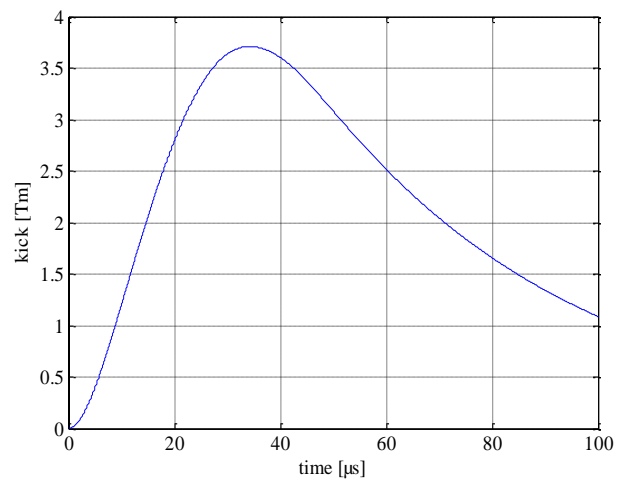


Figure 4.19: Simulated MKDH kicker pulse, 9 kV.

4.4.2 Failure cases

During 2006 SPS operation high voltage breakdowns in one of the MKDV magnets were observed. To fulfil the specifications for operation at 450 GeV, a third common Pulse Forming Network (PFN) was added to the two original PFNs. This implies that failures occurring in one magnet automatically have an impact on the field in the other magnet. The whole system has been simulated in Pspice [35]. Simulations of the current pulse for different failure cases (sparks after 1 µs, 11 µs and 16 µs) have been made and are included in Figure 4.18.

Two main failure cases have been analysed:

The first is an asynchronous beam dump, where the beam dump kickers are not fired in the abort gap. The kicker rise time and field shape are nominal for this case.

The second and more critical case is that sparks or short-circuits occur during a normal (or asynchronous) beam dump. In both cases not all particles are directly sent to the TIDV as foreseen. Particles are instead swept through the SPS-aperture during the kicker rise time for the asynchronous case, and are also swept with varying deflections in the short-circuit failure cases.

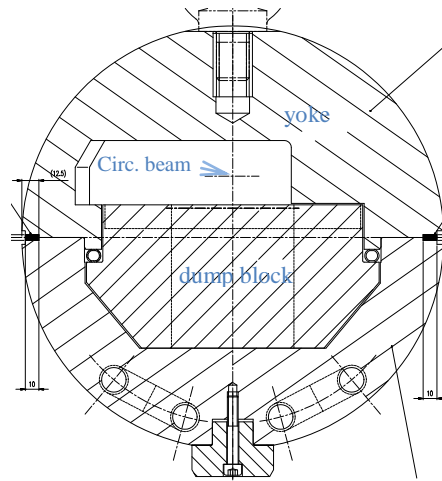


Figure 4.20: Design drawing of the TIDV dump (front view).

4.4.3 Tracking studies - Methodology

In order to quantify where and how such particles are lost around the accelerator, MAD-X tracking studies were performed.

A MAD-X tracking job using standard MAD-X functions was developed to fulfil the special requirements due to the fact that the particles which are not dumped within the first turn receive another, different, kick on subsequent turns. The job is designed for the whole time range over which the MKDV pulse is fluctuating and is divided into three sections. The first one consists of setting up nominal SPS conditions to create the orbit bump in LSS1 and to rematch several accelerator parameters. In the second part a Gaussian particle coordinate distribution in phase space is created and the calculation for the different kick values is done. The third part contains the tracking modules and contains loops which allow loading of different initial particle positions and a simulation from zero to $23.0543 \mu\text{s}$ (one SPS turn time) at intervals of 25 ns (corresponding to the LHC bunch spacing). As long as the particle is not lost in the accelerator it is restarted in a cascade of tracking routines with the appropriately modified kicker strength (which is a function of the turn and bunch numbers) until it is lost or it has survived several thousand turns. At this stage no optical, orbit or alignment errors were included in the simulation.

4.4.4 Beams and Aperture Model

The standard SPS aperture model was improved to obtain a better understanding of losses in the region of the TIDV and to make it possible to track particles. Therefore especially the apertures of the TIDV and TIDH including their SEM grids had to be defined in a more accurate way. Due to the use of the whole aperture model the CPU time rose above 14000 seconds for 180,000 initial particles. For all cases a fixed target beam with a normalised emittance of $\varepsilon_{xn}=12.0 \pi.\text{mm.mrad}$ and $\varepsilon_{yn}=7.0 \pi.\text{mm.mrad}$ was used. The time spacing for all calculations was set to 25 ns.

4.4.5 Post Processing

The MAD-X output files with the position data of the lost particles for each turn were sorted and filtered using MATLAB [36] to get the loss pattern around the SPS.

4.4.6 Simulation results for the asynchronous dump (sweep) cases

Figure 4.21 shows the loss pattern for an asynchronous dump with the kickers working under nominal conditions. The beam is painted onto the dump block as expected (blue) except the small part of the beam which had not seen enough deflection and therefore was transmitted into the

accelerator. Particles shown in red were not lost in other locations and did a full turn hitting the dump block consequently one turn after the particles shown in blue.

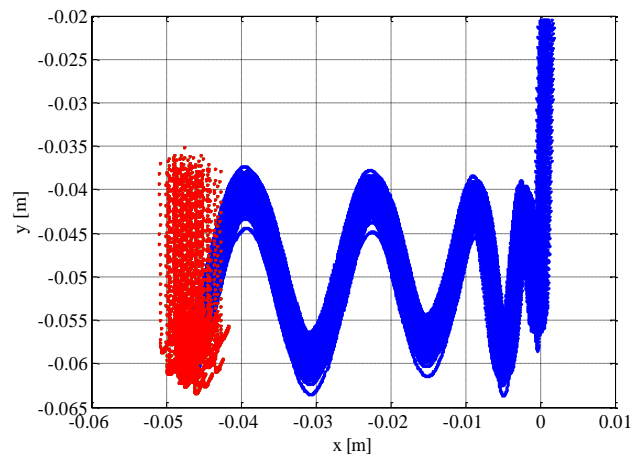


Figure 4.21: TIDV loss pattern, asynchronous beam dump (400 GeV, nominal pulse), blue: 1st turn, red: 2nd turn.

In Figure 4.22 loss patterns over the accelerator for asynchronous dumps (sweeps) under nominal conditions are shown for the two SPS versions. The upper part of the plot shows a peak in LSS4 at the MPLH 41672 (s=3986.48). This element is a bumper magnet used for beam extraction, with a small horizontal aperture. Abnormal irradiation was measured here in the past during SPS operation. This was clearly a limit and the layout in this region and in the other extraction channel in SPS LSS6 was therefore modified at the start of 2007, with the magnet moved to a position with a lower beta function, increasing the vertical beam aperture.

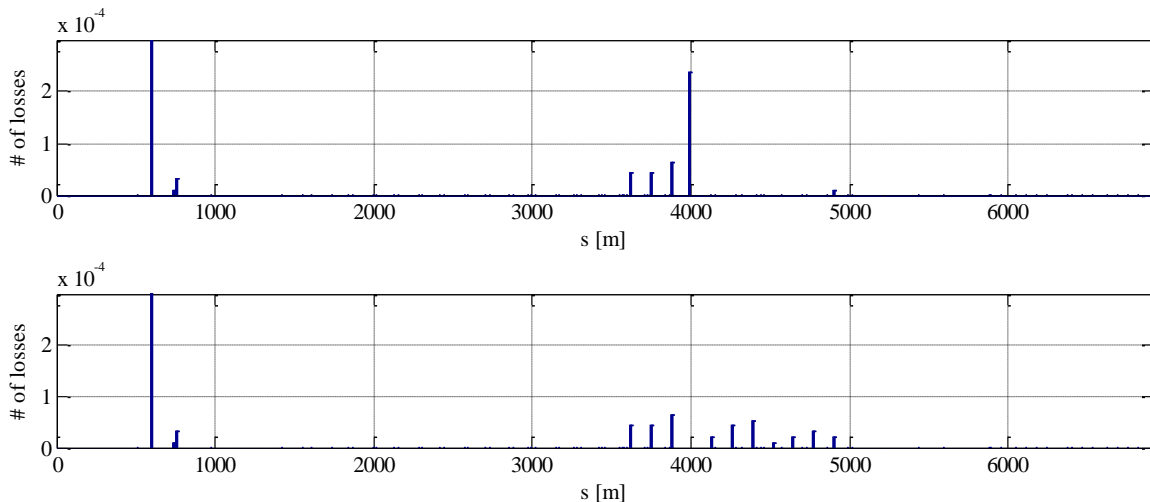


Figure 4.22: Loss pattern for a 400 GeV sweep with old bumper layout (top) compared to the new 2007 layout (bottom).

The lower part of Figure 4.22 shows the loss pattern of the simulation with this new layout. One can see dramatically reduced losses at the MPLH position. Some losses are now recorded on elements (main bending magnets) which were previously in the “shadow” of the MPLH magnet. The peak in LSS1 at s=602 m indicates the losses on the dump block.

4.4.7 Simulation results for the kicker failure (spark) cases

Figure 4.23 shows the loss patterns for dumps with MKDV short-circuits after 11 μ s for 30 GeV (top) and 400 GeV (bottom).

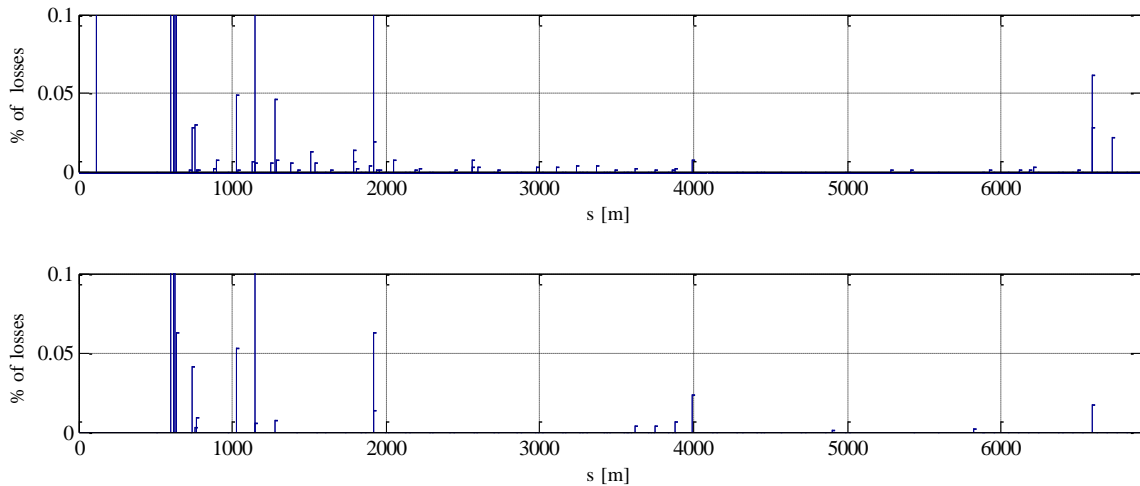


Figure 4.23: Losses for 30 GeV (top) 400 GeV (bottom), MKDV sparks after 11 μ s.

The 30 GeV simulation in the “forbidden” dump region (during the SPS ramp) was included because of a faulty dump which occurred in 2006 and which was suspected to have irradiated the MPLH magnet. Note the different vertical scale compared to Figure 4.22, with losses a factor of 10 higher around the SPS. Figure 4.24 shows the TIDV loss pattern of a 400 GeV dump with a short circuit after 1 μ s.

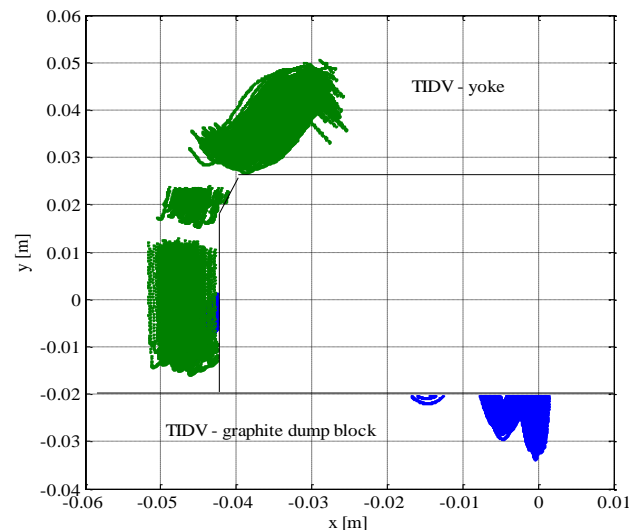


Figure 4.24: TIDV loss pattern, 400 GeV, short-circuit after 1 μ s, blue: losses 1st turn, green: losses 2nd turn.

One can see that most of the beam does a second turn in the SPS. Interestingly, due to the higher MKDH field in turn two and the break-down of the MKDV field, these particles do not hit the graphite block as intended: instead they are deposited onto the steel TIDV yoke. With high intensity low-emittance beam this could possibly damage the TIDV; more studies beyond the scope of this work are required to check if the energy deposition would be sufficient to damage the yoke.

4.4.8 Measurements

Figure 4.25 shows a plot (preliminary results) of the beam loss monitor readings during a deliberately provoked asynchronous dump for the new (2007) bumper layout, which was produced by adjusting the kicker timing. The relatively low peak in the TIDV region appears because the BLM is installed on the following quadrupole and not directly on the dump block. High losses are seen in SPS point 2 at $s \approx 1600$ m, on a main bending magnet while there are no losses in point 4, contrary to expectation. The measured loss pattern does not fully correspond to that obtained by simulations and looks

qualitatively more similar to that obtained with an MKDV spark, which could indicate an effect from the orbit, dump or aperture misalignment.

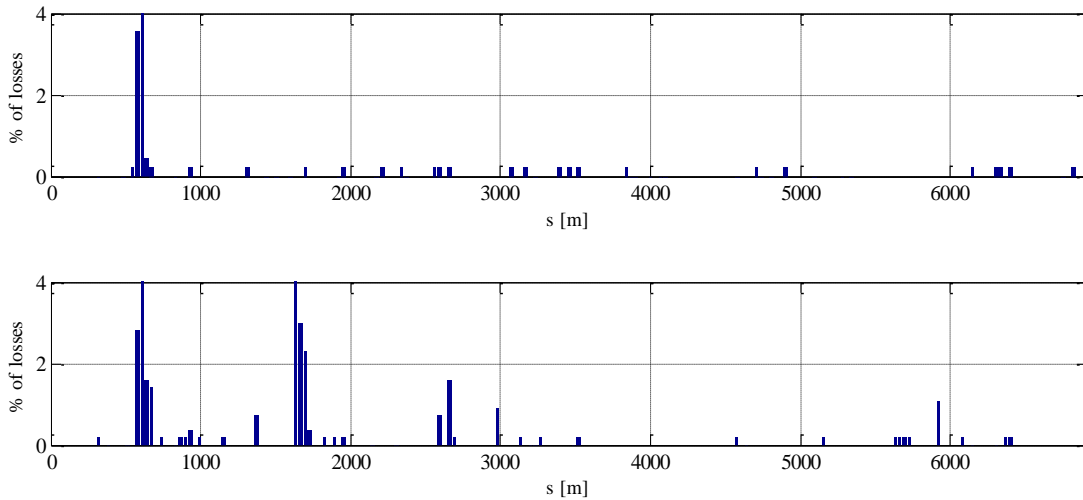


Figure 4.25: BLM readings during nominal dump (top) and sweep (bottom) with a 400 GeV fixed target low intensity beam.

4.4.9 Conclusions

Mad-X tracking and PSpice have been used to model failures of the SPS beam dump. Loss patterns for asynchronous and spark failures were compared with measurement. The studies show that during MKDV failures particles do not survive more than two turns due to the MKDH field. In the case of sparks the TIDV yoke is hit, not the graphite core. This might be a problem and requires further investigation. Irradiation and losses at the aperture limiting MPLH bumpers were confirmed for the previous layout: losses with the modified bumper position were shown to be negligible, in agreement with measurement. All major losses outside of LSS1 occurred on main bending magnets. An extension to include orbit and alignment errors to the study would be possible and would be required to explain better the observed loss patterns.

4.5 Design considerations for the PS2 beam dump system

This section gives a brief overview over the PS2 beam dump design considerations. The different beam dump functionalities required for the proposed PS2 machine and its transfer lines are briefly described, followed by first estimates about the expected beam loads. This data has been taken as input for comparing the different technical options for the dump systems, in particular to simulate the radiological impact for internal or external beam dump options. The numbers derived have been used to help decide which of the feasible technical alternatives are preferred.

4.5.1 Functions and Beam Loads

The PS2 accelerator is proposed to replace the existing Proton Synchrotron (PS) in the CERN accelerator chain, to provide more reliable operation and improved basic beam parameters for the foreseen LHC luminosity upgrade and other users. Beams with very high total intensities above 10^{14} p⁺ will be accelerated, providing a totally new challenge concerning the disposal of unwanted beam.

A 200-day nominal operation year is assumed for the calculations. The relatively short PS2 cycle (minimum 2.4 s) combined with the assumed maximum intensity of 1.5×10^{14} p⁺ results in about 7×10^6 cycles per year with about 10^{21} accelerated particles. This is several orders above the current PS level. The increase in energy (50 vs. 26 GeV) also raises the challenge of handling operational beam losses. Table 1 shows an overview of the basic PS2 parameters [37].

Table 4.1: PS2 - Basic parameters.

Injection energy (kinetic)	GeV	4
Extraction energy (kinetic)	GeV	50
Maximum beam intensity	p ⁺	1.5×10 ¹⁴
Minimum cycle period to 50 GeV	s	2.4
Maximum norm.emittance (H-V)	π.mm.mrad	15-8
Cycles per year		7,200,000
Protons accelerated per year	p ⁺	1.08×10 ²¹

The calculations assume maximum beam intensity at all times and no unforeseen losses. Loads were calculated for dump functionalities which were identified as necessary. Eight such functionalities were identified for the PS2:

Setting up of the injection transfer line:

A dump will be required for the injection transfer line, to enable setting-up and re-optimisation after changing the injection foils. Safety beam stoppers will also be required to allow downstream access. For setting-up it is assumed that 4 days per year are needed at 10 % intensity. This gives 0.2 % of the yearly total, or 2×10^{18} particles. Foil changes are assumed to imply one hour at 20 % intensity, and twenty foil changes p.a. gives 0.08 % of the yearly total, or 9×10^{17} particles. The sum of the two loads is 0.28 % or 3×10^{18} particles at 4 GeV.

- Fast injection setting-up and injection failures:

For setting up the fast injection of p⁺ (4 GeV) an internal beam dump is proposed which can also localise losses in case of injection kicker failures. The yearly start-up is assumed to give a beam load of 20 % intensity over 24 hours (0.1 %; 1.08×10^{18} p+ p.a.) The load due to the few injection kicker failures per year will be negligible.

- H⁻ injection:

A charge-exchange H⁻ system will be used to inject at 4 GeV. The stripping efficiency of a 500 μg/cm² foil is about 95 % giving ~2 kW of unstripped H⁰/H⁺ to be extracted and dumped. During nominal operation about 1.5×10^{14} H⁻ ions will be injected per cycle. A total of 5.4×10^{19} particles are then dumped p.a. Start-up will cause an additional beam load over the first 10 days, estimated at 30 % of the produced beam, or 0.75 % of the yearly production (8.1×10^{18} ions p.a.). Around 20 interventions due to foil exchanges are expected per year, causing an additional load at lower intensity (20 %) onto the injection dump for about 2 hours, giving 0.16 % or about 1.8×10^{18} particles p.a. The beam load for the H⁻ dump is therefore 5.92 % of the annual production (6.4×10^{19} p+ at 4 GeV).

- Emergency beam abort:

An emergency abort system is needed to safely dispose the 1.2 MJ of beam energy in case of equipment failures. It is assumed that 0.5 % of all cycles are aborted. This corresponds to about 5×10^3 emergency aborts p.a., or 5.4×10^{18} dumped particles. Half of this beam (2.7×10^{18}) is assumed to be dumped below 20 GeV. An external dump would require a fast extraction channel, but the aperture must be large enough to accept the beam at injection energy. An internal dump is easier to implement, cheaper and more compact but potentially generates more problems in terms of radiological protection due to local activation.

- Machine setting up

Six days of setting-up (two for each beam) with an average of 20 % of full intensity gives a total of 0.6 % (6.5×10^{18} p+) p.a. This must be sent to an internal dump at low energy until the ramp and extraction is commissioned; at high energy an external or transfer line dump could be used. 50 % of the load is assumed to be below 20 GeV.

- Setting up of the extraction transfer lines

A dump will be required for the extraction transfer line, to set up the line and stop the beam from the PS2. Safety beam stoppers will again be required. The annual load will be 0.3 % or 3.25×10^{18} particles at 50 GeV (assuming 2 days a year at 30 % intensity on average).

- Machine development (MD)

MD sessions will cause additional beam loads on a beam dump, which again may be internal or external. It is supposed that an average of 100 MD hours (with 20 % of full intensity) will cause 4.3×10^{18} dumped particles or 0.4 % of the yearly production. The beam load is assumed to be 50 % at 4-20 GeV and 50 % at 20-50 GeV.

- Particles remaining after slow extraction

Some particles remain in the machine at the end of each slow extraction cycle and must be dumped. A transfer line dump is difficult as the line will be needed for the slow extracted beam. It is assumed that 1 % remains and that slow extraction is used for 50 % of the time, giving a total of 3.6×10^{18} p+ or 0.33 % of the production at 50 GeV.

4.5.2 Dump concepts

Where possible, within operational boundary conditions, the functionalities were combined into a few dump devices. The figures are summarised in Table 4.2 together with the possible beam destinations. Some combinations of dump configurations are defined, and the expected loads are calculated. Some cases are complicated – to dump the remaining slow extracted beam on an external beam line dump would require a fast switch magnet system in the transfer line, which raises issues of machine safety to avoid sending beams to the wrong destination.

Due to the very high beam load the H⁻ injection requires an external beam line dump, necessitating an extraction septum and a large acceptance beam line. The injection systems would also require a dedicated transfer line dump and an injection dump, as in the SPS.

For setting up and MD a dedicated external dump or transfer line dump may only be feasible above a certain energy due to limited acceptance of the extraction channel. In the preferred scenario the PS2 would contain an internal emergency dump (as used in the SPS) which would work from 4 to 50 GeV for emergency aborts, for ‘cleaning’ the machine after slow extraction and MD beams below 20 GeV. A separate beam line-type dump (as used in the CERN PS) would be used for machine setting-up at high energy and for MD above 20 GeV.

The resulting loads are shown in Table 3. It is assumed that no external movable dump is needed for the SPS injection line, as it should be possible to use either the beam line dump or the existing SPS dump.

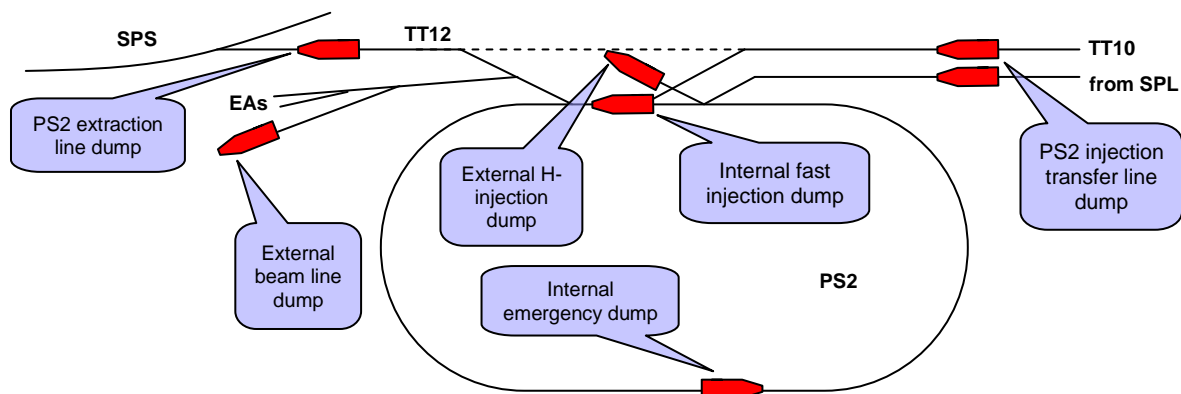


Figure 4.26: Schematic overview of the proposed PS2 dump concepts. The beam travels around the PS2 in the anti-clockwise direction.

Table 4.2: Dump functionalities, calculated beam loads and possible dump locations.

Function	E [GeV]	Load [p+]	% of total	Possible beam destinations					
				Int. or ext. emerg. dump	Ext. beam line or TL-dump	Inj. transfer line dump	Int. fast inj. dump	Int. or ext. H-dump	Int. or ext. emerg. dump
Emergency abort	20-50	2.7×10^{18}	0.25	X					
Machine development	20-50	2.2×10^{18}	0.2	X	X				
Machine setting up	20-50	3.3×10^{18}	0.3	X	X				
Extr. line setting up	50	3.3×10^{18}	0.3		X				
Slow extraction	50	3.6×10^{18}	0.33	X	X				
Inj. line setting up	4	3.1×10^{18}	0.28			X			
Fast inj. setting up	4	1.1×10^{18}	0.1				X		
H injection losses	4	6.4×10^{19}	5.92					X	
Emergency abort	20-50	2.7×10^{18}	0.25						X
Machine development	20-50	2.2×10^{18}	0.2						X
Machine setting up	20-50	3.3×10^{18}	0.3						X

Table 4.3: Proposed dumps and their beam loads

PS2 dumps	Beam loads [p+ /y]			
	4 GeV	4-20	20-50	50 GeV
TL (injection)	3.1×10^{18}	-	-	-
Fast inj. (I)	1.1×10^{18}	-	-	-
H- inj. (E)	6.4×10^{19}	-	-	-
Emergency (I)	-	8.2×10^{18}	2.7×10^{18}	-
Beamline (E)	-	-	5.5×10^{18}	6.9×10^{18}

4.5.3 Residual dose rate issues

With the load information derived above a preliminary study using FLUKA [38] was requested to get information about the order of magnitude of residual activation to be expected for the various dumps. This study [39] was based on activation calculations made for an SPS-type beam stopper (TED), which is in widespread use in the SPS beam extraction lines to the CNGS/LHC, and also as the basis for the SPS internal beam dump.

The simulations assumed 10 years of operation, each of 200 days of beam operation and 165 days of shutdown. Residual contact dose rates were calculated for 5 different cool down periods after the last 200 days of irradiation.

The results are shown in Figure 4.27, along with the measured values from the SPS internal beam dump. It can be seen that the radiation levels in the surroundings of the external beam dump and the internal emergency dump are higher than those seen around the SPS beam dump, while the two other internal dumps will have lower dose rates than seen in the SPS.

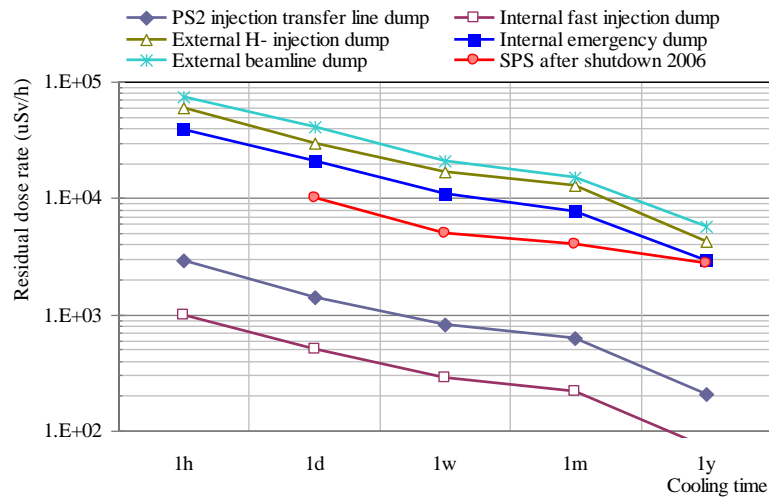


Figure 4.27: Results for preliminary residual dose rate calculations for PS2 beam dumps, assuming an SPS-type TED geometry. The SPS value for a cool down of 1 year was measured during the long shut down in 2004/2005 [39].

4.5.4 Conclusions

Beam loads for the PS2 and its transfer lines were estimated and beam dump concepts developed, taking account of potential radiological impact. The results confirm that the H- dump will have to be an external system, with an extraction septum and a large acceptance beam line. An internal emergency dump is also required but must only be used for beam which cannot be extracted to an external dump, located in a well shielded area. This scenario is preferred since it presents fewer difficulties for the beam dump system design while optimising the loss locations, and simplifies operation.

The systems finally proposed are: 1) an external movable transfer line dump for PS2 injection line setting-up, 2) an internal dump block for fast-injection setting-up and failures, 3) an external H⁻ dump system, 4) an internal 4-50 GeV dump system for emergency aborts, low-energy setting-up and low energy MDs, and 5) an external beam line dump (20-50 GeV) for all other beams.

The activation analysis confirms that significant efforts have to be put into the design of dumps and their surroundings. External dumps must be designed with a larger graphite core surrounded by heavy shielding, since the TED-like beam dump design is not adequate. The design of internal beam dumps needs to be optimized in terms of reduction of residual radiation (e.g. using marble layers), or by considering bypass tunnels or larger tunnel sections allowing to place shielding between the dumps and the passage.

5 The LHC Beam Dump System (LBDS)

The LHC beam dump system (LBDS) has been designed to safely dispose of proton and ion beams in a wide energy range from 450 GeV up to 7 TeV. An abort gap of 3 μs is foreseen in the beam structure to give time to switch the system on and avoid sweeping particles through the LHC ring aperture. This chapter gives an overview of the principles, the equipment used and the critical apertures in the extraction region and the two beam dump lines. The issue of LBDS failures during beam abort is a major concern for machine protection as well as a critical factor for safe operation of the experiments and their detectors.

5.1 The extraction region layout

The LBDS [40] is designed to fast extract beam from the LHC in a loss free way and transfer it to an external absorber. For each beam a system of 15 horizontal kicker magnets (MKD), 15 vertically deflecting magnetic septa (MSD) and 10 diluter kicker magnets (MKB) are installed. After the beam has passed the Q5 quadrupole and has been deflected by the MKD it sees an additional deflection when traversing the Q4 quadrupole off-centre. The MSD moves the beam in the vertical plane above the LHC machine before it is further deflected in the horizontal and vertical planes in a spiral shape by the MKB kickers. This dilution develops over several 100 m along the beam dump line until the beam is absorbed by the dump block (TDE). To protect the septa from miss-kicked beams a special fixed 6 m long carbon composite protection device (TCDS) is placed just in front of the MSD. For nominal operations the 2.8 μs MKD rise time should always be accurately synchronised with the 3 μs abort gap with a phase error of less than 40 ns, so that no beam is swept through the aperture. However, some failures can occur which lead to an “asynchronous” dump, where the kicker is not synchronised with the gap, and in addition some stray particles may also be present in the abort gap [chapter 7]. To protect the LHC aperture from these eventualities, a movable single-jawed 6 m long graphite protection device (TCDQ) is installed upstream of Q4, supplemented by a two-jaw 1 m long graphite secondary collimator (TCSG) and a 2 m long fixed iron mask (TCDQM). Figure 5.1 shows a schematic overview of the above described process concerning the hardware located in IR6.

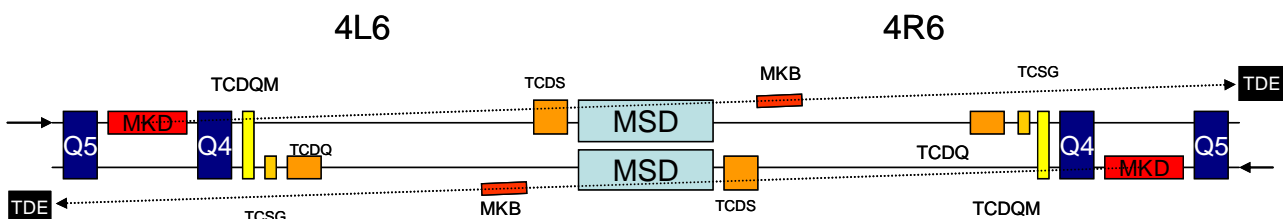


Figure 5.1: Schematic overview of the LBDS in LHC IR6. The extraction systems for the two beams are arranged together in the long straight section.

The beam dump system must be able to accept nominal LHC beams, like the scheduled beam aborts at the end of a physics run, and also beams with out-of-tolerance parameters as could arise from equipment failures or beam instabilities. The worst-case beam emittance is assumed to be a factor of two above nominal at injection energy, and a factor of four above nominal at 7 TeV. The system should also be tolerant to variations imposed by optical effects (beta-beating, power supply ripple etc.). The maximum orbit is assumed to be ± 4 mm and the beta beating 42%. [41]

5.2 The LBDS architecture

As already briefly discussed in chapter 1 a beam dump can be triggered by the Beam Interlock Controller (BIC) over the two 10 MHz beam permit signal loops. However, the LBDS can also be triggered by various other systems. Dump requests will come from different sources like the machine protection system for emergencies, the machine timing system for scheduled dumps and the LBDS itself if an internal failure occurs.

Direct triggers come from the access system in order to dump the beam immediately if a door to the tunnel is forced, and from special BLMs in IR 6. The Beam Energy Tracking System (BETS) can also trigger a dump if measurements with four Direct Current Current Transformers (DCCT) do not agree, to avoid a dump event with significantly wrong kick amplitude. Interfaces to the RF are needed for synchronization; consequently a lost RF signal will provoke a dump request. Several other systems like the powering system, the uninterruptable power supply, emergency switches and timing issues can cause a dump event as well.

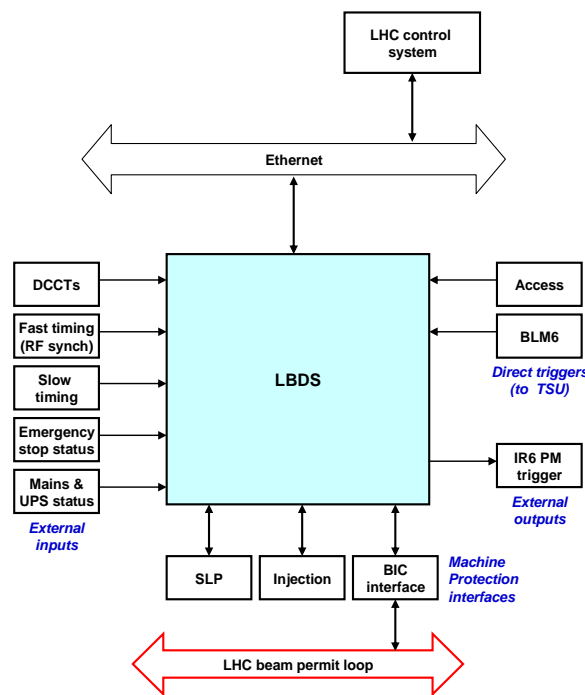


Figure 5.2: Interfaces between the LBDS and surrounding systems.

In addition to the systems directly connected to the LBDS - Figure 5.2, there are hardware systems which are required for the correct functioning of the LBDS, but which do not have a direct connection to the LBDS itself. Most of these systems (e.g. vacuum, collimators etc.) provide inputs to the Beam Interlock System. Figure 5.3 shows a more detailed overview of the LBDS interfaces and the internal LBDS connectivity. One can see that via the BIC several LBDS systems are interlocked e.g. all collimators and the dump itself.

To ensure clean dumps without losses in the extraction channel the circulating beam position should not deviate too much from its nominal position. At the MKD kicker and MSD septum a maximum peak to peak deviation of not more than 4 mm is specified. This orbit tolerance is monitored and interlocked with 4 dedicated BPMs (2 per Q4 quadrupole left and right of IP6 and per beam, for

redundancy). Thus any beam exceeding the threshold will be dumped. The interlock level is configurable using the CCC systems.

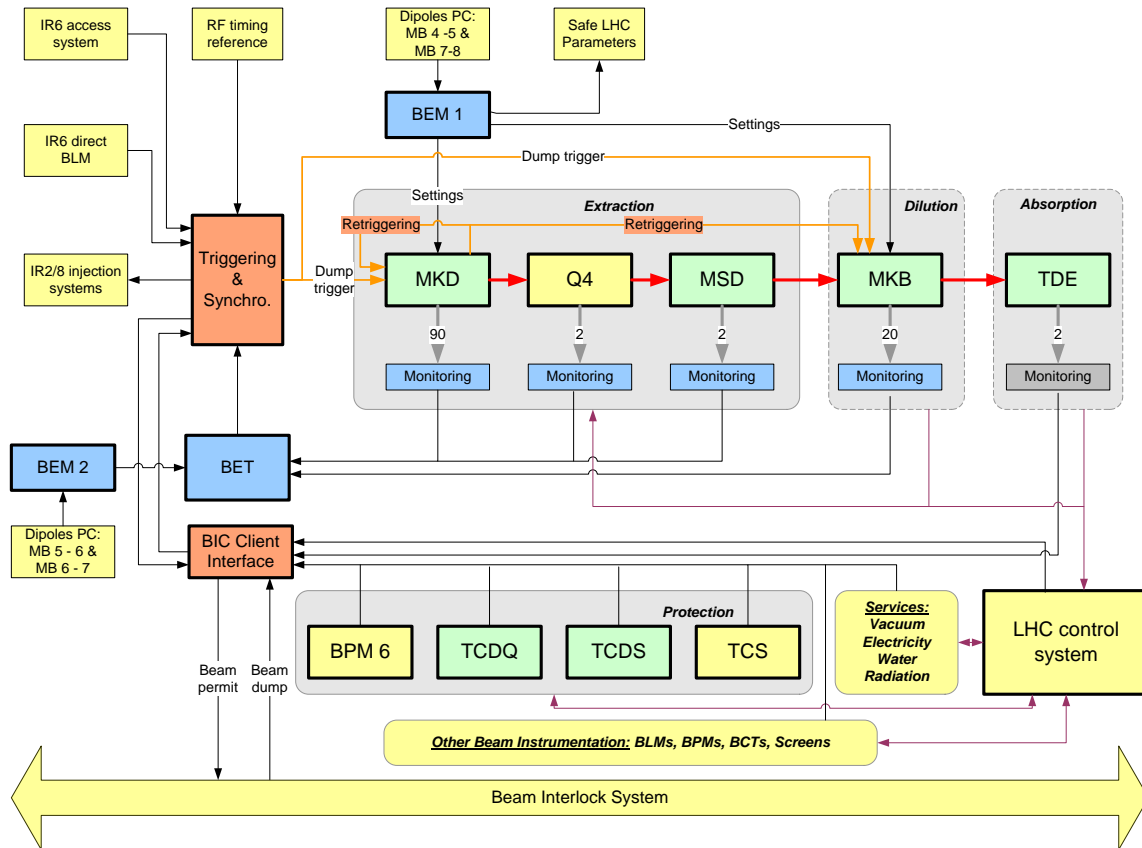


Figure 5.3: Schematic overview of the LBDS internal connectivity. [42]

Despite the surveillance of the general powering conditions (via the BIC) a special monitoring of the MSD extraction septum current via the Fast Magnet Current change Monitor (FMCM) has been installed, to request a beam dump if the MSD current changes by a relative amount of 5×10^{-4} , with a reaction time of 1 ms [43]. This system ensures that the total vertical septum deflection is always at the correct level (see section 6.4.5), even for very rapid changes of the magnet current.

5.3 The beam dump trigger and retrigger system

The propagation of the dump request through the beam dump triggering system is based on a redundant fail-safe logic up to the trigger synchronization unit (TSU) and then on a redundant fault tolerant system up to the high voltage generator power trigger unit (PTU). Figure 5.5 shows an overview of the dump trigger signal processing. Blue and red lines indicate the two redundant paths of the dump signal. The TSU is a module dedicated to synchronize the abort command with the next arriving abort gap. However, such a synchronisation system implies a certain additional risk, if the synchronisation were to be significantly delayed for some reason. Such a delay in the dump trigger propagation could have catastrophic effects. For this reason a special dump trigger delay line has been installed which automatically propagates the trigger to the retrigger box after $89 \mu\text{s}$ (1 turn). This ensures that the dump is triggered by the bypassed signal in any case at latest $89 \mu\text{s}$ after the dump request arrived. Figure 5.4 shows a block diagram of the TSU with the input lines at the bottom and the trigger output at the top. The TSU processes the RF signal to determine the exact location of the abort gap. The received trigger is delayed within the TSU until the rising edge of the kick waveform is synchronized with the beginning of the abort gap (within $86 \mu\text{s}$). All TSU systems are connected to a supervisory and diagnostics system.

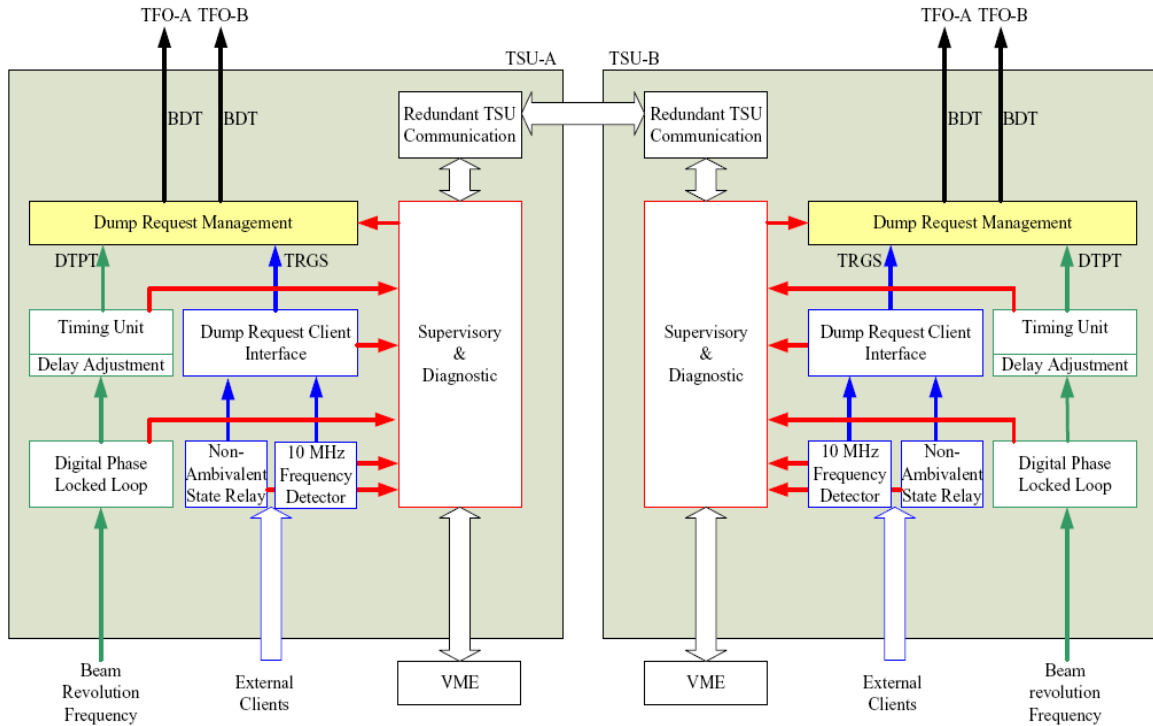


Figure 5.4: Block diagram of the Trigger synchronization unit (TSU) [44].

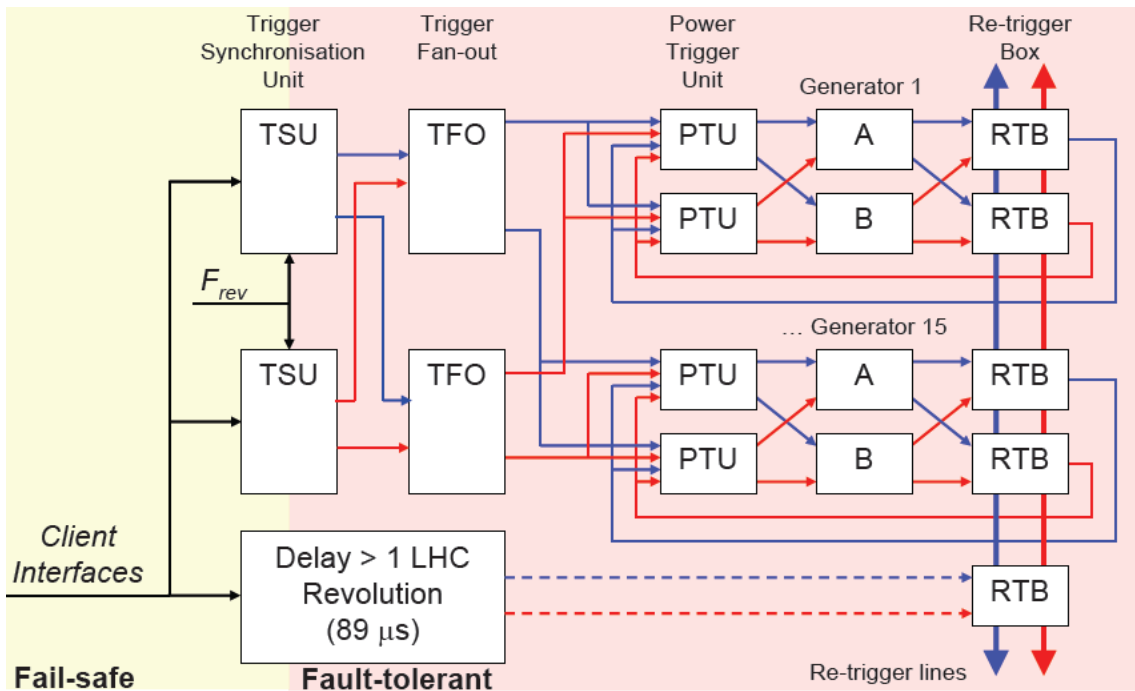


Figure 5.5: Architecture of the dump trigger signal processing and distribution [45].

A synchronised dump trigger will be propagated through both branches of the trigger fan out unit (TFO) which finally triggers the power trigger unit (PTU) and the 15 generators. Each signal is always distributed to both PTUs and generators per branch. The PTU is also redundantly connected to the retrigger distribution line.

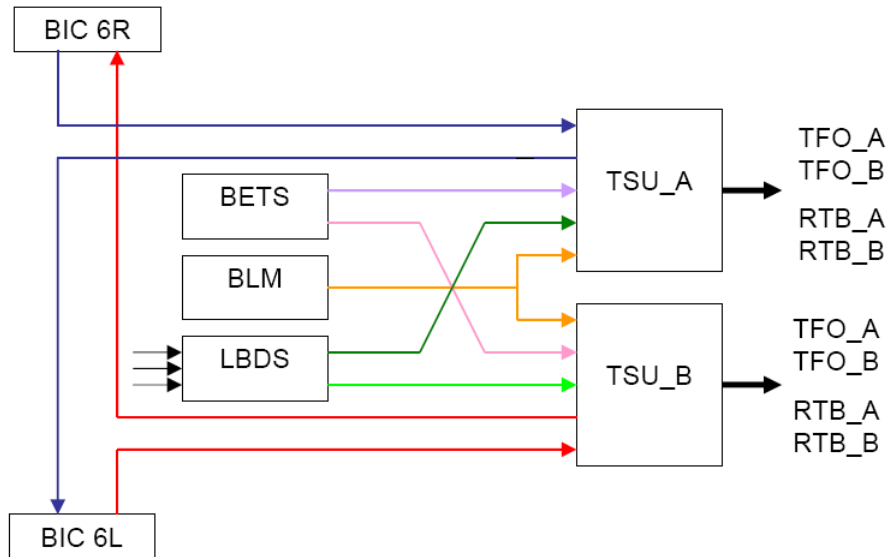


Figure 5.6: Connectivity of the TSU and surrounding systems. [46]

Figure 5.6 shows the previously discussed direct inputs of the IR6 BLM-system, the beam energy tracking system (BETS) and the LBDS internal triggers to the TSU. All dump requests from the BIS arrive redundantly via the beam interlock controllers in IR 6 (BIC 6R & 6L).

5.3.1 The MKD generators

The generator for each MKD extraction kicker consists of a double branch (for redundancy) with three main modules each: The capacitors, the switches and a free wheel circuit. Figure 5.7 shows a circuit diagram of a generator connected with transmission cables to the magnet itself. A switch consists of ten Fast High Current Thyristors (FHCT) and is designed for a voltage of 30 kV and a current of 20 kA. The FHCT disks have to fulfil the challenging constraint of a maximum di/dt of 12 kA per μs [47].

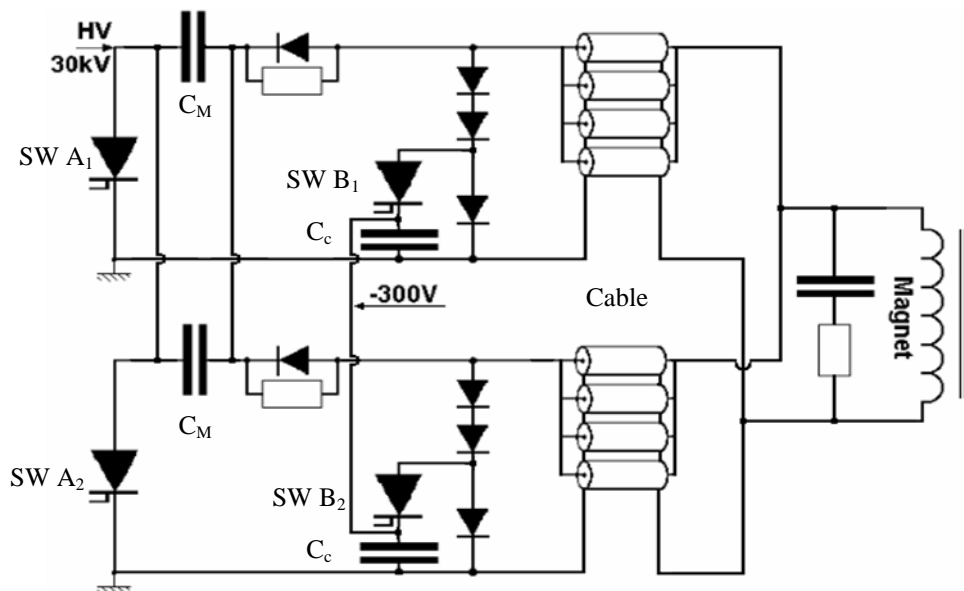


Figure 5.7: MKD generator circuit. Modified from [48].

When triggering the MKD system the FHCT switches (SW A₁, A₂) are fired and the energy stored in the main capacitors C_M can flow to the magnet. After the magnet current reaches its peak the polarity (voltage) of the generator will change and a current immediately starts to flow from the magnet over

the diodes in the freewheel branch. However for proper beam extraction a flat top of $89 \mu\text{s}$ is required so that the flat top current droop has to be compensated. This is done by closing the switches B_1 , B_2 , connected in series with a 3.25 mF , pre-charged compensation capacitor C_c so that the currents in the diodes are commutated. The capacitors are then connected in series with the magnet inductance and a current will oscillate with a superimposed half-sine wave. The initial capacitor voltage is precisely determined so that it compensates the resistive losses of the magnet current freewheel circuit. [49]

Figure 5.8 shows the MKD waveform and the definition of overshoot1 (OS1), overshoot2 (OS2) and the corresponding field levels. The overshoot values are quite large compared to e.g. the SPS extraction kicker, but since the beam is being dumped the only constraints on the overshoot are to preserve a certain beam trajectory envelope for aperture reasons.

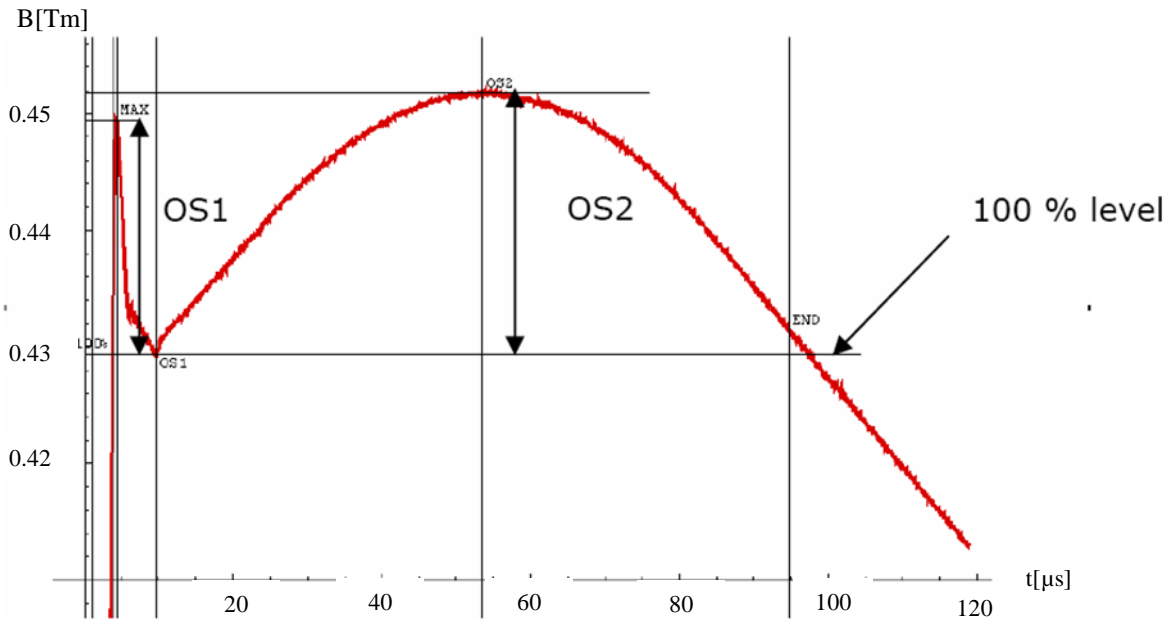


Figure 5.8: The MKD pulse waveform: Definition of overshoot and 100% level. [50]

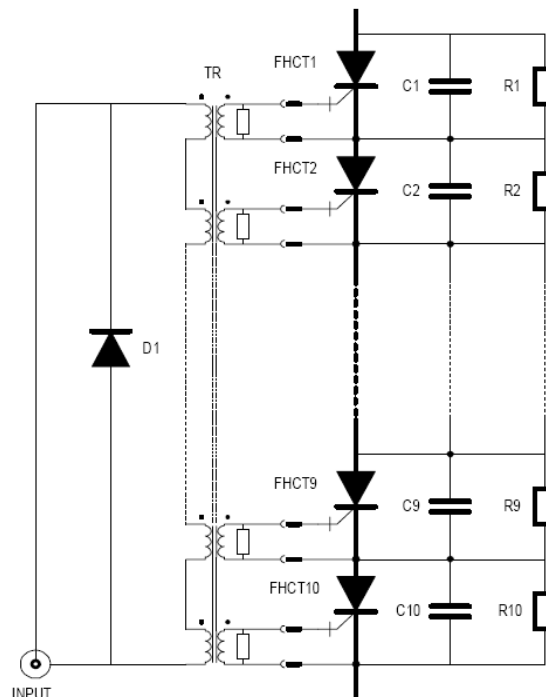


Figure 5.9: Circuit diagram of a MKD switch unit. [51]

5.3.2 Retrigger, prefire and asynchronous dumps.

Any dump signal not processed by the TSU within $89 \mu\text{s}$ is overruled by the delayed trigger signal distributed over the retrigger line. This signal is directly propagated to the PTU and the generators. As a consequence the kickers are fired without any synchronization to the abort gap. The duration of this retrigger process depends on the actual generator voltage settings (due to the measurement of the pre trigger signal) and hence on the energy as well. Total delays of up to $1.5 \mu\text{s}$ for injection energy and $1.3 \mu\text{s}$ for 7 TeV are possible [52]. The retrigger pulse itself has to travel to each generator over more than 40 meters of cable with a cable delay of 5 ns/m .

In case of spontaneous or too early triggering of one (or more) MKD modules (the so called “prefire” case), the undesired MKD action is detected and a trigger pulse is passively created and sent to the retrigger box where the same retrigger procedure applies to the other 14 generators. In this case the integral of the kicker waveform is slightly different, since one kicker has been fired earlier.

Figure 5.10 shows the measured waveforms of the individual MKD generators during pretrigger events in September 2009. One can clearly see the erratic trigger and prefire of one generator and the retrigger of the other MKD elements. The dispersion between the retriggered waveforms is due to the delay in the retrigger line and physical distance between the generators (cable delay). The delay between the prefired generator and the first retriggered one is at the peak below $1 \mu\text{s}$ - however in the very beginning of the prefire event the spread is much higher with up to $4 \mu\text{s}$ measured.

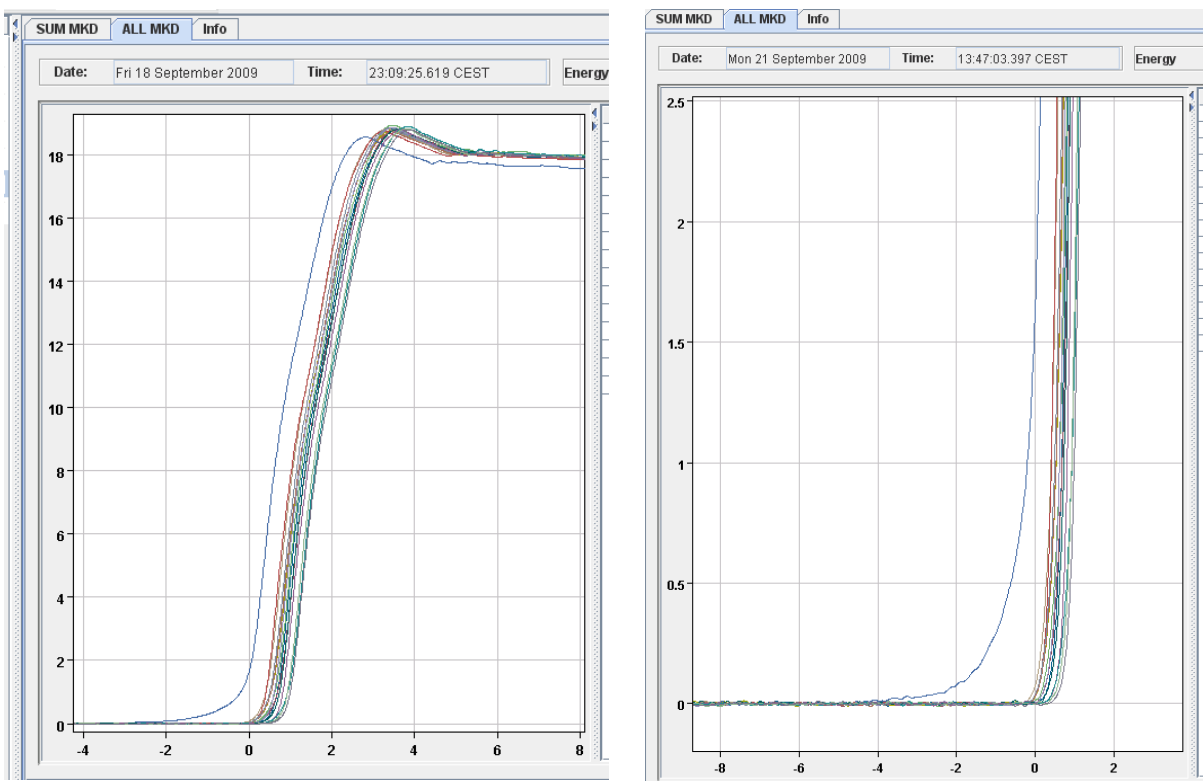


Figure 5.10: Measured individual MKD generators waveforms during prefire cases.

5.4 Beam energy tracking system (BETS)

To extract the beams with the correct trajectory the LBDS relies on accurate and reliable tracking of the LHC beam energy, since the strength of the deflection elements must scale with the beam energy to achieve a constant extraction angle. Therefore the LHC Beam Energy Tracking System (BETS) generates the kick strength reference signals with respect to the beam energy. The system also performs continuous surveillance of the charging voltage of the different circuits within the high

voltage generators, the Q4 current and the MSD current (Figure 5.11). If the measured values are not within the tolerance windows relative to the beam energy a dump request is generated (see Figure 5.6). The BETS acquires reference and surveillance signals of the beam energy (Beam Energy Acquisition - BEA) by measuring the main bend current with Direct Current Current Transformers (DCCT) in four LHC octants. The reference signal is processed and a kick strength reference signal is sent to the LBDS extraction elements as well as to the LHC controls system. If any signal is outside of predefined tolerance windows a dump request is directly submitted to the TSU. The main parameters of the BETS are given in Table 5.1 [53].

Table 5.1: Main parameters of the BETS.

Power converter DCCT precision	$\pm 0.1 \%$
Kicker HV divider precision	$\pm 0.2 \%$
BEA sampling frequency	65 kHz
BEA resolution	16 bit
Error during ramp (10 A/s)	$< 0.01\%$
Bending magnet look-up table precision	$\pm 0.1 \%$
Kicker magnet look-up table precision	$\pm 0.2 \%$
Beam energy reference precision to SLP /	$\pm 0.2 \%$
Beam energy reference error (with	$\pm 0.4 \%$
Beam Energy Interlock (BEI) tracking	1 ms
Bending magnet tolerance window	$\geq \pm 0.3 \%$
Kicker magnet tolerance window	$\geq \pm 0.5 \%$

The BETS has to meet high reliability standards and is therefore based on a fail-safe logic on FPGA standard redundantly powered and covered with uninterruptible power supplies. The data transmission is based on Manchester encoding including a Cyclic Redundancy Check (CRC) for transmission error detection and all fixed references are stored in look-up tables (EEPROM technology) which cannot be changed remotely.

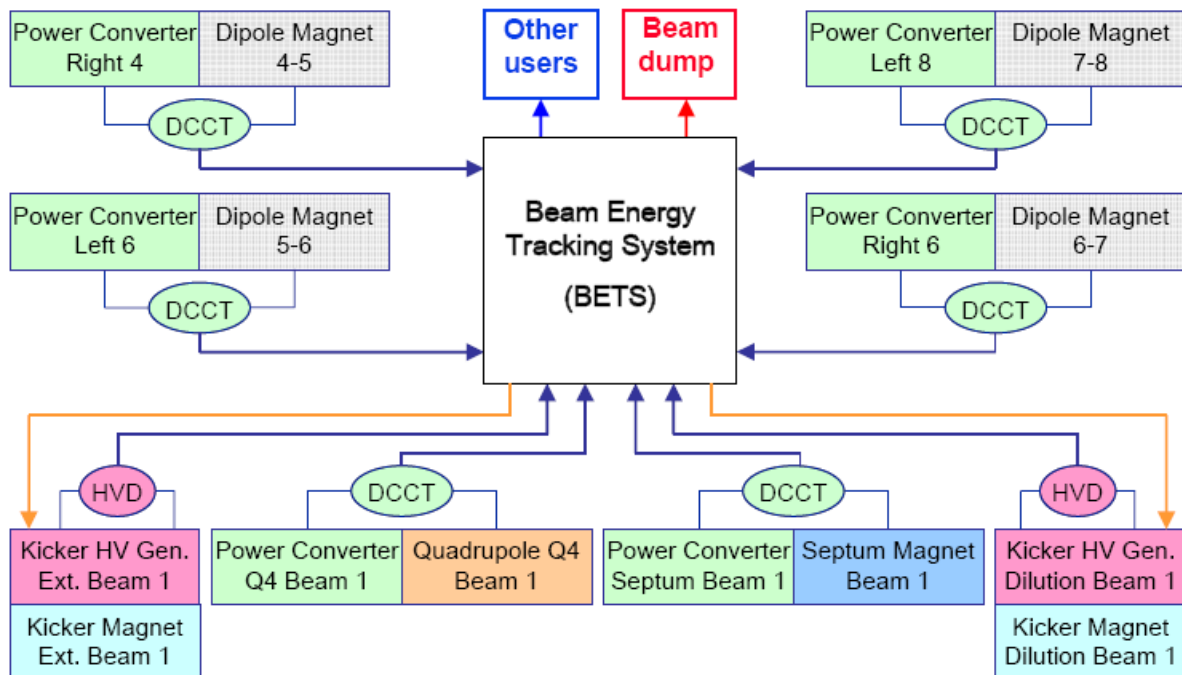


Figure 5.11: Schematic overview of the BETS [54].

5.5 Main hardware components of the extraction system

5.5.1 The beam extraction kicker (MKD)

Two sets of 15 fast-pulsed extraction magnets MKD are required to provide the horizontal deflection of 0.2858 mrad into the extraction channel of the MSD septum.

The MKD system is designed such that:

- the beam is still safely extracted with only 14 out of the 15 kicker magnets available.
- the kicker system field rise time is below 3 μs and the field ‘flat-top’ is at least 90 μs .
- any spontaneous trigger of one of the pulse generators can be detected such that a retrigger to the other generators is ensured.
- the kicker field tracks the energy signal better than $\pm 0.5\%$. [55]

The individual magnet current pulses have amplitudes of 18.5 kA with a rise time of 2.85 μs whilst the unipolar system voltage is 30 kV. The total jitter between the magnets is 150 ns. The ‘flat top’ duration of 90 μs is followed by an approximately exponential decay of 1900 μs . The maximum current corresponds to a magnetic field in the gap of 0.34 T. Table 5.2 summarizes the main parameters of the MKD kicker system. In contrast to the dilution kickers (MKB) the MKD magnets are built outside of the vacuum, thus the beam is housed in vacuum chambers. For impedance reasons metalized ceramic chambers are used. In order to insert such a ceramic chamber, with its two large vacuum flanges, the magnet can be opened horizontally. The operating pressure is in the 10^{-11} mbar range which requires bake out procedures of around 24 hours at 150°C.

Table 5.2: MKD System parameters

Number of magnets per system	15	
System deflection angle	0.2858	mrad
Kick strength per magnet	0.428	Tm
Vacuum chamber clear aperture (diameter)	56	mm
Operating charging voltage range	2 to 30	kV
Magnet field overshoot at 7 TeV	≤ 7.9	%
Magnet field overshoot at 450 GeV	≤ 10.0	%
Field flat top duration	≥ 90	μs
Field rise time 0.5%-100% (system)	≤ 3.0	μs
Effective magnet length (magnetic)	1.421	m
Yoke length (mechanical)	1.348	m
Magnet vacuum length (mechanical)	1.583	m

The MKD magnets are connected to the generators which are located in the tunnel galleries by parallel 19 m long, 18 Ω coaxial cables with an inductance of 104 nH/m.

5.5.2 Q4 Quadrupole

The Q4 quadrupole (MQY.4L6 for beam 1 and MQY.4R6 for beam 2) is downstream about 18.215 m of the centre of the MKD modules. As shown in chapter 2 any beam traversing a quadrupole field off centre will see a deflecting dipole component. The lattice cell for the kicker is chosen such that the following quadrupole is a defocusing one in the plane where the kick has been applied, so the beam sees an additional bend from the quadrupole magnet which enhances the original kick. For the LBDS the 3.4 m long MQY has a nominal gradient of $k_{MQY}=0.0048814$ [56]. Hence the additional deflection angle a_{MQY} is 83 μrad (4.2) what is about 30.2% of the deflection given by the MKD modules or 23.2% of the total deflection.

$$a_{MQY} = 15 \cdot a_{MKD} \cdot l_{MKD \to Q4} \cdot l_{MQY} \cdot k_{MQY} \quad (4.2)$$

The Q4 deflection contributes significantly to the extraction and thus the magnet current has been interlocked at $\pm 0.5\%$ [57].

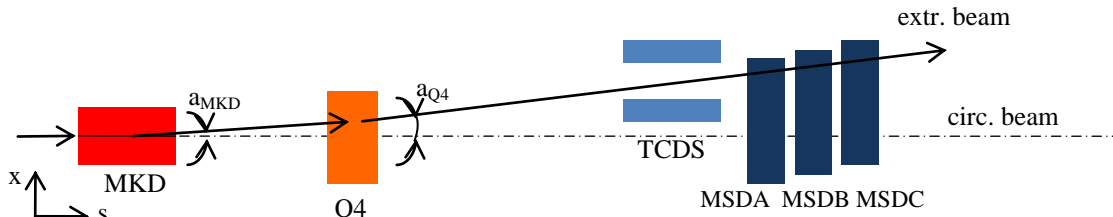


Figure 5.12: Sketch of the contribution of Q4 to the extraction trajectory (horizontal plane).

5.5.3 Extraction septa MSD

Each extracted beam is deflected in the vertical plane by 15 MSD septum magnets, by a total of 2.4 mrad. There are three different magnet types installed: MSDA, MSDB, and MSDC. All are powered in series but differ in septum thickness, number of coil layers and distance of the circulating beam hole from the pole [58]. The main parameters of the magnets are shown in Table 5.3.

Table 5.3: Main parameters of the MSD magnets.

	MSDA	MSDB	MSDC	
Septum core length	4460	4460	4460	mm
Gap width	44	44	44	mm
Septum thickness	6	12	18	mm
Design current	880	880	880	A
Nominal magnetic field in the gap	0.80	0.99	1.17	T
Magnet weight	10500	10600	10700	kg

The MSD magnets for beam 1 and 2 are installed back to back around the centre of IR 6. Figure 5.13 shows an overlay design drawing of the TCDS tank and the MSDA. The circulating beam orbit is indicated with the red dot, the TCDS protection blocks in front of the MSD are marked by the red rectangles (extracted beam is kicked to the left and passes between the TCDS jaws).

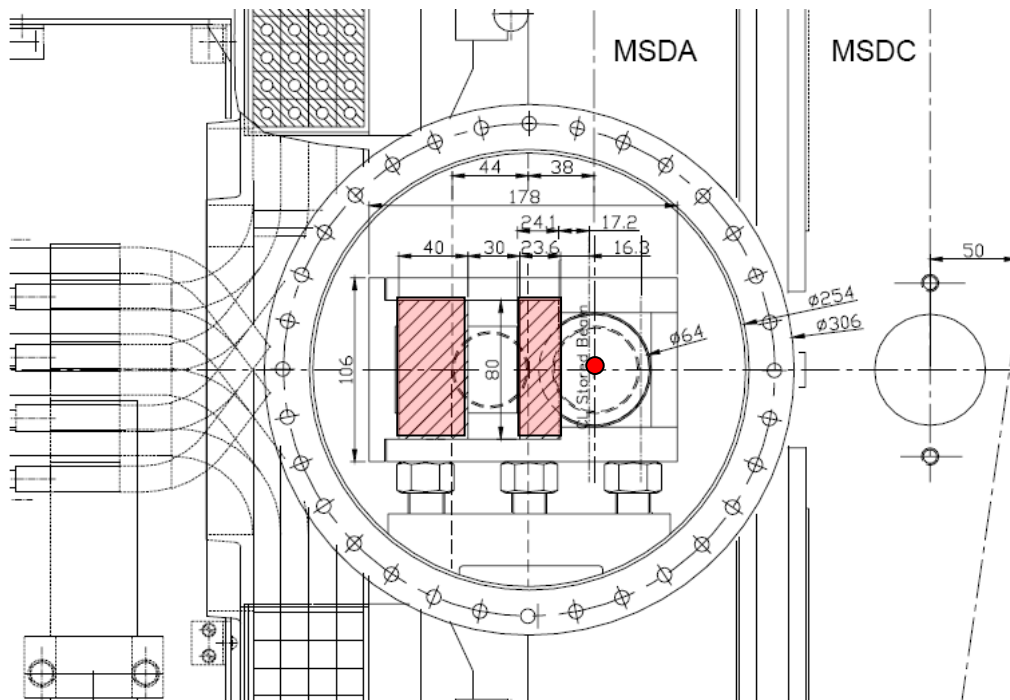


Figure 5.13: TCDS tank and MSDA overlay drawing, seen in beam direction.

5.5.4 Septum protection elements – TCDS

The fixed diluter block TCDS (Target Collimator Dump Septum) protects the MSD in the event of an asynchronous firing of the MKD kickers. The design criteria of the TCDS was to intercept about 40 LHC bunches (1.7% of the beam) containing about 6.1 MJ of energy [59], and to provide enough dilution such that the temperature in the MSD vacuum chambers does not exceed 300°C, and such that the temperature in the MSD yoke does not exceed 100°C. The main parameters of the TCDS are given in Table 5.4.

Table 5.4: Main parameters of the TCDS diluter.

	TCDSA [mm]	TCDSB [mm]
Diluter length	3000	3000
Diluter width (upstream)	23	24
Diluter width (downstream)	24	6
Diluter position w.r.t. beam axis (upstream)	16	14
Diluter position w.r.t. beam axis (downstream)	13	32

For mechanical reasons the TCDS is made out of two diluter elements each 3.0 m long, in separate vacuum tanks (TCDSA, TCDSB). The actual interception device is a series of graphite/composite blocks with different densities (Figure 5.15) such that the beam gets diluted by the denser graphite in the beginning. Afterwards when the full particle cascade develops, a 2 m composite bloc (with lower density) limits the locally absorbed energy in order not to exceed temperatures of 1200°C in the TCDS. Finally the TCDS structure ends with a 0.5 m titanium absorber.

A parallel row of diluter blocks on the outside of the extracted beam aperture protects the MSD magnets in the event of bunches having a too high amplitude.

The RF heating due to circulating beam results in a power deposition of several hundred Watts. To minimise this effect the non-metallic elements exposed to the circulating beam are coated with 5 µm copper and the entrance and exit are smoothed. A 1 kW water cooling system absorbs this power. Figure 5.14 shows an image of the TCDS aperture with the two graphite blocks and the metalized circulating beam channel (right).

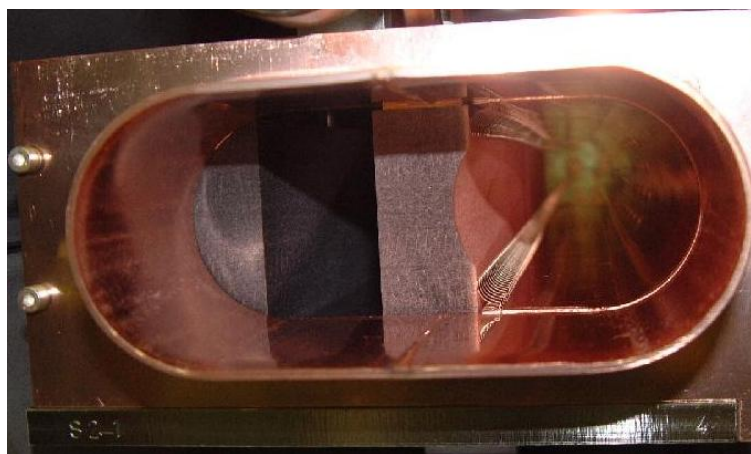


Figure 5.14: TCDS aperture, circulating beam right, extracted beam left (courtesy W.Weterings).

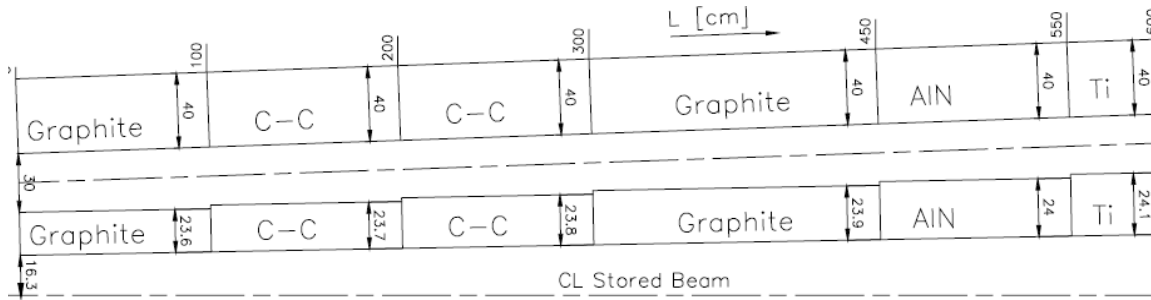


Figure 5.15: Structure of the TCDS protection element. [60]

The inner edge of the first (last) inner block is 16.3 mm (17.2) away from the circulating orbit whilst the outer edge of the same block is at 39.86 mm (41.3). A staircase approximation has been used to align the different blocks within the vacuum tank. A summary with detailed block positions can be found in [61]. Please note that knowledge of [62] is need for understanding of the alignment figures given by the LHC Layout Database as those values are taken from the flange centre which has an 15.5 mm offset to the tank centre.

5.5.5 Alignment of the TCDS and MSD

The TCDS horizontal aperture is calculated to protect the MSD and dump line elements whilst providing adequate circulating beam aperture [63]. The aperture of the TCDS and the positions of the extraction septa and their vacuum chambers were calculated [64] for the most demanding case at injection energy. Mechanical and alignment tolerances have been set to a maximum of ± 1 mm for the TCDS whilst the maximum allowed orbit excursion is ± 4 mm. Figure 5.16 shows an overview of the TCDS and MSD apertures together with the TCDS shadow and the 100% beam trajectory (red) as well as the 105% trajectory (purple).

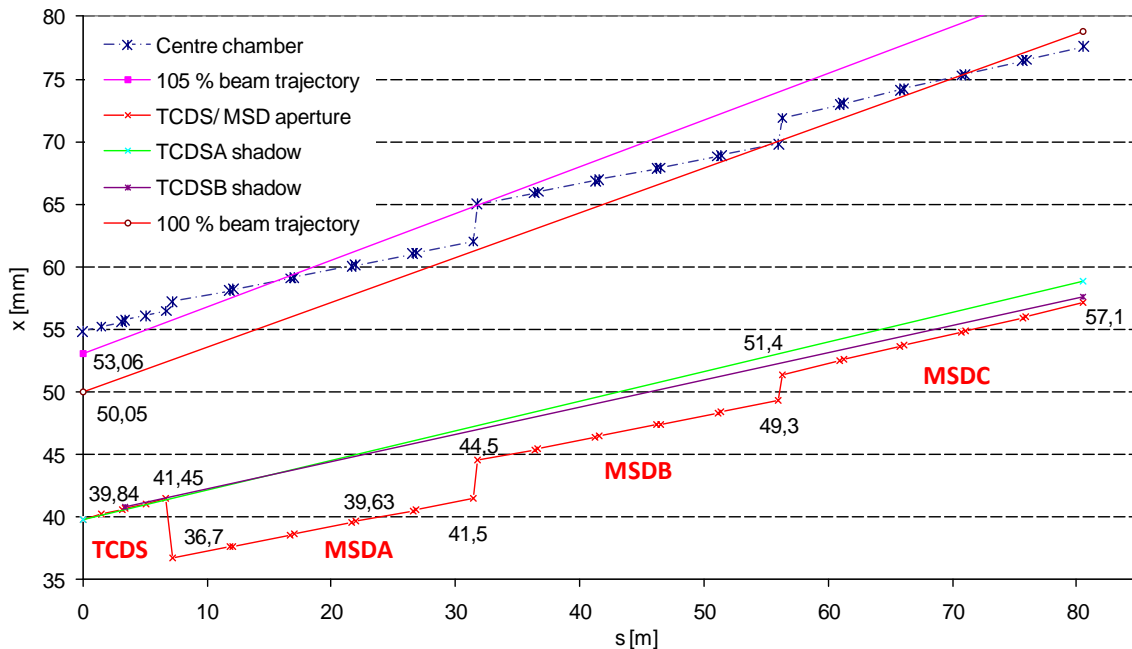


Figure 5.16: MSD alignment (horizontal) w.r.t. the circulating beam axis.

For Figure 5.16 values shown in [65] have been corrected by the misalignment measured in the tunnel after installation and realignment.

5.5.6 Fast-pulsed dilution magnets MKB

After the circulating beam has been extracted by the MKD and MSD magnets, a set of four horizontal and six vertical dilution magnets MKB is used to sweep the beam on the upstream face of the absorber graphite core (TDE), with a minimum sweep velocity of 10 mm/ μ s. Each magnet is powered by a pulse generator via a low impedance transmission line. Table 5.5 summarizes the main parameters of the MKB dilution kicker system.

The horizontal MKBH circuit produces an attenuated sinusoid. The vertical MKBV circuit is more complex because it requires a current phase shift of 90 degrees with respect to the horizontal system, to provide the desired total deflection shape for a simultaneous trigger of both systems. Figure 5.17 shows the diluter magnet circuits.

Table 5.5: MKB System parameters.

<i>Diluter magnet system</i>	<i>MKBH</i>	<i>MKBV</i>	
Number of magnets per system	4	6	
Max. system deflection angle	0.278	0.277	mrad
Kick strength per magnet	1.624	6.461	Tm
Magnet beam aperture - horizontal	58	66	mm
Magnet beam aperture - vertical	32	36	mm
Operating charging voltage	16.4	22.3	kV
Field rise time	18.9	34	μ s
Field oscillating frequency	14.2	12.7	kHz
Effective length (magnetic)	1.936	1.267	m
Yoke length (mechanical)	1.899	1.196	m
Vacuum length (mechanical), 2 magnets	4.582	4.076	m

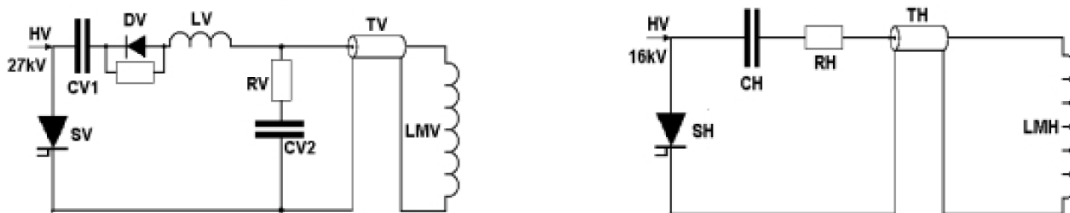


Figure 5.17: Horizontal (left) and vertical (right) diluter magnet circuit. [51]

The magnets are directly installed into vacuum tanks thus no special ceramic vacuum chambers are required. The dilution kicker magnets are horizontally slightly displaced in order to provide enough space for the extracted beam in case of asynchronous dump events. [66]

5.5.7 The TCDQ/TCSG/TCDQM protection devices

The mobile diluter block TCDQ protects the Q4 and the downstream arc at 450GeV and the insertion triplets at 7 TeV, and limits the number of bunches impacting on the LHC collimators in the event of an asynchronous dump. The quench limits in Q4 are assumed to be 10 mW/cm³ and 5 mW/cm³, at 450 GeV and 7 TeV respectively. [67]

Figure 5.18 shows the TCDQ.A4R6.B1 installed in the tunnel. The enlarged vacuum pipe for the extracted and already diluted beam 1 can be seen above the TCDQ. The parallel pipe in front accomodates cirulating beam 2.



Figure 5.18: TCDQ.A4R6.B1 installed in the tunnel with circulating beam 2 pipe (copper coloured pipe in front) and extracted beam 1 (big silver pipe) above.

The TCDQ has a single jaw, which is adjustable to keep the nominal setting of $\sim 8 \pm 0.5\sigma$ at injection and for 7 TeV. For mechanical reasons the TCDQ is made out of two 3.0 m long graphite diluter elements housed in separate vacuum tanks. For LHC optics version 6.503 the TCDQ is at a phase advance of 94° from the MKD kicker magnets. A movement range of about 35 mm is possible, with a resolution of 100 μm .

Precise control of the orbit at the TCDQ is required to ensure correct protection of the downstream machine elements. The position of the TCDQ is interlocked, with the measured position checked w.r.t a reference function which depends on the beam energy and β^* .

The RF heating due to the circulating beam results in a power deposition of several hundred Watts. To minimise this effect the non-metallic elements exposed to the circulating beam are coated with 5 μm copper. Figure 5.19 shows a coated TCDQ graphite block installed together with the beam screen. A 1 kW water cooling system absorbs the deposited power.



Figure 5.19: TCDQ aperture (courtesy W.Weterings).

The main parameters of the TCDQ are given in Table 5.6.

Table 5.6: Main parameters of the TCDQ diluter and TCSG collimator.

Device	TCDQ	TCSG	
Number of movable jaws	1	2	
Total diluter length	2x3000	1000	mm
Aperture when fully retracted	± 30	± 30	mm
Jaw minimum position	-2.5	-5	mm
Jaw maximum position	32.5	+30	mm

The TCDQ is followed by a TCSG collimator and the TCDQM iron mask. To ensure that the beam position with respect to the TCDQ cannot drift too far, a short two-sided 1 m long secondary collimator TCSG is installed immediately downstream of the TCDQ. A faster and higher precision movement is possible, as this device is equipped with a stepper motor compared to the linear motor system of the TCDQ. The introduction of the TCSG allows a relative retraction of the TCDQ jaw by about 0.5σ . A movement range of 35 mm with a resolution of below 20 μm is possible. The main parameters of the TCS collimator are given in Table 5.6. The TCDQM consist of two 1.15 m long iron absorber blocks and is installed for both beams (twin aperture) to protect the Q4 from the swept particle shower during MKD rise time.

5.5.8 Beam dump absorber block TDE

The 8.4 m long and external beam dump TDE is build in a sandwich like construction out of graphite layers with different densities in order to reduce the energy deposition (overheating) at a certain longitudinal TDE depth (for principle see TCDS section). Each absorber consists of a 7m long segmented carbon cylinder of 700 mm diameter, contained in a steel cylinder with a total weight of 7.2 t. This device is water cooled, and surrounded by about 750 tonnes of concrete and iron shielding. The TDE is housed in a dedicated cavern (UD) for each beam at the end of the transfer tunnels (TD68 and TD62).

The TDE is designed to safely absorb about 80% of the total LHC ultimate beam energy (i.e. 428 MJ out of 534 MJ). Approximately 2×10^4 abort cycles are assumed during an operational lifetime of 20 years. For safety reasons the core must be solid and it must keep its structural integrity under normal operating conditions over the dump lifetime. The risk of a loss of containment in the event of a total dilution failure means that the TDE core is kept under an overpressure of N_2 gas. An entrance window (VDWB) isolates the beam dump transfer lines, kept under vacuum (10^{-7} mbar), from the beam dump cores (100-400 mbar overpressure of nitrogen).

The entrance windows operate under a differential pressure of up to 1.4 bar. The design [68] must maintain the differential pressure, and avoid any implosion or collapse due to the beam impact, even in case of malfunction of the dilution kicker system.

5.5.9 Beam instrumentation

Beam instrumentation is needed to commission and operate the LBDS. This comprises (per beam) three beam screens (BTV), three beam position monitors (BPM), two beam current transformers (BCT) and 32 beam loss monitors (BLM). All beam instruments provide post-mortem data which is analyzed after every dump event to proof that all dump action was performed correctly before any further operation is allowed to continue.

Profile (BTV) and position (BPM) monitors are placed at positions around the extraction septa, after the dilution kickers and also in front of the dump block to monitor the extracted beam trajectory and sweep form.

Beam loss monitors (BLMs) are installed around the magnets and along the extraction line at every change of the vacuum cross-section, to monitor the quality of the extraction at the known aperture limitations and also to localize any unforeseen beam loss at those aperture restrictions.

Two redundant beam current transformers (BCT) are used to cross-check the intensity of the extracted beam w.r.t. the circulating beam (one turn) before extraction.

5.5.10 Abort gap cleaning and abort gap monitor

A dedicated instrument (abort gap monitor) is used to monitor the abort gap population, using an input from the synchrotron light monitor, in order to provide an alarm if the population exceeds the threshold values. The abort gap monitor uses the LHC energy, to calculate this threshold. Above these limits the energy deposition in the Q4 coil could exceed the quench level even during a synchronized dump action.

To ensure that the LHC abort gap population remains well below the limits, an active abort gap cleaning is required for nominal intensity. See chapter 7 for more detailed explanations.

5.6 Reliability of the LBDS

Above a certain intensity (and energy) the proper function of the LBDS is crucial for safe operation of the accelerator. Intensive work has been carried out in the past in order to understand the probability of different failure scenarios [69].

In general there are two groups of fault cases:

The acceptable fault case where the actual fault will affect operations but should not result in damage to the LHC. (e.g. self triggering, fault on only one MKB, etc.)

The unacceptable (beyond design) fault case: These group summaries all possible system faults which are unacceptable and could lead to damage. Examples are: wrong energy information, fewer than 14 MKD active, MSD field out of tolerance, TCDQ system completely retracted at the moment of asynchronous dump events, etc.

The strategy for the acceptable fault cases is to limit their occurrence and impact by various protection systems (e.g. abort gap monitor/cleaning to limit the number of quenches of the downstream Q4 during scheduled beam abort due to abort gap population, TCDS to limit beam induced damage on the septa during asynchronous beam abort, etc.), whilst the group of unacceptable fault cases has to be excluded as far as reasonably feasible.

Fault tolerance and online surveillance systems reduce the probability of unacceptable failures. The parallel dual branch generators, the redundant trigger paths, usage of solid state switches, capacitor voltage surveillance and last but not least the whole BETS itself with independently measured dipole and septa currents are solutions to ensure a high reliability of the correct MKD powering. The extraction system is designed such that 14 out of 15 MKD can still safely extract the beam at all energies and dilution with two out of ten MKB being sufficient to not destroy the TDE at nominal beam intensities [70]. Internal and external operational check systems (IPOC, XPOC) have been introduced in order to analyse the MKD and MKB waveforms with references, to make sure the full system worked correctly for each previous dump.

Reliability analysis showed a probability of 6 (± 2) false dumps per year coming from the LBDS itself. They were made under the assumption of 400 physics runs per year (each 10 hours followed by a 2 hours stop) and the assumption that failure rates stay constant. The calculated figure for unsafety of the LBDS is 2.4×10^{-7} events per year which corresponds largely to SIL4 level [71]. As a main source for false dumps the magnet powering was identified. Masking the false dump requests of the MKD and MKB power converters will significantly reduce the unavailability (2.1 false dumps less p.a.) with only a small increase of unsafety from 1.8×10^{-7} to 1.9×10^{-7} events per year. Not included

in this figures are false alarms coming from the BETS and the MPS which were not fully modelled and which are supposed to significantly raise the unavailability values [72].

During hardware commissioning long term reliability runs were done to validate the calculated data and to check for unexpected failure modes. During a period of 7 months, over 2×10^4 pulses were surveyed. The observed failure rates for the MKD switches was not as low as stated by the manufacturer (10^{-4} observed instead of 10^{-6}) and an unexpected common mode failure in the MKB system was also seen. A variation of 1.4% in MKD kick strength was identified as a temperature drift. Action was taken to rectify the latter two issues. No unacceptable or asynchronous dumps were recorded. [73]

6 LBDS – Results of Tracking Studies

The LHC beam dump system is one of the most critical systems concerning machine protection and safe operation. It is used to dispose of high intensity beams between 450 GeV and 7 TeV. Studies into the consequences of abnormal beam dump actions have been performed. Different error scenarios have been evaluated using particle tracking in MAD-X including asynchronous dump action, prefire cases, and the impact of different orbit and collimator settings. Losses at locations in the ring and the beam dump transfer lines have been quantified as a function of different settings of the dump system protection elements. The implications for the setup and operation of these protection elements are discussed.

6.1 Simulation principle, methods and used tools

6.1.1 Tracking Methodology

A system of MAD-X tracking jobs was set up to study failure cases and losses for various asynchronous dump events. Particle distributions are created according to the used orbit which is set up in a separate job. These input distributions are then sent to each of the tracking jobs for the TD68 ring part, the TD68 extracted beam part (if some beam was extracted), the rest of the long straight section in IR6 and finally the ring itself. Simulations with different collimator settings in IR6 can be done in parallel. The outputs of these jobs are then handed over to the ring tracking jobs which can also be processed in parallel as well. Figure 6.1 shows an overview of the job architecture.

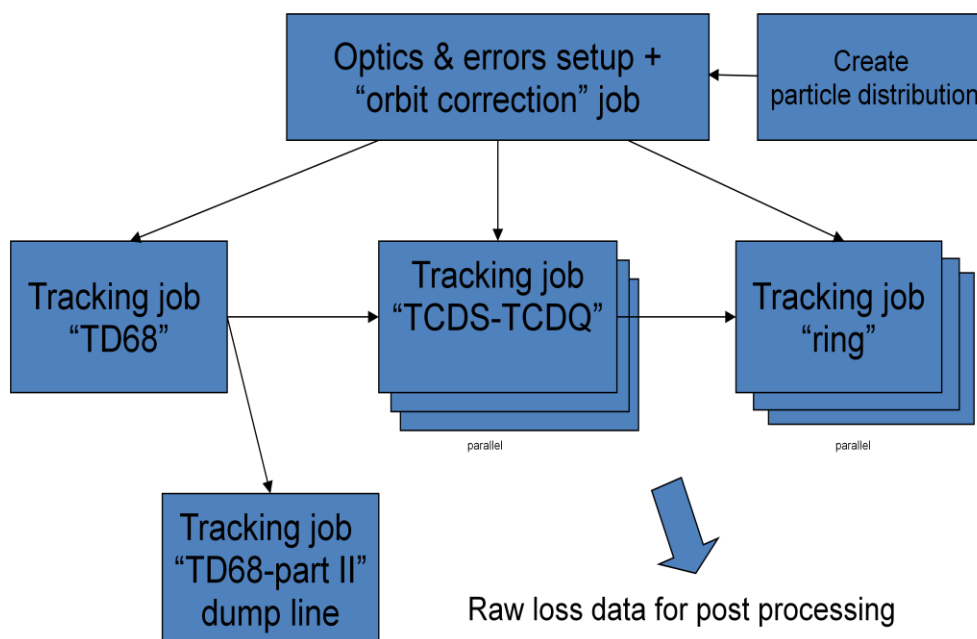
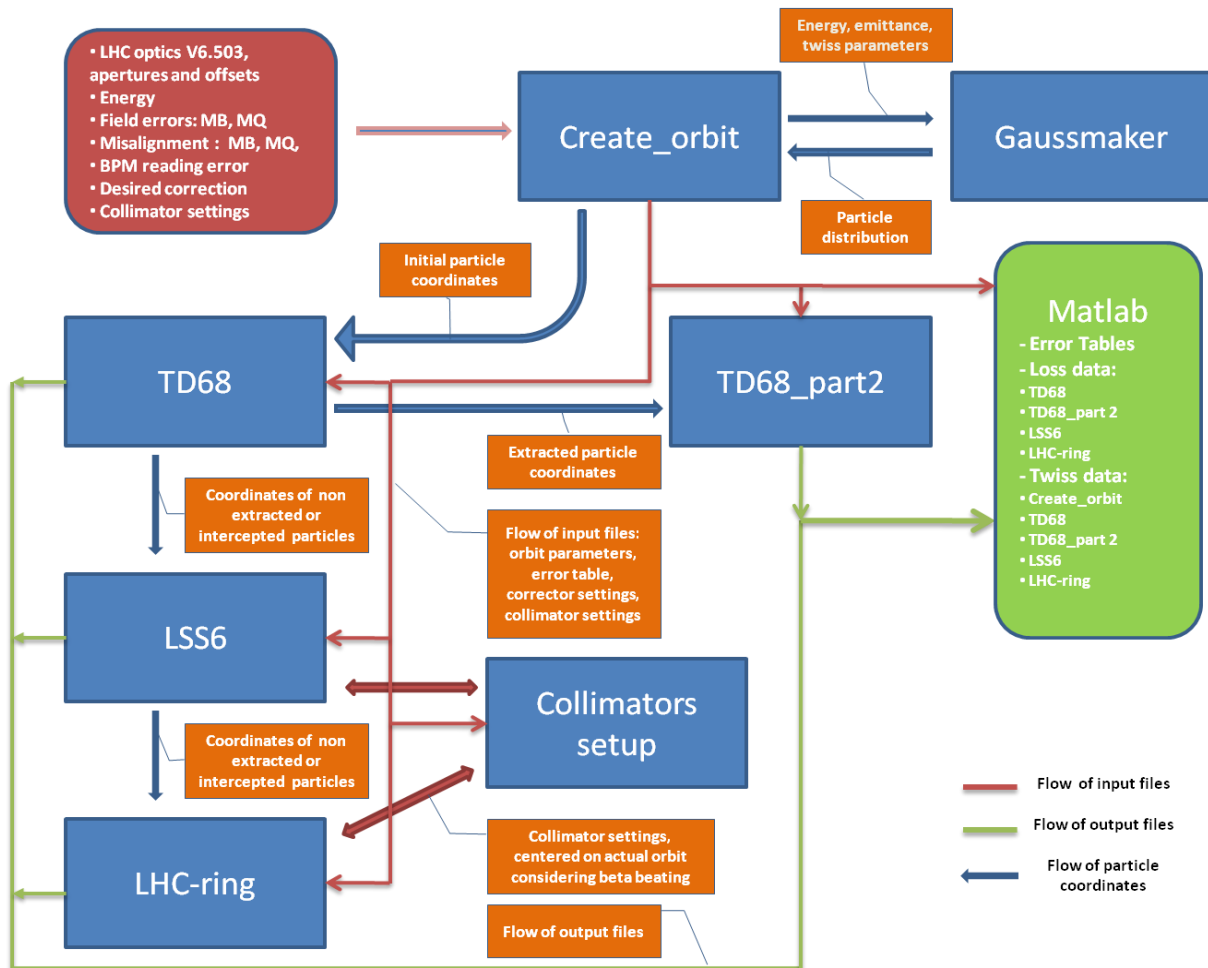


Figure 6.1: Architecture of the simulation programs.

The tracking itself is done in MAD-X-thintrack, which uses a thin-lens version of the LHC sequence and is adapted to handle time dependent kicks as well as skew collimators. All jobs are coordinated by shell scripts which handle the dispatching to the LSF batch farm [74]. Each of these jobs saves its results (raw loss data) in tables (tfs format) which are read into Matlab to be combined for further processing. The dataflow is shown in Figure 6.2. All results presented in this chapter are done for LHC Beam 1.

Table 6.1: LHC jobs and models used and developed.

Seq. No.	Name	Description	Comments
1	create_orbit	Generates realistic orbit with errors and correction applied	Based on LHC optics model v6.503
2	gaussmaker	Generates Gaussian distribution	Set up of particles distribution considering actual beam parameters and orbit
3	TD68	Tracks particles down TD68	Self made sequence with detailed aperture model
4	LSS6	Tracks particles down the section TCDS-MQY.5R6	Self made sequence with detailed aperture model
5	ring	Tracks particles outside LSS6	Based on LHC optics model v6.503 with improved aperture


Figure 6.2: Layout of the dataflow and program interaction.

6.1.2 Core tracking routine used within the various jobs

Where time dependent parameters had to be applied, as for the MKD or MKB kicker magnet strengths, a set of loops was programmed to allow the loading of different initial particle coordinates taking into account the changing magnet field in 5 ns steps. The value of the magnetic field is read

out of predefined tables which were computed from kicker waveform measurements of the real magnets and generators in the LHC tunnel.

6.1.3 Particle numbers

As shown in chapter 3 the actual CPU time for the orbit and tracking calculations is rather high, and the amount of data created is large. Therefore the number of simulation particles had to be restricted to 1.5×10^4 macro particles started in the TD68 job in order not to produce memory overflows in the subsequent jobs. For every call of the program loop one such simulation particle was started in intervals of 5 ns. The maximum number of total possible particles divided by the time range of the simulation counted in 5 ns steps gives then the actual started number of particles per 5 ns. As the time range varied for the different simulation types two typical numbers were chosen: 50 particles each 5 ns for the normal cases and 25 for the prefire cases. This corresponds to 4.6×10^8 particles of nominal LHC beam for each simulation particle (macro particle) for normal cases and to 9.2×10^8 particles for the prefire cases. As the simulations for each case were repeated several times with a different orbit setup for some orbit independent purposes this ratio is averaged down by the number of repetitions performed. It is an important number as it represents the minimum particle loss which can be resolved in the simulation.

Note that the LHC longitudinal bunch distribution is not reproduced in this simulation; however, a 5 ns spacing is representative since the synchronization between the MKD trigger and the beam bunch (abort gap) is unknown for asynchronous dump actions.

6.2 Simulation set up and input parameters

The simulation set up consisted of reading in the appropriate magnetic field and alignment error files with the LHC sequence, to be able to generate an LHC orbit, and perturbed optics. The orbit was then corrected to realistic values, using appropriate error distributions on the orbit monitors, and the tune and chromaticity were corrected to the nominal values. The aperture model was then read and collimator positions adjusted around the modified orbit at the specified settings. Particle distributions were then produced matched to the orbit and optics at the starting point of the simulation, and circulated for a number of turns, to produce a distribution ready for the tracking through the dump system.

6.2.1 Magnet field strengths and errors

In order to generate a realistic orbit and perturbed optics, the field errors for the LHC main magnets have been introduced, by plugging in the measured values from the magnet test facilities plus adding a small random error, according to the expected distribution given by LHC error table 9901 [75] which was used for injection and top energy for all simulations for errors up to 10th order in the main dipoles and quadrupoles. All correction magnet strengths were at their nominal settings, except for those explicitly used to correct the tune and chromaticity after the introduction of the errors in the main magnets.

Any error in the LSS6 Q4 quadrupole strength is of particular interest, since the beam deflected by the MKD traverses the Q4 quadrupole off-centre and therefore sees an additional deflection which is essential for the beam extraction. The strength of this magnet has been considered explicitly as a failure case.

6.2.2 Alignment errors and mechanical tolerances

The large 15 m long, 27.5 t LHC main magnets have to be precisely installed in the tunnel, but errors in alignment are invariably present due to mechanical tolerances, survey precision, temperature variations and ground movement.

The misalignments of the quadrupoles (MQ, MQM, and MQY) have a large effect on the closed orbit, since a transversely displaced quadrupole will give a dipole kick to the circulating beam. A peak maximum alignment error of 0.36 mm [76] has been applied randomly with a Gaussian distribution in the x and y axis, which represents survey errors and the effect of ground motion (1 year maximum). Azimuthal misalignments have not been considered in these simulations [77].

Misalignments for main bending magnets (MB) have not been considered as the beam in a vertically or horizontally misaligned MB does not see any change in dipole field. For the (small) multipole field errors any misalignment would have some consequences, mainly on the tune via feed-down of the sextupole component; this effect is neglected in this study. A potential reduction in aperture from misalignment has been considered by subtracting the aperture and beam screen tolerances generated from the layout database from the quoted element aperture.

6.2.3 Beam position monitor reading errors

The installed Beam Position Monitors have random misalignments as well as random reading errors, taken into account as a Gaussian distribution of errors in the reading for a particular monitor with a tolerance (σ) value of 0.2 mm in x and y planes [78]. This is important for the quality of the orbit correction.

6.2.4 Closed orbit correction

Orbits were generated once the errors described above were applied to the LHC sequence, and the correction made using the MICADO algorithm in MAD-X, with the errors applied to the BPM readings. The reference LHC orbit at 450 GeV is shown in Figure 6.3. The large excursions are the closed separation/crossing angle bumps at the experiments, used to avoid collisions between bunches at the IP and at parasitic encounters [79]. The uncorrected and corrected difference orbits with respect to this reference orbit are shown in Figure 6.4; the effectiveness of the orbit correction is apparent, with the maximum excursions reduced from about 20 mm to less than the specified 4 mm. Figure 6.5 shows the change of the closed orbit difference vector length as a function of the S location along the LHC.

The dispersion function is also affected by the orbit correction, since the off-axis passage through the LHC quadrupoles produces dipole kicks which perturb the off-momentum closed orbit. Figure 6.6 illustrates this.

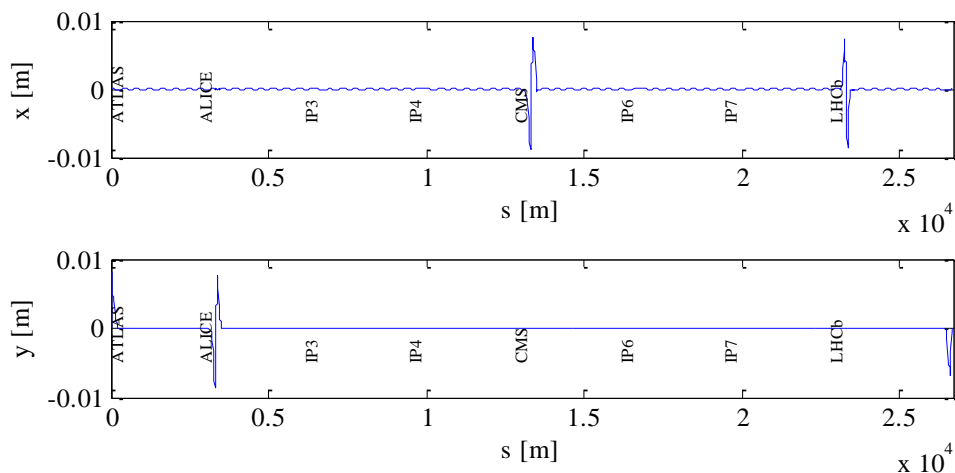


Figure 6.3: Horizontal and vertical ideal orbit model, 450 GeV.

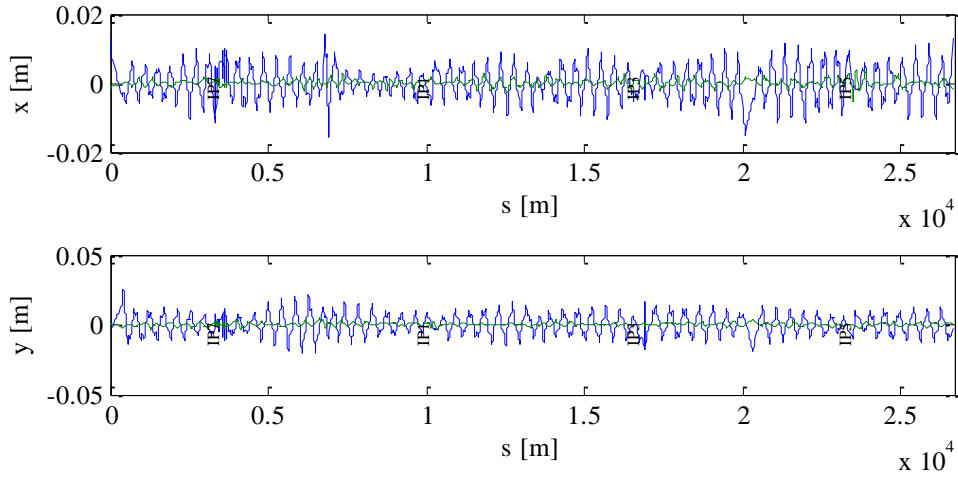


Figure 6.4: Horizontal and vertical difference orbit before (blue) and after correction (green), 450 GeV.

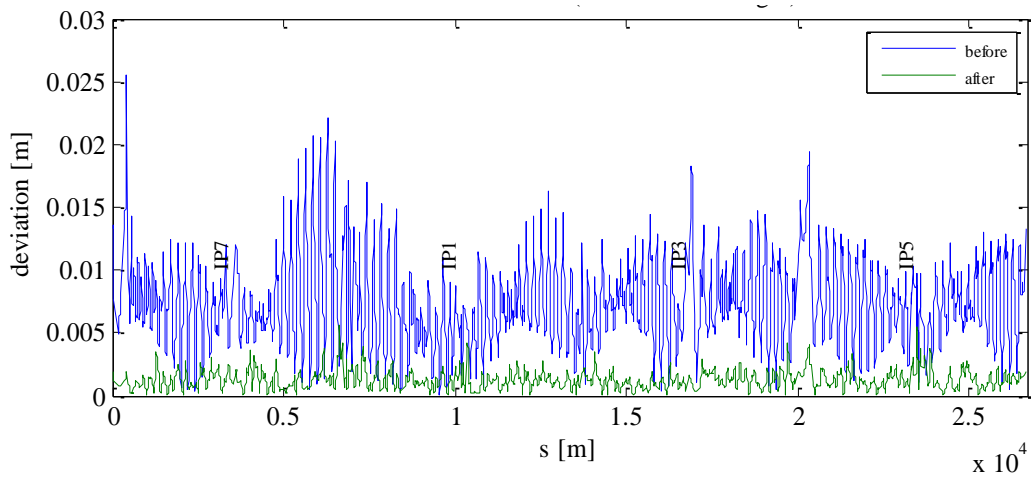


Figure 6.5: Horizontal and vertical difference orbit vector length before (blue) and after correction (green), 450 GeV.

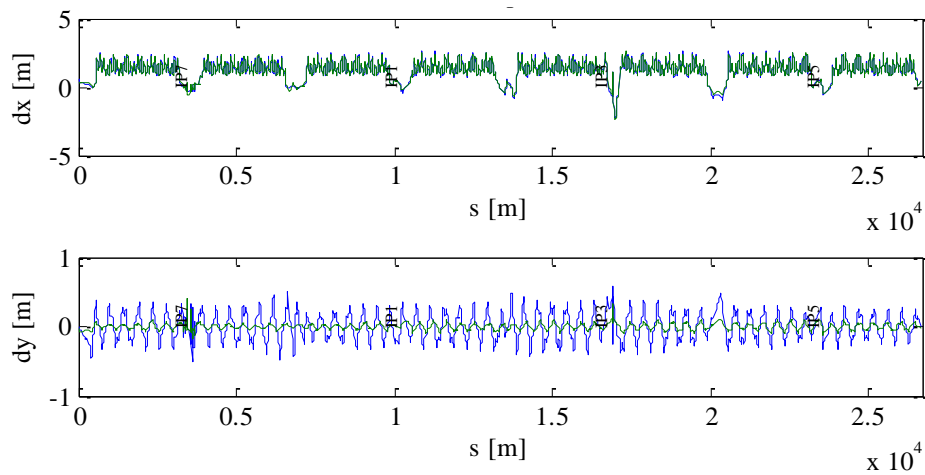


Figure 6.6: Dispersion function, 450 GeV.

6.2.5 Optics perturbation and correction

The errors in the higher order magnetic fields change the tune and the chromaticity; these quantities were corrected back to the nominal values in both planes using the corrector circuits KQF.B1/KQD.B1 and KSF.B1/KSD.B1. This changes slightly the beta-functions along the LHC and results in beta-beating, which is defined as the relative change of the beta function. Figure 6.7 shows the beta-beating in the horizontal plane after correction for a typical 450 GeV case. This beta-beat is important to include in the simulations since it will affect the collimator settings and the particle amplitudes at aperture limits.

Since the phase advance μ is defined as $\mu = \int ds/\beta$, this perturbation also affects the phase advance along the ring, as shown in Figure 6.8. This is also an important effect, since the protection systems like collimators are designed using the nominal phase advances of the LHC, and perturbations could affect the protection efficiency.

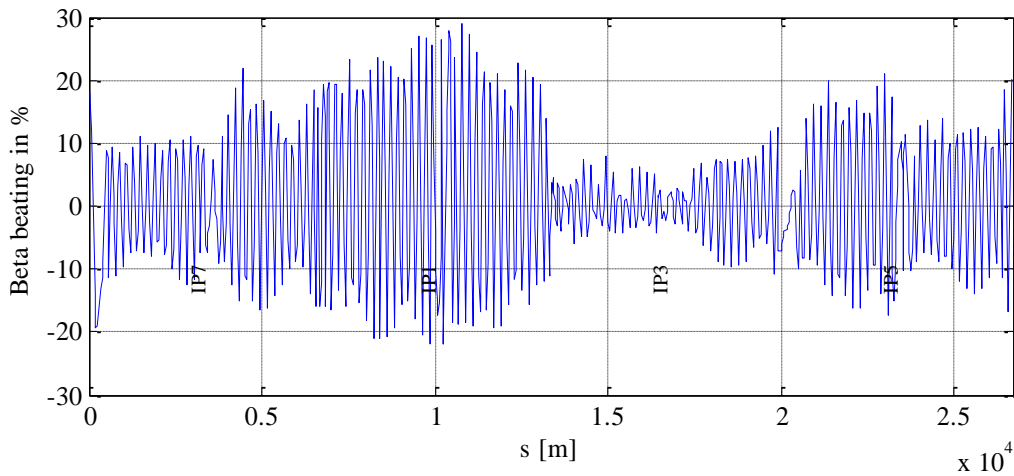


Figure 6.7: Beta beating for a typical 450 GeV case.

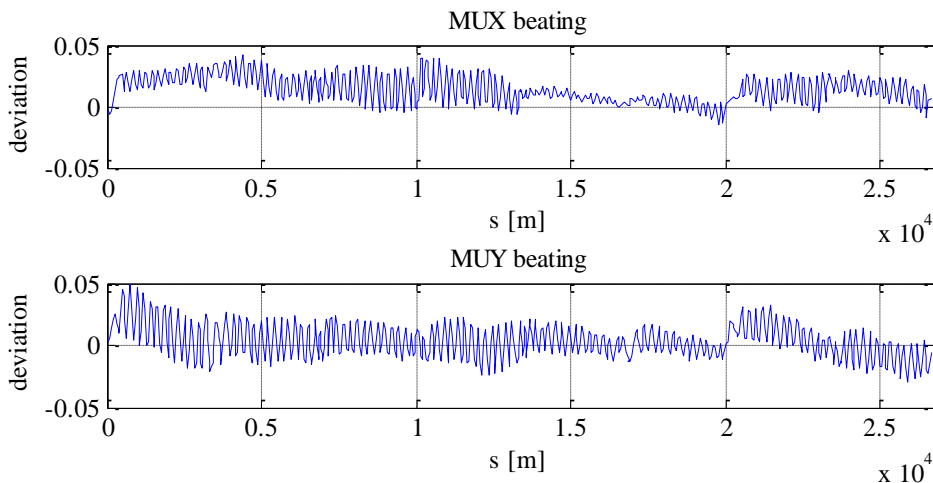


Figure 6.8: Phase advance deviation for a typical 450 GeV case.

6.2.6 Initial particle distribution

Equations (6.1) and (6.2) show the relations to describe a particle in the horizontal phase space, where ε_x is a Gaussian distributed random variable and ϕ an arbitrary phase angle in the interval $[0, 2\pi]$. These relations were used to create an ensemble of particles considering the actual simulation orbit.

$$x = \sqrt{\varepsilon_x \cdot \beta_x} \cdot \cos(\phi) \quad (6.1)$$

$$x' = -\frac{\sqrt{\varepsilon_x}}{\sqrt{\beta_x}} \cdot [\alpha_x \cdot \cos(\phi) + \sin(\phi)] \quad (6.2)$$

To simulate such a distribution correctly in MAD-X the Box-Muller relation was used, equation (6.3) and (6.4) with z_1 and z_2 , a pair of independent normally distributed numbers created from two numbers (u_1, u_2) with uniform distribution in the interval $[0, 1]$.

$$z_1 = \sqrt{-2 \cdot \ln u_1} \cdot \cos(2\pi \cdot u_2) \quad (6.3)$$

$$z_2 = \sqrt{-2 \cdot \ln u_1} \cdot \sin(2\pi \cdot u_2) \quad (6.4)$$

A merger of this method with the formulas given above leads to equation (6.5) where u_1 and u_2 are generated by the MAD-X “ranf” command [80].

$$x_{gauss} = \sqrt{-2 \cdot \ln(u_2)} \cdot \sqrt{\varepsilon_x \cdot \beta_x} \cdot \cos(2\pi \cdot u_2) \quad (6.5)$$

The same principle applies for the x' coordinate and for the vertical plane.

A separate Mad-X job was set up to create such a particle distribution at an exact point specified by the “create_orbit” routine, matched to the perturbed α and β values. For all simulations described in this chapter this starting point was the entrance of Q5 in front of the MKD magnets.

Finally the orbit position in real space (x, px, y, py) were simply added to the distribution coordinates. The particle phase space coordinates were checked against the Courant-Snyder Invariant for consistency and to measure the emittance of the distribution. Figure 6.9 shows a typical initial particle distribution with 5000 particles created for 450 GeV. These particles are then tracked around the LHC for 10 turns using the aperture model, to remove any high-amplitude particles which might otherwise bias the final tracking results. Figure 6.10 shows such a distribution in phase space and x, y space for 450 GeV.

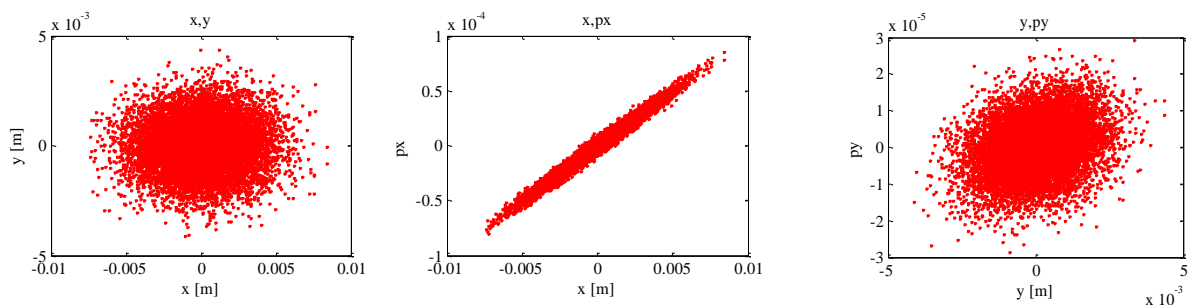


Figure 6.9: Typical created initial particle distribution, 450 GeV, 5000 particles.

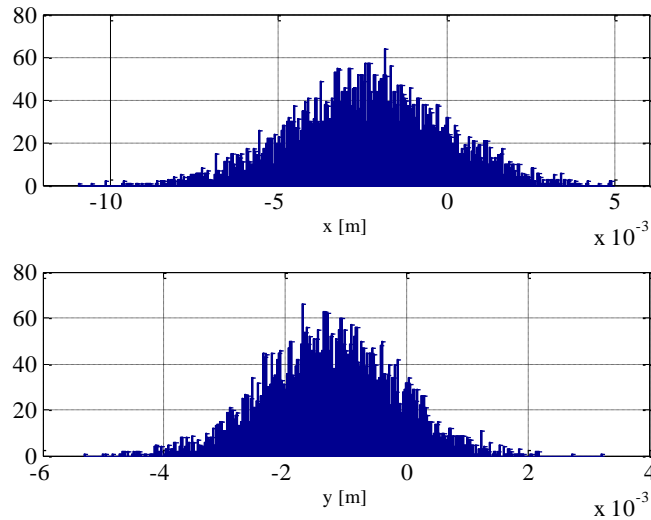


Figure 6.10: Typical particle distribution in real space after 10 turns, 450 GeV.

6.2.7 Apertures in the beam dump region LSS6

The MAD-X optical model of the LHC machine allows to track a particle around the ring and to monitor its trajectory. However, the basic code does not take account of any physical obstacles. Special aperture modules have to be added to define the physical accelerator aperture limits. For these studies the general layout database aperture file [81] has been used, which was improved and verified for special regions of interest like LSS6, all collimator and protection devices (see next subchapter), some experiment equipment and known aperture bottlenecks. For the dump line TD68 and TD62 a precise aperture model has been created from the layout and equipment drawings, Figure 1.6. [82]

Table 6.2 shows an overview of the most important apertures in the dump region. The RECTELLIPSE values are given in MAD-X convention, where the first value specifies the opening of a rectangular box and the second the semi-axis of an ellipse.

Table 6.2: Important apertures in the LBDS region

Location	Element	Aperture type	Horizontal Aperture [m]	Vertical Aperture [m]	References
5L6	MQY	RECTELLIPSE	0.029 / 0.029	0.0241 / 0.029	
4L6	MQY	RECTELLIPSE	0.0241 / 0.029	0.029 / 0.029	
4L6	MKD	ROUND	0.0288	0.0288	LHCMKDCA0001
4L6	TCDQM	RECTANGULAR	0.0275	0.0215	LHCTCDQM0001
4L6	TCDSA	RECTANGULAR	0.0163	-	EDMS393973
4L6	TCDSB	RECTANGULAR	0.01685	-	EDMS393973
TD68	MKB	RECTELLIPSE	0.0315 / 0.0362	0.018 / 0.0362	
TD68	VDDA	RECTELLIPSE	0.02725 / 0.03	0.0165 / 0.022	LHCVDD_A0001
4R6	MSD	ROUND	0.029	0.029	EDMS488061
4R6	TCDQ	RECTANGULAR	moveable	-	EDMS503490
4R6	TCSG	RECTANGULAR	moveable	-	EDMS503490
4R6	TCDQM	RECTANGULAR	0.0215	0.0275	LHCTCDQM0001
4R6	MQY	RECTELLIPSE	0.029 / 0.029	0.0241 / 0.029	
5R6	MQY	RECTELLIPSE	0.0241 / 0.029	0.029 / 0.029	

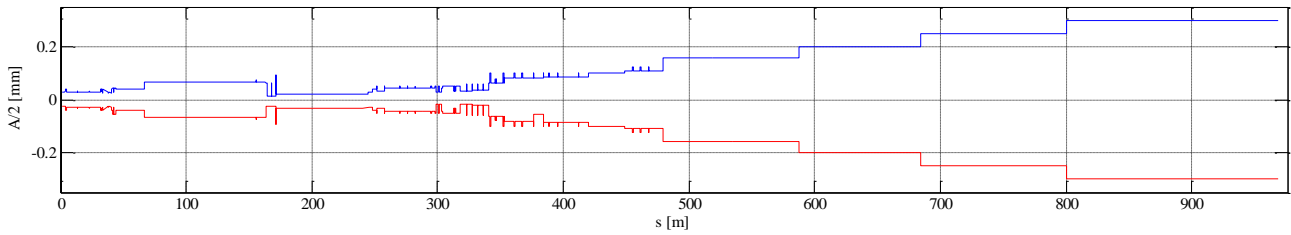


Figure 6.11: Plot of the horizontal (blue) and vertical (red) physical half aperture of the created T68 aperture model. For clarity the vertical half aperture is plotted with negative sign.

6.2.8 Collimator settings

The limiting physical aperture for the rest of the LHC ring is defined by collimators, since these are designed to intercept the beam before any other element. In order to be able to follow variations in beam position and beam size, most of the LHC collimators are moveable. Their settings depend on various operational parameters, like the actual orbit, the energy and the chosen tightness of the jaws to the beam, which in turn will depend on the sensitivity of the superconducting magnets to beam loss [83]. Table 6.3 shows an overview of the nominal collimator settings for 450 GeV and 7 TeV [84]. The hierarchy of primary, secondary and tertiary collimators is discussed in detail in chapter 1.5. Note that the TCDQ system is part of this hierarchy of collimator settings.

Table 6.3: Collimator settings in σ

IR	Type	450 GeV [σ]	7 TeV [σ]
IR 1/IR 5	TCT	17.0	8.3
	TCL	10.0	10.0
IR 2/IR 8	TCLI	6.8	15.0
	TDI	6.8	17.0
	TCT	17.0	8.3
IR 3	TCP	8.0	15.0
	TCSG	9.3	18.0
	TCLA	10.0	20.0
IR 6	TCSG	7.0	7.5
	TCDQ	8.0	8.0
IR 7	TCP	5.7	6.0
	TCSG	6.7	7.0
	TCLA	10.0	10.0

6.2.9 Mechanical tolerances

The LHC vacuum system provides a beam vacuum of less than 10^{15} H₂ per m³ for the cryo-parts and less than 10^{-10} mbar for the room temperature parts [85]. Inside the vacuum chambers, special beam screens at 20 K are used to reduce the heat load on the 1.9 K cryogenic parts. Vacuum chambers and beam screens are allocated misalignments due to mechanical tolerances, magnet installation alignment errors, survey precision and ground movement. In the simulations these alignment tolerances are grouped into a variable, which is subtracted from the specified element aperture and was taken from the LHC Layout database.

No tolerances have been included concerning the alignment and setup of movable collimation devices, since these are assumed to be regularly aligned to the beam with high precision.

6.3 Failure cases considered

Various cases are of interest for the beam dump system itself or for other machine components, and have been treated in simulation:

1. The ‘normal’ beam dump, to make sure with detailed tracking that all apertures are correctly implemented in the LHC, and that no losses are seen on any components;
2. Different types of asynchronous dump, since the kickers can either all be synchronized together (although still out of synchronism with the abort gap), or one kicker can trigger before the other 14, in the case of the pre-trigger asynchronous dump. The expected losses on the TCDS and on the MSD septa are important outputs;
3. Different number of missing MKD kickers – the system is designed to still extract correctly with 14 out of 15 MKD operating, and the verification of this redundancy is an important objective. Of particular interest here are possible losses in the dump line.
4. As a worst case scenario a prefire case together with a faulty retrigger line so that only the kick of one MKD is seen by the beam;
5. The maximum possible error in the Q4 and MSD field, before beam losses start occurring in the extraction channel, is an important input into the setting of the interlocks on the Q4 and MSD magnetic fields.
6. The maximum allowed orbit in IR6 is 4 mm, to protect the beam dump system elements from losses even with a missing MKD. A study of the losses for different maximum orbit amplitudes was made, to verify that this tolerance is correct.
7. A scan of the retraction of the TCDQ system setting. The TCDQ system is crucial in protecting downstream LHC components, including the collimators. The maximum tolerances for the setting up of the TCDQ are important information as well as the possible beam impact locations downstream of the TCDQ.
8. The potential beam losses on the triplet apertures in points 1 and 5 are a major concern, especially with fully squeezed optics. To simulate this with beam 1, the collimators in IR7 were fully retracted, and the losses on the TCTs and triplet apertures studied as a function of the TCDQ retraction.

6.4 Simulation results

6.4.1 Normal beam dump

The simulations were performed for the nominal conditions with a 450 GeV beam (the most pessimistic case because the beam size is largest) using a total of 20 orbit seeds. The results only showed beam losses on the TDE block, Figure 6.12, with no losses anywhere else in the extraction channel. The sweep form on the TDE is as expected, Figure 6.13. This confirms that the apertures are sufficient for normal operation, when all systems are in tolerance and the beam is synchronized with the abort gap.

For all simulations and energies no losses were seen in the LHC ring part of TD68, which is in front of the TCDS and encompasses a displaced and enlarged vacuum chamber and beam instrumentation.

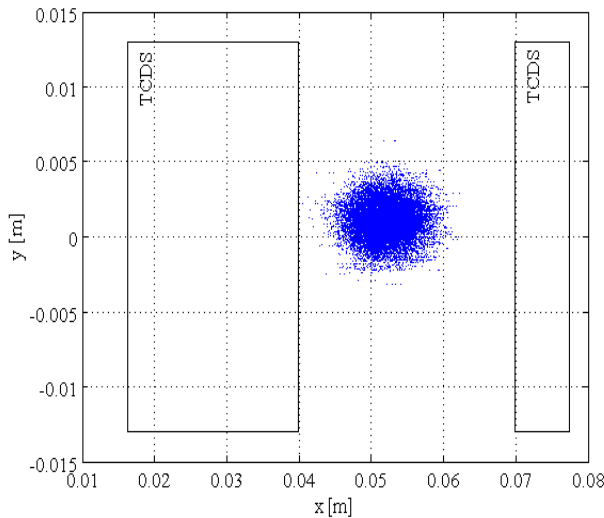


Figure 6.12: Extracted beam at the TCDS entrance for a beam abort under nominal conditions (synchronized, 15 MKD), 10 orbit seeds, 450 GeV.

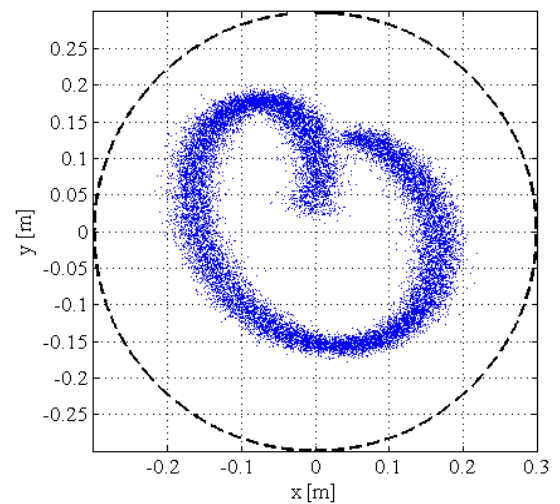


Figure 6.13: Sweep shape for a beam abort under nominal conditions (synchronized, 15 MKD), 10 orbit seeds, 450 GeV.

6.4.2 Asynchronous beam dump and MKD kicker pre-trigger

Figure 6.14 shows an overview of simulation losses in the LSS6 extraction region for a 7 TeV beam with an asynchronous dump. Only impacts on the TCDSA and TCDSB blocks were observed. Figure 6.15 shows the horizontal loss coordinates along the extracted beam channel starting from the entrance of the first TCDS graphite bloc up to the dump bloc TDE. No losses are seen on the known aperture bottlenecks MSD, MKB or VDDA. The plot shows the sweep in x direction over the TCDS surface and the final impact on the TDE with maximum dilution.

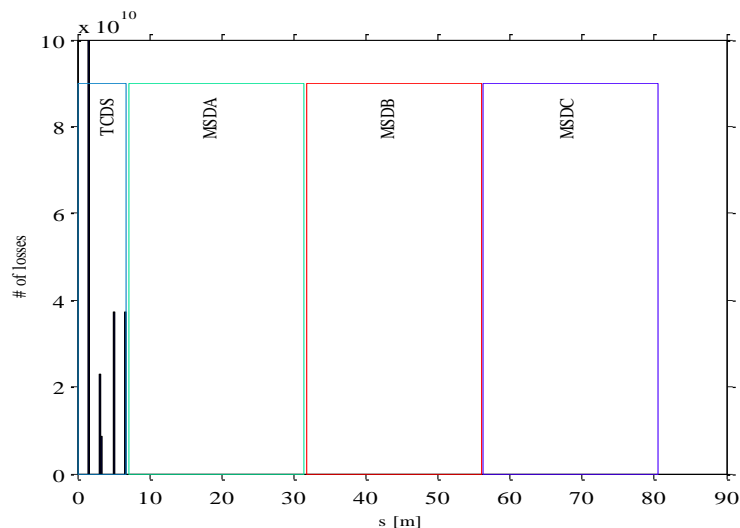


Figure 6.14: Losses in the TD68 extraction zoom.

In total 4.4×10^{12} particles hit the TCDS blocks. Figure 6.14 gives a more detailed view where one can clearly see some losses on the TCDSB and on the stairway-like surface along both protection devices. These loss locations show a maximum loss of 4×10^{10} particles per asynchronous extraction, in agreement with the specification for this device [86] and [87].

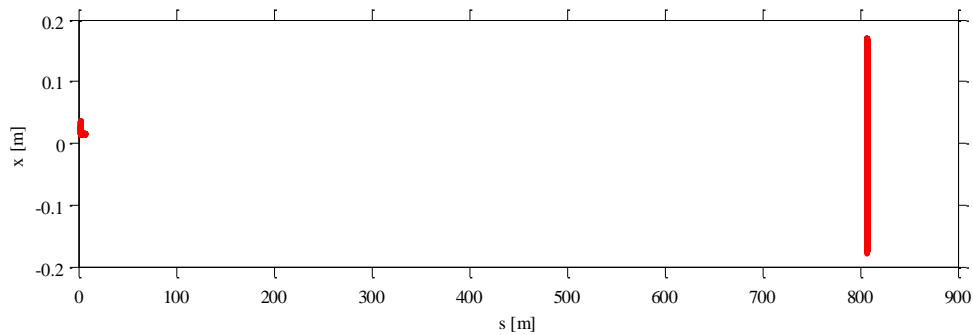


Figure 6.15: Horizontal loss coordinates in TD68 (from TCDS downstream), 10 orbit seeds, 7 TeV.

Figure 6.16 is a density plot of particles hitting the TCDSA front surface for an asynchronous beam abort. The image shows the front graphite block only; beam is swept over the TCDS from the left to the right. Higher densities on the right side can be explained by the MKD waveform (Figure 6.19) as the dB/dt already starts to slow down and therefore the sweep-velocity decreases which results in higher densities. Losses at the TCDS start at $1.1 \mu\text{s}$ after the dump kickers have been fired and continue for $1.125 \mu\text{s}$ ($2.25 \mu\text{s}$ after MKD trigger) until the beam is finally swept into the extraction channel.

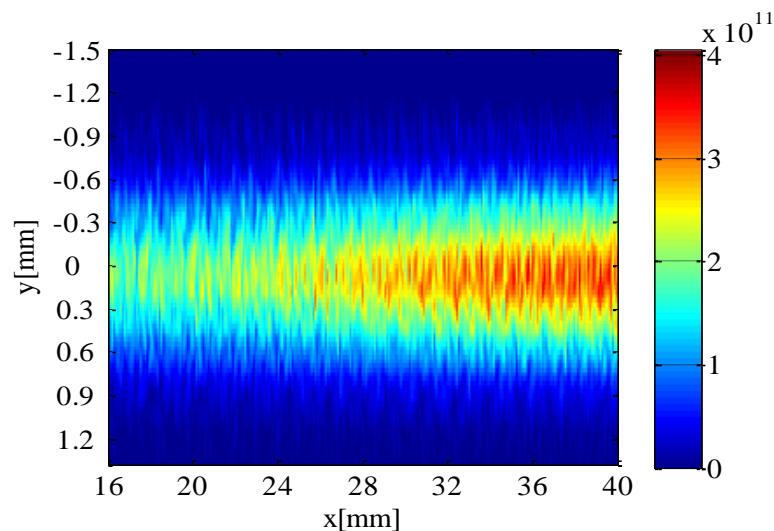


Figure 6.16: Particle density in $p+ / \text{mm}^2$ for a beam sweep over the TCDSA front surface, 7 TeV.

Figure 6.17 shows an overlay plot of the losses along the transfer line TD68 starting at the TCDS up to the dump seen from the origin of TD68. The small red horizontal line in the centre shows the sweep over the TCDS block around 166 meters from the origin of TD68 the e-shape like pattern represents the diluted beam on the TDE surface some 800 meters further down. Note that for those overlay plots the sweep comes from the right and goes to the left.

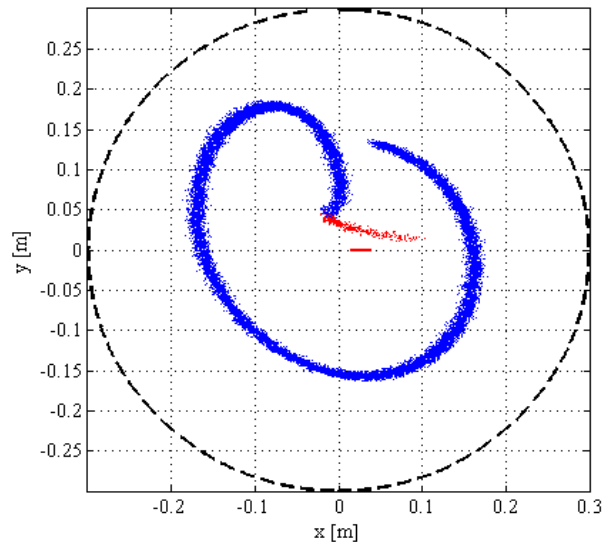


Figure 6.17: Overlay of particle loss coordinates in TD68 for 7 TeV; E-shape is on the TDE, the small line in the centre indicates lost particles whilst the sweep over the TCDS blocks. Red particles would be within the abort gap.

For the pre-trigger case no significant difference was seen regarding the losses on the TCDS and in the beam dump region. This is expected, as the large kick amplitudes needed to reach the TCDS the MKD waveform for asynchronous and pre-fire cases are very similar.

In addition to the beam extracted into the dump channel and the dump line, some particles stay on the circulating beam side of the TCDS. The TCDQ system should intercept any particles with amplitudes larger than 8σ , with particles at lower amplitudes either intercepted by some of the ring collimators, or making one full turn and being extracted by the MKD kick (which has to be of sufficient duration). Figure 6.18 shows the particle density on the TCDQ front surface after a 7 TeV asynchronous beam abort at 8σ TCDQ setting. The density is higher in the beginning of the sweep when the beam starts to hit the TCDQ inner edge. This takes place about 475 ns after the dump kickers were fired. The sweep continuous for 710 ns (1185 ns after MKD trigger) until it is cut off by the TCDS aperture and has been swept for 39 mm.

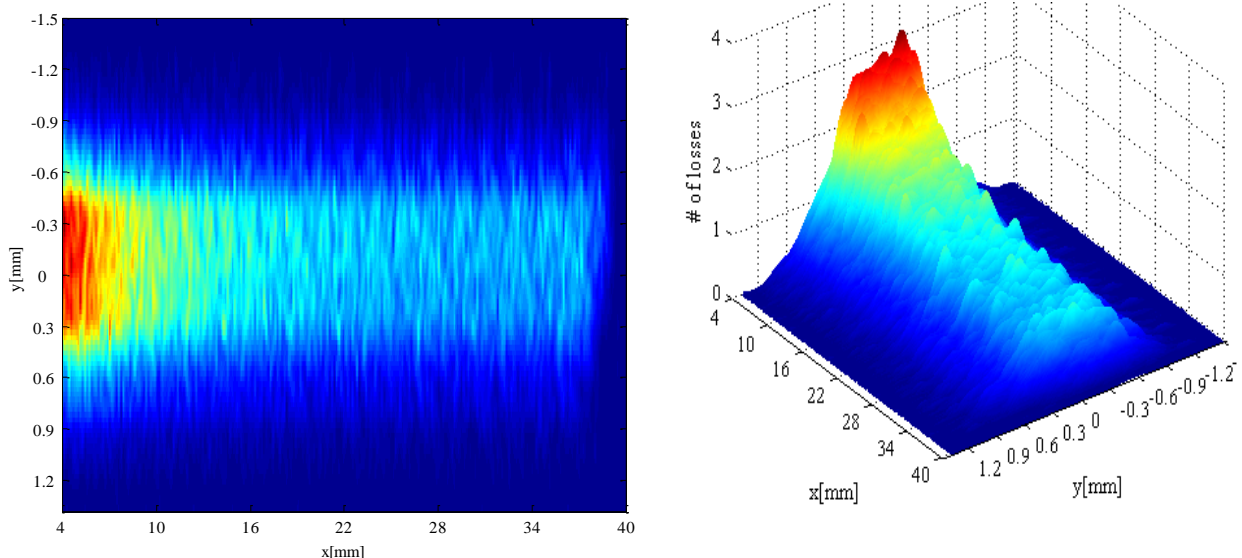


Figure 6.18: Particle density in p^+ / mm^2 for a beam sweep over the TCDQ front surface, 7 TeV.

Figure 6.19 shows the MKD kick-waveform and its first derivative in time. The TCDQ and TCDS apertures are marked with green and magenta lines. One can see that when the beam approaches the inner TCDQ edge (475 ns) the rate of change of the kick is still increasing until it reaches its peak

value when the beam gets intercepted by the TCDS in front and thus the losses at the TCDQ suddenly stop after $1.18\mu\text{s}$. This explains why a higher loss density is seen at the inner TCDQ edge. Also the following drop in sweep velocity is coherent with the increasing loss density at the extraction channel side of the TCDS block. 475 ns of beam (19 bunches) is deflected with low kick-angles but can still bypass the TCDQ and is therefore swept into the machine.

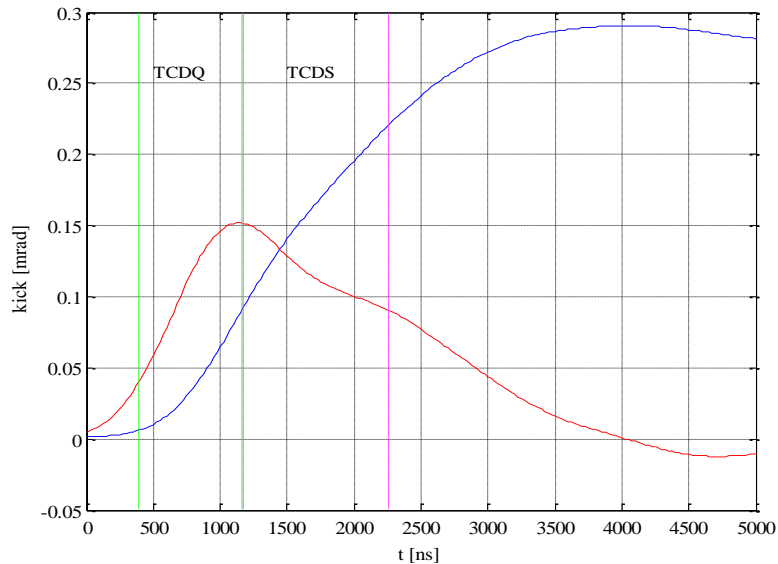


Figure 6.19: MKD kick waveform (blue) and its first deviation (red) with marked point in time when sweeping over the TCDQ (green) and TCDS (magenta) apertures.

Table 6.4 is a summary of the extraction sequence and shows durations and intensities for an asynchronous dump process sorted by time.

Table 6.4: Sweep parameters for asynchronous dumps under nominal conditions, MAD-X simulation.

Time	Duration	Intensity	Comments
0 - 475 ns	475 ns	19 bunches; 2.2×10^{12}	Beam swept over machine aperture
475 – 1185 ns	710 ns	28 bunches; 3.2×10^{12}	Beam swept over TCDQ
1185 – 2250 ns	1065 ns	43 bunches; 4.9×10^{12}	Beam swept over TCDS
2.3-90.5 μs	88.2 μs	Rest of beam	Beam extracted

For both the asynchronous and pre-fire cases, with all other systems and parameters within tolerance, no losses were seen anywhere in the LHC ring except for the collimators. Figure 6.20 shows a typical loss distribution along the LHC for a pre-fire case at 7 TeV, with losses only at the TCDQ and in the collimation insertion in IR7. Figure 6.21 shows a zoom of the collimation region in IR7, with the loss locations labelled. In these cases with the TCDQ at its nominal position the beam load on the robust graphite primary and secondary collimators remains within the specified level for this accident scenario [99].

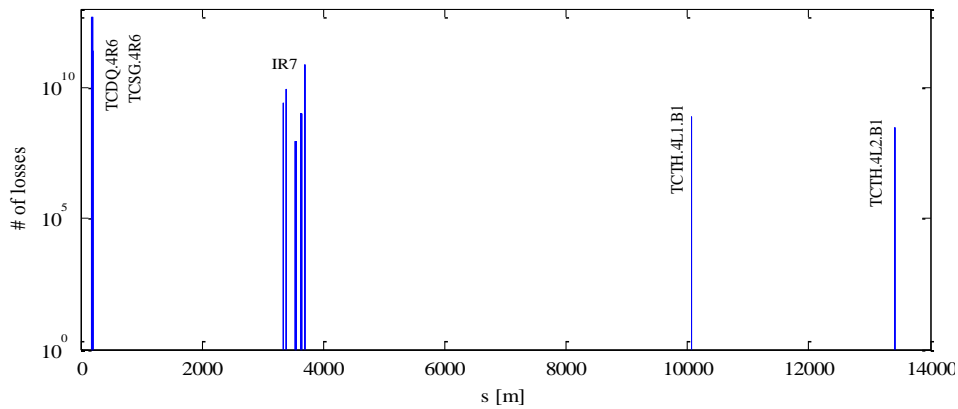


Figure 6.20: Losses around the LHC for the 7 TeV prefire case, average over 10 orbit seeds.

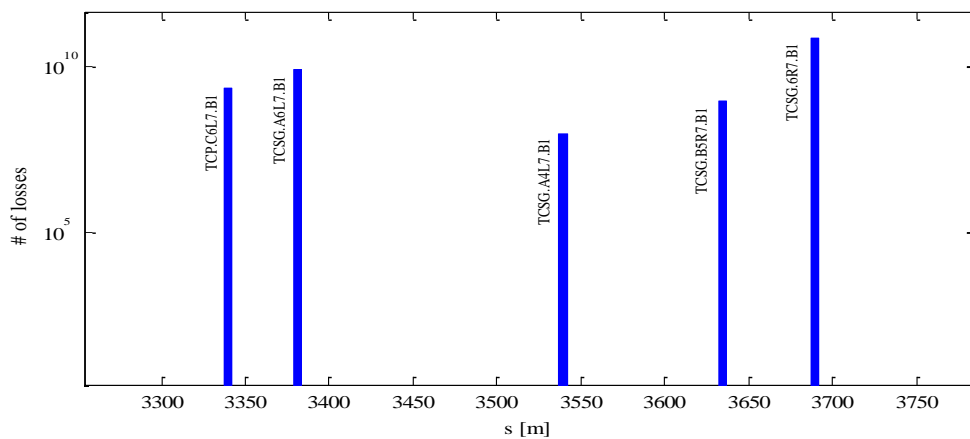


Figure 6.21: Losses in IR7 for the 7 TeV prefire case, average over 10 orbit seeds.

6.4.3 Missing MKD kickers

6.4.3.1 One missing MKD kicker at 450 GeV

The dump system is designed to work correctly with one missing MKD. Simulations were performed to check the beam losses in this case, using the worst-case 450 GeV beam energy. Figure 6.22 shows the sweep at the TCDS entrance for the case of one missing MKD at 450 GeV. The two boxes indicate the TCDS graphite interception devices. The sweep starts from the origin and moves to the outer side of the LHC ring which is into positive x direction in the MAD-X simulation. Particles displayed in red are within the abort gap, while particles in blue are those which should be normally extracted; in the case of a synchronized beam abort with an empty abort gap almost no particles would hit any aperture along TD68; only a very few losses are seen on the inner TCDS block. Figure 6.23 illustrates the losses along TD68, showing that no beam is lost at locations other than the TCDS and TDE.

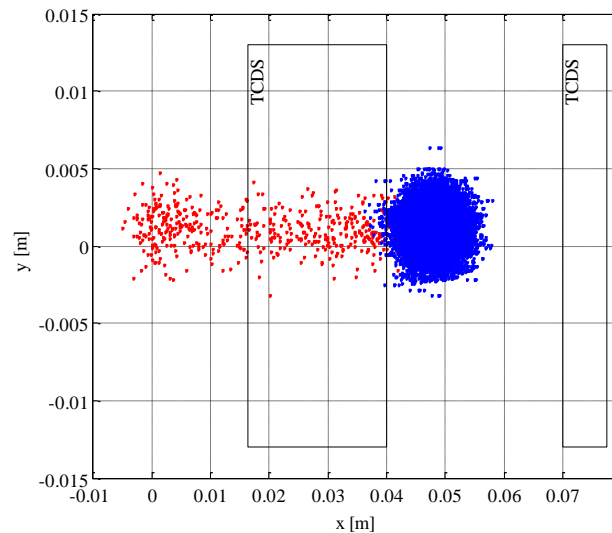


Figure 6.22: Beam sweep over the TCDS Aperture with 14 MKD at 450 GeV. Particles within the abort gap are indicated in red.

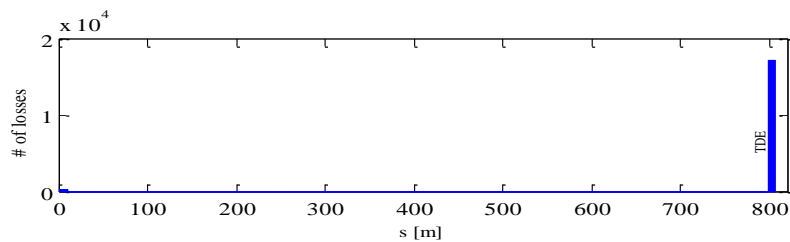


Figure 6.23: Losses of simulation macro particles along the extraction channel TD68 for an asynchronous dump with 14 MKD at 450 GeV.

6.4.3.2 Several missing MKD kickers at 7 TeV

The case of several missing MKD kickers is of interest to determine what operational margin exists in the system and also to quantify the beam loading in the case of a failure which leads to beam impact. Figure 6.24 shows the sweep at the TCDS entrance for the case of two missing MKD at 7 TeV, with nominal transverse emittance. In the case of a synchronized beam abort no particles would hit the TCDS or any aperture along TD68, although some extracted particles approach within about 1 mm of the TCDS. Compared to the nominal dump case no additional loss locations were seen. There is still some small margin between the beam and the MSD aperture to be found for the 7 TeV 13 MKD case in Figure 6.24, whilst this was observed for 450 GeV already for only one missing MKD (Figure 6.22). This difference can be explained because of the beam emittance decreasing with rising energy due to adiabatic damping, and thus the 7 TeV beam is much smaller.

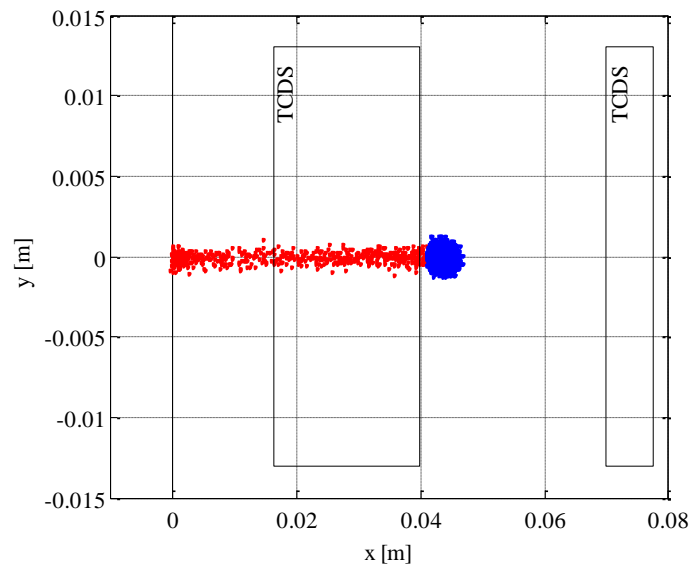


Figure 6.24: Beam sweep over the TCDS Aperture with 13 MKD at 7 TeV. Particles within the abort gap are indicated in red.

Figure 6.25 shows a longitudinal overlay plot of losses along TD68. One can clearly see the effect of two missing kickers with the beam pattern on the dump further to the right.

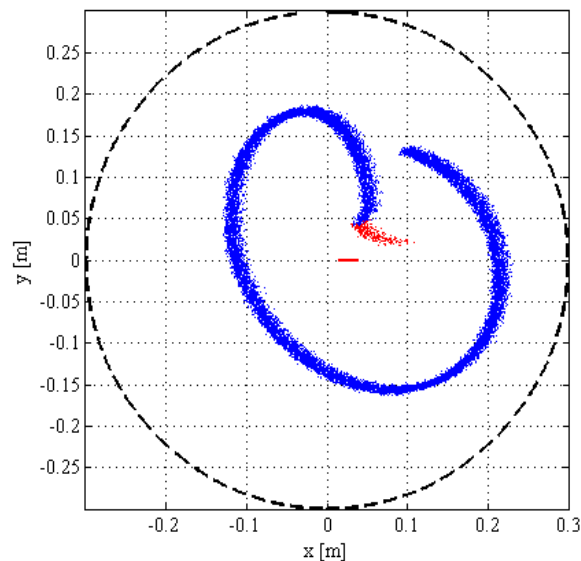


Figure 6.25: Overlay of particle loss coordinates in TD68 for an extraction with 13 MKD only, E-shape is on the TDE, the small line in the centre indicates particles lost whilst the sweep over the TCDS blocks (for asynchronous cases only).

Figure 6.26 shows the 7 TeV sweep with three missing MKD magnets. The extracted beam now impacts the inner TCDS aperture with parts of it intercepted by the TCDS graphite. The number of protons lost on the TCDS depends strongly on the actual orbit seed. Figure 6.27 shows the density map of an worst case impact on the front face of the TCDS, with the peak at 2.5×10^{14} p+/mm² which is a factor of 50 higher than the design load for the TCDS [88]. The TCDS would almost certainly be destroyed in such an incident, and possibly some of the downstream MSD magnets damaged.

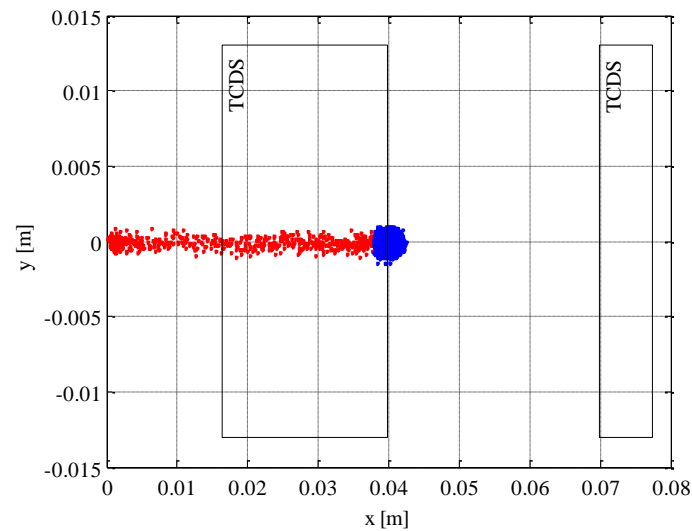


Figure 6.26: Beam sweep over the TCDS Aperture for 12 MKD. Particles within the abort gap are indicated in red, 10 orbit seeds, 7 TeV.

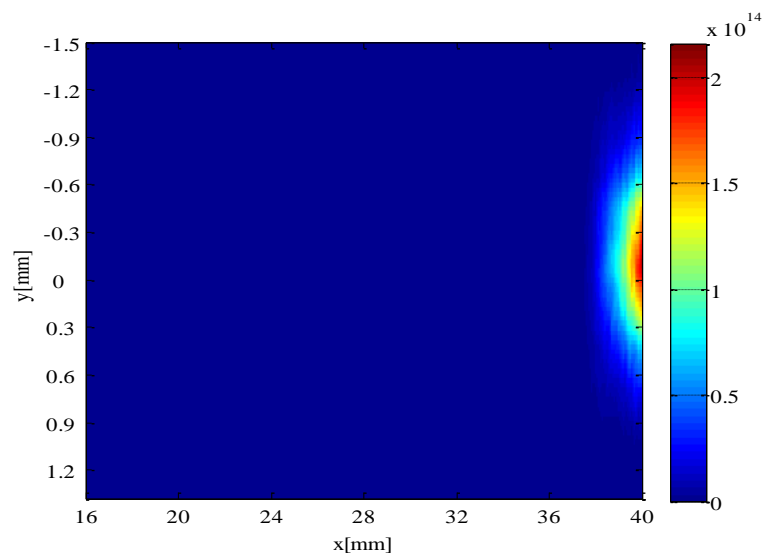


Figure 6.27: Density map in p^+ / mm^2 of the TCDS front face during 7 TeV beam impact for 12 MKD only.

Figure 6.28 shows the intercepted beam parts missing parts of the e-shape as well as the dump pattern moved to the very edge of the TDE block. Nevertheless, no losses were seen on the other possible limits in TD68, in particular the dilution kickers MKB. The pattern shown in Figure 6.28 is for the orbit seed with the smallest beam loss on the TCDS. Note that the losses occur exactly during the “undershoot” of the MKD waveform.

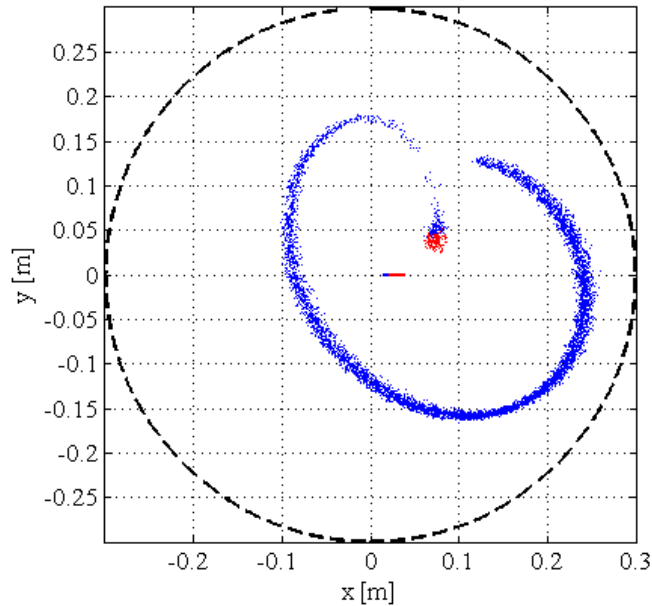


Figure 6.28: Overlay of particle loss coordinates in TD68 for an extraction with 12 MKD only, E-shape is on the TDE, the small line in the centre indicates particles losses whilst the sweep over the TCDS blocks.

6.4.4 Retriggering failure (one MKD-kicker only)

A failure scenario with one MKD kicker only deflecting the beam is very unlikely, and was considered extremely unlikely by the reliability analysis [89]. However, during system commissioning in 2009, broken resistors in the retrigger system were found in two of the 15 MKD waveform generators for beam 1 [90]. This component failure meant that after a flashover (and magnet kick) the retrigger system would not have worked properly. A tracking simulation with one kicker only was performed and results are shown in Figure 6.29. This simulation showed that the deflection of one MKD is sufficient to kick the beam onto the TCDQ - however it is insufficient to reach the TCDS aperture nor to extract the beam at all. Most of the beam is kicked on the TCDQ at a horizontal position of 11 mm. Beam starts to hit the TCDQ block (for $8\sigma / 4.464\text{ mm}$) around $1\ \mu\text{s}$ after the trigger with a variation of $\pm 150\ \text{ns}$ depending on the actual beam orbit. This is to be compared to the values given in Table 6.4 (470 ns for nominal conditions). Since only one kicker is operating, the time needed to reach the TCDQ for this case is longer than for all other cases. First losses at the TCDQ were seen at $0.9\ \mu\text{s}$ (for 8σ) which is twice the time needed for a nominal asynchronous case. As a result nearly 50 bunches or 5.8×10^{12} particles can pass into the LHC. This figure increases up to 1×10^{13} for a 15σ TCDQ setting. In this case around 5.8×10^{12} of the swept particles with very low angle are not intercepted by the LHC collimation and thus appear again at the MKD where they get a 2nd kick and are finally intercepted at the TCDQ.

With the nominal TCDQ setting (8σ) the losses are concentrated on the TCSG.6R7 in IR7, which received about 0.8×10^{12} particles, which is nearly 3 times the beam lost for an asynchronous dump. Already at 8.5σ the TCTH.4.L2 (brown area) sees 1.39×10^{10} particles which rise to 3.3×10^{11} for 11σ . From this TCDQ setting on the TCSG.D4L7.B1 collimator starts to see significant losses (up to 1.7×10^{12}).

The huge particle density seen on the TCDQ will result in the destruction of the device. In this event, extensive damage to the LHC machine will result. Firstly, the TCDQ will be destroyed, with the possibility of collateral damage to the elements immediately downstream, in particular the superconducting Q4 quadrupole which will see a huge vacuum pressure rise and possible contamination. Secondly, recent studies [91] have shown that it is likely that the TCDQ damage will occur on timescales short enough to allow matter transport during the beam passage, such that the TCDQ graphite is removed from the impact zone and the later part of the beam will encounter no obstacle.

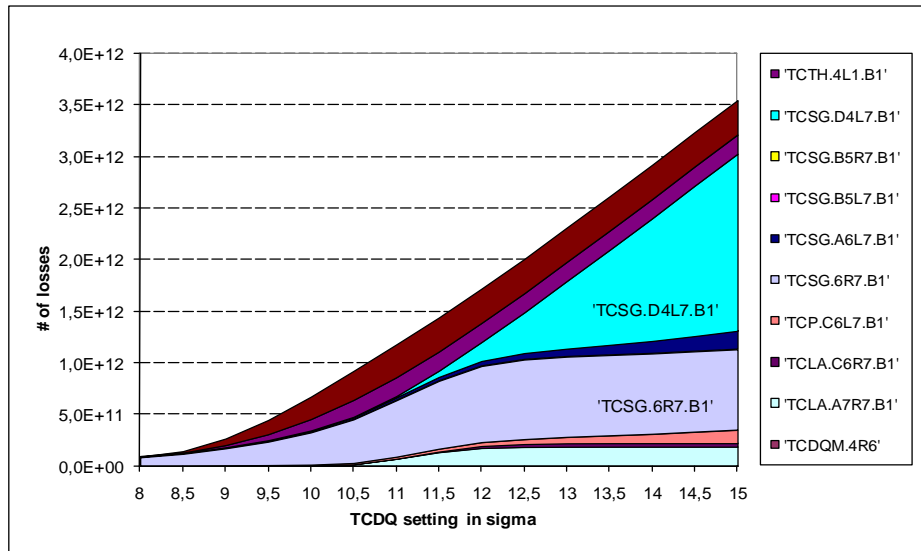


Figure 6.29: Losses in the LHC ring for a 7 TeV sweep with one MKD only, 10 orbit seeds.

All this could result in very large proton densities on elements far downstream, with attendant destruction and collateral damage, and if this penetration is repeated for the TCTs, possibly on the triplet apertures. Detailed studies of the consequences would be interesting but require coupled energy deposition calculations, hydrodynamic calculations and tracking, and are far beyond the scope of this thesis. It is fair to conclude, however, that the LHC down time would be very long, of the order of one year.

Even with the TCDQ remaining opaque to the impacting beam the LHC collimation system sees significant beam load, especially on the TCTH in point one and two. Those are shown in Figure 6.30 together with the TCLA in IR7. For the TCTs the 7 TeV damage level (1×10^{10}) is already reached at 8.5σ TCDQ settings. This indicates that tolerance for the TCDQ position with respect to the beam should be 0.5σ .

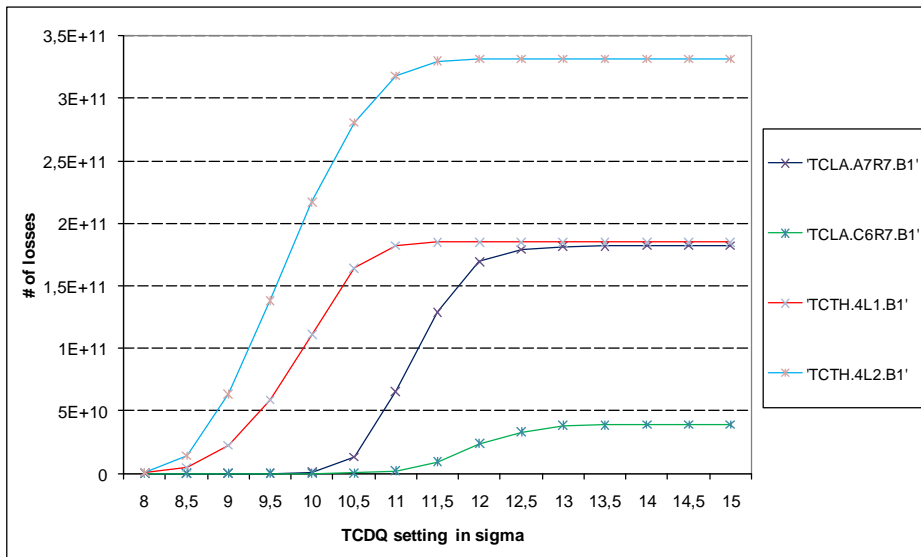


Figure 6.30: Losses for the TCTH and TCLA collimators for the 1 MKD case, 7 TeV, 10 orbit seeds.

6.4.5 Q4 or MSD strength error

The Q4 strengths was varied separately in simulations between 45% and 145% of the nominal value, for 450 GeV energy where the beam size is largest. Beam losses on the TCDS/MSD are plotted in Figure 6.31 as a function of the Q4 strength. Losses begin to occur at an error of about minus 6% and

plus 25% which is to be compared with the 3 ppm (half hour) stability and accuracy of the Q4 powering [92,93] and the $\pm 0.5\%$ interlocking of the Q4 field with the LBDS BETS system. Losses were seen on the differential pumping element VDDA and the MSD septa, but no losses on the dilution kickers MKB.

Concerning the MSD, the strength was varied between 80% and 120%. The losses on the MSD chambers, the MKBH kickers and on the VDDA pumping devices are plotted in Figure 6.33 as a function of the MSD strength. Losses begin to occur at an error of about $\pm 5\%$, with the losses on the differential pumping element VDDA and the dilution kickers MKBH. Again, these limits are to be compared with the stability and accuracy of the MSD powering (1%, [94]) and the 5×10^{-4} interlock limit from the special Fast Magnet Current Change Monitors [95].

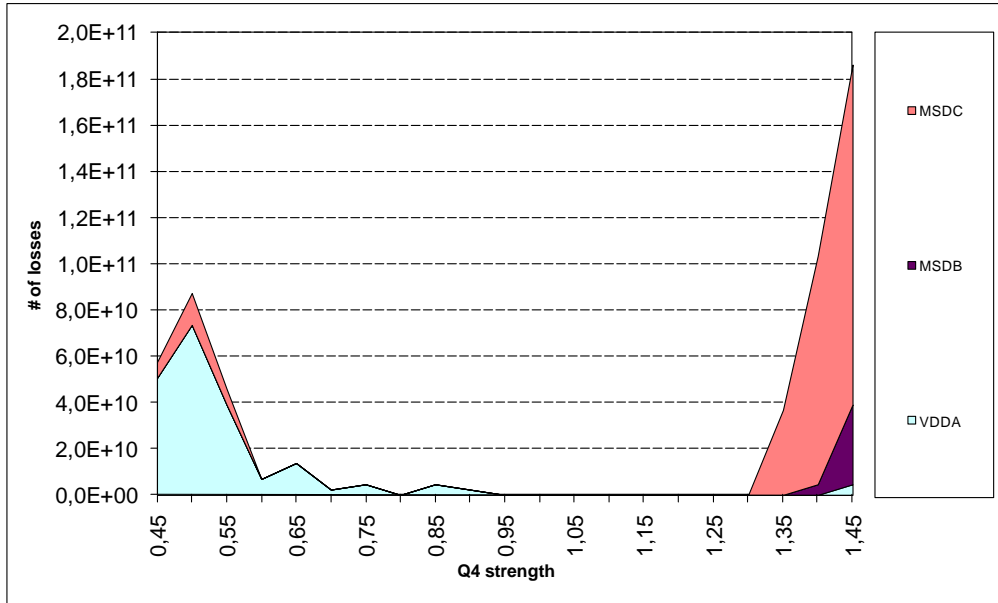


Figure 6.31: Beam losses for scan of Q4 strength for 450 GeV, 10 orbit seeds, 6 μ s.

Note that in Figure 6.31 the TCDS losses are not shown; Figure 6.32 shows losses on the TCDS for the Q4 scan explicitly. For both the Q4 and MSD strength scan just the first 6 μ s of beam have been simulated.

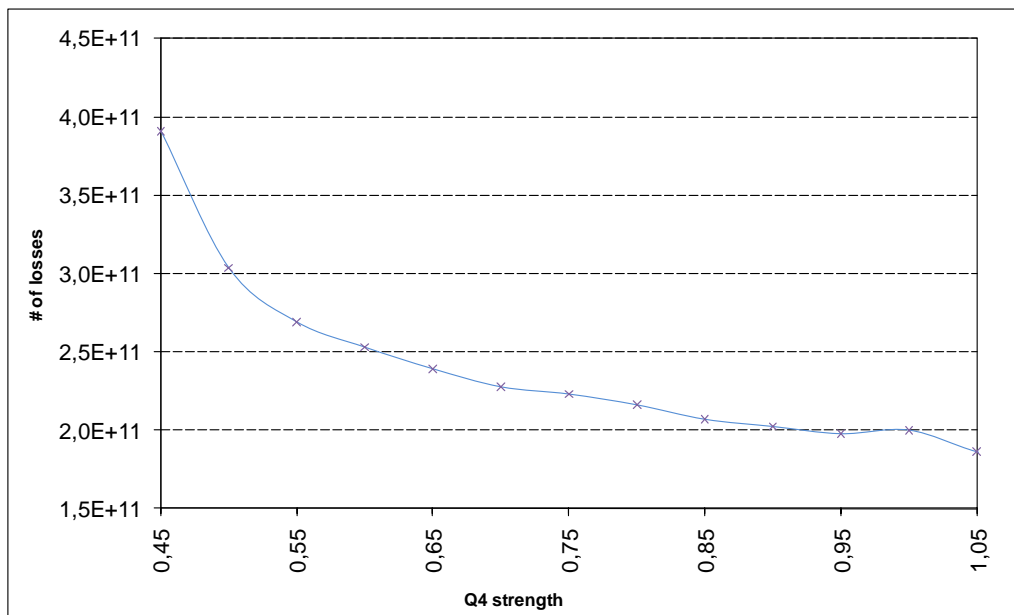


Figure 6.32: Beam losses on the TCDSA for scan of Q4 strength, 450 GeV, 10 orbit seeds, 6 μ s.

Figure 6.32 shows the losses on the TCDSA; a significant increase in losses can be seen at 40% less Q4 kick strength.

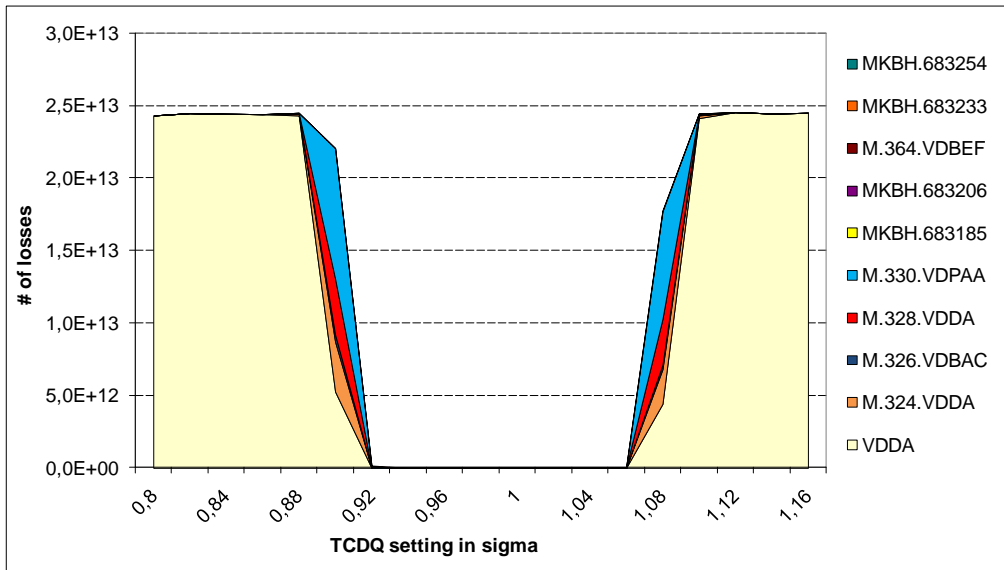


Figure 6.33: Beam losses for scan of MSD strength for 450 GeV.

6.4.6 IR6 orbit error

The orbit in IR6 is required to be stabilised by the orbit feedback to within ± 2.0 mm, and is interlocked via dedicated BPMs to ± 4.0 mm [41]. To investigate the suitability of these limits, the orbit in IR6 was artificially degraded, and then performing the asynchronous dump tracking simulations for each new orbit, with the 450 GeV beam (nominal LHC emittance). The losses on the dump system elements (TCDS, MSD) are plotted in Figure 6.34 as a function of the orbit offset in IR6. First losses appear at around -2.5 mm offset, where the beam starts hitting the outer side of the extraction channel at the MSDB, MSDC and VDDA position, which indicates that the interlock levels implemented might be not tight enough. For an offset into opposite direction the extraction channel is protected by the TCDS which sees some increase of lost particles. Around 3mm first losses on the VDDA are seen which increase only slowly as the offset gets bigger, since most of the beam is intercepted by the TCDS.

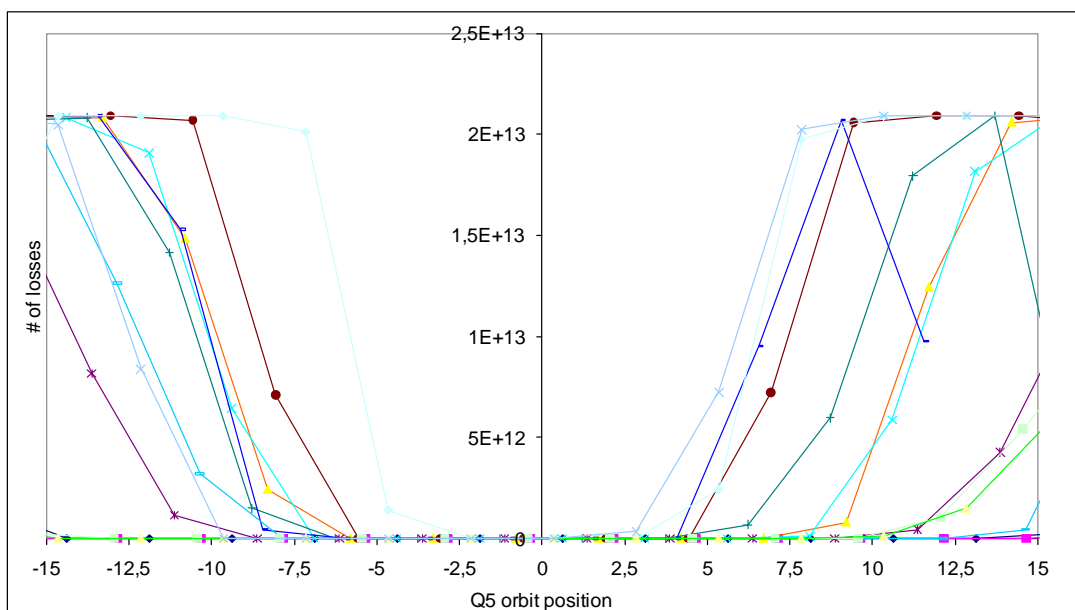


Figure 6.34: Losses along TD68 for asynchronous dumps as function of the orbit offset at the entrance of MQY.5L6, 450 GeV, each colour represents one orbit seed.

6.4.7 TCDQ positioning error

The position of the TCDQ with respect to the LHC beam is known to be a critical issue for the safety of the machine. The positioning tolerance and consequences of a positioning error during an asynchronous abort were studied by scanning the TCDQ/TCSG positions, retracting them together from the nominal position. This is a rather pessimistic scenario, since both devices are independently controlled, but one which could conceivably arise through a combination of errors or wrong settings in the high level control software. Both 450 GeV and 7 TeV were studied. All cases were investigated for both the pre-fire and the asynchronous dump cases.

6.4.7.1 450 GeV cases

The TCDQ position was retracted from 8.0 to 15.0 nominal σ , in steps of 0.5 σ . The losses around the LHC ring were recorded. Figure 6.35 shows the results of such a scan, averaged over 20 orbits, for the pre-fire case. The loss locations were on collimators, mainly primary and secondary in IR7, but also the adjustable TCLA masks in IR7. These are particularly interesting since the jaws are made from tungsten [96] and therefore have much lower damage thresholds than the carbon primary and secondary collimators.

In addition, a small beam loss (nine macroparticles) was seen on the TDI in IR8, which is a beam 2 injection protection device very close to the circulating beam. The loss on this element is independent of the TCDQ setting, Figure 1.40, which indicates that this could be an artefact of the simulation. The lost particles all have X coordinates of about -4.1 mm. Checks showed that in this simulation the TDI aperture plane was set to horizontal by mistake, and since the jaws are close to the beam (6.8σ) some beam was intercepted. In reality the horizontal aperture at this element is about 23 mm, so no losses should occur.

It is interesting to note that, beyond a retraction of 11 σ , the TCDQM starts intercepting the beam.

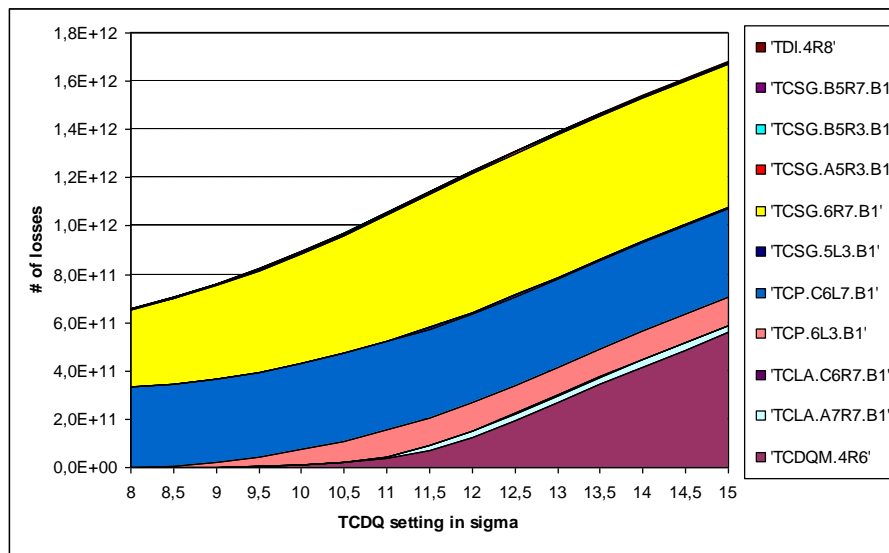


Figure 6.35: 450 GeV prefire case, LHC machine model with all errors, 20 orbit seeds,.

There were no losses in the arc downstream of the TCDQ, for any retraction. This is illustrated in Figure 6.36, which shows the losses between IR6 and IR7 for the maximum TCDQ retraction of 15 σ . This initially surprising result is explained by the small aperture of the TCDQM, which acts as a fixed mask and shadows the LHC arc even if the TCDQ is fully retracted.

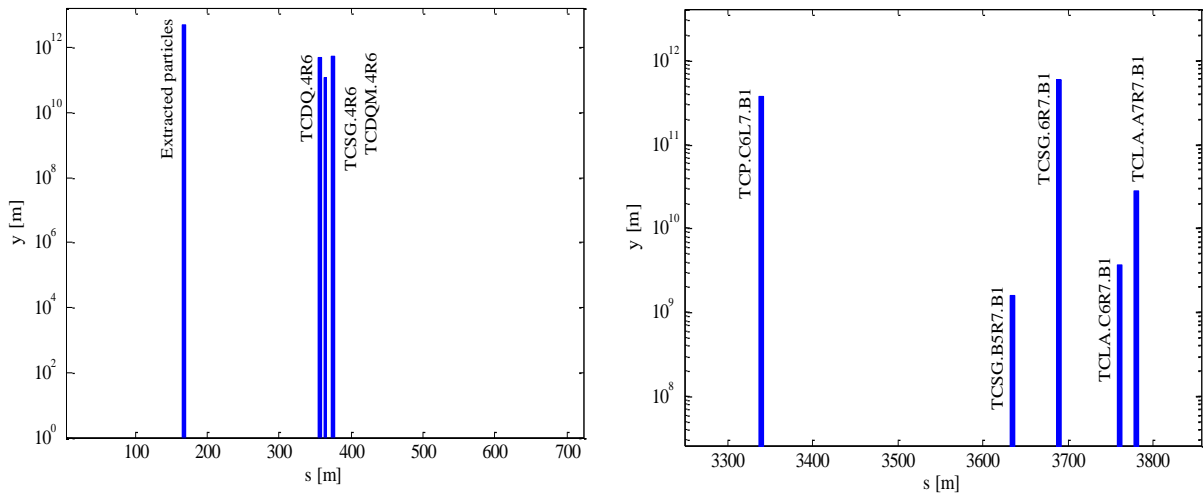


Figure 6.36: Losses in IR6 (left) and IR7 for the 450 GeV prefire case with all errors, 20 orbit seeds.

For the elements of most interest, the TDI, the two TCLAs and the TCDQM, the losses as a function of retraction are shown in Figure 6.37-Figure 6.40.

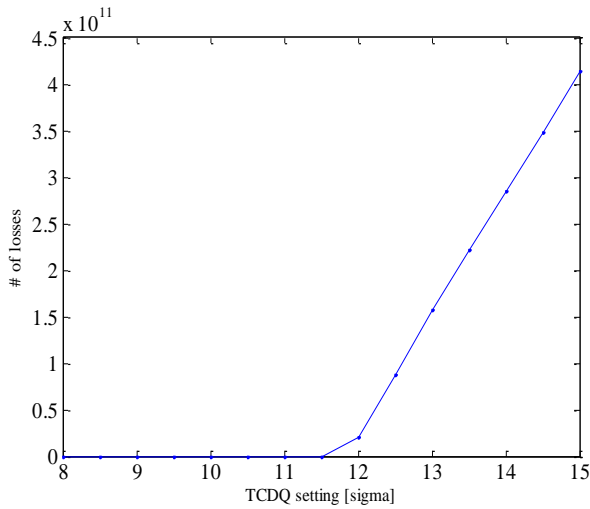


Figure 6.37: Losses on TCDQM for clean machine model.

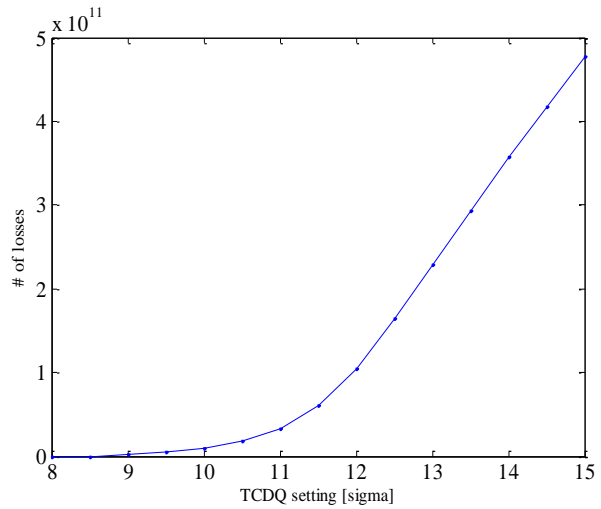


Figure 6.38: Losses on TCDQM for real machine model.

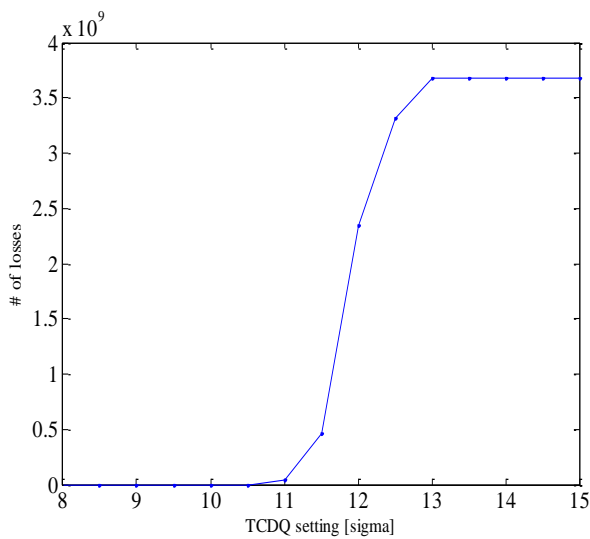


Figure 6.39: Losses on TCL.A.C6R7 for the 450 GeV prefire case with all errors.

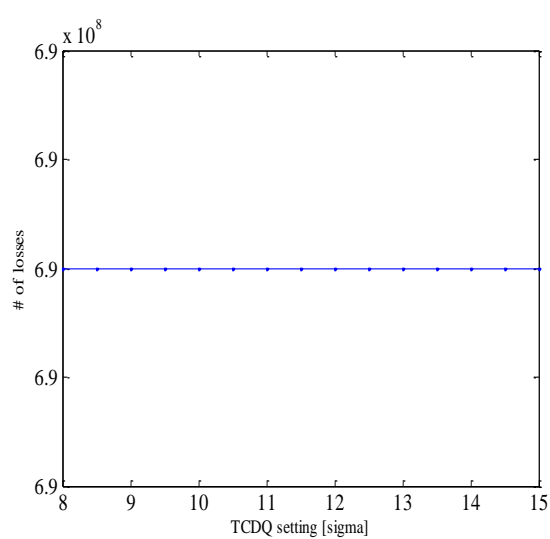


Figure 6.40: Losses on TDI.4R8 for the 450 GeV prefire case with all errors.

The case with asynchronous dumps rather than pre-trigger is shown in Figure 6.42. There are lower overall losses, in particular for small TCDQ retractions, where only about 1.6×10^{11} p+ are lost on the TCSG.6R7.B1, compared to almost 7×10^{11} p+ lost on the collimators TCP.6L7.B1 and TCSG.6R7.B1 for the pre-fire case. Again this difference is expected, since the pre-fire case results in a shallow slope of the overall kicker waveform at low amplitudes.

Figure 6.41 shows how the loss levels change for the two cases, at two particular IR7 collimators (TCSG.6R7 and TCLA.A7R7).

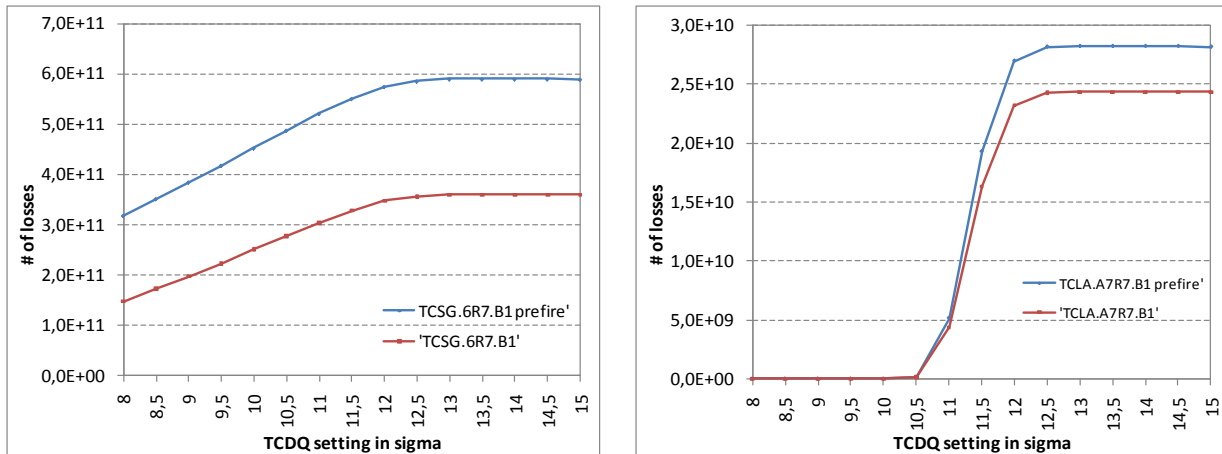


Figure 6.41: Comparison of losses on TCSG.6R7 (left) and TCLA.A7R7 (right) for the normal and prefire case at 450 GeV.

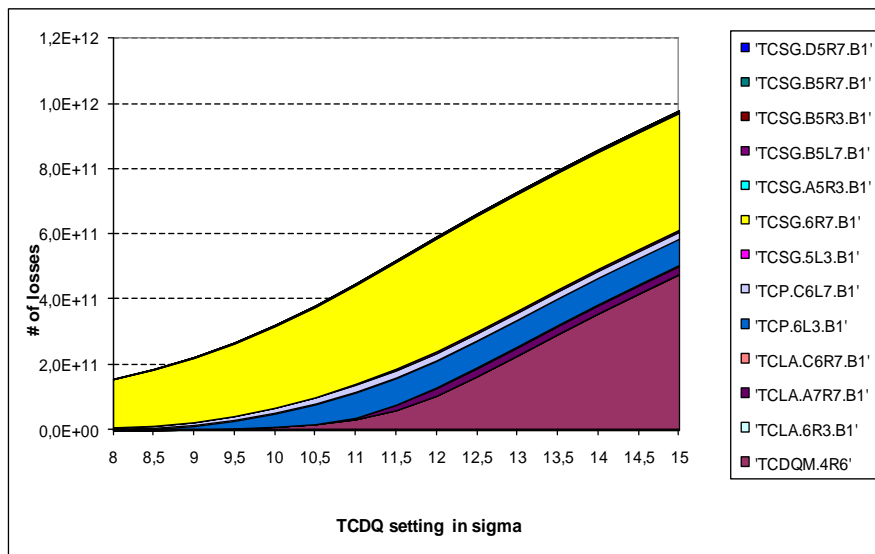


Figure 6.42: 450 GeV asynchronous dump case for LHC machine with errors, 20 orbit seeds.

The effect of the machine imperfections was studied by repeating the simulations with an ideal machine (without orbit, optics and alignment errors). The results are shown in Figure 6.43 and Figure 6.44 – it can be seen that the absence of machine imperfections significantly changes the results, with a very different loss pattern to Figure 6.35 and Figure 6.42. This was rather unexpected for these scenarios, since the collimators are adjusted around the beam orbit and to the perturbed beam size. However, the explanation is that the optics perturbations change the phase advance conditions between IR6 and IR7, and therefore the betatron amplitudes are significantly different in the two cases, resulting in losses for even the nominal TCDQ position of 8σ as would be expected from simple considerations. This result highlights the importance of including all imperfections and

corrections into the model of the LHC. Although this increases greatly the complexity of the simulation preparation, without it the results are not representative.

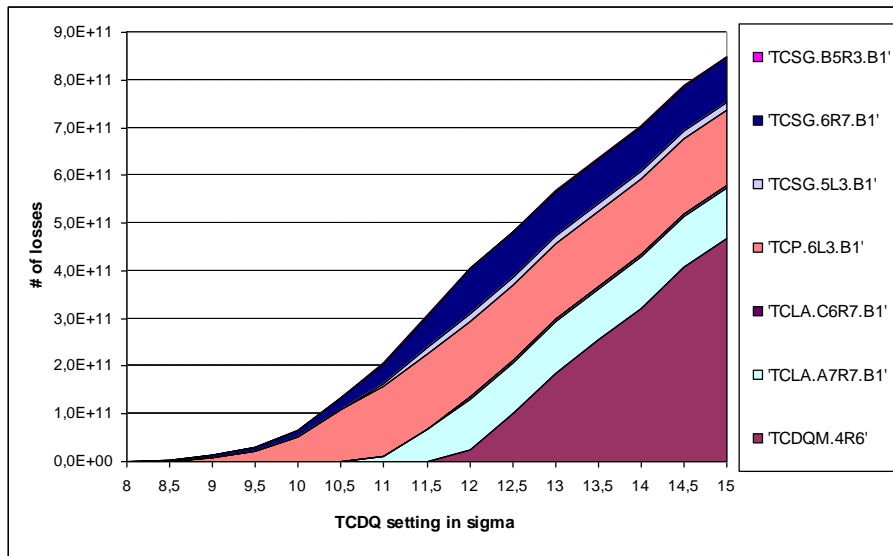


Figure 6.43: 450 GeV prefire dump case for LHC machine without errors, 20 orbit seeds.

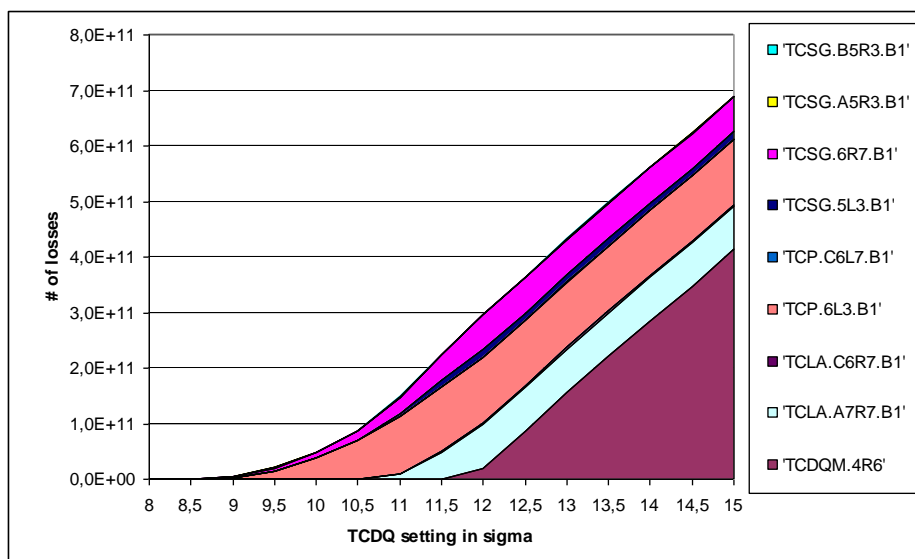


Figure 6.44: 450 GeV asynchronous dump case for LHC machine without errors, 20 orbit seeds.

6.4.7.2 7 TeV cases:

For 7 TeV the TCDQ position was retracted from 8.0 to 15.0 nominal σ , in steps of 0.5 σ , using the collision optics with 0.5 m β^* . The losses around the LHC ring were recorded. Figure 1.30 and Figure 1.31 show the results of such scans, averaged over 20 orbits, for the pre-fire case. As for the 450 GeV case, the losses are concentrated on collimators, mainly primary and secondary in IR7, but there are again losses on the TCLAs in IR7, and in this case losses on the tertiary collimators TCTH in IR1 and IR2. Since these are tungsten jaws with low damage thresholds, these locations are of particular interest.

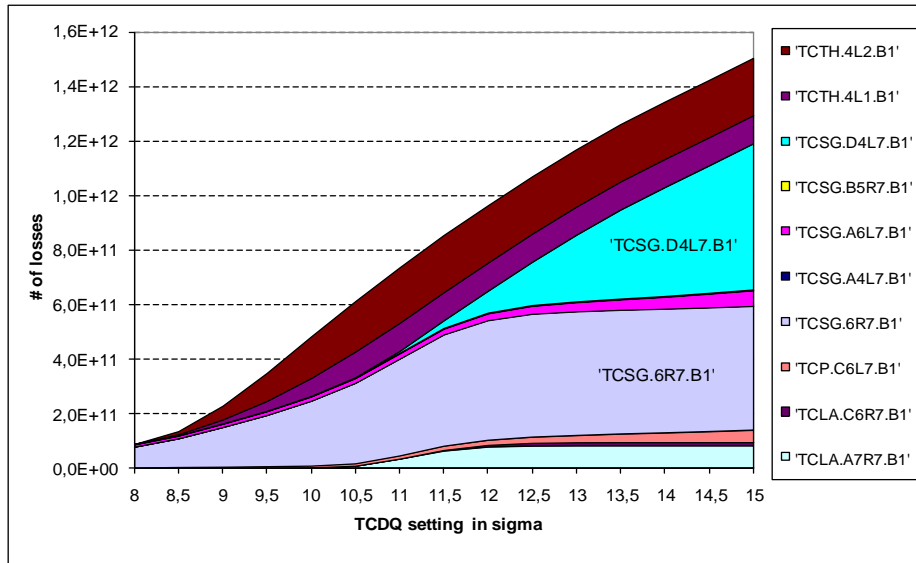


Figure 6.45: 7 TeV prefire dump case with $0.5 \text{ m } \beta^*$ and all LHC errors.

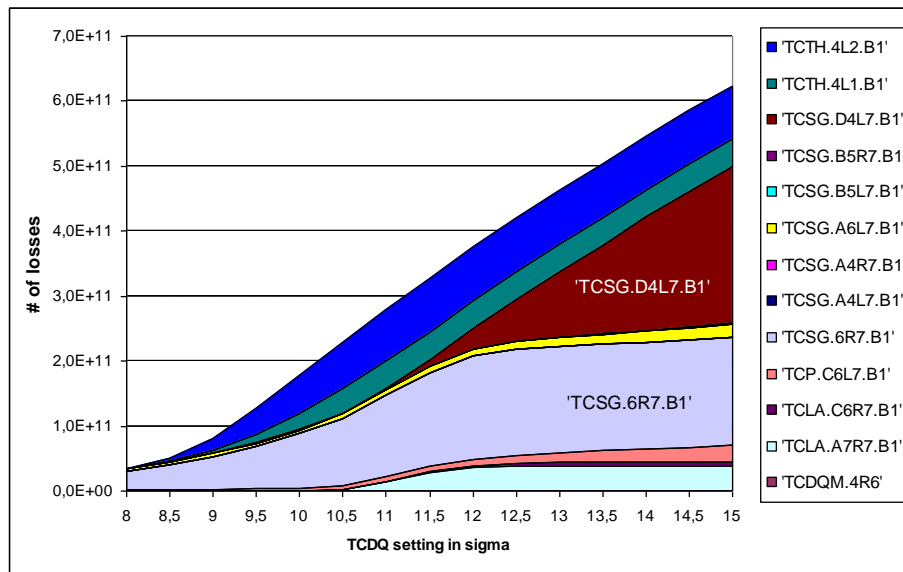


Figure 6.46: 7 TeV asynchronous dump case with $0.5 \text{ m } \beta^*$ and all LHC errors.

The comparison with the machine without errors was also made for the 7 TeV study, Figure 6.47; the differences are less pronounced than for 450 GeV, which may be because the optics perturbations are less at high energy, particularly with regard to the magnet multipoles.

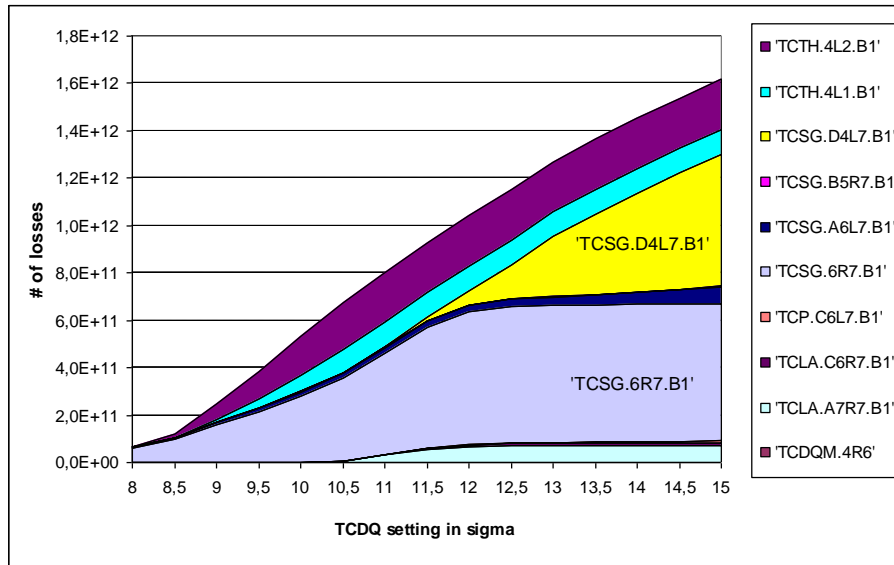


Figure 6.47: 7 TeV prefire dump case with 0.5 m β^* and no LHC errors.

The losses on the TCLA and TCTH collimators are of particular interest – from the average loss curves shown in Figure 6.47, these elements can start intercepting beam already at a TCDQ retraction of 0.5 σ . For some of the seeds the situation is worse. Figure 6.50 shows the same curves over 10 seeds which indicates that there is a risk of beam loss on these collimators for an asynchronous dump, for a very small error of a fraction of a sigma in the TCDQ position, and strongly depending on the actual machine optics. Hence the IR6 orbit interlock is of significant importance.

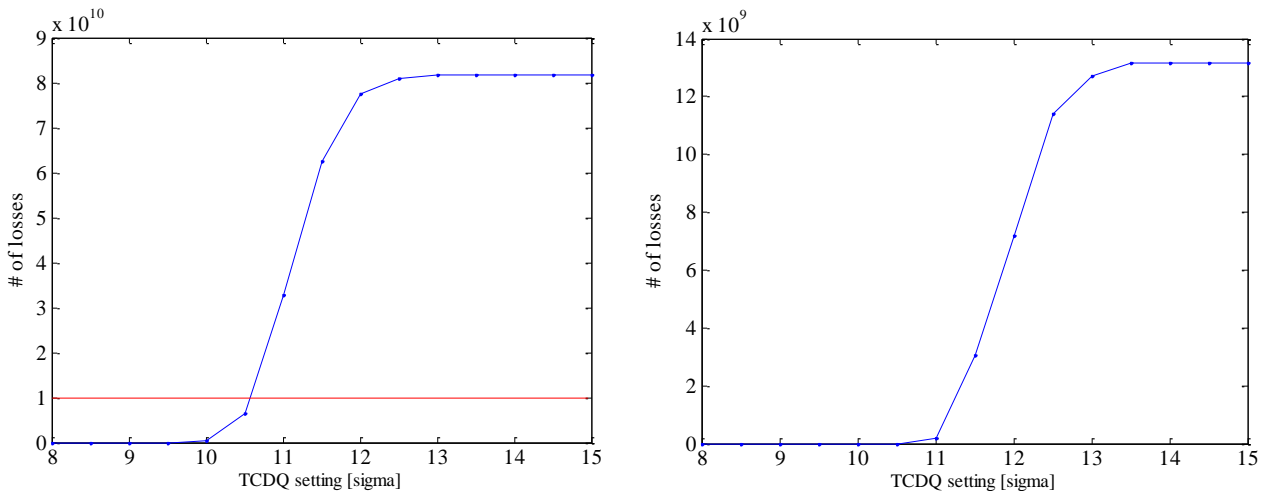


Figure 6.48: Average losses on TCLA.A7R7 (left) and TCLA.C6R7 (right) for the 7 TeV prefire case with all errors. The red line shows the assumed damage limit.

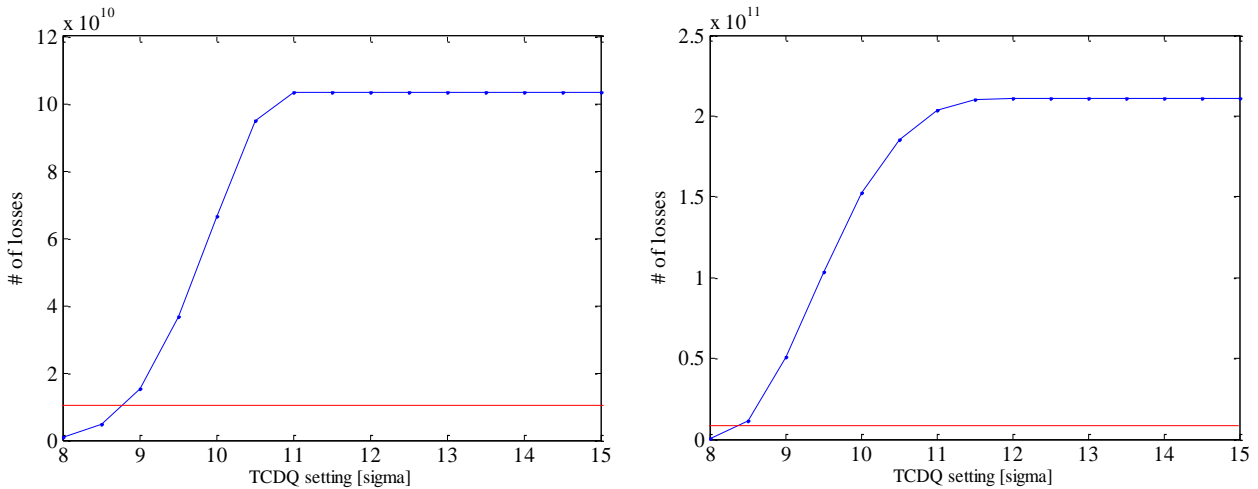


Figure 6.49: Average losses on TCTH.4L1 (left) and TCTH.4L2 (right) for the 7 TeV prefire case with all errors. The red line shows the assumed damage limit.

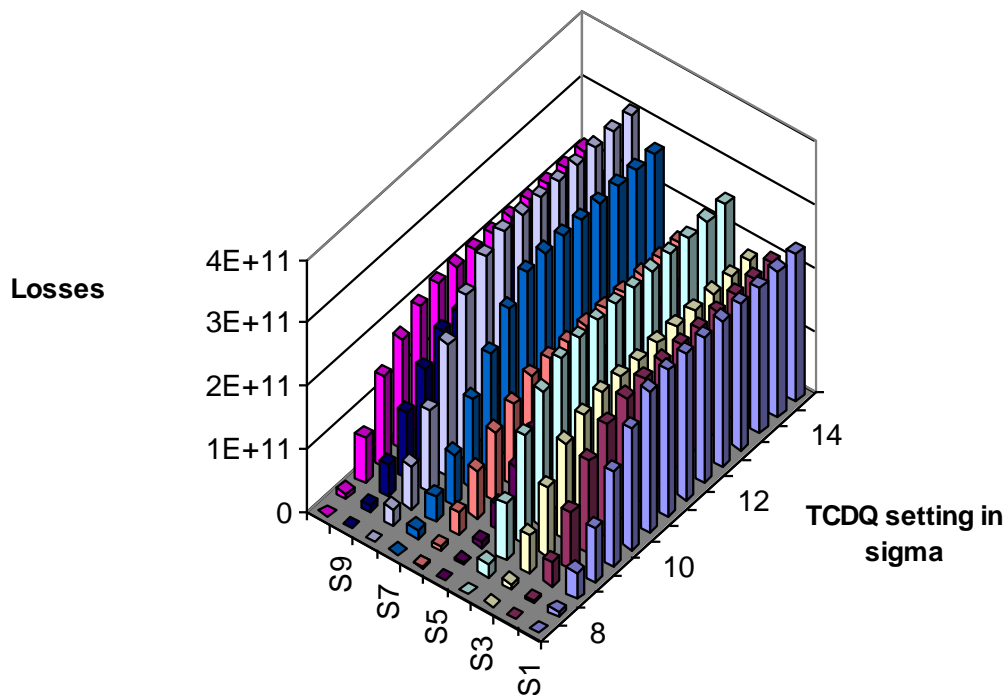


Figure 6.50: Losses on the TCTH.4L2 for 10 seeds; 7 TeV prefire case with all errors and correction applied.

6.4.8 TCDQ positioning error with IR7 collimators retracted

The retraction of the IR7 collimators will allow beam which is not captured by the TCDQ system to perform betatron oscillations around the LHC, potentially intercepting the TCT collimators which protect the triplet apertures in the experimental insertions. A set of simulations was performed with the collimators in IR7 fully retracted – although this is an unlikely failure scenario in itself, it gives some indications of what might be expected with beam 2, which has no collimation system between IR6 and the triplet aperture in IR5.

The average losses observed for the prefire case at 7 TeV with 20 seeds are shown in Figure 6.51. Losses are only seen on the TCTH devices, as now expected, and in fact these are exposed to dangerous levels of beam loss even for the nominal TCDQ position of 8σ , as expected. This illustrates clearly that the TCDQ system must be correctly set up to protect the TCTs from asynchronous beam abort. However, since the collimation system relies on multiple passages to provide full phase coverage, it is feared that machine imperfections and phase errors could lead easily to a situation where the TCTs are not protected by the TCDQ or by the collimators in IR7 or IR3 – in this case the risk of damage seems high, with several 10^{10} p+ deposited in the TCT jaw, even for a correctly positioned TCDQ. For Beam 2, with no other collimators between the TCDQ and the TCTs in IR5, the TCDQ must protect the TCTs. Results show clearly that the collimation system is in fact providing some protection of the Beam 1 TCTs against the asynchronous abort.

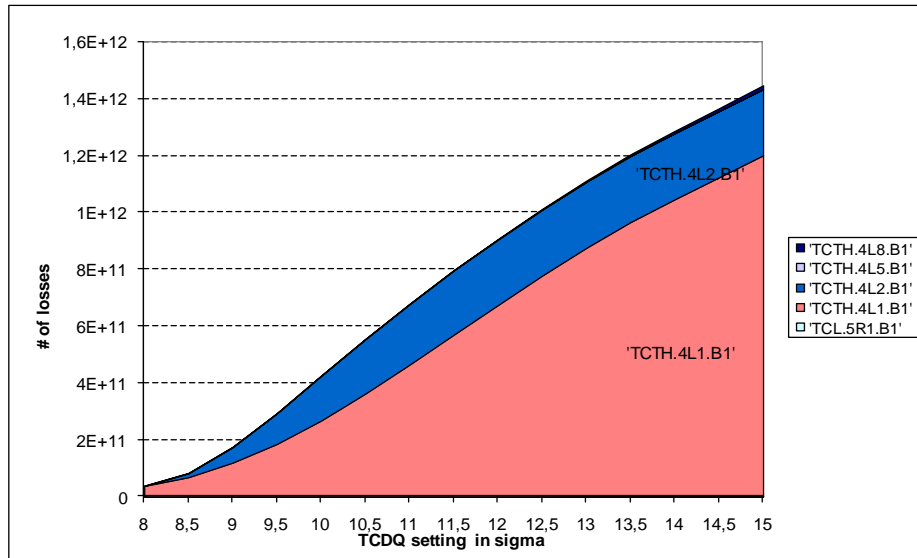


Figure 6.51: 7 TeV prefire dump case, no IR7 collimation, LHC machine model with all errors.

6.4.9 Analysis of particle transmission through the TCDQ system onto the TCT's

Tracking studies showed the unexpected result that during an asynchronous dump the TCDQ system can be bypassed by some particles even for TCDQ positions around 8σ . An explanation for this observation was developed and is illustrated in Figure 6.52. A beam with a finite normalized beam size n receives the MKD kick and is displaced in phase space along the px axis (blue lines). Due to the phase advance between MKD and TCDQ this beam is then rotated by ~ 90 degrees (green lines). The TCDQ limits the horizontal aperture and intercepts all particles exceeding a certain x -position. For an infinite small beam the necessary TCDQ position S would be less than the beam displacement R . However if the beam size is not infinite the minimum distance must be even less as particles with higher and lower initial (x, px) exist and therefore the possible transversal trajectory distance R increases to R_1 (6.6). Particles with an extreme initial x and px combination would therefore not be immediately intercepted by the initially calculated TCDQ setting as the trajectory is not moved close enough.

$$R_1 = \sqrt{S^2 + n^2} \quad (6.6)$$

This effect is even worse if an additional phase advance deviation is considered. The black lines indicate a finite beam size rotated by less than 90 degrees. One can see that due to that additional angle the distance R_2 (6.7) is much longer than the initial distance R and still longer than R_1 .

$$R_2 = \sqrt{S^2 + (S \tan \theta + n)^2} \quad (6.7)$$

Table 6.5: Parameters for the simulated MKD/TCDQ phase advance over 50 seeds at 7 TeV.

<i>Method</i>	$\Delta\psi [^\circ]$
nominal	93.80
Avg.	94.22
Max.	105.40
Min.	81.61
Stdv.	5.42
Max. dev. (pos.)	11.60
Max. dev. (neg.)	12.19

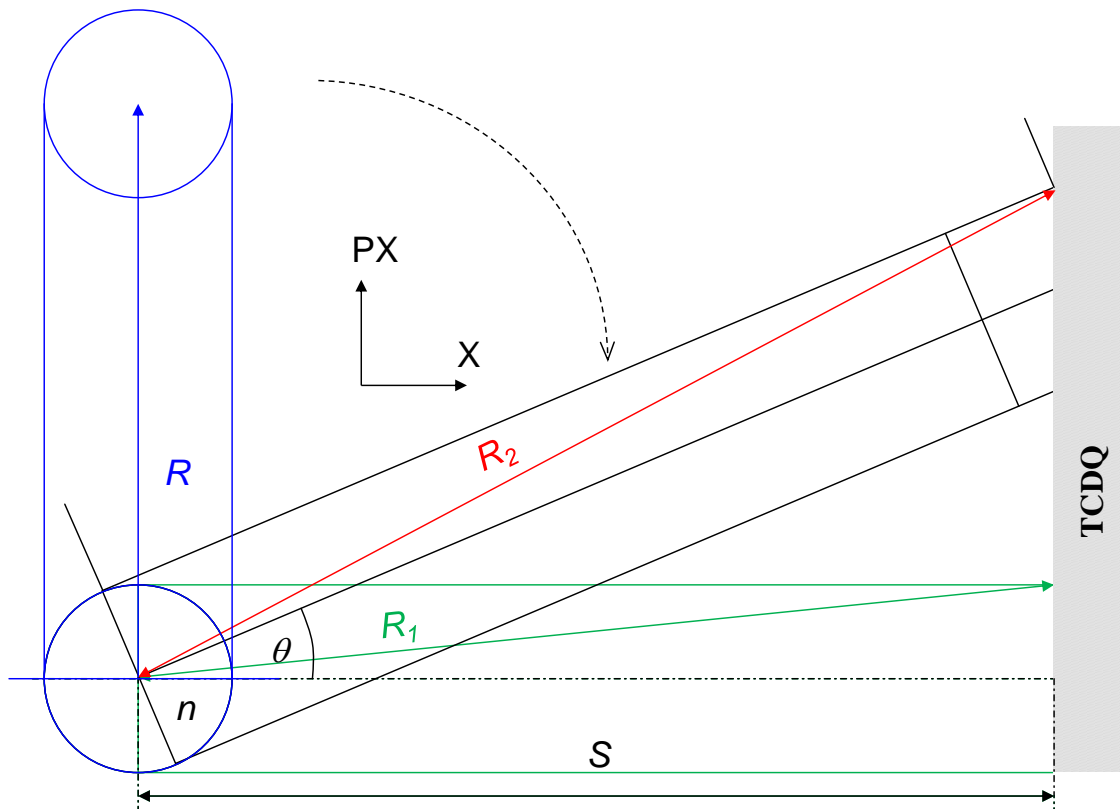


Figure 6.52: Schematic overview of a finite beam (size n) travelling down an idealised line from the MKD to the TCDQ receiving the MKD kick (blue) and being rotated in phase space by the nominal phase advance of 90 degree (green) or a phase advance with a certain deviation (θ) (black).

Figure 6.53 shows the distribution of the phase advance between the MKD and the TCDQ system over 50 orbit seeds, whilst

Table 6.5 shows the analysed parameters. Surprisingly the phase advance deviation is about $\pm 12^\circ$ which is higher than previously anticipated.

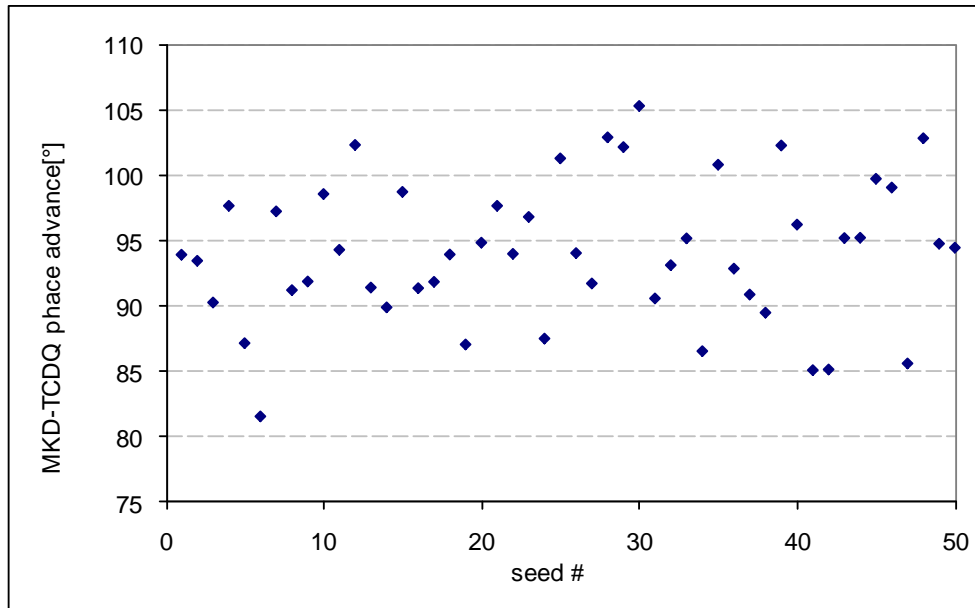


Figure 6.53: MKD to TCDQ phase advance for 50 orbit seeds at 7 TeV.

Figure 6.54 shows the dependency of the maximum transmitted particle amplitude (in equivalent TCDQ sigmas) from the beam size and the phase advance deviation. It can be seen that for particles within a 6σ beam envelope the actual 7.5σ TCDQ setting already behaves like a 9.6σ setting would for zero beam size and considering a phase advance deviation of 8.8 degrees it further increases to an equivalent setting of 10.4σ .

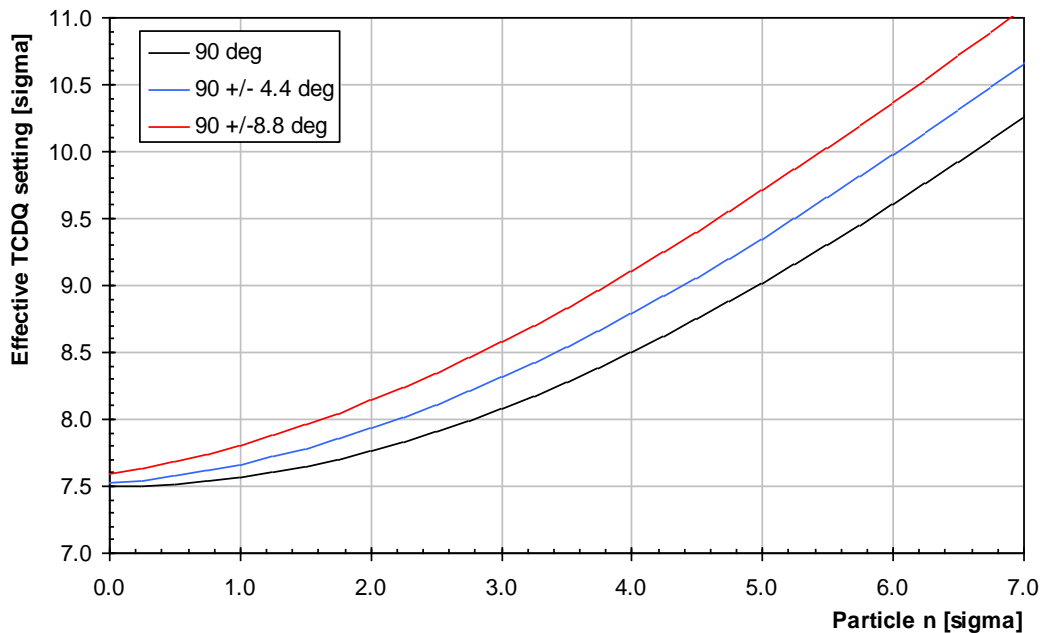


Figure 6.54: Dependency of transmitted particle amplitude (and its equivalent TCDQ setting) from the beam size and phase advance deviation.

Figure 6.55 shows an overview of used transverse beam shapes to simulate different horizontal particle populations. A Gaussian distribution with nominal emittance (black) has been used as well as a parabolic distribution which gives an uniform phase space density. Furthermore a Gaussian beam with nominal emittance and 10% in a parabolic tail (extending to 6σ , red) as well as one with only 1% in the tail (lower magenta curve) and one with doubled emittance and 10% in parabolic tail

(upper magenta curve) were simulated. For the simulations a nominal intensity (1.15×10^{11} p+ /bunch) and a bunch spacing of 25ns have been used. These simulations were done for the 2010 commissioning and early physics run so the maximum energy of 3.5 TeV was chosen. The TCDQ/TCSG system in IR6 was set to 10.2σ with a setting error of 0.8 mm (1σ).

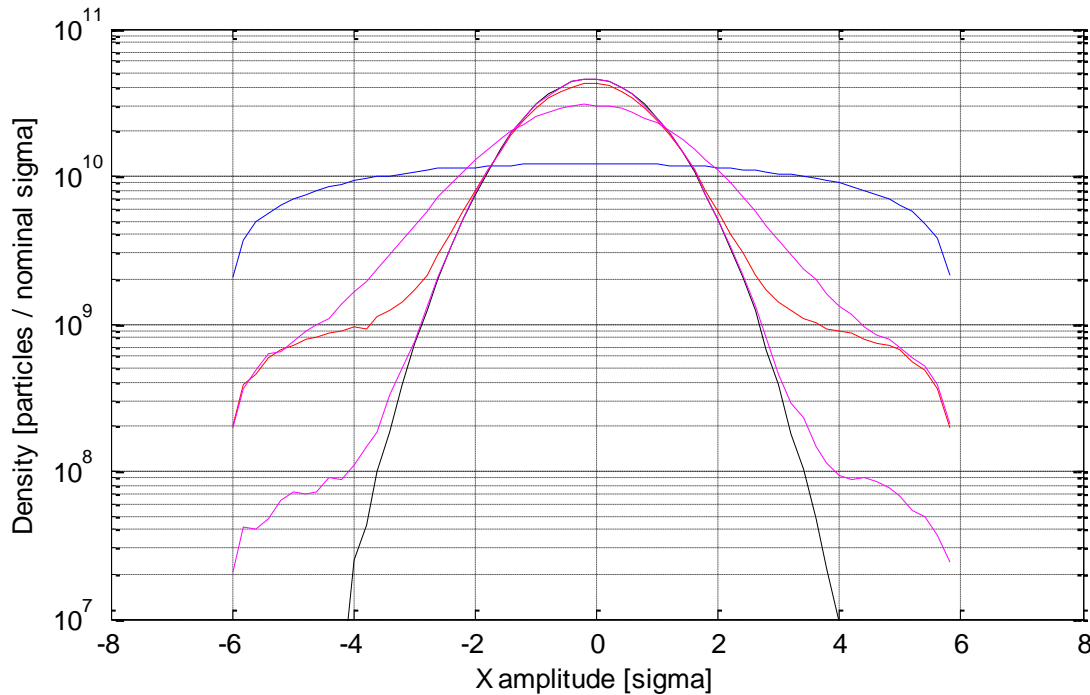


Figure 6.55: Simulated horizontal particle distributions: particle density over horizontal beam size for a Gaussian beam with nominal emittance (black), a parabolic beam (blue), and Gaussian beams with different parabolic tails (magenta, red). [97]

In Figure 6.56 the simulation results for a Gaussian beam shape are given: on the left for a nominal MKD-TCDQ phase advance of 94.6° and on the right for 106.6° . The graph shows the transmission rate as a function of the particles amplitude. The indicated TCT damage level (red horizontal line) was assumed to be 3×10^{11} p+. This figure was scaled down from the 7 TeV assumptions (see Table 6.6). As a worst case the total MKD system kick was assumed to be a prefire case starting with the pretrigger of MKD.O5L6 (kicker with highest β -function) and no collimators in the cleaning insertions have been considered. Figure 6.56 shows clearly that particles with amplitudes above the TCDQ setting (+ tolerance) are transmitted and that the transmission rate rises with the phase advance error between MKD and TCDQ. The TCDQ setting is indicated by the vertical red line.

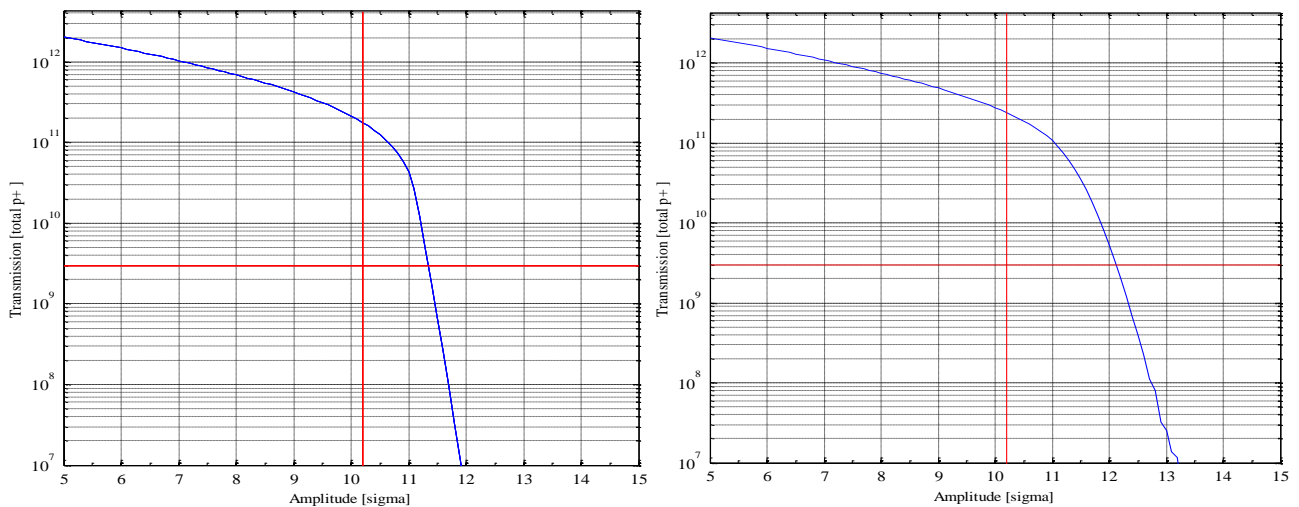


Figure 6.56: Transmission of particles through the TCDQ system for a Gaussian beam shape (nominal emittance) and for a MKD to TCDQ phase advance of 94.6° (left) and 106.6° (right).

Figure 6.57 shows the same simulation setup as it was used for Figure 6.56 but instead of a Gaussian beam shape a parabolic beam was used. The uniform phase space density is interesting, as the transmission figures are easier to compare over the particles amplitude and effects covered by the inhomogeneous Gaussian phase space density could be discovered. However this distribution does not represent the beam and its halo in the LHC machine. One can see that particles are basically transmitted with maximum amplitudes smaller than for the Gaussian beam shape.

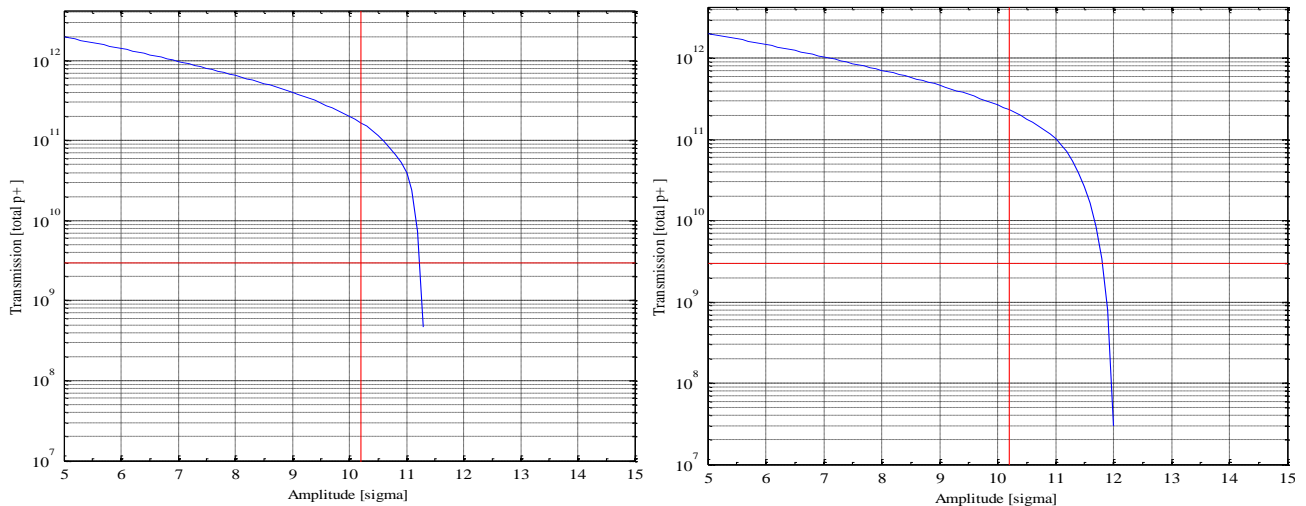


Figure 6.57: Transmission of particles trough the TCDQ system for a uniform phase space beam shape (parabolic beam with nominal emittance) and for a MKD to TCDQ phase advance of 94.6° (left) and 106.6° (right).

Figure 6.58 shows the transmission rates for Gaussian beam with doubled emittance and parabolic tails. This distribution was chosen in order to have more particles within the critical phase space area as it could be the case during emergency dump action (e.g. due to optics error) or in a possibly populated abort gap. Particles with high amplitudes (up to 14.5σ) are transmitted with intensities above the assumed damage level.

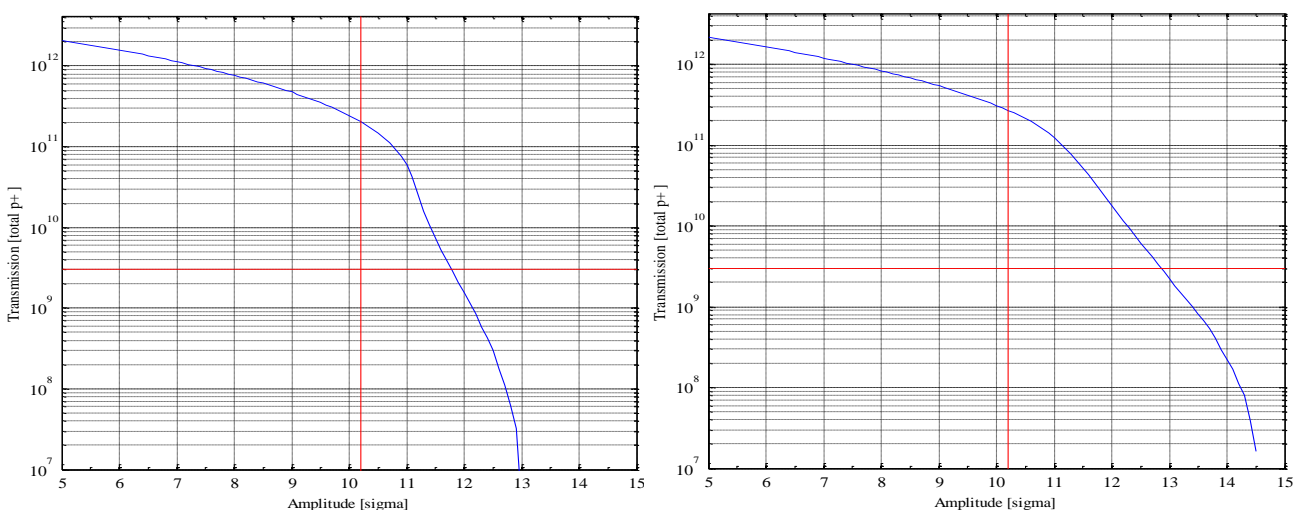


Figure 6.58: Transmission of particles trough the TCDQ system for a Gaussian beam (doubled emittance) with parabolic tails (10%) and for a MKD to TCDQ phase advance of 94.6° (left) and 106.6° (right).

6.4.10 Analysis of simulation deviations

An important question for numerical simulation is to what extent the results represent the real world. An evaluation of the errors inherent in the simulation process is important when deciding on the confidence to attach to the results and the extra engineering margins to be included in any resulting designs.

The importance of real random numbers for simulation input is significant for this study and was already discussed and analysed in chapter 3.4.

Some statistical analyses of the simulation results have been made. The minimum number of macro particles and the number of repetitions with different orbit seeds are of particularly interest. Figure 6.59 shows the average deviation of results between simulations with 20 and 60 orbit seeds over the order of magnitude of primary losses both done with an average of 25 macro particles per ns. It can be seen that for locations with high losses the average deviation is very small (0.2%) whilst for low loss positions the deviation can reach 100%. As at injection energy the damage levels for all equipment hit during this simulations is above 1×10^{12} , the difference between 20 and 60 orbit seeds in the low-loss level locations has been considered as acceptable so that one could stay with the less CPU time consuming 20 orbit seeds results.

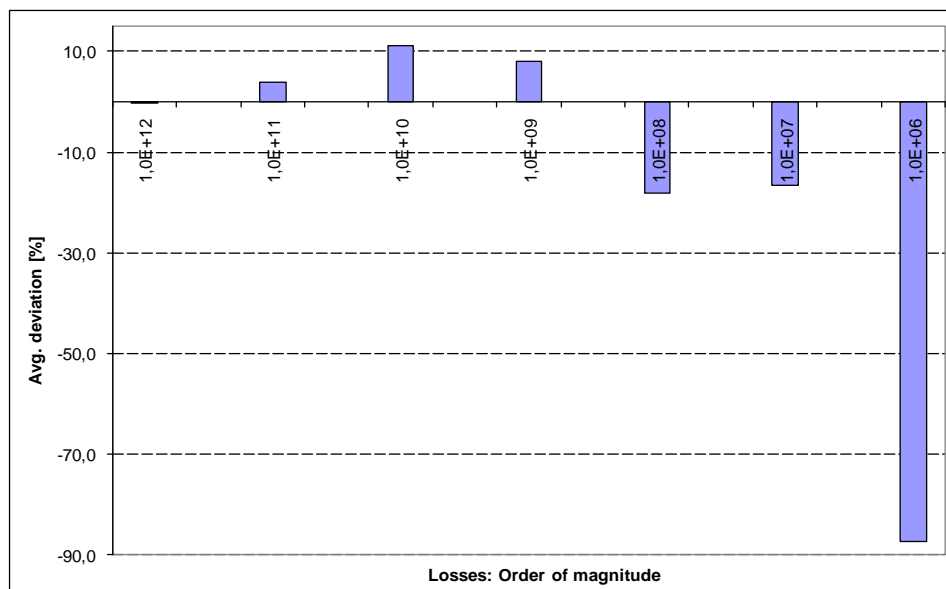


Figure 6.59: Average deviation between the results of the 450 GeV prefire case executed with 20 and 60 orbit seeds.

Figure 6.60 shows the factor between the maximum value seen and the average value over 20 orbit seeds for each TCDQ retraction step. Only loss points above a level of 1×10^9 have been considered and are displayed in this plot, as low level loss locations anyway show a higher variance due to the limited number of macro particles and orbit seeds.

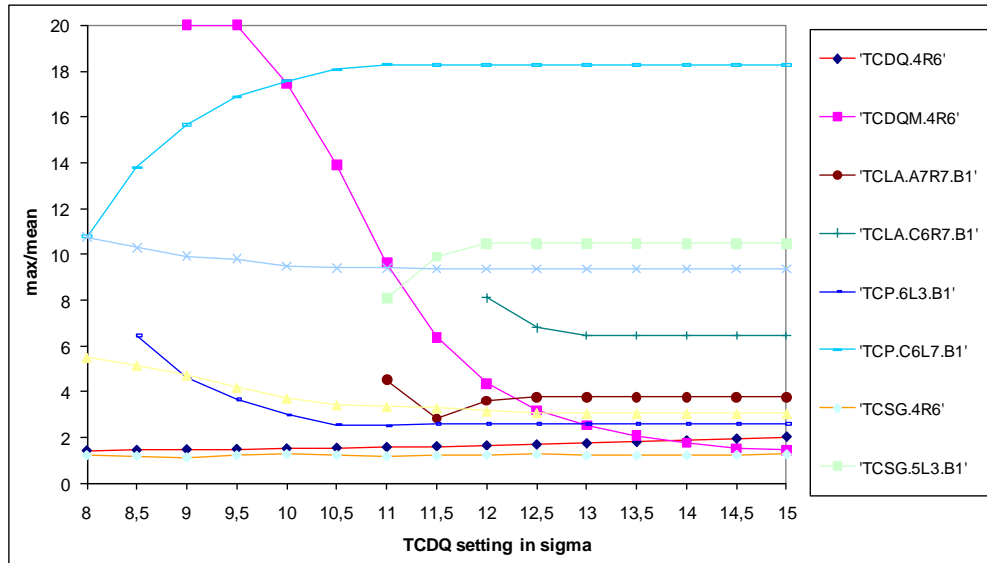


Figure 6.60: Factor between maximum and average losses for the 450 GeV asynchronous dump case.

It can be seen that a dependency of the ratio on collimator type is visible, i.e. an increased sensitivity of certain collimators to the orbit/optics perturbation. This sensitivity is generally highest when the collimator starts seeing beam for the first time as the TCDQ is further retracted, which can be explained since the absolute loss level is small at the jaw when it starts seeing beam, so that a given variation is relatively more important. This explains the decreasing curves seen for most collimators. A special case is the TCP.C6L7 which seems to be more sensitive for higher TCDQ settings. Interestingly, such behaviour for this specific collimator is not seen for the prefire case shown in Figure 6.61 where it sees much more impacting beam.

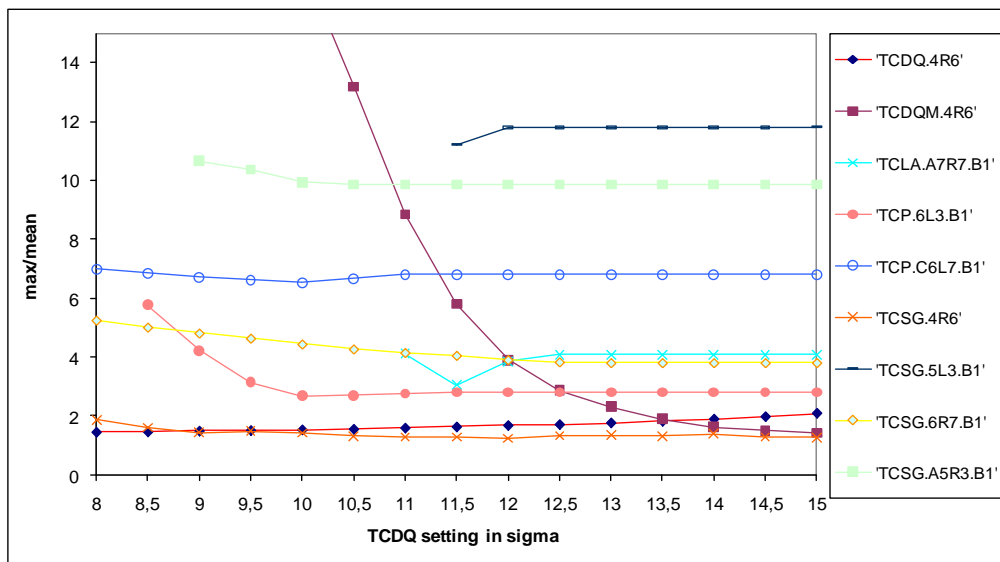


Figure 6.61: Factor between maximum and average losses for the 450 GeV prefire case.

Figure 6.62 and Figure 6.63 show the factor between maximum and average losses for the 7 TeV asynchronous dump and prefire case – the ratios are basically half of the amplitude shown for the 450 GeV cases.

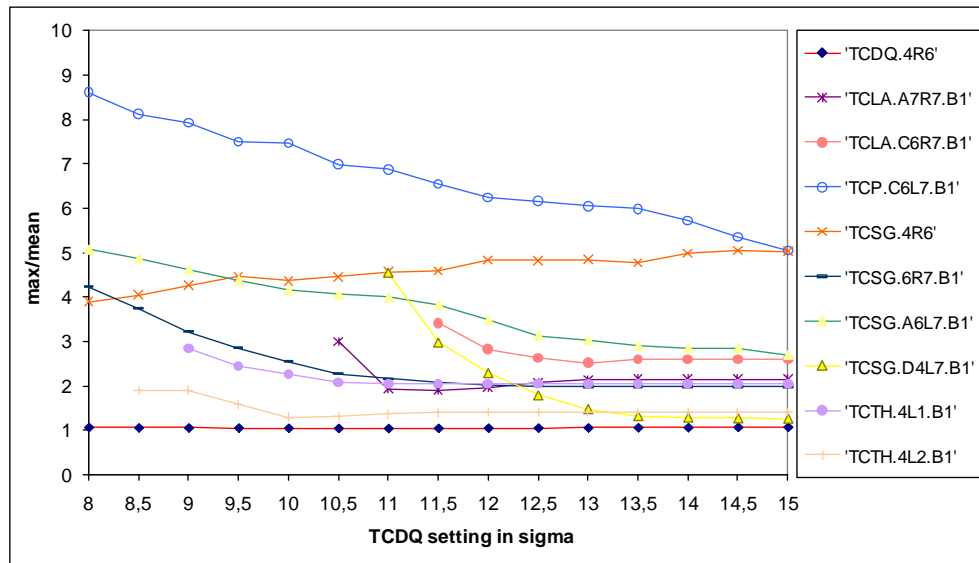


Figure 6.62: Factor between maximum and average losses for the 7 GeV normal case.

For all 7 TeV cases the beam load on the TCP.C6L7 shows the highest sensitivity to changing orbit conditions.

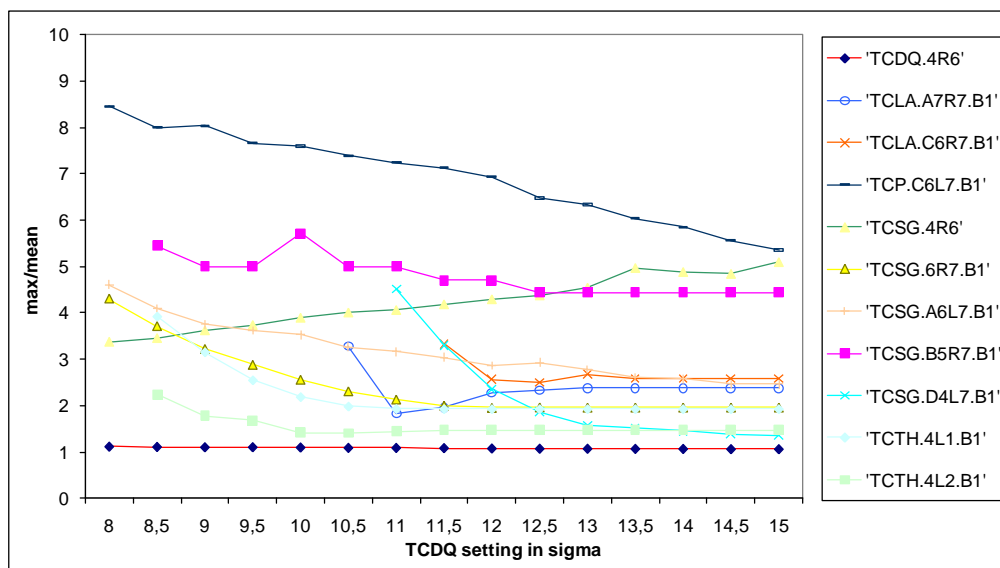


Figure 6.63: Factor between maximum and average losses for the 7 GeV prefire case.

6.5 Summary tables of tracking results

Table 6.6 gives an overview of the damage limits of collimators for slow losses and ultra fast losses. As there are no qualified experience for material behaviour under 7 TeV beam impact the 450 GeV damage limits have been scaled as a first assumption [98]. For the LHC commissioning, a safe beam limit has been announced which is 1×10^{12} protons for 450 GeV and 1×10^{10} protons for 7 TeV [102].

A summary table of different loss locations at a TCDQ setting of 8, 10 and 15 σ for different cases is given in Table 6.7 for 450 GeV and in Table 6.8 for 7 TeV.

Table 6.6: Overview of LHC collimator damage levels for 450 GeV and 7 TeV.

Energy [TeV]	Collimator Type	TCSG	TCP	TCLA	TCTH
0.45	Damage limit for slow losses[p+/s], [99]	1.5E12	1.5E13	7.5E9	3E9
0.45	Damage limit assumed for sweep	3.2E13 [100]	3.2E13 [21]	2.3E12 [101]	not used
7	Damage limit for slow losses[p+/s], [99]	4E10	4E11	2E9	2E8
7	Damage limit assumed for sweep	2E12 ¹	2E12 ¹	1E10[102]	1E10[22]

Table 6.7: Overview of loss numbers for different cases at 450 GeV.

'sigma'	With all errors						Clean machine					
	Prefire case			Normal case			Prefire case			Normal case		
	8	10	15	8	10	15	8	10	15	8	10	15
TCDQ.4R6'	1,66E+12	1,26E+12	5,07E+11	1,43E+12	1,13E+12	4,87E+11	1,88E+12	1,47E+12	6,89E+11	1,65E+12	1,33E+12	6,66E+11
TCDQM.4R6'	0	1,15E+10	5,58E+11	0	1,01E+10	4,78E+11	0	0	4,68E+11	0	0	4,13E+11
TCLA.A7R7.B1'	0	0	2,82E+10	0	0	2,43E+10	0	0	1,06E+11	0	0	7,82E+10
TCLA.C6R7.B1'	0	0	3,68E+09	0	0	3,36E+09	0	0	5,52E+09	0	0	2,94E+09
TCLA.6R3.B1'	x	x	x	0	0	9,20E+06	x	x	x	x	x	x
TCP.6L3.B1'	1,52E+09	6,15E+10	1,15E+11	9,02E+08	4,01E+10	8,10E+10	0	5,06E+10	1,58E+11	0	3,83E+10	1,18E+11
TCP.C6L7.B1'	3,34E+11	3,58E+11	3,67E+11	3,85E+09	1,49E+10	2,20E+10	x	x	x	0	0	1,84E+08
TCSG.4R6'	2,31E+11	1,79E+11	1,20E+11	1,40E+11	1,41E+11	1,07E+11	2,09E+11	1,89E+11	1,35E+11	1,56E+11	1,42E+11	1,19E+11
TCSG.5L3.B1'	0	0	7,08E+09	0	0	5,32E+09	0	0	1,66E+10	0	0	1,36E+10
TCSG.6R7.B1'	3,17E+11	4,52E+11	5,90E+11	1,48E+11	2,51E+11	3,60E+11	0	1,38E+10	9,29E+10	1,84E+08	9,38E+09	6,27E+10
TCSG.A5R3.B1'	3,54E+09	6,67E+09	6,72E+09	1,11E+09	3,24E+09	3,39E+09	x	x	x	0	3,68E+08	3,68E+08
TCSG.B5R3.B1'	4,14E+08	1,52E+09	1,79E+09	1,84E+08	7,27E+08	9,02E+08	0	0	1,84E+09	0	9,20E+08	1,10E+09
TCSG.B5R7.B1'	1,33E+09	1,56E+09	1,56E+09	1,10E+08	2,58E+08	3,40E+08	x	x	x	x	x	x
TCSG.B5L7.B1'	x	x	x	0	0	1,84E+07	x	x	x	x	x	x
TCSG.D5R7.B1'	x	x	x	0	0	9,20E+06	x	x	x	x	x	x
TDI.4R8'	6,90E+08	6,90E+08	6,90E+08	x	x	x	x	x	x	x	x	x
Extracted	4,97E+12	5,19E+12	5,21E+12	1,84E+11	3,18E+11	3,39E+11	5,59E+12	5,95E+12	6,00E+12	2,61E+11	5,44E+11	5,94E+11

Table 6.8: Overview of loss numbers for different cases at 7 TeV. Critical values are marked in red.

'sigma'	With all errors						Clean machine					
	Prefire case			Normal case			Prefire case			Normal case		
	8	10	15	8	10	15	8	10	15	8	10	15
TCDQ.4R6'	4,66E+12	4,07E+12	3,11E+12	3,08E+12	2,85E+12	2,42E+12	4,81E+12	4,15E+12	3,11E+12	3,12E+12	2,88E+12	2,42E+12
TCDQM.4R6'	0	0	0	0	0	0	0	0	0	0	0	0
TCLA.A7R7.B1'	0	2,76E+08	8,18E+10	0	0	3,87E+10	0	0	7,08E+10	0	0	3,40E+10
TCLA.C6R7.B1'	0	0	1,32E+10	0	0	5,84E+09	0	0	1,01E+10	0	0	5,06E+09
TCP.C6L7.B1'	2,39E+09	8,83E+09	4,60E+10	1,66E+09	4,19E+09	7,54E+10	0	0	1,01E+10	0	0	5,98E+09
TCSG.4R6'	2,32E+11	1,84E+11	1,24E+11	9,99E+10	8,11E+10	6,46E+10	1,79E+11	1,35E+11	8,56E+10	6,95E+10	4,83E+10	3,50E+10
TCSG.6R7.B1'	7,62E+10	2,38E+11	4,53E+11	2,87E+10	8,44E+10	1,64E+11	5,80E+10	2,82E+11	5,79E+11	2,21E+10	8,51E+10	2,01E+11
TCSG.A4L7.B1'	9,20E+07	1,84E+08	1,84E+08	0	0	4,60E+07	x	x	x	x	x	x
TCSG.A4R7.B1'	x	x	x	4,60E+07	4,60E+07	4,60E+07	x	x	x	x	x	x
TCSG.A5L7.B1'	x	x	x	0	0	4,60E+07	x	x	x	x	x	x
TCSG.A6L7.B1'	8,19E+09	1,56E+10	5,90E+10	3,17E+09	5,43E+09	6,56E+10	5,52E+09	1,75E+10	7,27E+10	3,68E+09	5,06E+09	2,48E+10
TCSG.B5L7.B1'	x	x	x	0	0	6,90E+08	x	x	x	x	x	x
TCSG.B5R7.B1'	9,20E+08	1,29E+09	1,66E+09	5,06E+08	5,06E+08	5,52E+08	1,84E+09	1,84E+09	1,84E+09	9,20E+08	9,20E+08	9,20E+08
TCSG.D4L7.B1'	0	2,76E+08	5,36E+11	0	0	2,85E+11	0	0	5,58E+11	0	0	2,57E+11
TCTH.4L1.B1'	7,36E+08	6,64E+10	1,04E+11	1,84E+08	2,54E+10	4,21E+10	0	6,53E+10	1,05E+11	0	3,40E+10	5,15E+10
TCTH.4L2.B1'	2,76E+08	1,53E+11	2,11E+11	1,38E+08	5,77E+10	8,24E+10	0	1,64E+11	2,11E+11	0	6,16E+10	8,37E+10
TCDSA.4L6.B1'	4,89E+12	5,14E+12	5,14E+12	2,00E+12	2,10E+12	2,10E+12	4,84E+12	5,08E+12	5,08E+12	1,98E+12	2,08E+12	2,08E+12

¹ Scaled linearly from 450 GeV values.

Table 6.9: Overview of TCDQ settings for safe operations at 7 TeV.

Case	TCDQ settings in σ for loss limits at critical locations			
	TCLA.A7R7	TCLA.C6R7	TCTH.4L1	TCTH.4L2
No errors	10.5	9.0	9.0	8.5
No errors, prefire	10.5	12.5	8.5	8.0
With errors	10.5	-	9.0	8.5
With errors, prefire	10.5	12	8.5	8.0
With errors, prefire, no IR7*	-	-	<8.0	8.0
With errors, one MKD	10	9.5	8.5	8.0

* For the prefire case with retracted IR7 collimators the TCTH.4L1 saw already at a 8σ TCDQ setting losses (3.7×10^{10}) three times above the damage limit and in addition the TCTH.4L8 saw losses above the damage limit for TCDQ settings $>14.5\sigma$.

6.6 Discussion

6.6.1 Consequences for Machine Elements and Experiments

For all the failures considered, no losses have been seen for beam 1 on any lattice magnets, instruments or experiments. All observed loss points were either a collimation/protection device or the LHC beam dump block. This is an important result for 450 GeV, which shows that the arc downstream of IR6 should be well protected by the fixed TCDQM for any TCDQ position, although this is likely to suffer some damage from an asynchronous dump at high intensity with TCDQ retracted. The results also show that the TCT collimators are frequent beam loss locations for 7 TeV beam only; since these are presently made of tungsten with a low damage threshold, it would be interesting to consider a more robust design or additional interception elements.

During early setup of the tracking jobs only one single macro particle corresponding to 4.6×10^8 real particles got lost on the CMS roman pots which was observed with a TCDQ setting of above 15σ and without IR7 collimation and skew collimators in place.

Simulations with missing MKD modules have shown that the TD68 beam transfer line and the setup of the TCDS seems to be well designed. No losses have been observed for all MKD failure cases (except on the TCDS for asynchronous dumps). The simulation with 12 MKD magnets only shows that all particles are either intercepted by the TCDS or still on the TDE – in this event the TCDS and possibly the downstream MSD magnets will be damaged or destroyed.

The case with one MKD only shows that most of the beam is intercepted by the TCDQ which will see a load far above its specification – in addition the TCT in IR1 and 2 are also critically loaded with beam. This worst case scenario is expected to seriously damage these components. To quantify the seriousness of such an incident, further damage to elements behind those by developed showers and the probability of beam finally penetrating the protection element should be studied.

Simulated proton density maps for the TCDQ show that, as expected, this element has a high beam load already at a nominal 8σ setting and is likely to be completely destroyed for the one MKD case. The possibility for tighter TCDQ settings below nominal ($<8\sigma$) which would clearly improve the downstream loss figures is limited by the maximum TCDQ beam load constraints.

The losses on the TCDQM for a relatively small TCDQ retraction at 450 GeV would seem to be a useful indicator for TCDQ setting tests using the dedicated beam loss monitoring on the TCDQM.

The mean losses on the TCTH elements are already above the damage limit for a TCDQ setting of 8.5σ - and for some seeds the losses at this small retraction were a factor of 3 above the damage limit. This indicates that the risk of damage to the TCTH elements may be larger than previously assumed, and that the protection concept or the settings hierarchy may need to be re-thought, for β^* at the minimum of 0.5 m.

Simulations and analytical analysis showed that the TCDQ protection system allows the transmission of particles into the ring for high amplitude particles already at a much smaller TCDQ gap setting than initially anticipated. This was identified to be due to the finite beam sizes and the phase advance deviations between the MKD and the TCDQ system.

In analyzing the results it must be considered that these simulations are based on worst case incidents, and that large retractions of the TCDQ in conjunction with the rare occurrence of an asynchronous dump are unlikely to happen in practice [103]. It must also be borne in mind, however, that beam in the abort gap will essentially produce an asynchronous dump at every beam dump event, which means that the abort gap cleaning and monitoring systems are very important in the machine protection of the LHC. This feature allows for an elegant method of checking the setting up of the TCDQ, since low intensity beam is readily debunched and can be extracted to check the loss pattern around the LHC ring. This should agree with the results shown in this chapter for the TCDQ settings, and it is proposed to use this method to qualitatively analyse the protection setup of the TCDQ during LHC commissioning. Preliminary data of this type taken during the few days of LBDS beam commissioning in 2008 are presented in chapter 8.

6.6.2 Directions for further simulation

The simulation tools developed should be used to make the analyses for LHC beam 2, which has the feature of the experimental insertion in IR5 before any collimators. The effect of closed-orbit bumps in the arc could be investigated, since these will effectively produce a local reduction in the aperture and could lead to beam losses on LHC elements. Another interesting topic would be a study of the (out of tolerance) perturbations in the LHC optics which could lead to beam losses at sensitive elements – it would be interesting for early commissioning to know what the maximum possible beta-beat is, compatible with safe machine operation. The tools developed and described here allow detailed studies of these effects, although the preparation, simulation and processing time are fairly consequent.

FLUKA studies of elements which see a huge beam load like the TCDS and TCDQ could bring some important and more precise information concerning the expected damage levels.

7 LHC Beam Dump - Abort Gap Cleaning

This chapter gives a short overview of the theoretical concept of abort gap cleaning (AGC), the equipment used and the potential dangers of a populated abort gap. Furthermore simulations done for the SPS are compared with measurements taken during SPS machine development sessions and conclusions are drawn for the LHC.

7.1 Introduction

The 3 μ s long abort gap allows the MKD system to switch on its magnetic field to safely extract the beam. Failures in triggering lead to asynchronous beam dumps which were already discussed in chapter 4 and 5. However there are other mechanisms leading to a populated abort gap. Thus a dump executed with a certain population in the abort gap would sweep beam across the LHC aperture in a similar way to an asynchronous dump, with a different particle intensity function.

7.1.1 Abort gap filling

Ideally the abort gap should be free of particles. However, there are two main types of mechanism leading to a populated abort gap:

- Fast population increase i.e. by synchronization errors and thus injecting the beam partly or full into the abort gap;
- slow population increase by migration of particles lost from RF buckets.

To keep the probability of injecting the beam into the abort gap as low as possible, a special abort gap keeper [104] has been implemented which creates a signal synchronized with the abort gap. This signal is used by the injection kickers to inhibit any injection trigger within the LHC abort gap.

The process of particle migration into the abort gap was studied in [105]. The main sources are capture losses at injection, intrabeam scattering, Touschek scattering [106], RF-noise and beam instabilities. For injection energy a particle density of 10^9 p⁺/m has been calculated as density in the gap consisting of uncaptured (off momentum) particles lost from their buckets which migrate into the gap whilst the LHC is being filled. Approximately 19 minutes is estimated as the time needed for one uncaptured particle to make one full extra turn with respect to the captured particles. During the ramp these particles will get lost on the momentum collimation system.

It has been discovered that at 7 TeV the abort gap is filled from the back to its head (where the kickers are fired) as the uncaptured particles lose energy through synchrotron radiation and hence move only in one direction around the ring with respect to the abort gap [107].

The particles in the abort gap could either damage the LHC if the intensity is high enough and the TCDQ positioning is not correct, or could cause a quench of the downstream superconducting magnets. If a high population happens on every beam dump, it would increase enormously the probability of a TCDQ positioning error being dangerous for the machine and would as well significantly impact the machine availability as the recovery time from quenches can be in the order of hours. It is clearly an important issue to keep the abort gap population within acceptable limits.

7.1.2 Abort gap cleaning hardware

It is possible to influence the orbit of just a certain group of particles. The most convenient one is to apply a kick to the beam at the selected time frame only. The rise and fall time of such a kicker is very important and fast devices must be used. BNL used their tune kickers at RHIC to excite the particles oscillation [108] and Fermilab cleaned the TEVATRON abort gap by using a pulsed electron lens and thus rely on the space charge effects of beam-beam interaction [109]. In both cases

only the small longitudinal part of the beam within the abort gap was excited. Thus only hardware fast enough to provide such a short kick is suitable. Electrostatic devices have a big advantage as they can build up their field much faster than magnetic devices, with the disadvantage of smaller kick strength.

7.1.2.1 Transverse damper

In the LHC it is foreseen to use the horizontal and vertical dampers (ADT) of the transverse feedback system which is installed to damp beam oscillations. If the sign in the feedback loop is switched the dampers provide sufficient kick to excite the beam until the oscillation amplitude is big enough to hit an aperture limit. The LHC transverse feedback system is installed in IR4 with four electrostatic kickers for each plane and beam. The 1.5 m long electrodes can provide a kick angle of 2 μ rad at injection energy and for a frequency of 1 MHz [110]. The bandwidth allows to change the polarity in very short times so that the 10% to 90% rise time is around 350 ns (1%-90% in 720 ns).

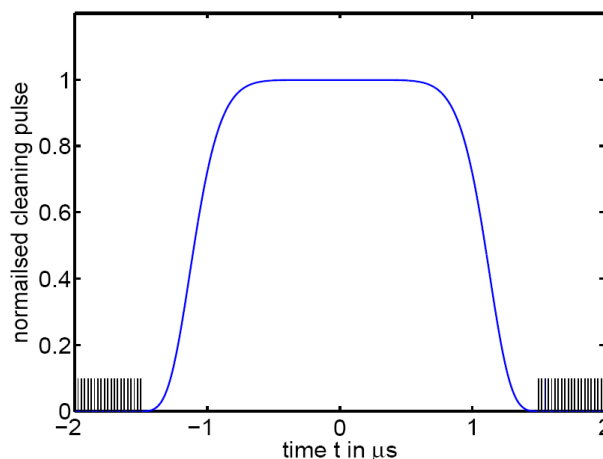


Figure 7.1: Normalised waveform of the damper pulse (blue) within the abort gap [111].

Figure 6.1 shows the normalised waveform (blue) of the transverse damper within the 3 μ s abort gap. The black bars on each side represent the bunch pattern.

The ADT as an electrostatic kicker is thus just fast enough to be considered for cleaning the 3 μ s LHC abort gap. The maximum kick angle is not big enough to deflect particles such that they would get lost immediately within one turn. Hence the kick has to be deployed onto each particle group to achieve a coherent excitation over several 10s or 100s of turns in a synchronized way, which is the major challenge for this method.

7.1.2.2 Abort gap monitor

In order to know when the abort gap population gets too high a special abort gap monitor has been developed [112]. It takes advantage of the already installed undulator-magnets which produce synchrotron light even for protons at LHC injection energy. This synchrotron light is monitored with a dedicated photomultiplier tube, digitized and taken as an input for the abort gap particle density which is integrated and calculated for thirty 100 ns long bins within the 3 μ s abort gap.

7.1.3 The principle of abort gap cleaning using the transverse damper

We can explain the basic ideas of AGC using the transverse damper if we consider an ideal beam with all particles circulating with the same tune and phase. Looking at just one of these particles in normalized transverse phase space (Figure 7.2, left image) we see it appearing on successive turns at the damper location in different positions along its circular track, the radius of which is defined by the actual amplitude for the particle's emittance. Each turn the particle appears at a different angle according to its turn-to-turn phase advance at this observation point. This turn-to-turn phase advance corresponds to the fractional tune. The circular track will not close exactly to its start, since the LHC cannot operate with the tune on a resonance.

Due to the limited strength of the damper, particles in the abort gap pass the damper for many turns and each time they pass they receive a kick. To maximise the particle amplitude growth with time it is essential that the frequency of changing the polarity of the kicker electrodes corresponds to the particles oscillation frequency – its tune – otherwise the particle would see a mixture of kicks which excite its oscillation (as wanted for AGC) and kicks which damp its oscillation (unwanted for AGC). If the AGC kicks are modulated in sign and amplitude at the particle tune, the damper is effectively driving the particle at its resonant frequency, and the amplitude will grow. Note that the modulation in amplitude reduces the effective kick strength by a factor of 2 compared to the full strength kick. The ideal AGC frequency for a beam which only contains particles at a fixed tune is therefore the fractional tune times the revolution frequency. Figure 7.2 (right image) shows such a particle getting always a kick into the right direction until its orbit reaches the maximum accelerator acceptance. Note that also the sidebands of that frequency ($1-q$, $1+q$) can excite the oscillation.

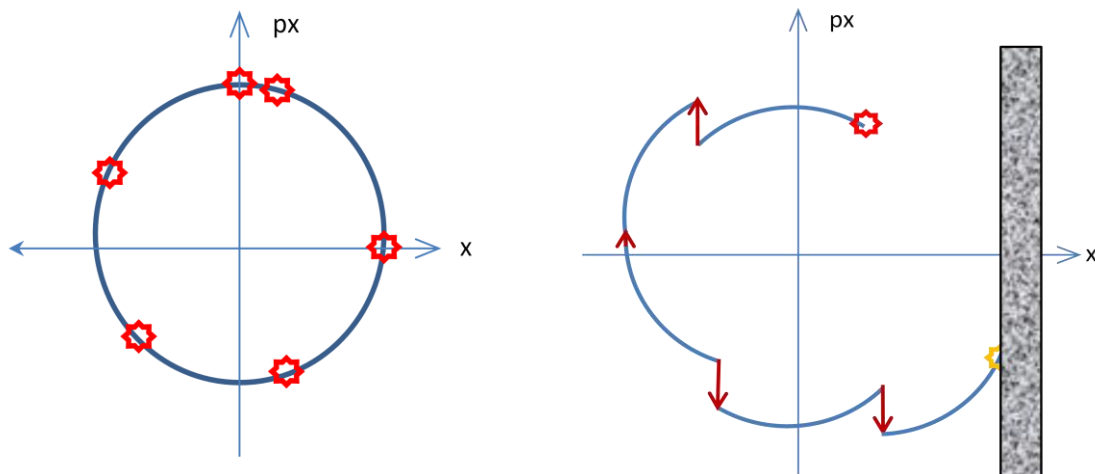


Figure 7.2: Transversal particle motion in phase space with (right) and without (left) AGC.

For a particle distribution with identical tunes, if the correct AGC frequency is found all particles can be excited and the abort gap would be cleaned within a couple of turns, depending on the actual aperture and the kick per turn.

For linear machines an estimation of the average cleaning time τ_{clean} is given in (7.1). T_{rev} is the particles revolution time, θ the maximum kick angle, β_{kick} and β_{coll} are the beta functions at the kicker and the intercepting collimator whilst A_{coll} is the collimator aperture; ν is the ratio of the applied frequency against the particles revolution frequency and q is finally the particles tune.

$$\frac{\tau_{clean}}{T_{rev}} \cong \frac{1}{\pi|q-\nu|} \cdot \arcsin \left[\frac{A_{coll}}{\hat{\theta} \sqrt{\beta_{coll} \cdot \beta_{kick}}} \pi |q-\nu| \right] \quad (7.1)$$

In reality, and especially in the LHC the actual situation is more complicated. The particles have a spread in tune, which occurs because of their spread in momentum and the chromaticity and higher-order non-linearities. In addition the particles in the abort gap are a long way from the nominal momentum, and so have very different optical parameters. This means that for a realistic beam the effects of dispersion, chromaticity and other non-linearities mean that the tune of a single particle depends on its momentum and its amplitude of betatron oscillation. These effects have to be taken into account when searching for the ideal excitation frequency; already since there is an inherent spread in single particle tunes it is obvious that there is not only one ideal frequency anymore; instead a certain spectrum has to be covered. Furthermore the tune changes as the particle amplitude increases, since the non-linearities are stronger at larger amplitude, which means that the excitation frequency changes as a function of excitation turns.

The frequency of the excitation should therefore be modulated in time, to cover the tune spread and the detuning with amplitude. The approach for the LHC was to make simulations of the optimum frequency patterns, using all non-linearities in the LHC machine model, to optimise the frequency pattern for the excitation. This approach was validated by experiments in the SPS accelerator, where the transverse damper was operated in the same way to excite particles to the machine aperture, with a variety of frequency programmes and settings of non-linear elements which were tested in simulations before.

7.2 Results of 2007 SPS Machine development sessions dedicated to AGC

In the 2nd half of 2007 some SPS beam time was dedicated to AGC studies. For the MDs only the vertical SPS damper was used, as the SPS vertical aperture limit at the high energy dump block TIDV is the smallest in the ring. Four different frequency programs were studied: Fixed frequency, frequency sweep, modulated frequency and modulated frequency on a carrier that is itself swept. The SPS was running at 26 GeV with a vertical tune of 26.1807 and the vertical transverse damper (BDV.214) was operated at a voltage of 0.82 kV which allowed maximum kicks of around 1.5 μ rad. A single bunch with an intensity of 5×10^{10} p+ was used for these measurements. The AGC-program was activated in the vertical damper 2000 ms after injection and stayed active for 2000 turns. The horizontal damper stayed switched on in damping mode all the time. The coupling between horizontal and vertical planes was measured to be negligible, which excluded any unwanted influence coming from the horizontal damper.

In the SPS the (normalized) chromaticity definition is as (7.2) where Q is the machines tune and p the particles momentum.

$$\xi = \frac{\Delta Q/Q}{\Delta p/p} \quad (7.2)$$

The chromaticity was varied from the normal value of +0.03 up to +0.93 units and the octupole strength was changed from zero to +50 units to introduce strong nonlinearities.

The fixed frequency program worked well only for low chromaticity settings and octupoles switched off, as expected from theoretical considerations. A cleaning efficiency of 97.3% was achieved with a cleaning time of 5 ms (220 turns), Figure 7.3. For a setup with strong octupoles and medium chromaticity ($k_3=+20$ units, chromaticity at +0.43 units) no cleaning could be achieved at all.

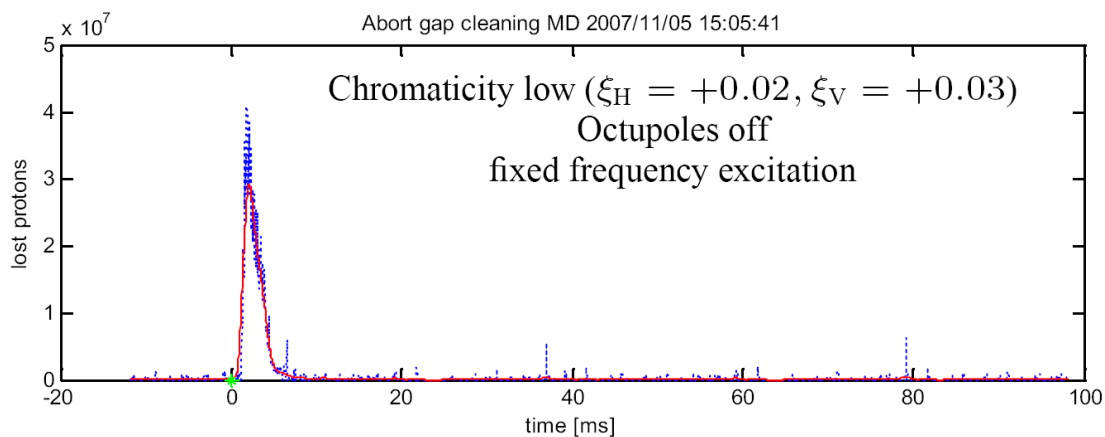


Figure 7.3: Measured loss rates (blue) and fit (red) at the SPS high energy dump block (TIDV) for a fixed frequency excitation during a dedicated AGC machine development session in 2007; The green dot represents the start of the AGC program. [113].

The excitation program using a frequency sweep was then tried with medium chromaticity and strong octupoles, and showed a higher efficiency of 99.9%, compared to 0% with fixed frequency. However, the cleaning time was much higher (40 ms, 1740 turns), Figure 7.4. This increase in cleaning time is expected since the frequency sweep effectively reduces the time during which each particle is excited at its particular resonance frequency.

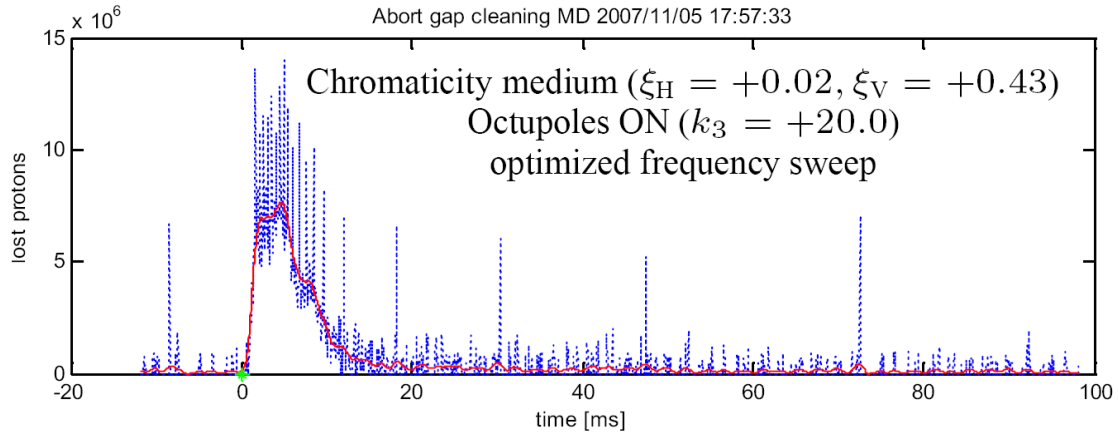


Figure 7.4: Measured loss rates (blue) and fit (red) at the TIDV for AGC using a frequency sweep program. The green dot represents the start of the AGC program. [113]

A further improved program using a frequency modulation showed good results also for high chromaticity settings (+0.93 units) with octupoles on. The cleaning efficiency was around 99.7% and the cleaning time 80 ms, Figure 7.5 and Figure 7.6.

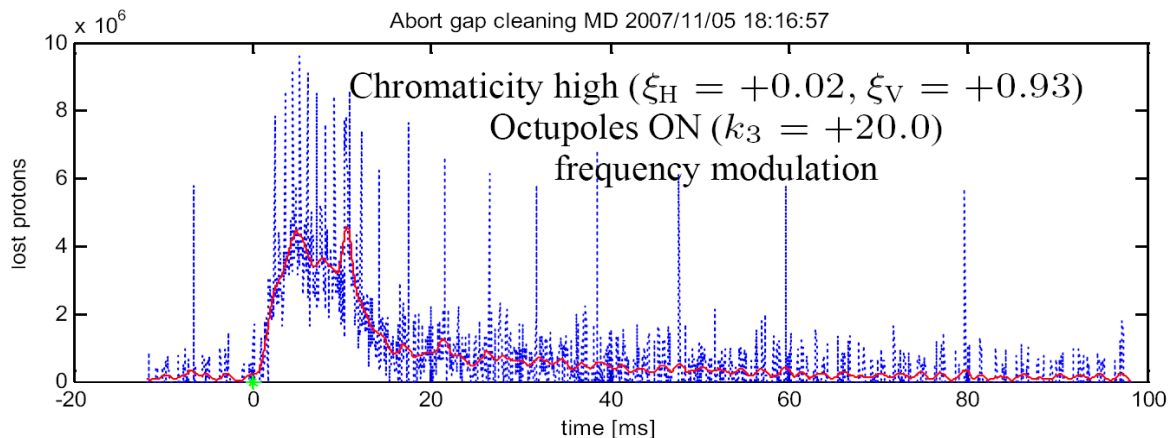


Figure 7.5: Measured loss rates (blue) and fit (red) at the dump block (TIDV) for a frequency modulation program. The green dot represents the start of the AGC program. [113]

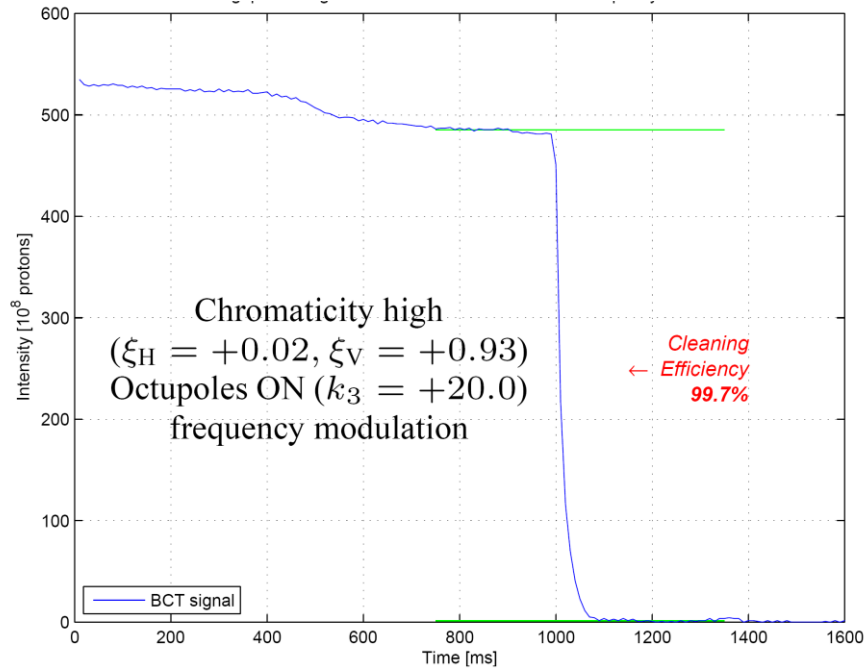


Figure 7.6: Measured intensity for one SPS cycle with frequency modulated AGC program. The green lines represent the 100% level at the damper program start [113].

The SPS results showed that the abort gap cleaning can be simulated with reasonable agreement and that the effects of non-linear elements can be accurately described. The optimum frequency programme in the simulations was tested in the SPS and found to effectively clean the beam in the presence of strong chromaticity and strong octupoles. This gave good confidence in the ability to simulate the LHC conditions and in the proposed approach with the transverse damper.

7.3 LHC simulations

7.3.1 Results from tracking studies with filled abort gap

Tracking studies for with a filled abort gap were performed for 7 TeV (chapter 6), using the asynchronous beam dump case. Since the time structure of the beam used in the simulations was 5 ns, this is a reasonable approximation to the continuous particle flux in the abort gap, and is a pessimistic evaluation, since the real distribution is expected to be empty of particles at the low-amplitude end of the MKD kick.

The loss patterns can be scaled by the maximum intensity expected in the abort gap to give some worst-case estimates of proton losses, in terms of location and loss level, and to quantify possible main loss locations and their rough time structure. Table 6.4 shows the structure in time of a nominal 7 TeV asynchronous dump case without errors. It can be seen, that the swept beam is completely intercepted by the IR6 collimation (TCDQ/TCSG) about 495 ns after the MKD kick started. Within the first 80 ns no single macro particle was lost, with the first loss then occurring in the collimation region of IR7. The average loss-time for the first 10 particles lost is 260 ns after the MKD were fired. It is interesting to note that a progressive increase of losses in the LHC starts around 325 ns after the kicker were fired. This should be compared to the 10% to 90% rise time of around 350 ns of the transverse damper system. It is obvious that these two times overlap so it might well be that the AGC is not very effective at this position within the abort gap. No detailed simulations have been made of the AGC with the real damper bandwidth – at present the assumption of low particle numbers in the abort gap at these short times relies on the prediction that the abort gap will only be filled from the other side.

If this proves to be a problem, two solutions are possible. One is to increase the bandwidth of the damper, such that the edge of the exciting pulse is closer to the edge of the abort gap. The second would be to increase the abort gap length, by about 700 ns which would allow the damper kick to effectively rise and fall during a period less critical considering asynchronous dumps. This would reduce the luminosity of the LHC by about 1%. Simulations showed that the beam sweep over the TCDS ended around 2.3 μ s after the MKD is triggered, so one may conclude that with some margin the beam gets well extracted after 2.5 μ s and thus one could shift the MKD timing accordingly. However, this is only true for a nominal dump case. Any extraction with missing kickers will then result in higher losses at the TCDS.

Since the AGC may show a significant lower efficiency during the damper fall time and considering that for higher energies the abort gap is populated from its back, at 7 TeV it might be the best solution to constantly apply AGC to prevent the filling of the head of the abort gap by particles migrating from the back to the front.

Table 7.1: Sweep parameters for asynchronous dumps under nominal conditions, TCDQ at 8σ , without errors, MAD-X simulation.

Time	Duration	Intensity	Comments
0 - 80 ns	80 ns	3.2 bunches; 3.7×10^{11}	Beam swept over machine aperture
80 ns	-	-	First macro particle lost on collimation in IR7
260 ns	-	-	Average of first 10 macro particles lost on collimators
325 ns	-	-	Strong increase of losses
335-495 ns	160 ns	6.4 bunches; 7.4×10^{11}	Kick amplitude reaches TCDQ/TCSG in IR6 (first loss/last loss)
345 ns	-	-	First particle lost at TCDQ
450 – 1150 ns	700 ns	28 bunches; 3.2×10^{12}	Beam swept over TCDQ
1105 ns	-	-	First particle lost at TCDS
1150 – 2250 ns	1100 ns	44 bunches; 5×10^{12}	Beam swept over TCDS
2.3-90.5 μ s	88.2 μ s	Rest of beam	Beam extracted

7.3.2 Results from dedicated LHC- AGC simulations done at FNAL

MAD-X tracking studies were made for LHC beam one using a optics model containing magnet errors and considering a turn by turn variation of the damper kick strength according to the used cleaning frequency program. These simulations have been carried out by Fermi National Accelerator Laboratory (FNAL). [114]

For injection energy, the simulations showed that all particles were kicked out by the vertical damper within 50 turns using the maximum available kick strength whilst simulations with the vertical damper showed less effectiveness (2% of particles remaining in the LHC). Frequency programs using a sweep or band limited noise did not show a better performance in this study.

For 7 TeV, 72% of the particles were kicked out by the vertical damper within 250 turns using a frequency corresponding to the fractional tune and the rest whilst applying kicks with a frequency scan in four steps between values corresponding to a fractional tune of 0.315 to 0.319. In the horizontal plane a much better performance was observed and all particles were removed within 250 turns. This can be explained because of the smaller horizontal chromaticity, which means that the particle distribution has a smaller tune spread for a given momentum spread.

7.4 Conclusions

The abort gap cleaning with the transverse damper has been shown to work in simulation for the SPS and LHC, with a strong dependence on the strength of the non-linear fields in the model. The principle was tested in experiments on the SPS using the transverse damper for different non-linear element strengths, with a good agreement between measurement and model.

The tracking studies and SPS measurements show that the cleaning effectiveness is very sensitive to tune changes and high chromaticity. The frequency programme can be adapted to effectively clean the abort gap, but to cover all possibilities a future AGC program should allow frequency modulation and needs a good tune input signal.

For further studies it would be interesting to create a more realistic particle distribution within the abort gap. Such a distribution could then be used for tracking studies as presented in this thesis. It can be expected that due to the high amplitudes and the unusual distribution of particle parameters within the abort gap also the possible loss pattern during beam abort will show some differences.

The rise time of the transverse damper overlaps with the critical area in the abort gap where the beam is swept over the LHC aperture. It is of interest to do measurements in the LHC machine to determine the actual efficiency of different AGC frequency programs especially during the damper rise and fall time.

8 Beam Commissioning of LHC

The beam commissioning of the newly build beam transfer systems for the LHC began already in 2003 [115] and continued with annual beam tests of new systems [116, 117, 119] up to and including the commissioning of the LHC injections and beam dump systems in late 2008 [120]. The commissioning periods between 2006 and 2008 were important opportunities to deploy and test the simulation software modules and tools being developed for the LHC beam dump, and to compare the results with experimental data.

8.1 SPS extraction beam tests

The TT60 line is the first part of the transfer line TI 2 between the SPS and the LHC. The SPS fast extraction system in long straight section 6 and the first 100 m of transfer line TT60 were commissioned with low intensity beam for the first time in autumn 2006. The new extraction channel installed in LSS6 [117] is a conventional fast extraction system working in the horizontal plane. It comprises horizontal closed orbit bumpers, extraction kickers and DC magnetic septa, together with protection devices and beam instrumentation. In the 2006 test program, extraction systems and all elements up to the 1st safety beam stopper (TED) were commissioned using a single LHC pilot as well as multiple bunches [117]. The same tests were made already in 2003 for the new fast extraction system in LSS4 and the subsequent part TT40.

In addition to achieving the project milestone of transporting the beam to the TED, the main objectives for the commissioning test were to:

- verify the design and performance of the extraction system and beam transport;
- verify the correct installation and alignment of all extraction equipment and the correct implementation to the control system;
- verify the trajectory and settings;
- measure the acceptance of the extraction channels;
- check the performance of the beam instrumentation;
- check the trajectory correction
- measure the MKE kicker ripple;
- check the possibility of operating with 3 MKE to enable operation in short-circuit mode.

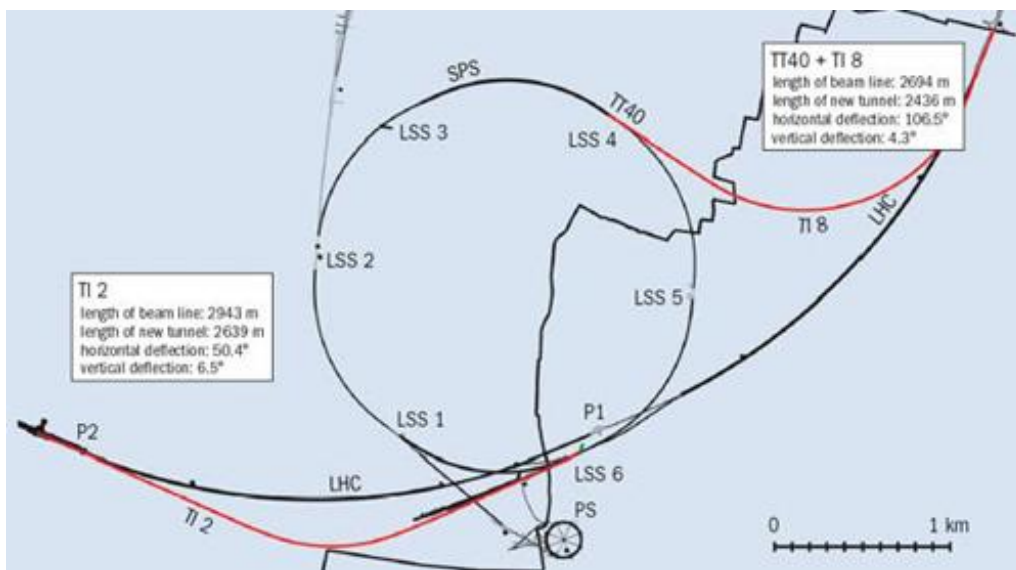


Figure 8.1: Overview of the SPS to LHC transfer lines TI2 and TI8 [118].

The beam was successfully extracted and transported onto the TED beam dump at the end of the line, and in the subsequent tests all of the measurement objectives mentioned above were attained. Equipment and instrumentation performance was quantified and found generally to be as expected, with the exception of the LSS6 extraction kicker where the pulse length was too long (see chapter 4.3) and the flat-top ripple was out of tolerance, requiring some adjustment to the pulse forming network to correct. The feasibility of operating with only three instead of four extraction kickers in LSS6 was demonstrated by checking that the ferrites did not saturate up to a voltage of 34.5 kV, Figure 8.2. The reduction in number of kicker modules gave a cost saving and a reduction of the SPS impedance.

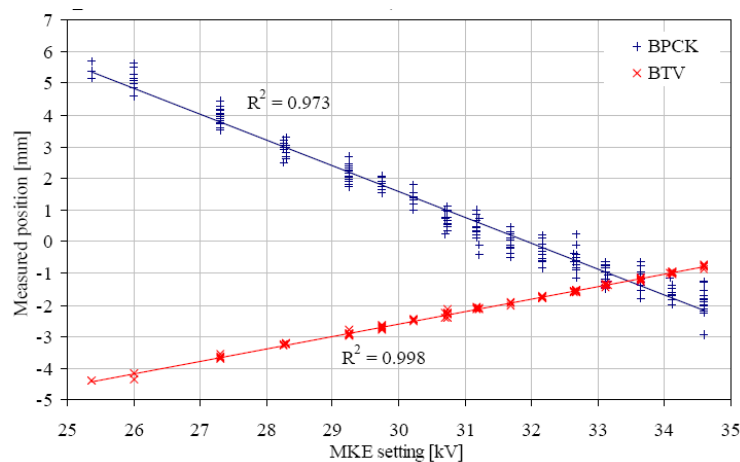


Figure 8.2: Response measurement of beam displacement with MKE6 voltage. No sign of saturation is seen up to 34.5 kV, which demonstrated that the kicker system could be modified to work in short-circuit mode with only 3 magnets.

8.2 SPS to LHC transfer line beam tests

New transfer lines between the CERN SPS and the LHC had to be built, as the existing transfer lines for LEP were designed for 4 GeV leptons and could not be used for the much higher rigidity of 450 GeV protons. The two new lines TI 2 and TI 8 comprise some 420 dipole magnets, 181 quadrupole magnets and 93 corrector magnets [119]. The TI 8 transfer line carries beam from SPS Long Straight Section 4 to the counter-clockwise LHC ring (beam 2) near Interaction Region (IR) 8. Installation of the TI 8 line up to a few metres before the LHC tunnel was already completed in summer 2004 whilst TI 2 was finished in 2007. TI8 was therefore successfully commissioned in autumn 2004, with subsequent annual tests to be ready for LHC operation.

The transfer line for the LHC Ring 1 (TI 2) was successfully commissioned with beam in the autumn of 2007. After extraction from the SPS accelerator and about 2.7 km of new transfer line, the beam arrived at the temporarily installed beam dump, about 50 m before the start of the LHC tunnel, without the need of any beam threading. The detailed verification of the aperture of the transfer line was made in a global fashion using oscillating unclosed bumps, by varying the phase of the oscillation and measuring the transmission to the end of the line. Figure 1.3 shows the measurement result in the horizontal plane, where the TI 2 aperture model is plotted together with the aperture limit at the different phases measured from the transmitted trajectories. Using this technique the physical aperture of the line was confirmed to correspond to the design value of at least $\pm 6 \sigma$ in both planes, after trajectory and tolerances are taken into account.

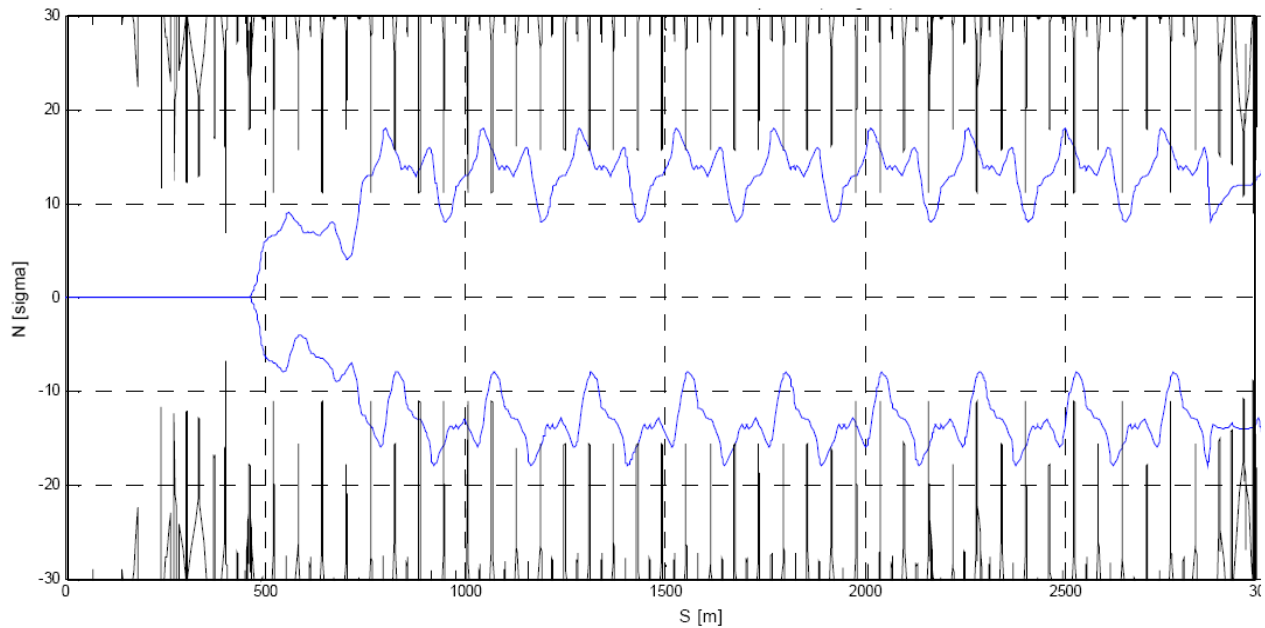


Figure 8.2: Measurement of physical aperture of TI 2 in the horizontal plane.

8.3 LHC sector tests and ring commissioning

A series of LHC injection beam tests was scheduled for late summer 2008 in order to prepare for the 10th September objective to establish circulating beam. Table 8.1 shows a summary of this test program, which was built on the foundations of the TI 2 and TI 8 transfer line beam test organisation, methods and teams.

Table 8.1: Summary of performed Beam tests during LHC Beam commissioning 2008 [120].

<i>Date</i>	<i>Test Outline</i>
8-11 August	Beam 1 through sector 23
22-25 August	Beam 2 through sector 78, beam 1 through sector 23
5-8 September	Beam 2 through sectors 78,67, beam 1 through sectors 23, 34, 45
9 September	Preparation for 10th September – beam 1 through sectors 23, 34, 45
10 September	Beam 1 and beam 2 around the whole circumference of the LHC

The first beam seen in the LHC arrived at 18:53 pm on 8th August 2008, injected via the TI 2 transfer line and stopped after injection by the closed jaws of the protection device TDI (Figure 8.2). After verification of the injection process with beam, the TDI was opened and the beam was sent through sector 2-3, travelling about 3.5 km to be stopped on the collimators in IR 3.

Two weeks later the same procedure was done for beam 2 which was successfully injected into the LHC and transported anti-clockwise through sector 7-8. A careful series of checks were made and no major equipment or aperture problems were observed.

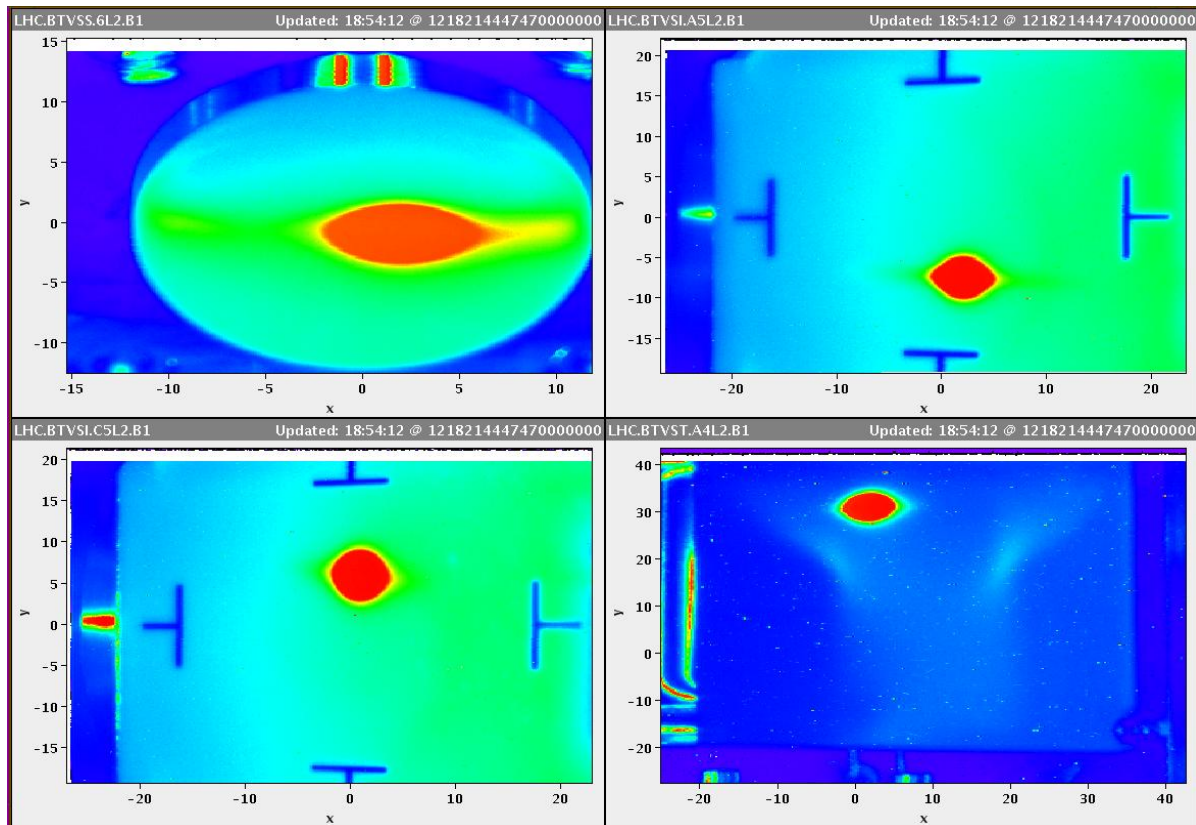


Figure 8.2: First beam ever in the LHC seen by the BTVs in IR2 (after MSI (1st row, left), before MKI(1st row, right), after MKI(2nd row, left) and at the TDI (2nd row, right)).

8.3.1 Beam dump commissioning during the 3rd sector test

On the weekend before the 10th September both beams were injected in an interleaved mode, with beam 1 transported through sectors 2-3, 3-4 and 4-5, and beam 2 through sectors 7-8 and 6-7 to the beam dump. These tests enabled the testing and debugging of a number of critical control and hardware systems as well as the testing and validation of LHC instrumentation with beam for the very first time. These beam based measurements revealed a number of machine configuration issues which could be solved rapidly.

In this 3rd sector test beam 2 was transported to sector 6 where it was initially extracted without the MKD kickers, using two upstream horizontal orbit correctors to provide the correct 0.35 mrad kick angle and 50 mm opening at the MSD septum entrance. The beam trajectory along the extraction channel TD62 was seen to be wrong in the vertical plane, with large beam losses along the TD line. In a first instance vertical correctors were used to steer through, with an angle of over 100 μ rad required to reduce the losses. Later analysis of the strengths showed a 200 μ rad error in the setting of the MSD strength, which was set erroneously at a total of 2.6 mrad for the 15 septa units instead of the nominal 2.4 mrad [121]. Figure 8.3 shows the first shot onto the dump at the end of TD62.

During the subsequent tests the corrector magnets were set back to their normal injection level values and the extraction kickers MKD were switched on to extract the beam in the designed way, synchronized with the injected beam. This was successful on the first attempt, a testimony to the careful preparation. A lot of work was also spent on timing signals and synchronization of the SPS to the LHC to inject the beam into the right buckets which is essential for luminosity production, the experiments and of course for the dump synchronization.

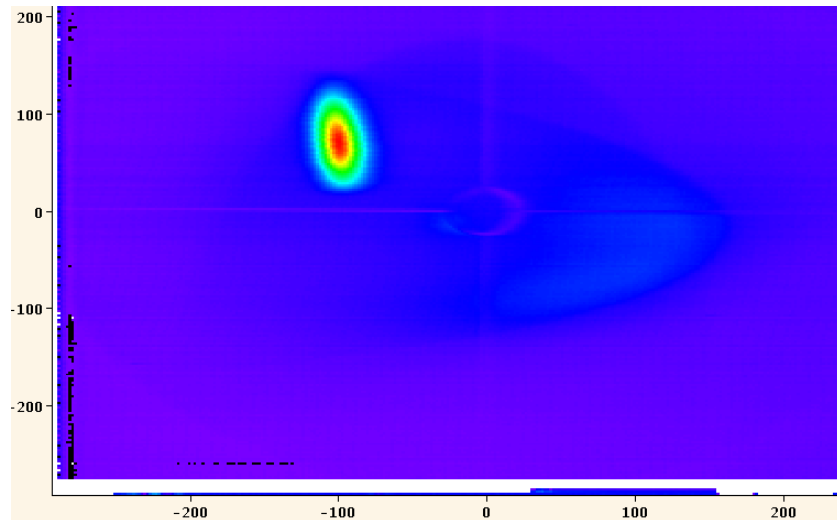


Figure 8.3: First shot to the beam dump seen by the BTVD in TD62.

8.3.2 LHC ring commissioning

On the 10th of September LHC was officially commissioned by circulating beam in both directions. As widely reported [122] the first days of operation were outstandingly successful and various measurement programs were performed until disaster struck on the 19th of September when a superconducting electrical interconnection between the magnets quenched and burned away. It destroyed the insulation vacuum and launched a series of subsequent incidents which lead to widespread damage to sector 3-4 and more than 12 months of LHC down time. However some useful measurement for the LBDS were done in the first days of circulating beam which are further explained in the following sections.

8.4 Aperture scans

Performing aperture scans is one of the first tasks to do when commissioning a brand new beam line. The information gained is important for verifying the correct alignments by a beam based measurement and to define constraints for the possible safe and loss free maximum operational orbits.

8.4.1 Measurement technique

There exist different approaches to measure the aperture of an accelerator. One is to increase the emittance by a controlled beam blow up until the beam gets lost at the closest aperture bottleneck. Another approach is to use closed bumps to measure local aperture. The final approach – the one tested in the TI 2 and TI 8 transfer lines, and used in our studies - is to manipulate the beam oscillations by using two subsequent orbit correctors so that the amplitude extremes scan the given aperture. Equation (8.1) and (8.2) show the position and angle for a trajectory kicked by such a corrector with the kick angle k . A plot illustrating that idea is shown in Figure 8.4 for phases in a 30 degree interval for the measurements planned in TD68.

$$x_s = k \sqrt{\beta_{x(k)} \cdot \beta_{x(s)}} \cdot \sin \Delta\phi \quad (8.1)$$

$$x'_s = k \sqrt{\frac{\beta_k}{\beta_s}} \cdot (\cos \Delta\phi + \alpha_s \sin \Delta\phi) \quad (8.2)$$

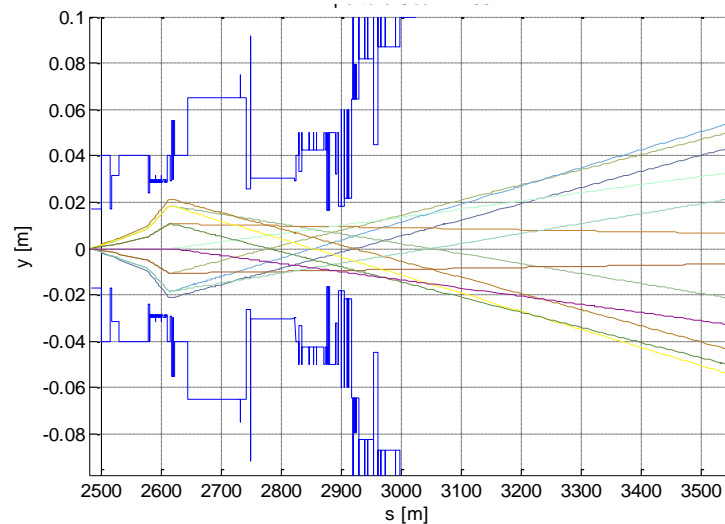


Figure 8.4: Theoretical trajectories for vertical aperture scan in TD68.

The final position is given by eq. (8.3) where the indices 1 and 2 indicate the two positions of the correctors and φ is the phase difference between the two correctors [123]. The individual phase difference $\Delta\phi$ is then measured from the corrector position (indices 1, 2) to the observer position s .

$$x_s = \frac{\sqrt{\beta_s}}{2 \sin(\varphi \cdot Q)} \cdot \left[\sqrt{\beta_1} \cdot k_1 \cdot \cos\left(\left|\Delta\phi_{1(s)}\right| - \varphi \cdot Q\right) + \sqrt{\beta_2} \cdot k_2 \cdot \cos\left(\left|\Delta\phi_{2(s)}\right| - \varphi \cdot Q\right) \right] \quad (8.3)$$

The actual measurement is done by selecting a phase and increasing the amplitude until the beam hits an aperture which is detected by the beam loss monitoring system. The physical aperture can then be derived from the trajectory and the estimated beam size.

8.4.2 Measurement results in the injection regions

Aperture measurements of the injection channel and the first sectors were done as well as instrumentation and optic checks. Interestingly, a significant 10 mm aperture restriction was found in the injection region using the techniques developed in the transfer lines, Figure 8.5, and was discovered to be due to a badly aligned vacuum valve. This was corrected immediately by a physical displacement after the first beam 1 injection test and provided a very good proof of the power of the measurement method.



Figure 8.5: Results of aperture measurements in the vertical plane showing the predicted aperture limit at a vacuum valve between the injection septum and the Q5 quadrupole.

8.4.3 Measurement results for beam dump systems

Aperture measurements in the IP6 and down TD68 started in the late evening of the 18th September and were actually stopped by the 19th September incident. For this reason the scans were not completed and only a few phases could be measured. The results obtained are shown in Table 8.2 for the horizontal plane and

Table 8.3 for the vertical plane. In addition Figure 8.6 and Figure 8.7 show the horizontal and vertical trajectories for the measurements done. A pilot bunch with an emittance of 1.74 nm (horizontal) and 2.42 nm (vertical) was used.

Table 8.2: Horizontal measurement results.

phases	horizontal					
	positive phase			negative phase		
	+ sigma	[mm]	loss location	- sigma	[mm]	loss location
0	11	14.2	Q4	5	6.1	Q5,TCDS
30	12	15.5	Q4	5	7.1	TCDSA
60	12	13.5	TCDSA			
90	6	6.9	TCDSA	12	12.6	MSDC

Table 8.3: Vertical measurement results.

phases	vertical					
	positive phase			negative phase		
	+ sigma	[mm]	loss location	- sigma	[mm]	loss location
0	11	14.2	Q4			
90	15	20.8	MKBH	15	15.7	MKBH

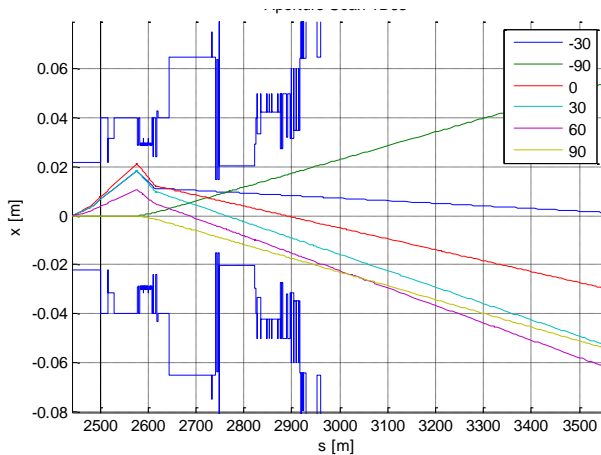


Figure 8.6: Horizontal aperture scan in TD68, measured phases.

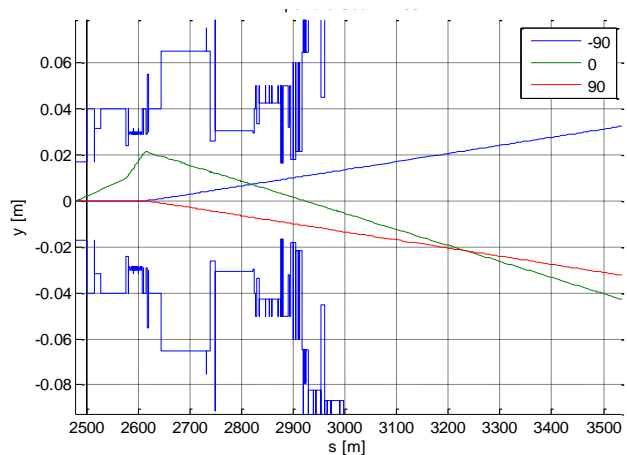


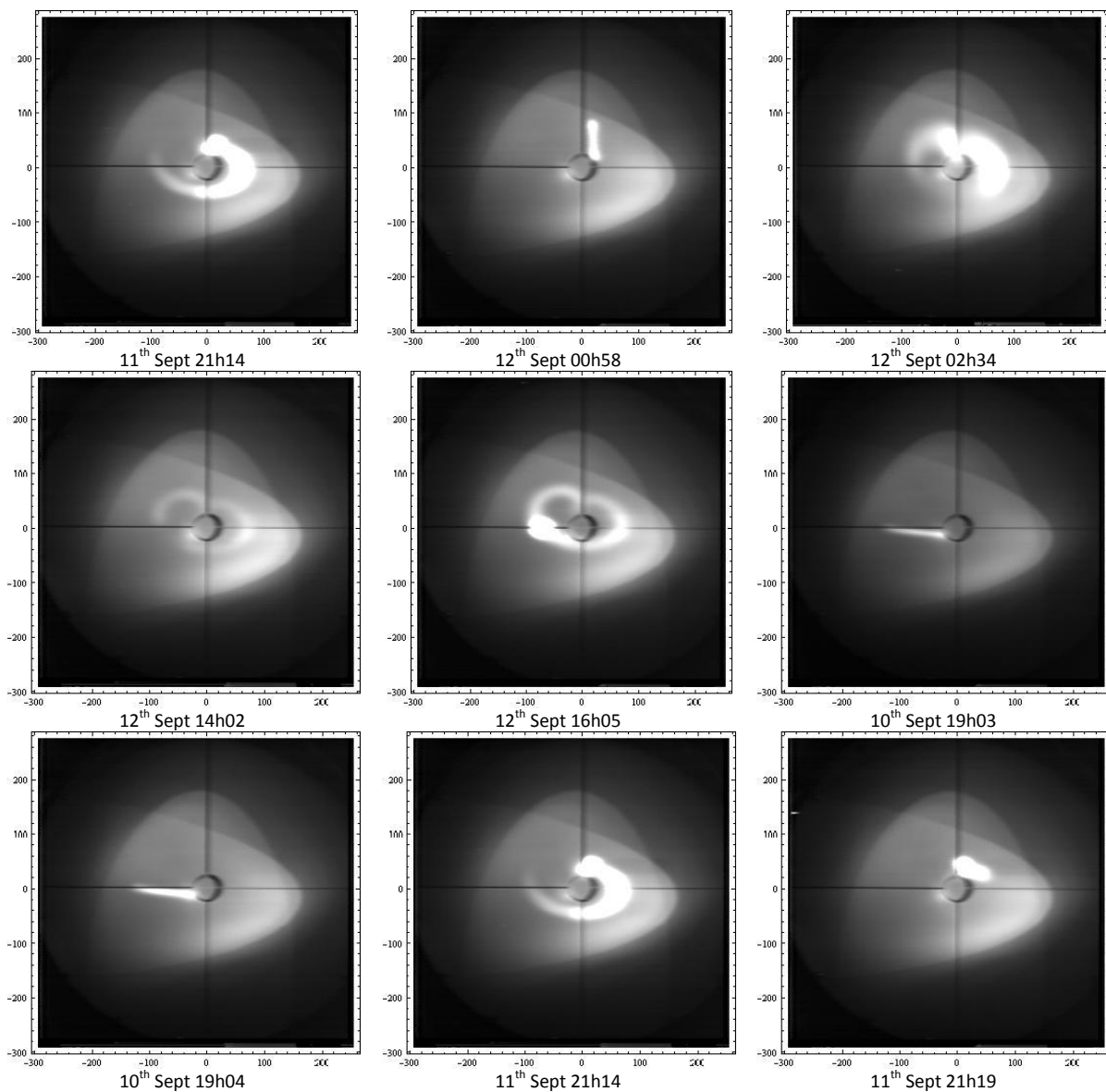
Figure 8.7: Vertical aperture scan in TD68, measured phases.

During the beam commissioning in late 2009 further aperture measurements were done and especially the correct positioning of the protection elements were verified. No significant restrictions or deviations were found. [124]

8.5 Beam dilution

The beam dilution performed by the MKB system is explained in detail in chapter 4.2. Normally the shape of the diluted beam on TDE is also seen by the BTVD in front of the TDE. For early commissioning only a safe beam with one pilot bunch was used, so that this BTVD image is generally not very meaningful for dilution characterisation. Thus a procedure was developed to measure the dilution shape with one bunch only by injecting it into different buckets along the LHC ring so that it would be dumped at different times during the MKB cycle. Unfortunately these measurements could not be done within the 2008 test program. However, it turned out that during RF commissioning the injected particles were frequently longitudinally debunched and distributed along the ring, so that during beam abort a low intensity beam which filled the whole accelerator was dumped. The BTVD sensitivity was high enough to record these traces, which provided excellent sweeps allowing the dilution kicker performance to be quantified. Such events are shown in the table below where one can see the dilution and also images of possibly unstable bunches in the vertical plane (2nd, top row) and the horizontal plane (1st, last row).

Table 8.4: Various sweep shapes measured by the BTVD in TD62 and TD68.



In 2009 the sweep was measured explicitly. Figure 8.8 shows the measured bunch positions (blue) compared to calculated values (red) for single bunches extracted at 450 GeV. The measurements were done with one bunch per shot, injected each time into another dedicated RF bucket around the

ring. Thus the bunch passes the MKB system at a different time after the MKB system was triggered, corresponding to its actual bucket number. Figure 8.9 shows the measured vertical and horizontal deflection corresponding to the MKBV and MKBH system. The pattern measured at the BTVDD (in front of the TDE) showed a great coherence with dilution shapes derived from numerical simulations. Only small offsets (30 mm) were seen due to slight kick strength mismatches and small orbit deviations.

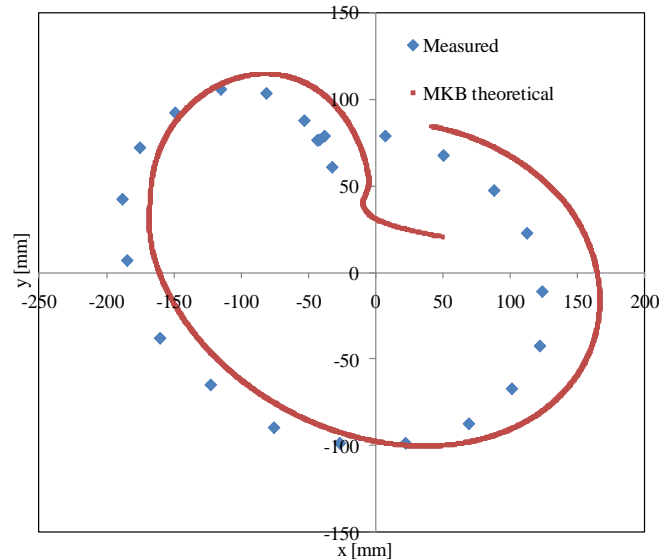


Figure 8.8: Measured bunch position (blue) and theoretical MKB-deflection (red), 450 GeV.

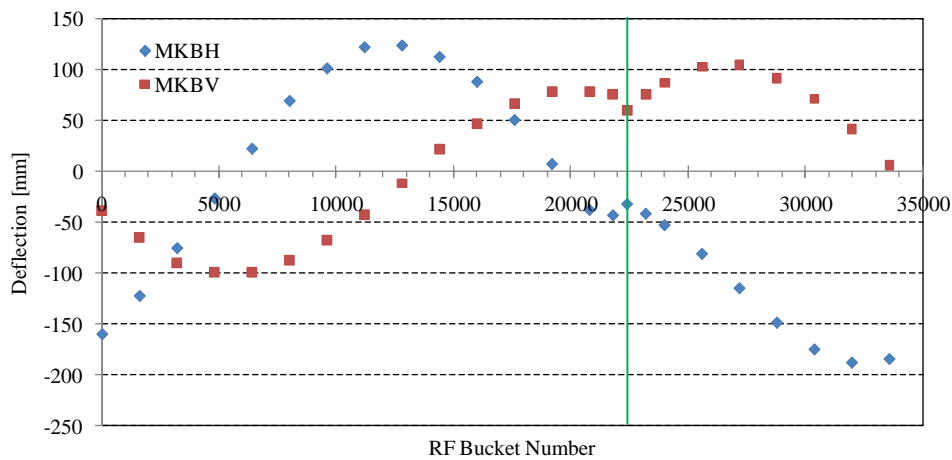


Figure 8.9: MKBH (blue) and MKBV (red) deflection versus RF-bucket number for measured bunch positions, 450 GeV (green line indicates extraction in the subsequent turn).

8.6 Beam loss monitors

The images shown in Table 8.4 were taken during beam abort with debunched beam. This implies that also the abort gap was filled and so every dump swept particles over the TCDS aperture as for an asynchronous dump. When we discovered the BTVD images of the diluted debunched beam the conclusion was self-evident that we should see the swept beam on the LHC ring BLMs. This provides a good opportunity to check the simulation predications in terms of loss locations, although since the collimators were all retracted the situation does not reflect the final LHC configuration. For further studies the dump event from the 12th September 2008, 02h34 has been used (3rd picture top row in Table 8.4), as it nicely shows the expected losses along LHC IP 6. Figure 8.10 shows the BLM readings in IP6 at the time of the dump action described above. The biggest readings are seen

for the TCDS and the TCDQ as expected, but also some small readings on the MSDA and MQY are seen which are most likely to be the developed showers from the impact on the TCDS respectively TCDQ. No losses were seen anywhere else around the LHC ring.

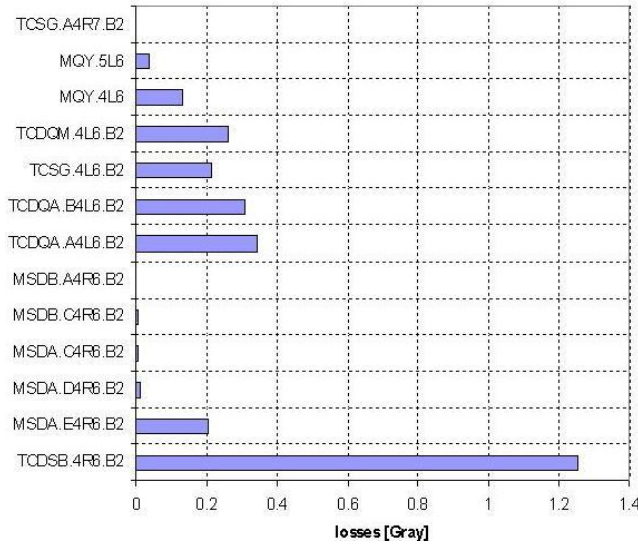


Figure 8.10: 2h34 incident BLMs.

Figure 8.11 shows an overview of such asynchronous like dump events on the 12th of September 2008 in IP6 which all show more or less a similar pattern.

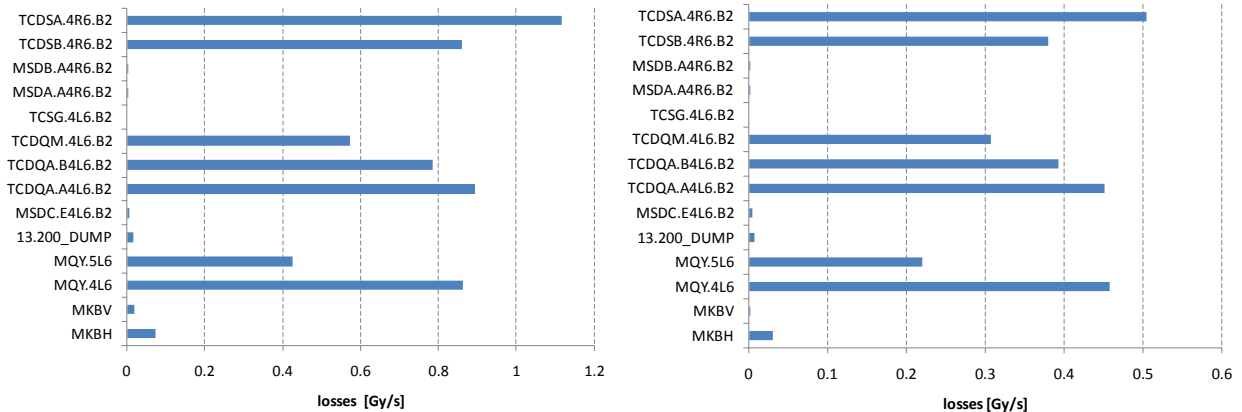


Figure 8.11: Losses for beam 2, extraction region, 12.09.2008, 12h53 (left) and 18h28 (right).

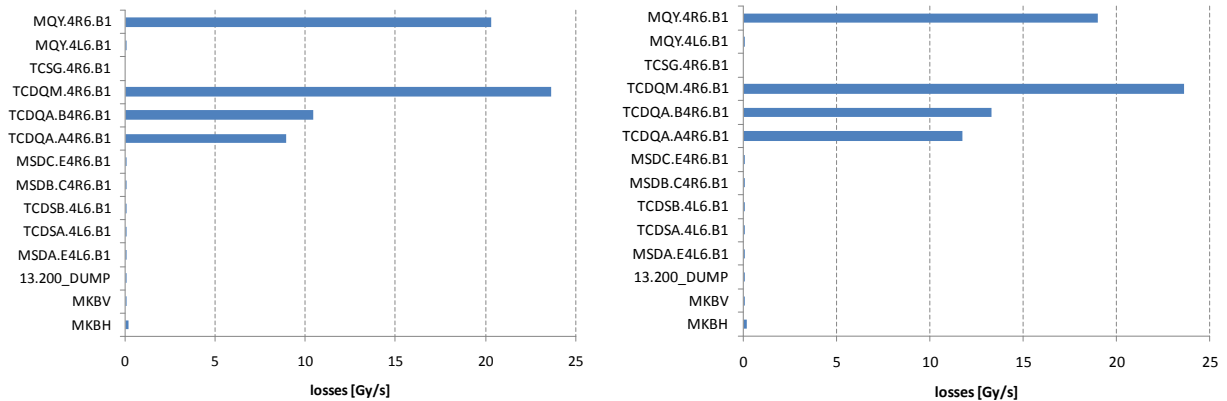


Figure 8.12: Losses for beam 1, extraction region, 18.09.2008 beam 1 23h23 (left) and 23h44 (right)

Figure 8.12 shows the observed BLM signals during the aperture scan performed in the night from the 18th to the 19th of September. No losses are seen on the TCDS for these scans as the excitation amplitudes were not big enough to reach the TCDS aperture but losses appear as foreseen at the TCDQ. This device was set to -1mm in order to intercept the excited beam. Interestingly the highest loss amplitude can be seen on the TCDQM and MQY downstreams of the TCDQ.

These first results of the 2008 beam commissioning are very important as they show that one possibility to measure the loss pattern during asynchronous dumps is to unbunch low intensity beam which then fills the abort gap and is swept over the aperture even during “synchronized” beam abort. For a given beam energy and momentum spread, the expected abort gap population as a function of time can be derived for the filling pattern used; in reality the abort gap population can be measured by the abort gap monitor in 100 ns bins. A uniform density in the abort gap would be easiest to analyse.

In such a way different collimator settings can be studied for preferred machine optics versions and simulations can be verified. Furthermore it should be possible to identify critical thresholds for collimator positions (especially in IR6), orbit offsets and beta beating. BCT’s can be used to determine the beam intensity before the dump in order to have a reference value for observed losses.

8.7 Measurements during 2010 commissioning

The experience gained during the 2008 tests was used to measure first loss patterns with unbunched beam at 450 GeV in early 2010. Figure 8.13 shows a screenshot of the BLM readings for a provoked asynchronous dump of beam 1 at 450 GeV and with a total intensity of 1×10^{11} protons. Losses are limited to the dump protection elements and the beam cleaning collimation system in IR7 and IR3, with no losses in the LHC arcs or experimental insertions. [125]

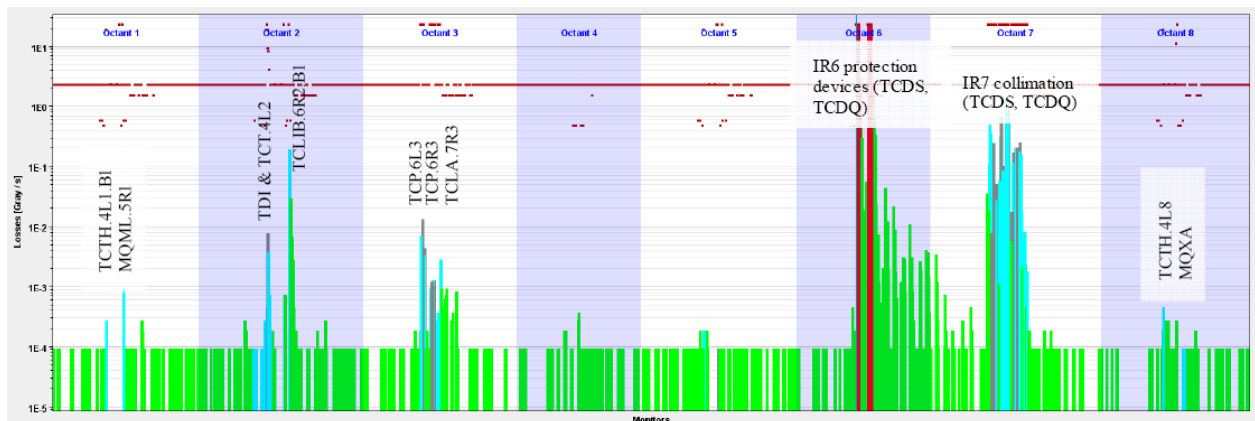


Figure 8.13: BLM signals during a provoked asynchronous dump at 450 GeV, 1×10^{11} p⁺ total intensity.

8.8 Conclusions

The well prepared sector and synchronization tests were the key to the very successful beam commissioning on the 10th of September 2008. In the first days of LHC operations the further commissioning phase went on very quickly, but due to the 9/19 incident the major test programs concerning the LBDS were not accomplished. However the basic functionality of the system was established and measurement techniques were validated and improved on.

The analysis of the obtained data showed that beam was transported through to both dumps without any major problems. BTVDD data showed that the beam dilution is working properly. A few minor issues were resolved, and a significant error of almost 10% in the MSD strength setting was quickly diagnosed and corrected.

Aperture scans of the extraction channel were performed but could not be completed in 2008. They show loss positions as one would expect from the aperture values, and for the phases covered there were no suspicions of any aperture restrictions. Those first results were later confirmed by more detailed measurements during the commissioning phase in the end of 2009.

The studies of different BTV images with dump shapes brought the conclusion that some data on asynchronous-like dump events with debunched beam was recorded by the BLMs. Detailed analysis of this data showed that loss patterns obtained from simulations agreed with what was seen from BLMs. Small losses on subsequent BLMs after the protection devices can be explained by the monitoring of developed showers. The same is true for the MKBH monitors in the dump line which are still situated close to the circulating beam line in the region after the beam1 TCDQ.

Future tests should make advantage of this newly proposed technique by using debunched beam to verify the simulation results against loss positions in the accelerator, to check the setup of the TCDQ protection device with respect to the tertiary collimators and general machine aperture.

9 Summary, Conclusions and Outlook

In this thesis beam dump and extraction systems were studied in general and beam physics aspects associated with beam in the abort gap during the dump process were analyzed in detail. The work described was essentially carried out over the period from September 2006 to early 2009, although some significant results obtained in later 2009 and early 2010 have been quoted where relevant for specific items.

Mad-X tracking and PSpice have been used to model failures of the SPS beam dump. This exercise showed the general feasibility of the developed concept on an already commissioned and well understood machine. Current waveforms for spark failures have been simulated for an existing PFN-model and were interfaced to MAD-X. Tracking programs have been developed for the challenging and so far not used case of time dependent kicks. With this new tool loss patterns were created and compared to measurement. The studies show that during MKDV failures particles do not survive more than two turns due to the MKDH field. In the case of sparks the TIDV yoke is hit, not the graphite core. This might be a problem and requires further investigation. All major losses outside of LSS1 occurred on main bending magnets. Irradiation and losses at the aperture limiting MPLH bumpers were confirmed for the previous layout: losses with a modified bumper position were shown to be negligible, in agreement with measurement. An extension to include orbit and alignment errors to the study was identified to be required to explain all the observations.

Based on the techniques developed for the SPS study case the model was adapted and deployed to the much more challenging LHC machine. Sequences for the LHC extraction and dump lines were written including a detailed study and description of these regions aperture. The developed MAD-X tracking tool was extended to allow to include multiple failures and errors as well as their correction in order to get a machine model which reflects reality as closely as possible for tracking of LHC asynchronous dump events.

Simulations of asynchronous dumps were performed and loss patterns analysed, where surprisingly unwanted losses at the TCTs could be identified and their origin confirmed. Measurements with beam were started, to validate the system protection.

For all the failure cases considered, no losses have been seen for beam 1 on any lattice magnets, instruments or experiments, even for the TCDQ fully retracted. All observed loss points were either a collimation/protection device or the LHC beam dump block. This is an important result for 450 GeV, which shows that the arc downstream of IR6 should be well protected by the fixed TCDQM, although this is likely to suffer some damage from an asynchronous dump at high intensity. The results also show that the TCT collimators are frequent beam loss locations for the discussed settings and 7 TeV beam only; since these are presently made of tungsten with a low damage threshold, it would be interesting to consider a more robust design.

The application of the beam 1 results to LHC beam 2 is not straightforward, since the LHC is not symmetric with respect to the layout and sequence of beam dump, collimators and experiments. In particular, for beam 2 IR5 is immediately downstream of IR6 without any intervening collimation system. Beam 1 simulations were performed with all collimators retracted, to approach these conditions, and higher losses were seen on the TCTs; however, dedicated beam 2 simulations should be made, in particular to investigate the effects of the different phase advances.

Simulations with missing MKD modules have shown that the TD68 beam transfer line and the setup of the TCDS seems to be well designed. No losses have been observed for all MKD failure cases (except on the TCDS for asynchronous dumps, and whilst remaining within specifications for simulated error cases). The simulation with 12 MKD magnets only shows that all particles are either intercepted by the TCDS or still on the TDE – in this event the TCDS and possibly the downstream MSD magnets will be damaged or destroyed.

The case with one MKD only shows that most of the beam is intercepted by the TCDQ which will see a load far above its specification – in addition the TCT in IR1 and 2 are also critically loaded with beam. This worst case scenario is expected to seriously damage these components. To quantify the seriousness of such an incident, further damage to elements behind those by developed showers and the probability of beam finally penetrating the protection element should be studied.

The mean losses on the TCTH elements are already above the damage limit for a TCDQ setting of 8.5σ - and for some seeds the losses at this small retraction were a factor of 3 above the damage limit. This indicates that the risk of damage to the TCTH elements may be larger than previously assumed, and that the protection concept may need to be re-thought or additional measures considered. Otherwise this effect may limit the minimum β^* which can be achieved.

Simulations and analytical analysis showed that the TCDQ protection system allows the transmission of particles into the ring for high amplitude particles already at a smaller TCDQ gap setting than initially anticipated. This was identified to be the case because of the finite beam sizes and the phase advance deviations between the MKD and the TCDQ system, and was confirmed with analytical estimates.

In analyzing the results it must be considered that these simulations are based on worst case incidents, and that large retractions of the TCDQ in conjunction with the rare occurrence of an asynchronous dump are unlikely to happen in practice. It must also be in mind, that beam in the abort gap will essentially produce an asynchronous dump at every beam dump event, which means that the abort gap cleaning and monitoring systems are very important in the machine protection of the LHC.

The abort gap cleaning with the transverse damper has been shown to work in simulation for the SPS and LHC, with a strong dependence on the strength of the non-linear fields in the model. The principle was tested in experiments on the SPS using the transverse damper for different non-linear element strengths, with a good agreement between measurement and model. The tracking studies and SPS measurements show that the cleaning effectiveness is very sensitive to tune changes and high chromaticity. The rise time of the transverse damper overlaps with the critical area in the abort gap where the beam is swept over the LHC aperture. It is of interest to do measurements in the LHC machine to determine the actual efficiency of different AGC frequency programs especially during the damper rise and fall time.

The analysis of already obtained commissioning data shows that beam is transported through to both dumps without any major problems. BTVDD data indicates that the beam dilution is working properly for energies up to 3.5 TeV. Aperture scans of the extraction channel were performed. They show loss positions as one would expect from the aperture values and simulations performed and presented in this thesis.

The studies of different BTV images with dump shapes brought the conclusion that some data on asynchronous like dump events was recorded by the BLMs. Detailed analysis of this data showed that loss patterns obtained from simulations agreed with what was seen from BLMs. A measurement procedure was invented on that observation which uses debunched beam to verify the simulation results against loss positions in the accelerator. This procedure has been used systematically during the 2010 LHC commissioning.

Overall the simulations showed that the LHC beam dump system is well designed, with sufficient margin to accept the failure cases which are expected to happen during its operation. The only real concern is the allowed margin of retraction of the TCDQ, which could lead to high beam loss on the TCT collimators and might pose a limit to operation.

9.1 Outlook

For further studies it would be interesting to create a more realistic abort gap particle distribution. Such a distribution could then be used for tracking studies as presented in this thesis. It can be expected that due to the high amplitudes and the unusual distribution of particle parameters within the abort gap also the possible loss pattern during beam abort will show some differences.

Future work has to focus on calculations and settings adjustments to minimize the transmission of potentially dangerous swept particles from the TCDQ system onto the TCTs, for operation with high energy and small β^* .

First measurements for beam 2 show similar results than simulations for the assumed beam 2 (beam 1 simulations with disabled collimators in IR7); however, observations show the need for an implementation of the beam 2 sequence to get more precise information. This is particularly important to check for swept particle trajectories in IR5 which play a potential danger for measurement equipment (e.g. roman pots) installed close to the beam.

Future developments should focus on further automatization of the developed processes. Due to the huge amount of data, extreme calculation times during simulation and post processing have been observed. An efficient data management on particle level would significantly improve the usability. The automatized selection of “interesting” particles and particle groups identified by selected parameters would boost the efficiency in understanding complex processes which lead to suspicious particle depositions. An online matching of the results with measurements procedures (which need to be embedded) would help to quickly compare simulation results to real machine measurements.

The future precise validation of simulation results will allow to use such techniques to evaluate safety and operation parameter settings for higher energy levels. This is particularly interesting as machine development and measurement at top energy is time consuming due to long beam generation cycles as well as it is a concern of machine safety. Hence simulations can give useful starting points to minimize the measurement effort and should be closely interfaced to real machine data.

Appendix

Used acronyms

ADT	LHC Transverse Damper
AGC	Abort Gap Cleaning
BEA	Beam Energy Acquisition
BETS	Beam Energy Tracking System
BIC	Beam Interlock Controller
BIS	Beam Interlock System
BLM	Beam Loss Monitor
BPM	Beam Position Monitor
BRSA	Abort gap monitor
BTV	Beam TV
BTVDD	Dump line BTV - in front of the TDE
DCCT	Direct Current Current Transformer
EPAC	European Particle Accelerator Conference
FMCM	Fast Magnet Current change Monitor
IPAC	International Particle Accelerator Conference
IP	Interaction Point
IR	Interaction Region
LBDS	LHC Beam Dump System
LHC	Large Hadron Collider
MKB	Dilution Kicker
MKD	Magnetic Kicker -Dump
MPS	Machine Protection System
MQY	Quadrupole with enlarged aperture
MSD	Magnetic Septa - Dump
PAC	Particle Accelerator Conference
PTU	Power Trigger Unit
SPS	Super Proton Synchrotron
TCSG	Secondary collimators
TCDS	Fixed septa protection element
TCDQ	Quadrupole protection element in IR6
TCDQM	Fixed iron mask installed close to the TCDQ
TCP	Primary collimators
TCT	Tertiary collimators

TD62	Beam 2 Dump line
TD68	Beam 1 Dump line
TDE	LHC external beam dump
TDI	Moveable injection protection dump block
TI2	Beam 1 SPS-LHC transfer line
TI8	Beam 2 SPS-LHC transfer line
TSU	Trigger Synchronization Unit
TT40	short transferline leading from SPS LSS4 to TI8
TT60	short transferline leading from SPS LSS6 to TI2
VDDA	Differential vacuum pumping device

Bibliography

- 1 M.L. de Broglie, Recherches sur la théorie des Quanta, Annales de Physique 10^e Serie, January 1925, p.33
- 2 R. B. Appleby, et al., Beam-related machine protection for the CERN Large Hadron Collider experiments, Phys. Rev. ST Accel. Beams, Vol. 13, 061002, June 2010
- 3 B. Goddard, et al., Initial Results from Beam Commissioning of the LHC Beam Dump System, proc. PAC09, Vancouver, 2009, p. 1584 ff.
- 4 O. Brüning, et al., The Nominal Operational Cycle of the LHC with Beam, LHC Project Note 313, CERN, Geneva, Feb. 2003, p.8
- 5 O. Brüning, et al., LHC Design Report Volume I The LHC Main Ring, CERN, Geneva, June 2004, p.4
- 6 O. Brüning, et al., LHC Design Report Volume I The LHC Main Ring, CERN, Geneva, June 2004, p.468
- 7 R. Schmidt, Machine Protection, proceedings CAS 2009, unpublished
- 8 B. Holzer, et al., Beam Loss Monitoring system for the LHC, proc. IEE NSS 2005, San Juan, 2005
- 9 A. Gómez Alonso, Redundancy of the LHC Machine Protection Systems in Case of Magnet Failures, PhD thesis, CERN, Geneva, 2009, p.42
- 10 J. Wenninger, Beam Interlocks, proc. Chamonix workshop 2009, Chamonix, 2009, p.252
- 11 B. Todd, A Beam Interlock System for CERN High Energy Accelerators, PhD thesis, CERN, Geneva, 2006
- 12 R.Schmidt, et al., LHC Maschine Protection, Proceedings of PAC07, Albuquerque, 2007, p.887
- 13 O. Brüning, et al., LHC Design Report Volume I The LHC Main Ring, Chapter 18, CERN, Geneva, June 2004
- 14 R. Assmann, et al., The final collimation system for the LHC, CERN-LHC-Proj.-Report-919, Geneva, 2006
- 15 A. Chao, M. Tinger, Handbook of Accelerator Physics and Engineering, 2nd printing, ISBN 9810235005, 2002, p.7
- 16 D.A. Edwards, M.J. Syphers, An Introduction to the Physics of High Energy Accelerators, Wiley, New York, 1993, Chapter 3
- 17 K. Wille, Physik der Teilchenbeschleuniger und Synchrotronstrahlungsquellen, 2. Auflage, Teubner Stuttgart, 1996, p.89-91
- 18 E.D. Courant and H.S. Snyder, Theory of the Alternating Gradient Synchrotron, in annals of physics vol.3, BNL, New York, 1958
- 19 <http://mad.web.cern.ch/mad/> , MAD-X webpage, Dec. 2009
- 20 H. Grote, F. Schmidt, MAD-X: An upgrade from MAD-8, proc. PAC 2003, Portland, May 2003, p.3497 ff
- 21 F. Schmidt, et al., User Guide, http://mad.web.cern.ch/mad/madx_manual.pdf, Dec. 2009
- 22 cern.ch/lhcoptics , LHC optics homepage, dec. 2009
- 23 B.Autin, Y.Marti, Closed orbit correction of A.G. machines using a small number of magnets, CERN ISR-MA-73-17, Geneva, March 1973, p.9 ff
- 24 K. D. Metzmacher, CTF3 Kickers and Septa, CLIC collaboration meeting, Geneva , Nov. 2004
- 25 M.J. Barnes, G.D. Wait, et al., A fast 66 KV Resonant Charging Power Supply for the LHC Inflectors, Proc. Of PAC97, Vancouver, 1997, p. 1325
- 26 M.J. Barnes, L. Ducimetière, T. Fowler, V. Senaj, L. Sermeus, Injection and Extraction Magnets: Kicker Magnets, proc. of specialized CERN Accelerator School on Magnets, Brugge, 2009, unpublished
- 27 EV2 Technologies, Hydrogen Thyatron Preample, Elmsford, 2002, p. 3
- 28 S.Bidon, M. Gyr, et al., Steel septum magnets for the LHC beam injection and extraction, proc. EPAC02, Paris, 2514 ff, 2002
- 29 M.J. Barnes, J. Borburgh, B. Goddard, M. Hourican, Injection and Extraction Magnets: Septa, proc. of specialized CERN Accelerator School on Magnets, Brugge, 2009, unpublished
- 30 B. Goddard, Injection & Extraction, presentation at CERN Accelerator School, Zakopane, Oct. 2006
- 31 B. Balhan, et al., Beam Commissioning of the SPS LSS6 Extraction and TT60 for LHC, proc. PAC07, Albuquerque, 2007
- 32 T. Kramer, et al., Studies of beam losses from failures of SPS beam dump kickers, proc. PAC07, Albuquerque, 2007
- 33 The 300 GeV Programme, CERN, Geneva, Jan. 1972
- 34 P. Faugeras, et al., Beam Dumping in the SPS, CERN LAB II/BT/Int./72-5, Geneva, Oct. 1972
- 35 Cadence Design Systems, Pspice A/D tech brief, San Jose, http://www.cadence.com/rl/Resources/technical_briefs/PSpice_tb.pdf , April 2010
- 36 Mathworks, MATLAB R2009a, Massachusetts, <http://www.mathworks.com/> , Feb. 2010
- 37 B. Goddard et al., “PS2 Beam Transfer Systems: Conceptual Design Considerations“, AB-Note-2007-001-BT, Geneva, January 2007
- 38 A.Fassò et al., “The FLUKA code: description and benchmarking“, AIP Conf. Proc. 896, 2007, pp. 31-49
- 39 T. Kramer, M. Benedikt, B. Goddard, Hel.Vincke, Design considerations for the PS2 beam dumps, proceedings of EPAC08, Genoa, 2008

-
- 40 The LHC Design Report, Vol.1, Chapter 17, CERN, Geneva, 2004, p. 441 ff.
- 41 R.B. Appleby, et al., Beam-related machine protection for the LHC experiments, Phys. Rev. ST Accel. Beams, Vol. 13, 061002, June 2010
- 42 B. Goddard, et al., The Commissioning of the LHC Machine Protection System – Beam Dump System Commissioning, EDMS 896392, CERN, Geneva 2009
- 43 M. Zerlauth, et al., Requirements for the Fast Magnet Current Change Monitors (FMCM) in the LHC and the SPS-LHC transfer lines, functional specification LHC-CIW-ES-0002, CERN, Geneva, Nov. 2005, p. 21
- 44 A. Antoine, E. Carlier, N. Voumard, The LHC Beam Dumping System Trigger Synchronisation and Distribution System, 10th ICALEPCS Int. Conf. on Accelerator & Large Expt. Physics Control Systems, Geneva, Oct. 2005
- 45 E. Carlier, Jean-Louis Bretin, Power Triggering, external LBDS Audit, CERN, Geneva, January 2007
- 46 E. Carlier, LHC extraction kicker – triggering and retriggering, presentation in: LHC Machine Protection Working Group, 25. Nov. 2005
- 47 E. Vossenbergl, L. Ducimetière, G. Schröder, Improved Turn-on Characteristics of Fast High Current Thyristors, proceedings of 23rd Int. Power Modulator symposium, California, 1998
- 48 L. Ducimetire, LHC Beam Dump System Kicker magnets and generators, LBDS Audit, Geneva, Jan. 2008
- 49 The LHC Design Report, Vol.1, Chapter 17, CERN, Geneva, 2004, p. 449
- 50 J. Uythoven, B. Goddard, MKD and MKB System Calibration Requirements, Functional Specification EDMS 626873, CERN, Geneva, 2005
- 51 J. Bonthond, L. Ducimetière, P. Faure, E.B. Vossenbergl, Modular Solid-State Switch for the SPS and LHC Beam Dump Systems, proceedings of 5th Modular Klystron Workshop for future linear colliders MDK 2001, Geneva, April 2001
- 52 R. Aßmann, B. Goddard, E. Vossenbergl, E. Weisse, The Consequences of Abnormal Beam Dump Actions on the LHC Collimation System, LHC Project Note 293, CERN, Geneva, May 2002, p. 4
- 53 R.A.Barlow, et al., The beam energy tracking system of the LHC beam dumping system, 10th International Conference on Accelerator and Large Experimental Physics Control Systems, Geneva, Oct. 2005
- 54 E. Carlier, et al., Safe Beam Energy Tracking, presentation in LHC Machine Protection Review, Geneva, April 2005
- 55 The LHC Design Report, Vol.1, Chapter 17, CERN, Geneva, 2004, p. 446
- 56 LHC optics version 6.503, LHC optics webpage: <http://proj-lhc-optics-web.web.cern.ch/proj-lhc-optics-web/>
- 57 M.Gyr, J. Uythoven, A. Verdier, Tolerance on MQY.4L6.B1 gradient, Beam physics note 75, Geneva, February 2004, p.3
- 58 S.Bidon et al., Steel septum magnets for the LHC beam injection and extraction, CERN-SL-2002-019-MS, 2002.
- 59 N.V. Mokhov et al., Further studies on protecting LHC components against radiation resulting from unsynchronized beam abort, FERMILAB-FN-724, Batavia, 2002
- 60 W.Weterings et al., TCDS diluter to protect MSD septum magnets, LHC-TCDS-ES-0001 rev 1.3, 393973 CERN, Geneva, 2006.
- 61 W.Weterings et al., Alignment of Extraction Septa (MSD) and their Protection Device (TCDS), CERN EDMS 631718, Geneva, April 2007
- 62 W.Weterings, Alignment Procedure for the Extraction Protection Device TCDS, CERN EDMS 704000, January 2007
- 63 J.B. Jeanneret, R.Ostojic, Geometrical acceptance in LHC Version 5.0, LHC Project Note 111, CERN, Geneva, Sept. 1997, p.2
- 64 B. Goddard, M. Gyr, The Aperture and Layout of the LHC Extraction Septa and TCDS Diluter with an Enlarged MSDC Vacuum Chamber, LHC Project Note 320, Geneva, August 2003
- 65 M.Gyr, Alignment of the injection (MSI) and extraction septa (MSD), CERN EDMS 4888061, Geneva, June 2007
- 66 M. Gyr, Horizontal Offset of the Diluter Magnets and Beam Instruments in the Dump Lines, CERN EDMS 849665, Geneva, 2007
- 67 W.Weterings et al., TCDQ Collimator to protect the LHC against unsynchronized beam dumps, LHC-TCDQ-ES-0001 rev 1.0, CERN EDMS 503490, Geneva, 2003.
- 68 A. Presland, et al., A Large Diameter Entrance Window for the LHC Beam Dump Line, PAC05, Knoxville, May 2005
- 69 R. Filipini, Dependability Analysis of a Safety Critical System: The LHC Beam Dumping System at CERN, PhD Thesis, Universita di Pisa, 2006
- 70 R. Filipini, et al., Reliability analysis of the LHC beam dumping system, proceedings of PAC05, Knoxville, 2005, p. 1201 ff.
- 71 R. Filipini, J. Uythoven, Update and Summary of the Dependability Assessment of the LHC Beam Dumping System, proceedings of EPAC06, Edinburgh, 2006, p. 2706 ff.
- 72 R. Fillipini, et al., Reliability Assesment of the LHC Machine Protection System, proceedings of PAC05, Knoxville, 2005, p. 1257 ff.
-

- 73 J. Uythoven, et al., Results from the LHC Beam Dump Reliability Run, proceedings of EPAC08, Genoa, 2008, p. 2671 ff.
- 74 Running Jobs with Platform LSF, version 7.0, CERN, Geneva, March 2006
- 75 S. Fartoukh, O. Brüning, Field Quality Specification for the LHC Main Dipole Magnets, LHC Project Report 501, CERN, Geneva, October 2001
- 76 A. Verdier (ed.), Report on the mini-workshop on the LHC alignment, LHC Project Note 247, CERN, Geneva, February 2001
- 77 S. Fartoukh, M. Giovanozzi, Target values for the azimuthal misalignment of the LHC magnets, LHC Project Note 866, CERN, Geneva, February 2006
- 78 A. Verdier, K-modulation in the LHC arcs?, LHC project note 347, CERN, Geneva, June 2004, p.3
- 79 O. Brüning, Optics Solution in IR1 and IR5 for Ring-1 and Ring-2 of the LHC Versiom6.0, LHC Project Note 187, CERN, Geneva, April 1999
- 80 MAD-X Users Guide, Version 2002, CERN, Geneva, June 2002, p. 57
- 81 P. Le Roux, et al., LHC Reference Database: Towards a Mechanical, Optical and Electrical Layout Database, proc. EPAC04, Luzern, June 2004
- 82 T. Kramer, B. Goddard, et al., Apertures in the LHC Beam Dump System and Beam Losses during Beam Abort, proc. EPAC08, Genoa, 2008, p. 2665 ff.
- 83 D. Bocian, et al., Modeling of Quench Limit for Steady State Heat Deposits in LHC Magnets, IEEE transactions on applied superconductivity, vol. 18, no. 2, June 2008, p. 112
- 84 T. Kramer, et al., LHC Beam Dump System – Consequences of Abnormal Operation, proc. PAC09, Vancouver, May 2009
- 85 The LHC Design Report, Vol.1, Chapter 12, CERN, Geneva, 2004, p. 339
- 86 B. Goddard, W. Weterings, et al., Conceptual Design of the LHC Beam Dumping Protection Elements TCDS and TCDQ, proc. EPAC 04, Luzern, July 2004
- 87 W. Weterings, TCDS diluter to protect MSD septum magnets, functional specification EDMS 393973, CERN, Geneva, May 2006
- 88 B. Goddard, L. Massidda, et al., Dynamic Stresses in the LHC TCDS Diluter from 7 TeV Beam Loading, proc. EPAC 06, Edinburgh, June 2006
- 89 R. Filippini, Dependability Analysis of a Safety Critical System: The LHC Beam Dumping System at CERN, CERN-Thesis-2006-054, University of Pisa, 2006
- 90 Summary of the 16th LHC Injection and Beam Dump Coordination Meeting, 28th July 2009, CERN, Geneva, <https://proj-lti.web.cern.ch>
- 91 N.A. Tahir, et al., Large Hadron Collider at CERN: Beams generating high-energy-density matter, Phys. Rev. E 79, 046410 (2009)
- 92 The LHC Design Report, Vol.1, Chapter 10, CERN, Geneva, 2004, p. 278
- 93 M. Gyr, J. Uythoven, A. Verdier, Tolerance on MQY.4L6.B1 gradient, Beam physics note 75, CERN, Geneva, Feb. 2004
- 94 G. de Rijk, Workshop on LHC powering, chapter warm magnets, CERN, Geneva, Nov. 2000
- 95 M. Zerlauth, et al., Requirements for the Fast Magnet Current Change Monitors (FMCM) in the LHC and the SPS-LHC transfer lines, functional specification LHC-CIW-ES-0002, CERN, Geneva, Nov. 2005, p. 21
- 96 The LHC Collimation Project, Collimator Database, <http://lhc-collimation-project.web.cern.ch/lhc-collimation-project/>, CERN, Geneva, August 2010
- 97 T. Kramer, B. Goddard, TCDQ positioning and losses on TCT's, presentation at the LHC Machine Protection Panel, CERN, Geneva, October 2009
- 98 A. Presland, B. Goddard, Performance of the TCDQ diluter system, LHC Project Note 362, CERN, Geneva, Feb. 2005
- 99 R. Assmann, Damage Limits for LHC Collimators, Collimation WG Note, CERN, Geneva, April 2008
- 100 A. Bertarelli, et al., Mechanical Design for Robustness of the LHC Collimators, proc. PAC 05, Knoxville, 2005
- 101 V. Kain, Machine Protection and Beam Quality during the LHC Injection Process, PhD-Thesis, Wien, Sept. 2005, p.28 ff.
- 102 V. Kain, et al., Beam Induced Damage – What is a Safe Beam?, Proceedings of Charmonix 2009, CERN, Geneva, June 2009, p. 171-176
- 103 R. Filipini, J. Uythoven, Safety Analysis of the Movable Absorber TCDQ in the LHC Beam Dumping System, CERN-ATS-2009-004, Geneva, March 2009
- 104 B. Goddard, Initial Beam Commissioning of Injection and Beam Dump, proc. Chamonix 2009 workshop, Chamonix, February 2009, p. 222
- 105 E. Shaposhnikova, S. Fartoukh, B. Jeanneret, LHC Abort gap filling by proton beam, proc. EPAC04, p. 611-613, Luzern, June 2004
- 106 F. Zimmermann, M. P. Zorzano, Touschek Scattering in HERA and LHC, LHC Project Note 244, CERN, Geneva, 2000

- 107 E. Shaposhnikova, Abort Gap Cleaning and the RF system, proc. LHC Performance Workshop - Chamonix XII, p. 182 ff, Chamonix, 2003
- 108 A. Drees, et al., Continuous Abort Gap Cleaning at RHIC, proc. EPAC04, p. 908 ff, Luzern, June 2004
- 109 X.-L. Zhang, et al., Tevatron electron lenses: Design and operation, Phys. Rev. ST Accel. Beams 11, 051002 (2008)
- 110 The LHC Design Report, Vol.1, Chapter 6, p. 140 ff, CERN, Geneva, 2004
- 111 W. Höfle, Experience gained in the SPS for the future LHC abort gap cleaning, proc. EPAC04, p. 577, Luzern, June 2004
- 112 Alan S. Fisher, Expected Performance of the LHC Synchrotron-Light Telescope (BSRT) and Abort-Gap Monitor (BSRA), LHC Performance Note-014, CERN, Geneva, December 2009
- 113 A. Koschik, B. Goddard, W. Höfle, G. Kotzian, D. Kramer, T. Kramer, Abort Gap Cleaning using the Transverse Feedback System: Simulation and Measurements in the SPS for the LHC Beam Dump System, proc. EPAC08, p. 2658, Genoa, June 2008
- 114 E. Gianfelice-Wendt, et al., LHC Abort Gap Cleaning with the Transverse Damper, proc. PAC09, Vancouver, May 2009
- 115 J.Uythoven, TT40 Experience and TI 8 Beam Tests, proc. 1st LHC Chamonix Workshop, Chamonix, Jan. 2004, p.77 ff
- 116 B. Goddard, V. Kain, et.al., Aperture Studies of the SPS to LHC Transfer Lines, proc. PAC05, Knoxville, 2005, p.1664 ff
- 117 B. Goddard, T. Kramer, et al., Beam Commissioning of the SPS LSS6 Extraction and TT60 for LHC, proc. PAC07, Albuquerque, 2007
- 118 LHC Transferlines and Injection Project, Schematic overviews, <http://proj-lti.web.cern.ch/proj-lti/Photos/Default.htm>
- 119 J. Uythoven et al., Beam Commissioning of the SPS-to-LHC Transfer Line TI2, EPAC08, Genoa, 2007
- 120 M. Lamont et al., The LHC Injection Tests, LHC Performance Note 1, CERN, Geneva, 2008
- 121 V. Mertens et al., Beam commissioning of injection into the LHC, Proc. PAC09, Vancouver, May 2009.
- 122 CERN Bulletin, 10 September: CERN in the media spotlight, CERN, Geneva, September 2008
- 123 P.J. Bryant, Kjell Johnsen, The principles of circular accelerators and storage rings, Cambridge University Press, 1993, p. 93
- 124 B. Goddard, et al., Aperture Measurements of the LHC Injection Regions and Beam Dump Systems, proc. IPAC10, Kyoto, May 2010
- 125 T. Kramer, et al., Performance Studies for Protection against Asynchronous Dumps in the LHC, proc. IPAC10, Kyoto, May 2010